A Study of Water Management in Polymer Electrolyte Fuel Cells: Compression Effect on Multiphase Flow

Thomas George Tranter

Centre for Integrated Energy Research (CIER)
School of Chemical and Process Engineering

University of Leeds

Submitted in accordance with the requirements for the degree of

Doctor of Philosophy

10th October 2016

The candidate confirms that the work submitted is his/her own, except where work which has formed part of jointly authored publications has been included. The contribution of the candidate and the other authors to this work has been explicitly indicated below. The candidate confirms that appropriate credit has been given within the thesis where reference has been made to the work of others.

Published articles for which the author is the primary author:

- Chapter 3: T. G. Tranter, A. D. Burns, D. B. Ingham, and M. Pourkashanian, "The effects of compression on single and multiphase flow in a model polymer electrolyte membrane fuel cell gas diffusion layer," *International Journal of Hydrogen Energy*, vol. 40, pp. 652–664, dec 2014. All results collection and analysis was performed by the first author.

- Chapter 4: T. G. Tranter, J. T. Gostick, A. D. Burns, and W. F. Gale, "Pore Network Modeling of Compressed Fuel Cell Components with OpenPNM," *Fuel Cells*, vol. 16, no. 4, pp. 504–515, 2016. All results collection and analysis was performed by the first author.

Articles submitted for review for which the author is the primary author:

- Chapter 5: T. G. Tranter, P. Stogornyuk, J. T. Gostick, A. D. Burns and W. F. Gale, "A method for measuring relative in-plane diffusivity of thin and partially saturated porous media: an application to fuel cell gas diffusion layers". Two data-sets were collected by the second author and three data-sets and all analysis was performed by the first author.

- Chapter 6: T. G. Tranter, J. T. Gostick, A. D. Burns and W. F. Gale, "Pore network modeling of capillary hysteresis in neutrally wettable fibrous media". All results collection and analysis was performed by the first author.

Published articles for which the author is **not** the primary author:

- Chapter 4: J. T. Gostick, M. Aghighi, J. Hinebaugh, T. G. Tranter, M. Höh, H. Day, A. Bazylak, A. D. Burns, W. Lehnert, and A. Putz, "Openpnm: A pore network modeling package," *CISE*, vol. 18, pp. 60 – 74, 2016. The

author played a major role in developing the code for which this publication is based upon. All documentation was written by Professor Gostick and the author performed a comprehensive review and edit of the main text. Some explanations of the code are taken from this publication and presented in Chapter 4 but do not form any results or discussions.

This thesis is dedicated to my wife Katherine for her unwavering support and love.

Acknowledgements

My thanks to Professors Derek Ingham, Alan Burns, William Gale and Mohamed Pourkashanian for providing supervisory support and funding to embark upon and continue this project. My special thanks also to Professor Jeff Gostick for providing additional supervision and continued support and guidance throughout the final two years of my studies. Without the initiative of Professor Gostick to begin an open source pore network modelling project, my studies would have taken a significantly different, and probably less fruitful direction. My thanks also to Dr. Mohammed Ismail for his initial tuition and guidance in the field of fuel cells and for providing the SEM images presented in Chapter 2, to Dr. Sandy Black and Dr. Alistair Clements for their help and guidance in the field of computational fluid dynamics and to Matthew Kok for his experimental expertise and friendship during my time at McGill University. Thanks also to my OpenPNM collaborators James Hinebaugh, Harold Day, Michael Hoh, Professors Aimy Bazylak and Werner Lehnert, Dr. Andreas Putz and especially Mahmoud Aghighi for his dedicated efforts and insightful conversations. I acknowledge with thanks the contribution of Pavel Stogornyuk, an undergraduate at McGill University who assisted me by collecting the raw SGL 10BA and Toray 120 datasets in chapter 5. I would also like to acknowledge the EPSRC for the grant funding I have received to pursue this project. And finally I would like to thank my family and friends for their love and encouragement throughout.

Abstract

One of the main obstacles to overcome regarding the uptake of renewable energy technologies, specifically wind and solar energy, is their intermittency. Current energy storage techniques are costly and in-efficient. Fuel cells are a promising candidate for future energy storage, as part of an integrated system combining renewable energy with hydrogen production as the storage vector with reconversion. The Polymer Electrolyte Fuel Cell (PEFC) has the greatest potential for use with micro-generated renewable power and is suitable for the widest range of applications. Hence it has received a great deal of attention from research institutions and industry over the last few decades. However, they suffer performance limitations due to flooding by liquid water in the porous components forming the electrodes of the cell.

Two numerical investigations utilising different methods to probe multiphase transport in porous media, and one experimental investigation into the flow through partially saturated porous media, are presented. The porous media under investigation are typical materials for PEFC gas diffusion layers (GDLs), and the influence of compression of the material on the multiphase transport is investigated. In addition, a further study assessing the suitability of pore-scale capillary pressure models for predicting multiphase flow behaviour is included as a final research chapter.

Nomenclature

Abbreviations	
ALOP	Access Limited Ordinary Percolation
CAD	Contact Angle Distribution
CESFF	Convection Enhanced Serpentine Flow Field
CFD	Computational Fluid Dynamics
CL	Catalyst Layer
CNFS	Carbon Nano Fibre Sheet
CR	Compression Ratio
CSF	Continuum Surface Force
EOD	Electro Osmotic Drag
EW	Effective Weight
ESEM	Environmental Scanning Electron Microscopy
FC	Fuel Cell
FCEV	Fuel Cell Electric Vehicle
FCTS	Fuel Cell Test Station
FM	Full Morphology
GCI	Grid Convergence Index
GDL	Gas Diffusion Layer
IP	In-plane
LBM	Lattice-Boltzmann Method
LPF	Late Pore Filling
MEA	Membrane Electrode Assembly
MIO	Morphological Image Opening
MPL	Micro-porous Layer
NMR	Nuclear Magnetic Resonance

Abbreviations Continued	
(HT-)PEFC	(High Temperature-)Polymer Electrolyte Fuel Cell
PCI	Phase Change Induced
PNM	Pore Network Model
PSD	Pore Size Distribution
PTFE	Polytetrafluoroethylene
TEPN	Topologically Equivalent Pore Network
TP	Through-plane
UFT	Unsaturated Flow Theory
VOF	Volume of Fluid

Roman		
A	m^2	Cross-sectional area
C_i	kmol m^{-3}	Concentration of species i
D	m^2 s^{-1}	Diffusion coefficient
d	m	Diameter (Pore, Throat, Fibre)
EW	kg $kmol^{-1}$	Effective Weight
F	96485 [C mol^{-1}]	Faraday's Constant
g	$m^2 s^{-1}$	Gravitational constant
I	A m^{-2}	Current Density
J_{Diff}	m^2 s^{-1}	Diffusional flux
J_{cap}	kg m^{-2} s^{-1}	Capillary Flux
K	m^2	Permeability
N	mol m^{-2} s^{-1}	Molar Flux
P	Pa	Pressure, Partial Pressure of species i
Q	m^3 s^{-1}	Volumetric flow rate
q	kg m^{-2} s^{-1}	Mass Flux
R_g	8.314 [J K^{-1} mol^{-1}]	Universal gas constant
R & r	m	Various radii
S	-	Saturation
s	-	Shape (of distribution)
T	K	Temperature
t	s	Time
$\mathbf{T}$	Pa	Stress Tensor
u_i	m s^{-1}	Velocity of phase i
V	m^3	Volume
v_s	m s^{-1}	Superficial velocity
W	J	Work
X	-	Random variable
x	-	Mole fraction

Suffices	
C	Capillary
g	Gas
l	Liquid
NW	Non-wetting
p	pore
r	relative
v	viscous
w	water
W	Wetting

Greek		
α	-	Volume Fraction
β	deg	Filling angle
β_F	m^{-1}	Inertial Permeability (Forchheimer term)
Γ	-	Relative Mobility
ϵ	-	Porosity
η	V	Late Pore Filling Fitting Parameter
θ	deg	Contact Angle
κ	m^{-1}	Curvature of interface
λ	-	Membrane Water Content
μ	Pa s	Dynamic Viscosity
ν	m^2 s^{-1}	Kinematic Viscosity
ρ	kg m^{-3}	Density
σ	Pa m^{-1}	Surface Tension Coefficient
τ	-	Tortuosity
ϕ	V	Cell potential
Φ	-	General Transport Property

Chemical Symbols	
CH_4	Methane
CO	Carbon Monoxide
e^-	Electron
H^+	Proton
H_2	Hydrogen
H_2O	Water
O_2	Oxygen
SO_3^-	Sulphur Trioxide

Contents

List of Figures

Chapter 1

Introduction

1.1 Energy

Climate change is one of the great challenges facing mankind. The impacts are now being felt and can be seen in changing weather patterns, an increasing frequency of extreme weather events and melting polar ice-caps [19]. However, the worst effects might still be avoided if current energy and transport systems are changed to less polluting ones. Renewable energy sources have great potential to displace emissions of greenhouse gases from the combustion of fossil fuels and thereby to mitigate climate change. If implemented properly, renewable energy sources can contribute to social and economic development, to energy access, to a secure and sustainable energy supply, and to a reduction of negative impacts of energy provision on the environment and human health.

The infrastructure, supply lines and markets for fossil fuels are all well established and new technologies are slow to come on board. The general increase in energy consumption, and dominance of the traditional energy sources over the past five decades can be seen in figure 1.1. However, we now know that burning fossil fuels releases greenhouse gases which contribute to climate change. The IPCC's Fourth Assessment Report concluded that most of the observed increase in global average temperature since the mid-20th century is very likely due to the observed increase in greenhouse gas concentrations. The term "very likely" refers to a greater than 90% probability of occurrence. Sceptics point to the fact that climate change has previously happened without anthropogenic cause but

the link between CO_2 concentration and temperature is now held in general scientific consensus, [20]. The concentration of CO_2 in the atmosphere has increased unnaturally to around 390 ppm, which is 39% above pre-industrial levels. At the time of writing, the most recent (5th) report from the IPCC puts the scientific evidence for climate change beyond doubt stating that: "Warming of the climate system is unequivocal, and since the 1950s, many of the observed changes are unprecedented over decades to millennia. The atmosphere and ocean have warmed, the amounts of snow and ice have diminished, and sea level has risen." [21].

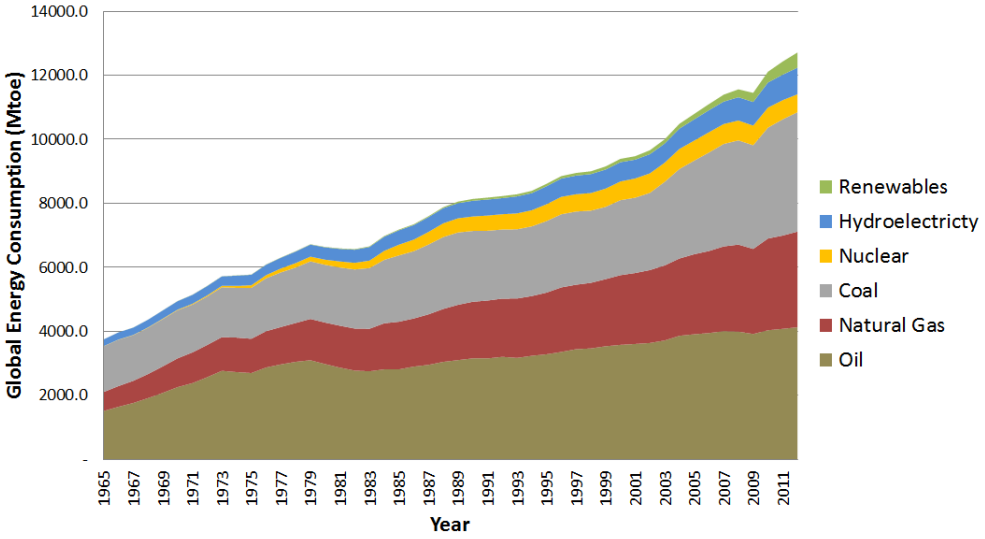

Figure 1.1: Global Energy Consumption by Resource, [4].

Figure 1.1 shows that, whilst the overall contribution from renewable energy sources to global energy consumption is still relatively small, interest and uptake is growing rapidly. This is primarily due to three reasons: Firstly, a growing awareness and public pressure on governments to de-carbonise the energy supply for environmental reasons. Secondly, a growing uncertainty about fossil-based energy supply in terms of existing capacity (e.g peak oil) and security issues surrounding external trade partnerships. Thirdly, the falling cost of producing energy from renewable sources, especially in comparison with other low-carbon technologies such as nuclear power. The final reason concerning cost is especially encouraging as renewable energy has historically been prohibitively expensive to

implement in developing countries, where it could have the most benefit. Clean and efficient energy production and storage is key to achieving global carbon reduction targets aimed at mitigating climate change. The trend towards electricity as the primary source of energy means that storage of electrical energy is particularly important. Currently the production of electricity is highly centralized and often far away from the consumer but in the next few decades we will see a move towards the decentralisation of heat and power generation, primarily from renewable sources.

Arguably the largest drawback of renewable energy sources is their intermittent output and inability to easily match supply and demand. This problem only increases when trying to integrate a large renewable contribution into the power network which has strict regulations on voltage and frequency [22]. For example, the impact of integrating a large number of wind turbines into an electricity grid is to reduce the overall generation efficiency, as conventional generating units may need to operate at sub-prime levels. A greater level of reserve power may also need to be maintained on standby, should a sudden drop in wind occur for a sustained period. In periods of strong wind the power output from the turbines may need to be curtailed, especially when local demand is low and transmission capacity is reaching a thermal limit [23]. The problem is lessened when a natural correlation between supply and demand exists, air conditioning and solar energy for example, but these correlations are too small to be relied upon.

Greater deployment of smart energy storage devices and techniques will one day solve the problem of intermittency and lead to far greater uptake of renewable energy. The fate of renewable energy is inextricably linked to the development of efficient, clean, reliable and affordable energy storage. Also, an important point to make is that energy storage must also be practical across a range of power scales and applications, including stationary and portable. Hydrogen storage with fuel cell conversion could be implemented on any number of scales due to the modularity of the fuel cell. Together with renewable energy producing hydrogen through electrolysis, the use of fuel cells in transport and stationary power could result in a permanent sustainable energy system. Although one technology alone is unlikely to provide the "silver bullet", much progress has been made in the general field of electrochemical energy storage (EES) [24], [25]. In addition to

grid level or stationary power solutions, fuel cells are likely to have the biggest market penetration in the transport sector [26], [27]. Technologies for hydrogen production, storage and utilization have already been developed, and although these technologies are not mature, the lack of widespread adoption is largely economic. There is a "chicken-egg" scenario with hydrogen production and fuel cells where the development of each technology is intrinsically linked to the other. Currently small-scale niche applications such as small bus fleets and off-grid power are the most common for these technologies, although a growth in commercial development in the automotive sector, especially in Japan, is very promising. Toyota have recently released a new fuel cell electric vehicle (FCEV) called the "Mirai", meaning future in Japanese. The company states that performance has been increased by 2.5 times compared with their prototype model developed in 2008 [28].

1.2 Fuel Cells

A fuel cell is an electrochemical device that continuously converts fuel (typically hydrogen and oxygen) into energy in the form of electricity and heat. Fuel cells are therefore similar to batteries and conventional engines but with the important difference that they are not thermodynamically constrained by the Carnot efficiency [29]. Fuel cells are considered by many to be the most promising energy conversion device currently in development. This is primarily due to the advantage of having an electrochemical conversion rather than a thermal combustion to generate mechanical energy via a Rankine or Otto cycle. They are static, highly efficient, and in the case of the Polymer Electrolyte Fuel Cell (PEFC), will only produce potable water and heat as a by-product of the reactions taking place. Many of the fuel cell components are also easily recovered and recycled after use, unlike conventional batteries. If the 19th century was defined by the proliferation of steam power, and the 20th by the internal combustion engine, many believe that the 21st century will be defined by the fuel cell [30]. It is also worth mentioning that recent progress in other electrochemical devices such as Li-air batteries [31] and Redox Flow Batteries [32] is promising too, but is out of the scope of this thesis.

The term "zero-emission engine" is often used to describe a fuel cell when operated with pure hydrogen. However, pure hydrogen exists very rarely on Earth, as the gas is light enough to escape from the atmosphere. Therefore, hydrogen must be reformed or produced by electrolysis using electricity from a primary generator and stored in a controlled environment. Extensive research into hydrogen storage is currently being undertaken, as summarized by [33]. If the primary generator is renewable then the fuel cell converting the hydrogen into energy can be considered truly zero-emission, if emissions associated with the construction, installation of the generator and transport of fuel are neglected or balanced. However, the most common form of hydrogen production is steam reforming of natural gas, of which methane (CH_4), is the main component. The following reactions take place in succession [34]:

$$CH_4 + H_2O \longrightarrow CO + 3\,H_2 \tag{1.2.1}$$

and

$$CO + H_2O \longrightarrow CO_2 + H_2 \tag{1.2.2}$$

The first reaction involves a catalyst (usually nickel) and a temperature of around 850 °C and a pressure of around 2.5 MPa. CO is then fed to a second reactor and combined with ambient steam to extract more hydrogen and produce carbon dioxide. Heat is recovered from the second stage and fed back to the first to increase efficiency but the majority of the heat energy required to drive the primary reaction is usually obtained from the direct combustion of the methane gas which also produces carbon dioxide. Hydrogen production in this way is therefore very energy intensive and has a large carbon-footprint but is currently the most wide-spread method. A cost analysis of the different methods of hydrogen production currently places coal as the cheapest feed-stock, but the author's acknowledge that alternative fuel sources may become cheaper than fossil fuels in the future [35]. Although very important to the future of fuel cell technology, a discussion of hydrogen production, storage and distribution is out of the scope of this thesis.

It is now becoming clear that fuel cells will become prevalent through three major applications: portable devices, stationary power and transportation. There

are different types of fuel cells and they can be grouped by the type of electrolyte they use. The various fuel cells are reviewed by [36] along with typical output power and applications. The PEFC, which is the subject of this investigation, is best suited to portable devices and transportation but could also be used in small scale stationary power generation up to 100 kW, for example as a back-up generator. The PEFC has a low operating temperature, quicker start-up, longer durability and equivalent power density compared with other fuel cells [37]. PEFC can easily be combined into stacks of varying power outputs, making them very versatile. For these reasons, the PEFC has received the greatest attention from researchers and industry and it is likely that developments within the PEFC industry will lead to cost-savings across the fuel cell industry as a whole. Therefore, it was decided to focus research efforts on the PEFC to enable greater understanding of its performance limitations.

The UK H2 Mobility project was established by the UK government to evaluate the benefit of FCEVs to the UK and develop a roadmap for the introduction of the vehicles and re-fuelling stations [38]. Their first major report published in 2013 predicts that 1.6 million FCEVs will be operational by 2030 in the UK, with annual sales of 300,000. The report also finds that hydrogen should be immediately cost competitive with diesel, with 60% of the carbon footprint by 2020 reducing over time as electrolysis increases and the electricity supply decarbonises. If the uptake figures are correct then by 2030 the net reduction in carbon dioxide emissions from FCEVs could be three million tonnes per annum. Several auto-manufacturers including Daimler, Hyundai, Toyota and Honda have released prototype FCEVs, and most are now stating that the first production batches will be available to the general public in the immediate future. The Toyota Mirai was released in Japan in December 2014 and at the time of writing the UK has also received a small number of deliveries to "early adopters" such as Transport for London. The main goals of research into fuel cells are to improve their power density, reduce their cost, improve durability and simplify their operation.

For the PEFC the following anodic and cathodic half-cell reactions take place respectively:

$$H_2 \longrightarrow 2\,H^+ + 2\,e^- \tag{1.2.3}$$

$$2\,H^+ + 2\,e^- + \tfrac{1}{2}\,O_2 \longrightarrow H_2O \tag{1.2.4}$$

The components of the PEFC are summarised in Table 1.1 and a schematic diagram of a single cell with pertinent transport processes is shown in Figure 1.2. The PEFC is comprised of a semi-permeable membrane, sandwiched between two porous electrodes connected to current collector plates, often referred to as bipolar plates. The reactant gases are distributed via the current collectors which have channels machined into them, and then diffuses through the gas diffusion layer (GDL) and microporous layer (MPL), if one is applied, towards a central catalyst layer (CL) where reactions take place. Once the protons are liberated from the hydrogen supplied on the anode side of the cell, they are transported across the membrane to the cathode side where they combine with oxygen and electrons to form water. This proton transport is coupled with liquid water transport and requires a hydrated membrane to function well. The electrons produced at the anode conduct back through the GDL and current collector plate, follow an external circuit producing work, and enter the cell on the cathode side to complete the reaction.

The key to good cell performance is ensuring that the transport processes described are as facile as possible. Starting with the membrane, protons only migrate across if the membrane is hydrated; although water is produced in the cathodic reaction, often the reactant streams are also humidified to aid the hydration of the membrane. At high current density water vapour pressure may exceed saturation pressure in parts of the cell and liquid water may form. This blocks the reactant gases and reduces the power output of the cell. Therefore, water balance is critical to cell performance where too little or too much will lead to decreased performance. This is especially true when operating at high current density and power, as more water is produced inside the cell. The need for water management has implications for the materials used in the cell. A highly porous gas diffusion layer in the electrode will aid the supply and removal of reactants and products, but will have reduced thermal and electrical conductivity compared

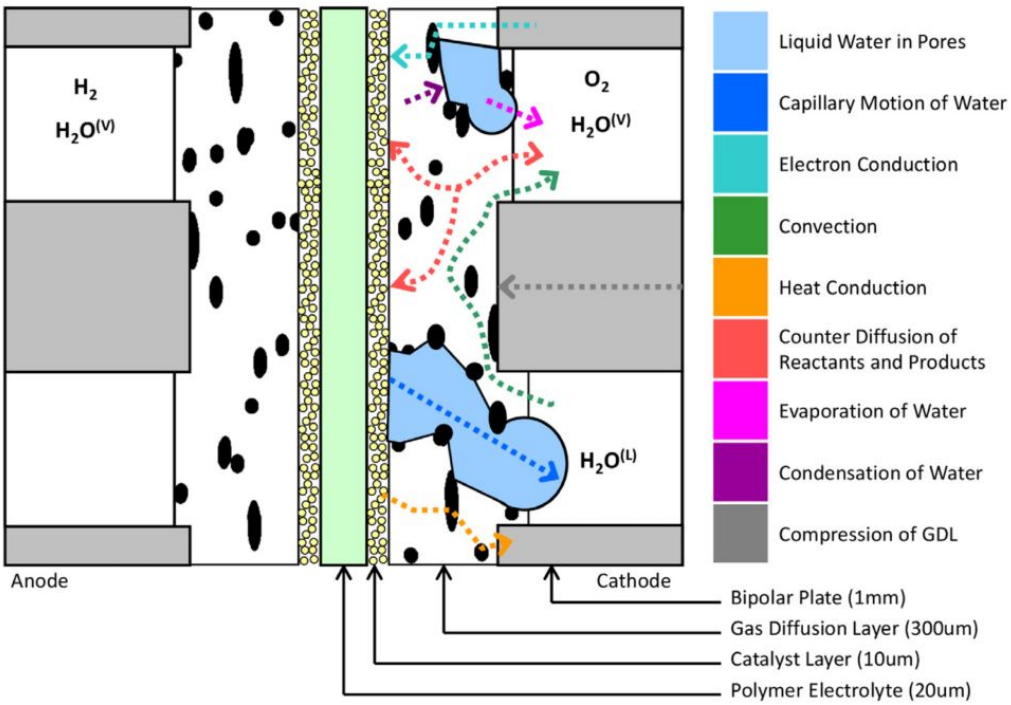

Figure 1.2: Schematic of a PEFC assembly illustrating mass transport and phase change mechanisms [5].

with a less porous material. The design of the flow fields in the collector plates is also important for managing the performance of the cell whilst minimising the pressure required to distribute the gases. Certain designs, such as the serpentine flow field, facilitate the removal of water but require larger pressure differentials between inlets and outlets. Some of the major advances in the new Mirai fuel cell stacks have come from a new flow field design which enhances convection in the porous electrodes and new water management strategies based on using non-humidified gases and recycling the purged water from the cathode side back into the anode to keep the membrane hydrated [28].

In the broad sense, the optimisation of fuel cell performance by increased understanding of water management is the focus of this thesis. However, the subject of water management is multi-faceted and the narrower focus of the thesis is elaborated in Chapter 2, as a study of the effects of compressing cell components on multiphase flow. Both numerical and experimental tools are used to investigate the phenomena affecting water distribution and transport within the fuel cell with a particular focus on the gas diffusion layer, as the GDL is really the key to managing water effectively.

1.3 Structure of this Thesis

This thesis is organized into seven chapters. An introduction and summary of the background and motivation have been presented in Chapter 1, along with an overview of the contributions of the thesis. In Chapter 2, an extensive literature review provides an overview of the major topic of water management in PEFCs, the broader theme of this thesis. The literature review covers an overview of transport mechanisms in the various fuel cell components, a critical review of two-phase flow modelling approaches, a summary of common visualisation techniques, which are not a direct focus of this research but serve as an important validation tool for modelling work, and a critical review of experimental characterization techniques for fuel cell components. The literature review concludes with a summary and explanation for the choice for the narrower topic of the effects of compression on multiphase flow in GDLs. Chapter 3 covers the first major research topic which is a computational fluid dynamics study of the effects of compression on liquid

Fuel Cell Component	Functions	Material Composition
Membrane	Proton conduction Water transport Electronic insulation	Solid polymer electrolyte Perfluorinated version such as Nafion
Catalyst Layer	Catalysis of cathode reaction Proton conduction from membrane to reaction sites Electron conduction from cathode GDL Water removal from reaction zone into GDL Heat generation/removal	Catalyst ink applied to membrane
Micro-porous layer (MPL)	Enhance electrical conductivity Enhance gas diffusion Aid water management	Carbon powder with 20% wt PTFE Carbon nano tubes
GDL	Oxidant supply and distribution Electron conduction towards reaction zone Heat removal 2-phase Water transport (liquid/vapor)	Carbon fibre paper or carbon cloth
Bipolar Plate	Supply reactant gases Electron conduction Heat conduction and convection 2-phase Water removal (liquid/vapor)	Graphite or metal

Table 1.1: Fuel Cell Components: Functions and Material Composition.

water transport in a model PEFC GDL, this chapter lays the initial groundwork for the second modelling approach and provides useful insights on the key structural parameters important for capillary dominated flow. Chapter 4 covers the pore network modelling approach and extends the work covered in Chapter 3 to investigate the effect of compression on the constitutive relations used in multiphase fuel cell modelling, namely the relative permeability and diffusivity of the GDL. The effect of spatially varying porosity caused by compression of the GDL by the grooved bipolar plates on the fuel cell performance is also investigated. In Chapter 5 an experimental method for measuring relative in-plane diffusivity is presented with results for some common GDLs and the effect of wet-proof coating is discussed. The method is extended from work on dry materials with the building of a custom sample holder that regulates the temperature and saturation of partially flooded GDLs. An oxygen sensor is used to monitor transient changes to concentration at the sample boundaries and Fick's 2nd Law is used to calculate the diffusion coefficient. Chapter 6 covers in greater detail the consequences of choosing the correct pore-scale capillary pressure model for use in pore network modelling. Light is shed on the effect of saturation distribution on the relative diffusivity of GDLs for drainage and imbibition scenarios. This is important to consider when different percolation and drying processes occur within the cell, under different operating conditions. Finally, conclusions and recommendations for future research are presented in Chapter 7. Figures and tables are provided in-line with the text for each chapter.

Chapter 2

Literature Review

2.1 Fuel Cell Overview

Springer describes water management in his seminal paper on modelling the PEFC [39] as "walking a tightrope between the two extremes" of membrane dehydration, leading to a loss of proton conductivity, and electrode flooding leading to a blocking of reactant gas. Water is usually transported into the cell via the humidified inlet streams, electro-osmotic drag (EOD) transports water across the cell coupled with proton migration from anode to cathode, and back-diffusion occurs along the concentration gradient from cathode to anode. Water is produced at the cathode catalyst layer by the reduction of oxygen when combined with the migrated protons and electrons which flow around an external circuit to complete the redox reactions (Equations 1.2.3 and 1.2.4). Optimum performance and current density is achieved when the membrane is fully hydrated and water is expelled at the same rate that it enters and is created without saturating the porous media of the electrodes.

Since water can exist in both a liquid and vapour phase, when talking of water management it should be understood that we are talking about the liquid phase. Careful thermal management can also be used to effectively manage water by producing vapour. Water vapour will transport with sufficient ease along the pressure gradient existing between the inlet and outlet of each flow stream. On the other hand, liquid water is liable to remain within the porous media, flooding the electrodes and also forming droplets on the surface of the GDL.

Under different flow channel configurations and gas-phase flow rates, droplets may grow to form slugs that block the flow streams or films which may travel in stratified configurations with the gas streams towards the outlets. When vapour pressure exceeds saturation pressure a phase change will occur and vapour will condense into liquid water. This may happen in regions of the cell where diffusion is limited, such as the catalyst and microporous layers, or where permeability in the porous media is reduced or temperature decreased such as portions of the GDL that have become compressed by the flow channel ribs.

Water management strategies can be broadly categorised into the following three areas [40]:

i Optimisation of the operating conditions such as temperature and pressure between the inlet and outlet, which can lead to parasitic losses in fuel cell performance or degradation of materials.

ii Cell design and balance of plant such as the inclusion of humidifiers, pumps and flow field design within the bipolar plates.

iii Membrane Electrode Assembly (MEA) component materials (which includes the membrane, CL, MPL and the GDL) structure and design: such as hydrophobic treating, inclusion of a microporous layer or coating of the catalyst layer with an anti-flooding material.

The classic indicator of fuel cell performance is the polarisation curve which can be seen in Figure 2.1 to dip sharply in voltage at high current density due to the mass transport limitations of reactant gases. Other polarization losses are also shown in separated form in Figure 2.1 as deviations from the equilibrium potential, which is dependent on temperature and pressure. Briefly, activation losses are the potential losses required to start the electrochemical reactions and are associated with sluggish kinetics. The oxygen reduction reaction (ORR) occurring at the cathode is much slower than the hydrogen oxidation reaction (HOR) at the anode, and much research is focused on improving these losses for conventional platinum catalysts and non-conventional cheaper alternatives [41], [42]. Ohmic losses occur due to resistance to flow of ions through the membrane electrolyte and

electrons around the electrically conducting circuit formed by the fuel cell components. Bulk resistance to electronic flow is almost negligible, however contact resistance between components is of the same order as ionic resistance through the membrane. Membrane water content decreases ionic resistance and clamping pressure decreases contact resistance. Over clamping of the components, however, reduces diffusive transport and damages components. Performance losses due to a lack of water management are broadly categorised as mass transport or concentration loss which dominate the voltage and performance drop at higher current densities. The presence of liquid in the porous media reduces porosity and creates more barriers to reactant gas transport. Therefore, effective water management will mitigate mass transport loss and lead to greater power output. This has implications for fuel cell performance and cost, as greater power per unit cell will result in fewer cells and fewer materials.

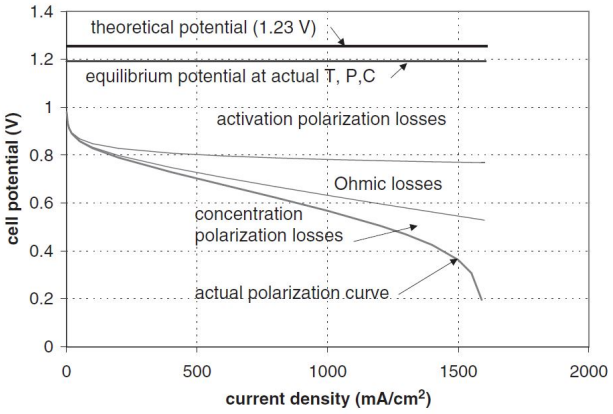

Figure 2.1: Typical Polarisation curve for PEFC [6].

The polarisation curve is usually measured as an average over the entire terminal area. In general, designers will aim to create uniform distribution of gases and current, but certain flow field designs inevitably lead to non-uniformities in concentration, which in turn lead to non-uniform current distributions. Cell potential, ϕ, depends upon the partial pressures, P, of the reactants and products as shown by the Nernst equation:

$$\phi = \phi_0 - \frac{R_g T}{n_e F} ln \left(\frac{P_{H_2O}}{P_{H_2} P_{O_2}^{1/2}} \right) \quad (2.1.1)$$

where ϕ_0 is the reversible cell potential, R_g is the universal gas constant, T is the temperature, n_e is the number of electrons in the electron transfer step and F is Faraday's constant. As the partial pressure of oxygen decreases and water increases towards the outlet the voltage will decrease. Concentration loss is also termed mass transport loss as the blocking of reactant gas by liquid water has the same detrimental effect [7].

The simplest form of fuel cell operation is to use un-humidified gases. The relative humidity of the atmosphere, when not using pure oxygen, and product water is used to humidify the membrane. In this situation a balance is usually created by supplying the gases in counter-flow configuration but inevitably portions of the membrane will remain dryer than others, especially at higher current densities. This method of operation imposes a limit on the temperature at which the cell can function without drying out which is typically 60°C and this limits the electrochemical activity and proton conductivity. In practice, fuel cells are typically operated at around 80°C which means that humidified gases are required to maintain a hydrated membrane [7]. However, when humidifying the gases the risk of flooding is greatly increased and management of excess water will usually rely on pumping the reactant gases at greater pressure to clear the channels. This method is effective but also energy intensive and a preferable solution is to minimise the accumulation of liquid water passively by enhancing the properties of the MEA components. This review will analyse water management strategies for each of the fuel cell components comprising a single cell, as listed in Table 1.1 but will not extend discussions to balance of plant and stack design.

For a discussion about water management it is also useful to know the average pore sizes and typical thickness of each component, which are listed in Table 2.1. The fact that the length scales are very small and that average pore size varies by several orders of magnitude presents challenges when modelling the fuel cell. As a result, different modelling techniques are often most suitable for

Fuel Cell Component	Typical Thickness µm	Average Pore Size µm
Membrane	200	NA
Catalyst Layer (CL)	50	0.05
Micro-porous layer (MPL)	100	0.5
Gas Diffusion Layer (GDL)	400	10
Gas Flow Channel	1500	500

Table 2.1: Fuel Cell Components: Typical Thickness and Pore Sizes.

different parts of the fuel cell and when modelling a whole fuel cell, instead of representing the physical geometry of each component it is more common to work with average properties for simplicity and to save on computational expense. However, macro-scale models for two-phase transport cannot fully describe the processes occurring in the porous media of the fuel cell because the discretisation of the computational domain is often on a scale larger than the average pore size of the media. These models must therefore employ empirical relationships between microscopic features and macroscopic averaged behaviour and properties.

A review of the dominant water transport mechanisms in each of the PEFC components is presented in this section followed by a detailed discussion of different modelling approaches. To put the modelling in context and overview of common visualisation techniques is also presented and a review of experimental characterisation of porous media. Finally the subject of porous structure and the influence of compression of the porous components during cell assembly is discussed and a brief note on phase change is given.

2.2 Water Transport in PEFC Gas Diffusion Layers (GDL)

The main transport mechanisms in the gas diffusion layers on both sides of the cell are diffusion along concentration gradients and convection due to the pressure difference in the flow channel adjacent to the diffusion layers and within the pores due to the capillary effect. Logically it follows that a higher flow rate will exert

greater pressure on the reactants and products of the reactions ensuring greater dispersion and removal. However, the parasitic power required to operate with high flow rates may reduce the overall efficiency of the cell, so diffusion and capillary action are the dominant transport mechanisms. Two-phase flow exists and flooding occurs when the liquid water volume fraction begins to dominate the gaseous phase. A review of gas diffusion layer properties and characterisation is provided by Park et al. [43]. The most common materials used as GDLs are carbon-based fibrous woven cloths and non-woven papers, pictured in Figure 2.2.

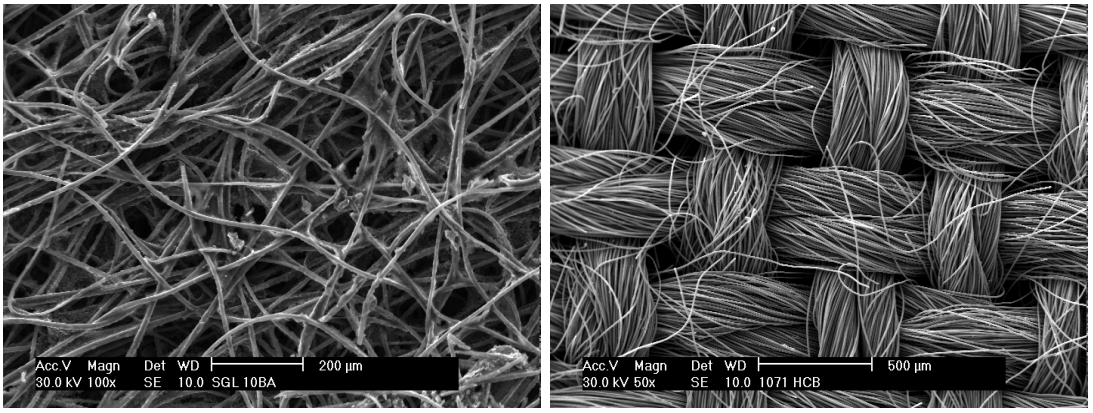

(a) SGL 10 BA carbon paper (b) Typical woven carbon cloth

Figure 2.2: SEM micrographs of two typical carbon based GDLs, courtesy of Dr. Mohammed Ismail

Park investigated the effect of using the different carbon-based GDLs and found that paper gave better all round performance as electrical conductivity is higher and when an MPL is applied the water management properties led to better oxygen distribution and higher limiting current [44]. Under certain conditions, however, such as high RH, carbon cloths are found to perform better [43]. Many of the physical properties of common GDLs have been studied [45], [46] with ex-situ methods, such as the porosity, pore-size distribution, Polytetrafluoroethylene (PTFE) content, wetting properties, permeability and diffusivity yet gaps in knowledge still remain concerning multiphase transport properties. GDLs are thin and have anisotropic structure due to the general alignment of fibres along the in-plane direction. This alters the transport properties in favour of the in-plane direction which has increased permeability, electrical and thermal

conductivity, compared with through-plane [47], [48]. The thin nature of GDLs and their anisotropic properties make multiphase characterisation a challenge, and this has led to a general focus on modelling approaches. The key transport mechanisms relevant to the GDL are now summarized in greater detail.

2.2.1 Diffusional Transport

The diffusional flux through the porous GDL is proportional to the porosity, ϵ, and inversely proportional to the tortuosity, τ, of the media as a straighter pathway will create fewer physical barriers. The general conservation of mass equation for a species in a fluid passing through porous media, without source terms since no reactions or phase changes are taking place, is given by Shen and Chen [49] as:

$$\frac{\partial(\epsilon c\rho)}{\partial t} = -\nabla.(c\rho\mathbf{u} - \rho\mathbf{D}\nabla c) \tag{2.2.1}$$

where ρ is the fluid density (assumed to be constant), $\mathbf{u}$ is the Darcy velocity which is zero in the absence of a pressure gradient across the sample, c is the concentration of the species, and $\mathbf{D}$ is a general diffusion-dispersion tensor defined as:

$$\mathbf{D} = \epsilon\left\{d_m\mathbf{I} + |\mathbf{u}|\left[d_l\mathbf{E}(\mathbf{u}) + d_t\mathbf{E}^{\perp}(\mathbf{u})\right]\right\} \tag{2.2.2}$$

where $\mathbf{I}$ is the identity tensor, d_m is the molecular diffusion coefficient and is assumed to be spatially constant for a given temperature. The other terms inside the square brackets are dispersion related and can be ignored for the purposes of this study. The GDL is assumed to be isotropic in the cross-sectional plane normal to diffusion, so Equation 2.2.1 can be simplified to its one dimensional form, known as Fick's 2nd Law of Diffusion:

$$\frac{\partial(c)}{\partial t} = d_m\Delta c \tag{2.2.3}$$

Note that ϵ has disappeared because the impact of the reduction in pore volume on the time-dependent accumulation term (LHS) and the reduction in

flux of species incorporated into **D** (RHS) cancel each other. Shen and Chen warn that cancelling of the porosity term leads to identical concentrations at a given point in space and time regardless of the material's porosity, an incorrect result. This implies that an effective diffusion coefficient should be used instead and must scale inversely with tortuosity as:

$$D_{EFF} = d_m \frac{\epsilon}{\tau} \tag{2.2.4}$$

where tortuosity τ represents the increase in diffusion path length in the presence of obstacles. A simple definition of tortuosity follows from considering a porous medium as a bundle of tubes or capillaries which are winding and parallel and is defined here as:

$$\tau = \left(\frac{\Delta l}{\Delta x}\right)^2 \tag{2.2.5}$$

where Δl is the diffusion path length and Δx is the physical length of the medium. Using the effective diffusion coefficient Equation 2.2.3 becomes:

$$\frac{\partial(c)}{\partial t} = \frac{d_m}{\tau}\Delta c = D'\Delta c \tag{2.2.6}$$

Here we have used the notation D' to represent a reduced diffusion coefficient, dependent only on tortuosity. There is much confusion surrounding the definition of tortuosity owing to the inconsistent mathematical treatments throughout the literature as documented by Epstein [50]. It is common in fuel cell literature to express the normalised effective diffusivity of dry materials purely in terms of porosity such as:

$$\frac{D_{EFF}}{d_m} = f(\epsilon) = \frac{\epsilon}{\tau} \tag{2.2.7}$$

since the tortuosity is some function of porosity. A common expression for τ is $\epsilon^{-0.5}$ leading to the commonly used Bruggeman correlation [51]:

$$f(\epsilon) = \epsilon^{1.5} \tag{2.2.8}$$

Other common expressions for $f(\epsilon)$ are presented by Shen and Chen [49] and

Hwang and Weber [18]. The effective diffusivity is also reviewed by Zamel and Li [52] and Ismail et al. [53] who find the Bruggeman correlation to be a poor approximation for anisotropic fibrous GDLs, as it was originally conceived for the electrical conductivity of a porous medium composed of uniformly distributed spheres. Ismail et al. model the effects of the different relations and find that the Bruggeman relation, and others that do not incorporate a percolation threshold, over-predict the diffusive flux by up to a factor of two.

When considering a partially saturated domain, liquid can be treated in a similar fashion to the solid phase, with the effect of both reducing the pore volume and increasing the tortuosity. So if saturation, S, is the fraction of the pore volume occupied by water, then all the porosity terms can be multiplied by $(1-S)$ and the effective diffusivity can be formulated as follows:

$$\frac{D_{EFF}}{d_m} = f(\epsilon).g(S) = \frac{\epsilon}{\tau_\epsilon}.\frac{(1-S)}{\tau_S} \tag{2.2.9}$$

In Equation 2.2.9 we have decoupled the contributions of gas phase blockages, from solid and liquid respectively, into: 1) volume reduction as the numerators and 2) tortuosity increase as the denominators. When Equation 2.2.9 is substituted into Equation 2.2.1 the following is obtained:

$$\frac{\partial(c)}{\partial t} = \frac{d_m}{\tau_\epsilon \tau_S}\Delta c = D'_S \Delta c \tag{2.2.10}$$

Note that as before, where porosity related terms cancel for Equation 2.2.6, so does the contribution of saturation to a reduction in pore volume in Equation 2.2.10. The transient experiment, detailed in Chapter 5, only measures the reduced diffusion coefficient (D'_S) due to an increase in tortuosity i.e. diffusional path-length. Therefore, by normalising the measured reduced diffusion coefficients by the dry values, one obtains the saturation dependent tortuosity: $\tau_S = D'/D'_S$. This relation is often described using a power-law function such as:

$$\tau_S = (1-S)^{-m} \tag{2.2.11}$$

Therefore, the combined saturation dependent function in Equation 2.2.9 can be expressed as follows, with $n = 1 + m$:

$$g(S) = \frac{(1-S)}{\tau_S} = (1-S)^n \tag{2.2.12}$$

This is the familiar form used throughout the fuel cell literature, but it must be remembered that it includes both saturation dependent modifications to the effective diffusion coefficient. This is particularly important when used in transient simulations, where the reduced coefficient should be used.

Different relations for the effects of structure and multiple phases are possible and have also been reviewed by Zamel and Li [52]. Understanding how the multiphase relationship, $g(S)$, is influenced by the anisotropic nature of GDLs, and how it may change under compression is the central topic of investigation for Chapters 3 and 4. Measuring the relationship for the in-plane direction is the focus of Chapter 5 as all previous experiments have focused on the through-plane direction.

2.2.2 Convective Transport

Convective flow will suffer resistance from the porous media and undergo a pressure drop according to Darcy's Law which applies to each phase (i):

$$v_s = \frac{-K_i}{\mu_i}\nabla P \tag{2.2.13}$$

where $v_{s,i}$ is the flux of each phase, measured as the volumetric discharge per unit area so has units of ms^{-1}, also referred to as the superficial velocity ($v_s = u\epsilon$). K_i is the effective permeability of the media and μ_i is the dynamic viscosity of each phase. At high flow rates inertial effects become important and the flow rate may depend non-linearly upon the pressure drop. An additional term is then added to the Darcy equation to make the Forchheimer equation:

$$\nabla P = -\frac{\mu_i}{K_i}v_{s,i} - \beta_F \rho_i v_{s,i}^2 \tag{2.2.14}$$

where β_F is the inertial permeability.

The effective permeability, K_i, is related to the absolute permeability, K_0, by dimensionless relative permeability functions dependent on the saturation equiv-

alent to Equation 2.2.12 for diffusivity:

$$K_i = K_{ri} K_0 \tag{2.2.15}$$

$$K_{rg} = (1 - S)^n \tag{2.2.16}$$

$$K_{rl} = (S)^n \tag{2.2.17}$$

Values for the exponent ranging from 1 to 7 (normally 3) ([54], [55], [56]) have been reported and a straight-forward dependence on saturation alone may be too simplistic. Kaviany states that relative permeability is a function of matrix structure, saturation, surface tension, wettability (contact angle) of the solid phase, the ratio of the liquid and gas phase densities and history of the system as drainage and imbibition will often produce hysteresis in the capillary pressure vs. saturation curves [57]. If the flow is Darcean then the intrinsic permeability should be a property of the porous structure and not depend on the phase flowing through it, this is reflected in Equation K_{ri} by noticing that both effective permeabilities reduce to the intrinsic permeability when saturation is zero and one respectively. It is therefore implied that, when n is equal to one, the sum of the relative permeability of each phase is:

$$\frac{K_{rg}}{K_0} + \frac{K_{rl}}{K_0} = 1 \tag{2.2.18}$$

However, at intermediate saturation it is found that the presence of both phases presents a significant resistance to the flow of each phase where:

$$\frac{K_{rg}}{K_0} + \frac{K_{rl}}{K_0} < 1 \tag{2.2.19}$$

and has sometimes been found to be less than 0.1, and therefore n is usually greater than one. Kaviany states that the wetting phase tends to cover the solid surface area in a manner that results in the smallest liquid–fluid interfacial area and this results in a large resistance to the flow of this phase; as the minimisation of the interfacial area requires spreading over many pores this results in a more tortuous flow path for the wetting phase [57].

In general, Darcy's law can only be applied to flow with low Reynolds number

which is true for both phases under typical fuel cell operation in the GDL [58]. Intrinsic permeability itself is not straightforward to measure and has been shown by Fishman and Bazylak to vary though-out the GDL in both through-plane and in-plane directions [59]. When comparing GDLs of different material, the tortuosity of felt exhibited a more uniform core region than paper GDLs, however both core regions had approximately the same tortuosity. Convective contributions to mass transfer through the GDL are typically small [60]. However, with certain flow-field designs considerable pressure gradients may exist between channels and this is discussed later in Section 2.3.4.

2.2.3 Capillary Pressure Transport

The capillary effect occurs in the GDL when both phases are in contact with the pore walls. It results from the surface tension between the phases and wall adhesion force which in turn depends on the surface wettability. Surface tension arises from the intermolecular forces of the fluid molecules. Molecules within the bulk of a fluid will have a net force of zero where the mutual attraction of all the neighbouring molecules is balanced. Molecules at the interface between a liquid phase and a gas phase will have fewer neighbours and therefore more free energy. Surface tension is an expression of this free energy per unit area (but is also commonly expressed by the equivalent force per unit length) and is minimised by a tendency to reduce the overall surface area of the fluid phase. A perfectly spherical surface will have the smallest surface area to volume ratio which is why spherical droplets will form when liquid emerges from the pores of the GDL into the flow channels of the fuel cell.

Pore Scale Models of Capillary Pressure

In straight capillary tubes, the shape of the interface between the liquid and gas phases inside a pore or capillary is influenced by the surface wettability and characterised by the contact angle made by the liquid phase with the surface walls, as shown in figure 2.3. A completely flat surface inside a capillary tube makes a contact angle of 90°. A concave surface curved towards the liquid phase makes a contact angle less than 90° and will occur when the surface is hydrophilic

or wettable. Liquid is drawn up the sides of the tube overcoming gravitational forces which creates a pressure difference in favour of the gas phase. Conversely, a convex interface will form when the surface is hydrophobic creating a contact angle greater than 90° and an adverse pressure difference in favour of the liquid phase.

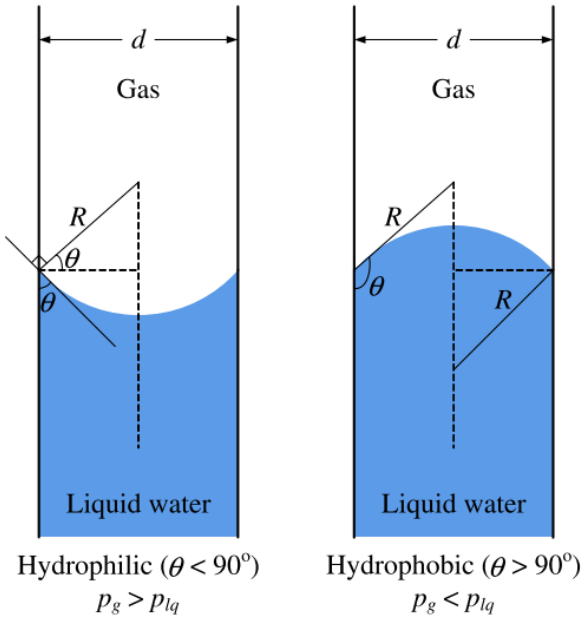

Figure 2.3: Two-phase behaviours in small pores with different surface wettabilities [7].

It is this pressure difference which drives the fluid motion and is quantified by the Young-Laplace equation which, for a spherical interface, simplifies to:

$$\Delta P \quad = \sigma(\tfrac{1}{R_1} + \tfrac{1}{R_2}) = \tfrac{2\sigma}{R} \tag{2.2.20}$$

where σ is the surface tension between the liquid and gas phases and R is the radius of curvature of the interface. A good approximation between the radius of curvature and the pore diameter for relatively uniform continuous pores is:

$$R = \frac{d}{2cos\theta} \tag{2.2.21}$$

which leads to the following relation for capillary pressure, P_C, referred to here-on as the Washburn relation [61]:

$$P_C = -\frac{2\sigma cos\theta}{r} \tag{2.2.22}$$

where r is the radius of the capillary tube. In real porous media used for GDLs the fibrous geometry is not uniform and liquid phases will be dispersed at random.

The Purcell model for capillary pressure accounts for the converging-diverging nature of fibrous material structures by imagining the meniscus passing through the centre of a torus as follows:

$$P_C = \frac{(-2\sigma)}{r}\frac{(cos(\theta-\beta))}{(1+R/r(1-cos\beta))} \tag{2.2.23}$$

where r is half the minimum fibre spacing or pore/throat radius, R is the fibre radius and β is the filling angle, defined as zero when the interface reaches the smallest constriction.

The filling angle at which the maximum meniscus curvature occurs was shown by Mason and Morrow [62] to be:

$$\beta^{max} = \theta - \pi + arcsin[sin(\theta)/(1+r/R)] \tag{2.2.24}$$

The implications for choosing an appropriate pore scale model are explored in Chapter 6.

Constitutive Relations for Capillary Pressure and Saturation

The semi-empirical Leverett J-function is widely used in fuel cell modelling to represent the capillary pressure in a porous media is given by [63]:

$$\begin{aligned} P_C &= \frac{\sigma cos\theta}{(\frac{\epsilon}{K_0})^{0.5}}J(S) \qquad (2.2.25)\\ J(S) &= [1.42(1-S) - 2.12(1-S)^2 + 1.26(1-S)^3] \text{ (if } \theta < 90)\\ J(S) &= [1.42(S) - 2.12(S)^2 + 1.26(S)^3] \text{ (if } \theta > 90) \end{aligned}$$

This equation accounts for the average pore size and includes three factors ad-

justing the pressure based on liquid saturation. However, the Leverett J-function was originally deduced from studies of various soils with uniform porosity and wettability. As the diffusion media used in fuel cells is topologically different from soil, anisotropic, often treated with hydrophobic PTFE, contains a wide distribution of pore sizes and is often multi-layered, improving on the function has been the subject of research [64], [54], [17] as reviewed by Liu et al [65]. Now many experimentally and numerically determined alternative relations exist. However, because there are many types of diffusion media used in fuel cells no single function has been considered favourable to any other and the Leverett J-function remains the most widely used [7].

A physical description of the transport of liquid water was presented by Pasaogullari and Wang [8] in which the wetting properties of the fibrous GDL material was considered. Condensation results in a "branching tree"-like liquid pattern formed by percolation in the GDL. When the liquid reaches the surface of the GDL droplets form. Inside the GDL liquid is wicked by capillary action and the pressure difference caused by the saturation build-up at the catalyst layer. Figure 2.4 shows the dependence of capillary pressure on saturation in porous media with different wetting characteristics. Gas phase pressure is assumed constant and the driving force behind the capillary action is the gradient of the liquid phase pressure. In both cases capillary pressure acts to drive water towards lower saturation but the magnitude of this force is different for the different media. A hydrophobic surface has a greater driving force at lower saturation, i.e. near the evaporation front, than a hydrophilic exhibiting better water removal ability.

Treatment of the fibres within the diffusion media with hydrophobic substances (such as PTFE) is known to have a positive effect on water management at high current densities but until recently, very little was known about the actual mechanism by which this happens. Measurements, made by Gostick et al. [55] of the water-air capillary pressure curve with varying water saturation using a porosimetry technique show that water withdrawal is associated with negative capillary pressure. The conclusion was this behaviour could be attributed to the presence of a network of hydrophilic pores. However, Benziger et al. [66] found that the converse, i.e. a positive capillary pressure is required to inject water, was true even without the presence of a hydrophobic coating. If the presence of

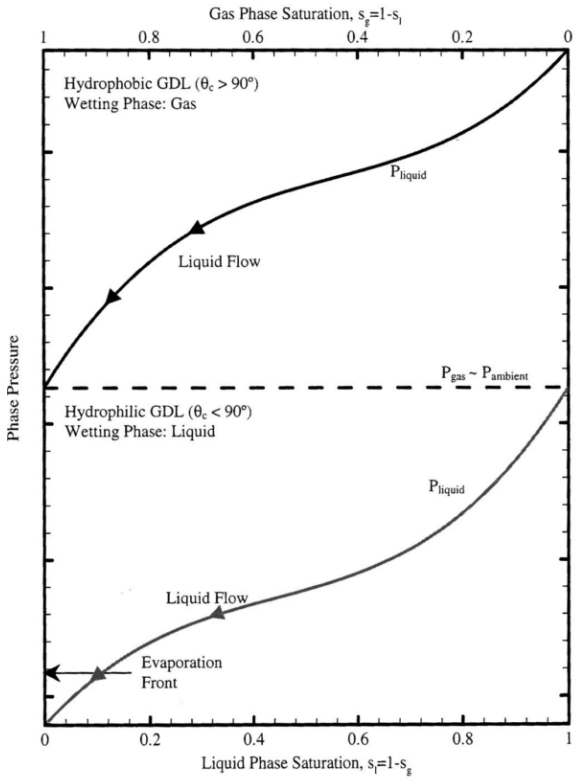

Figure 2.4: Schematic illustration of liquid and gas-phase pressure profiles in hydrophilic and hydrophobic porous media [8].

the coating had been the dominant factor determining water uptake then spontaneous water-uptake would have been expected at negative capillary pressures, but this was not observed. Furthermore, the report highlighted that pressure (likely from membrane swelling) is required to force the water into the GDL and this pressure is greater than the capillary pressure required to drive the water inside the pores.

In later work Gostick et al. confirmed that GDL samples show a significant hysteresis whereby water injection occurs at positive capillary pressure while water withdrawal occurs at negative capillary pressure [17], [9]. This hysteresis is pictured in Figure 2.5 and includes internal scanning loops for intermediate saturation produced using the method of Gostick et al. [67]. Furthermore in materials with hydrophobic treatment, much higher pressure was required for water injec-

tion, whereas water withdrawal occurred at considerably less negative capillary pressure. No difference was observed between the capillary pressure-saturation curves for samples containing more than 10% PTFE, suggesting that there is no advantage to adding more polymer. This behaviour corresponds to a switch in wettability where the media resists both uptake and extraction. This would indicate that the material is relatively neutral in terms of wettability (contact angle close to 90°) and the Washburn relation between contact angle and capillary pressure may not be the best description. An alternative, mentioned in the previous section, that accounts for the converging-diverging nature of the constrictions between fibres was proposed by Purcell [68] and was shown by Gostick [69] to fit well with experimental data when used in a pore network model when replicating water injection.

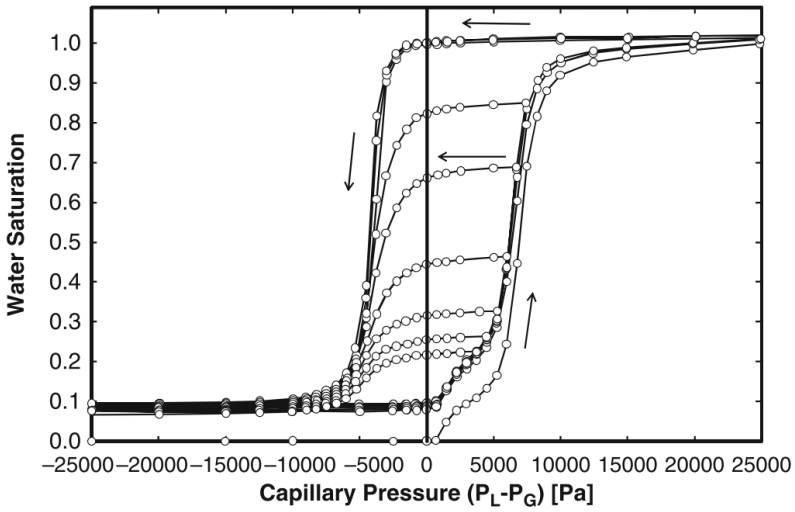

Figure 2.5: Air-water capillary pressure curves for treated Toray 120 carbon paper showing scanning loops and hysteresis [9].

The focus of Chapter 6 is to explore the effect of choosing the correct pore-scale capillary pressure model in order to produce the capillary pressure characteristic curves under drainage and imbibition. Consequently the predicted liquid saturation distribution and resulting transport characteristics are also investigated under these different scenarios.

2.3 Water Transport in other PEFC components

2.3.1 Membrane

The main water transport mechanisms occurring within the membrane are diffusion and electro-osmotic drag (EOD). Back-diffusion (referring to the opposing direction of proton exchange and EOD) occurs when a concentration gradient between the anode and cathode side exists and is dependent on the water content (λ) of the membrane which is defined as the number of water molecules per sulphuric proton exchange site [7]. The diffusional water flux J_{Diff} is defined as:

$$J_{Diff} = -\frac{\rho_{mem}}{EW} D \nabla \lambda \tag{2.3.1}$$

where water content is defined as:

$$\lambda = \frac{EW}{\rho_{mem}} c_{H_2O} \tag{2.3.2}$$

and the effective weight is defined as:

$$EW = \frac{\text{dry ionomer mass in g}}{\text{Mole of proton exchange sites } (SO_3^-)} \tag{2.3.3}$$

where ρ_{mem} is the density of the dry membrane, EW is the effective weight, c_{H_2O} is the water concentration. The diffusion coefficient is a function of temperature and water content with peak diffusion rates occurring at higher temperatures and a water content of 3 [39], [70]. Nafion is the most common material used for PEFC membranes, although membrane development is an intensive area of research [71], and can vary structurally depending on the required application. A smaller effective weight will facilitate water and proton transport but will have a lower mechanical and thermal strength than a membrane with higher effective weight.

The water flux caused by the electro-osmotic drag of water by migrating

protons J_{EOD} is defined as:

$$J_{EOD} = n_d \frac{I_{ion}}{F} \tag{2.3.4}$$

where I_{ion} $[Am^{-2}]$ is the ionic current density and n_d is the electro-osmotic drag coefficient; n_d depends on the water content of the membrane and has been experimentally measured at many different values for various membranes but is generally approximated to be [39]:

$$n_d = \frac{2.5\lambda}{22} \tag{2.3.5}$$

The main findings of Springer's investigation were that the net water flux is from anode to cathode. Increasing relative humidity and stoichiometry of the anode inlet stream leads to a higher membrane water content and lower ionic resistance, and therefore better cell performance. Springer also showed that a thinner membrane will perform better than a thicker one, as the back-diffusion of water from cathode to anode is higher compared with a thicker membrane, leading to an overall lower net water flux towards the cathode. Springer comments on the suitability of his model and concludes that cathodic water transport is not fully represented because no need to humidify the cathode inlet stream is predicted, and this is required in practice to achieve the best performance. Thinner membranes are generally preferred due to the better proton conductivity associated with better hydration tendencies. However, they are mechanically less stable and can sometimes permit fuel cross-over which limits the electrochemical reactions. A practical thickness limit was found to be 25 - 40 µm [72]. Environmental MRI has been used to investigate the membrane water content profiles under differing relative humidity conditions [73]. At 40% RH the water content in the membrane was around 3 and chemical diffusion dominated the water transport. At higher RH the anode side became dehydrated and a concentration gradient established due to increased EOD. However, at an RH level of 92% and current density of 0.2 A/cm^2 the water content stabilized at around 22 and the content profile became flat, indicating that liquid was permeating into the membrane from the catalyst layers.

If a pressure differential exists across the membrane, limited hydraulic permeation can occur, but on a scale many orders of magnitude lower than the other transport factors, so it is usually ignored when modelling fuel cells. The effect of membrane expansion, which can increase the pore sizes and reactant transport or cross-over, is also usually ignored but may in-fact be important for the expulsion of water from the catalyst layer. Mason et al. observed significant changes to membrane thickness from the uptake of water and also found this can increase GDL degradation through cyclic compression [74]. Some earlier models [75] make the assumption that, under steady state conditions, the membrane is fully hydrated and there is no concentration variance of species across the membrane. Under this condition no diffusional transport will occur, and water transport is governed by EOD and pressure driven flux dependent on the permeability of the membrane.

In practice the membrane of a fuel cell can take several hours to become fully hydrated, and a steady state may never be reached, so species concentrations may vary significantly within the membrane. A branch of membrane models based on chemical potential simulating transient properties of the membrane has also been developed whereby a coupled system of water, protons and electric charge is solved [76]. However, these models are too complex to be implemented within a full cell model as they depend on interactions with the structure of the membrane.

Much interest in membrane research surrounds developing alternatives to the Nafion like materials. Membranes that conduct protons without the requirements for liquid water would allow fuel cells to operate at higher temperatures, therefore helping the water management issue, as water would only exist in the vapour state. These high temperature PEFCs and the membranes developed to work inside them are reviewed by [77]. Electrode kinetics would also be enhanced at higher temperatures, and waste heat could be recovered and used for other purposes. However, fuel cross-over is a significant issue for these alternative membranes, as well as degradation and limited operational life-times. The high temperature operation has the advantage of having to reject less heat energy as waste and so requires simpler cooling systems [77]. However, high temperature operation requires containment which renders the devices unsuitable for many

low power applications. For these reasons normal PEFCs still receive the greatest attention and this literature review and subsequent research will focus on operation below 100°C.

2.3.2 Microporous Layer (MPL)

The Microporous Layer (MPL) is normally composed of carbon agglomerates mixed with a hydrophobic agent such as PTFE, applied to the interface between the GDL and CL in order to smooth the transition in porosity between the two layers, enhance electrical contact, and increase mechanical stability of the membrane when compressed [78].

It is well known that the MPL aids water management within the fuel cell but the mechanism is still up for debate. Some researchers conclude that the MPL acts like a valve by inducing strong hydraulic capillary pressure which forces water into the membrane and increases back-diffusion [79]. Other researchers postulate that hydrophilic regions in the MPL provide a wicking mechanism from CL to GDL and subsequently force liquid along a well-defined path towards the gas flow channel [15]. Nam et al. have studied the liquid transport in the MPL with ESEM [10]. They conclude that it performs two functions beneficial to water management and enhancing oxygen transport. Firstly, an MPL reduces the size of droplets that gather at the CL surface. Secondly, the MPL reduces the number of liquid water breakthroughs towards the GDL, reducing the overall saturation in the GDL as pictured in Figure 2.6

Like the CL, the MPL is difficult to analyse ex-situ, but recent studies have demonstrated its effect on water vapour diffusion by applying an MPL to three different carbon paper electrodes [80]. The findings agreed with numerical simulations performed by concluding that the diffusion co-efficient is reduced and the effect is more pronounced in the through-plane direction [81]. The extent to which the overall diffusion co-efficient is reduced depends on the thickness of the layer and its porosity as well as PTFE loading. Studies have found that the intrinsic permeability of the GDL with applied MPL can decrease by 2 orders of magnitude owing to the smaller pores [82].

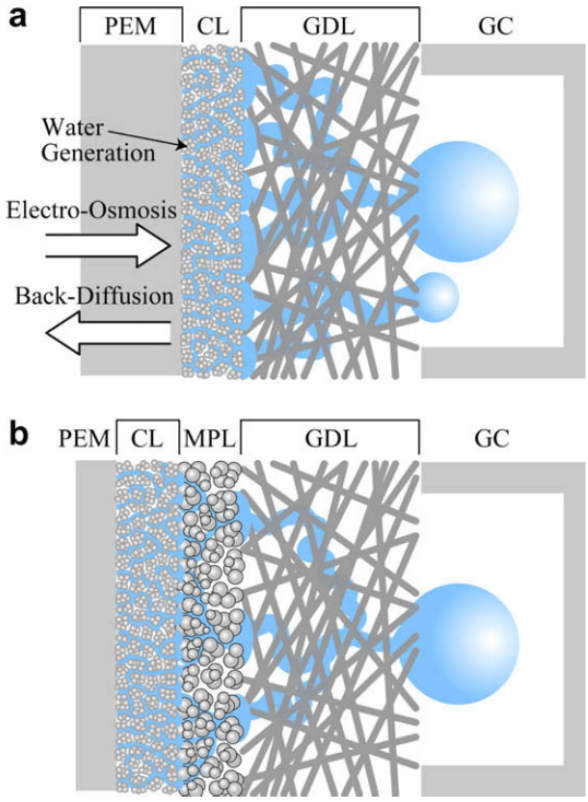

Figure 2.6: Illustration of water transport in the cathode without (a) and with (b) an MPL, [10].

Gostick et al. used capillary pressure curves to illustrate the effect of the MPL, and found that liquid water saturation at breakthrough pressure drops to around 3% in the presence of an MPL, compared with 27% without [83]. In effect the MPL acts as a barrier to mass water transport into the GDL. This increases the capillary pressure on the CL side until breakthrough and percolation of water towards the flow channel occurs. Liquid water breakthrough has been studied in GDLs with and without an applied MPL [84], [85]. It was observed that dynamic capillary pressures are present in GDLs without an MPL, and a dynamic change in breakthrough location occurs repeatedly. Average water saturation is significantly lower with the MPL, and breakthrough locations remain fairly static, suggesting stabilised water pathways dependent on the structure of the MPL layer, such as the presence of cracks. This behaviour also influences the development of

water within the gas channel. Samples without MPLs promote film flow, whereas samples with an MPL promote droplet and slug flow. Kang et al. also conclude by means of similarity experiments that the role of the microporous layer in water management is to reduce the number of water breakthrough sites from CL to GDL and thereby reduce the liquid saturation [86]. This theory was recently supported by a Lattice Boltzmann simulation conducted by Kim et al. [87].

However, if a greater saturation occurs on the CL side of the MPL, one would expect gas transport to inner regions of the CL to be hindered. Owejan et al. state that the primary role of the MPL is to prevent liquid water which has condensed in the pores of the GDL forming films in the CL and therefore enabling gaseous diffusion [88]. They also state that the vapour concentration gradient between CL and gas flow channel is enough to evacuate liquid vapour without condensation into liquid form.

Wang et al. also conclude that GDLs and MPLs with porosity grading can enhance fuel cell performance by performing multiple functions and separating transport of the different phases [89]. Hydrophilic micro-pores are required for the transport of liquid water from CL to MPL to GDL, largely hydrophobic meso-pores are required for reactant transport to the CL, and hydrophobic macro-pores are required for bulk diffusion and water flow under certain pressures. Other researchers have also found that pore-size distribution in the MPL is a more influential parameter on flooding and fuel cell performance than total porosity [90]. Condensation occurs within smaller pores, and larger pores mainly contribute to gas transport, until all the smaller pores are filled and liquid begins to penetrate larger pores. Designers of MPL and GDL material should strive to strike an optimum balance between micro and macro-pores, as too many macro-pores will lead to pore electrical and thermal conductivity, whereas too many micro-pores will lead to excessive condensation of water vapour and flooding.

An interesting area of research is the use of carbon nano-technology to create MPLs. Electrospinning techniques have been used to fabricate a carbon nanofibre sheet (CNFS) which was used inside a working fuel cell [91]. The authors report enhanced performance and power density owing to excellent electrical conductivity, gas permeability and hydrophobicity with a static contact angle of 136° and more uniform structure.

2.3.3 Catalyst Layer (CL)

The gas diffusion layer has received much attention in the literature, partly owing to its size and relative easiness to study ex-situ. The catalyst layer, on the other hand is much smaller, both in the size of the pores and the thickness of the layer, and is more difficult to study both in-situ and ex-situ due to the fabrication process. It is also the area where water transport is most complex and possibly most important. The layer is often referred to as the triple-phase boundary between solid polymer and catalyst, gaseous reactant and liquid product. The pore diameters depend on the platinum/carbon fraction used and can range from several nm to 1 µm [92].

Two types of diffusion occur on significant levels when considering pore diameters on this scale, binary diffusion from the collision of gas molecules with each other, and Knudsen diffusion from the collision of gas molecules with the pore walls [52]. The respective diffusion coefficients are given below for gas species i in relation to a reference diffusion coefficient, temperature and pressure:

$$D_i^B = D_i^{B,ref} \left(\frac{T}{T_{ref}} \right)^{1.5} \left(\frac{P_{ref}}{P} \right) \tag{2.3.6}$$

$$D_i^K = \frac{1}{3} \left(\frac{8RT}{\pi M_i} \right)^{0.5} d \tag{2.3.7}$$

where R is the universal gas constant, M_i is the molecular weight of species i and d is the pore diameter. The diffusion coefficients can be combined as:

$$D_i = \left(\frac{1}{D_i^B} + \frac{1}{D_i^K} \right)^{-1} \tag{2.3.8}$$

The water transfer between the membrane and the CL pore regions plays an important role in cell performance because a well hydrated membrane is beneficial for proton transport. It was first observed by Schroeder in 1903 that the amount of absorption/desorption is different for different phases. The membrane prefers to absorb water in the liquid phase, which may explain why the presence of an MPL is beneficial to water management, as water unable to penetrate the MPL

will encourage more water in the CL region and therefore membrane uptake is greater.

Capillary pressure is also an important factor determining the transport of water in the CL, and is generally treated by modellers in the same way as the GDL with the same empirical approximations. However, recent experimental evidence by Das has shown that this assumption is likely not valid, as ex-situ measurements of saturation vs. pressure reveal less extreme hysteresis than typical GDL samples [93]. This is most likely caused by the fundamental differences in pore structures where GDLs have a fibrous structure and are neutrally wettable, whereas CLs are particle agglomerates and are hydrophilic.

A technique for visualising water droplet formation at the CL surface has been devised by making a micro hole in the GDL beneath the flow channel, and using a transparent current collector and an optical system with high-resolution camera [94]. The authors observed periodic droplet emergence and detachment or evaporation in preferential sites. Their observations don't necessarily reflect the true behaviour throughout the region as the method of exposing the layer undoubtedly changes the forces and dynamics of the surrounding gas flow. However, the continuous emergence of droplets at preferential sites is interesting and the authors recognise that this could be a controllable factor in fuel cell design to aid the removal of water.

Ji and Wei propose that water flooding in the catalyst layer is inevitable because water is produced in liquid form, stating that the CL would be flooded as soon as the first drop is produced [40]. Wu et al. also argue that water produced from the ORR is not in the vapour phase, stating that the ionic group ($SO_3^-H^+$) will retain at least one water molecule and often the water content is rarely below 3 molecules per proton [95]. The water molecules cannot be considered to be in a gaseous state because the mean free path is closer to that of a liquid. Hence, when a water molecule is produced, it is already part of a dissolved group of liquid water molecules.

Ji et al. have proposed a novel anti-flooding electrode which contains a water-proofing agent, dimethyl silicon oil (DMS), applied to the porous media [96]. Their results indicate that the agent mainly attaches to pores with diameters ranging from 20 to 80nm (i.e. the catalyst and micro-porous regions). The idea is

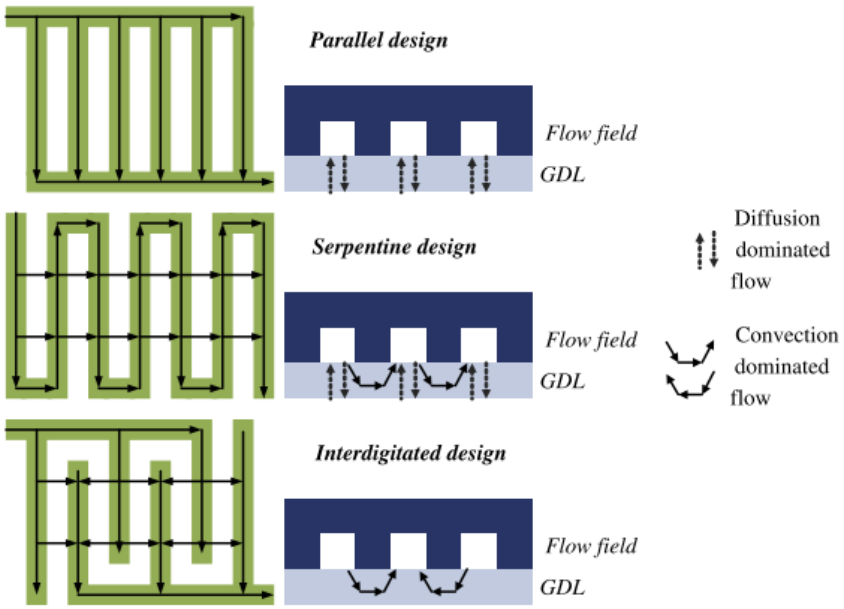

Figure 2.7: Flow characteristics in GDL with different flow channel designs [7].

that the DMS replaces the water in the pores and acts as a conduit for dissolved oxygen transport. Their results show promising performance enhancement in both high and normal current density regimes.

2.3.4 Gas Flow Channels

The geometry and material composition of the flow channels within the bipolar plates of the fuel cell have received much attention in the literature. The main objectives for the bipolar plate designer are to minimise the contact resistance between the plates and GDL, create uniform gas distribution with minimal additional work, and manage the removal of water ensuring the flow channels do not periodically block with water at high current densities. Three designs are the most common and widely accepted; the conventional parallel design, serpentine and interdigitated designs, as shown in figure 2.7 with characteristic gas flows.

Figure 2.7 clearly shows that the channel design has an impact on the dominant flow regime in the adjacent GDL. The flow within the channels is convection dominated and depends on the pressure at the inlets. The conventional parallel

channel design requires the smallest pressure difference but the diffusion dominated flow within the GDL leads to excessive water accumulation [40]. It has been observed that the development of blocked channels by the formation of liquid water can also lead to the mal-distribution of gases along those channels as gas will naturally follow the path of least resistance along the unblocked channels [97].

Serpentine designs are considered to be the most effective conventional design for water management because the relative pressure drop across parallel channels is greater than along a single channel. This creates a strong cross-channel convective flow, ensuring that reactant gas reaches the catalyst layer and removes the product water simultaneously. However, due to the length of the connected flow path, large differences in concentration tend to occur between inlet and outlet; a large pressure drop is required to force the reactants all the way through, leading to parasitic power loss. The non-uniform concentration of reactants and products leads to additional non-uniformities in temperature and liquid water distribution. This in turn leads to non-uniform membrane hydration with hotspots and degradation developing near the inlet, and large concentration loss due to flooding near the outlet. Interdigitated flow fields create dead-ends for the reactant gas flow which creates convective flow toward the reaction sites. This strong convective flow helps to flush liquid water out of the GDL and aids water management but again requires a large pressure drop to be effective.

Variations on each of the established designs are numerous and nature-inspired designs are also promising [98]. A particularly noteworthy example is the convective enhanced serpentine flow-field (CESFF) proposed by Xu and Zhao [11] shown in Figure 2.8. The CESFF aligns sections of the continuous flow channel with greater pressure differentials when compared to the conventional serpentine design without the need to adjust the overall pressure difference. This increases the convective force and leads to better water removal from within the GDL and consequently stronger performance at high current densities.

As well as the distribution pattern, the channel shape and dimensions are also important factors to consider when designing the bipolar plate. The geometry of the channel with key dimensions: channel width (c), land or rib width (l), channel depth (d) and land angle (a) is shown in Figure 2.9. Many studies have

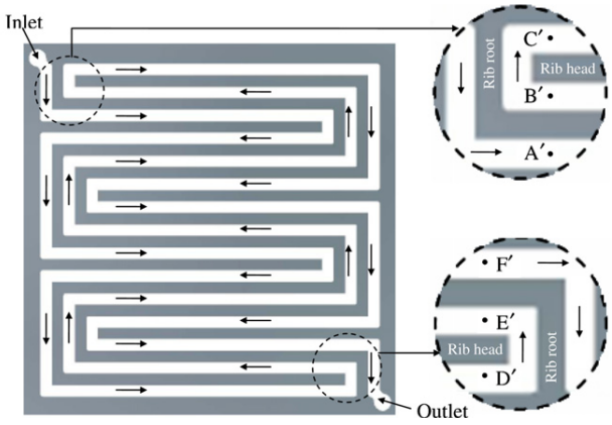

Figure 2.8: Convective Enhanced Serpentine Flow-Field (CESFF) [11].

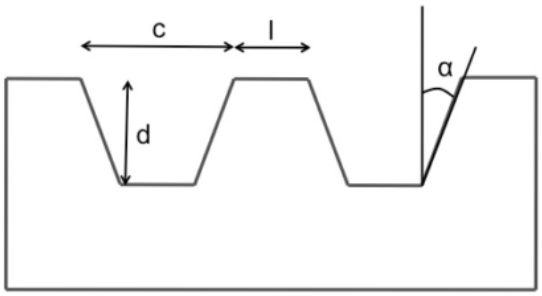

Figure 2.9: Flow Field Geometries [12].

been conducted to optimise the channel geometries w.r.t fuel utilisation/distribution, water removal, operating conditions and current distribution. Scholta et al. determined that increasing channel depth could lead to a decrease in oxygen utilisation, and increasing the land width decreased the oxygen concentration underneath the land for a parallel flow design [99]. Optimisation of channel geometry is flow design and operating condition dependent, with smaller channel areas preferable for high current densities, and wider channels preferable for low current densities.

Owejan et al. observed that channel geometry and surface properties both have appreciable effects on the accumulated water and the morphology of water droplets retained in the flow field [100]. Triangular geometries were found to

accumulate less water than rectangular, and coating the channels with PTFE reduced water accumulation.

Droplet dynamics have also been studied by a number of research groups with emphasis on elucidating the important factors determining the detachment of the droplet and subsequent entrainment in the gas flow. Cho et al. studied the forces on a single droplet in a straight channel and computed the drag forces under various conditions [101]. They concluded that the viscous force has a large impact on smaller droplets in low velocity flow field, whereas pressure drag is more important for larger droplets. Deformation from a spherical shape to one with greater advancing contact angle than receding contact angle is limited to larger droplets. A correlation between droplet size and detachment velocity was derived and validated with experimental and numerical studies, with larger droplets requiring smaller gas flow velocities to detach. Whether a droplet will reach critical detachment size is influenced by the water profile in the attached pore network, temperature, humidity of the flowing gas and detachment of other droplets further upstream. Theodorakakos et al. conducted a parametric study on droplet detachment factors, including the dynamic and static contact angles of the GDL surface and location of emergence within the channel (i.e. in the centre or next to a side wall) [102]. They conclude that uniform air velocity detaches the droplet at lower mean air velocity, and that temperature was found to be the most influential parameter affecting detachment at lower velocity, due to lesser surface tension and easier deformation.

Chen et al. studied the effect of surface roughness on the detachment, and found that rougher surfaces tended to preferentially influence the detachment by reducing the adhesion forces between droplet and GDL surface [103]. When no detachment occurs and additional liquid water is allowed to accumulate at the droplet location, slugs that block the entire flow channel can occur as shown in figure 2.10.

Colosqui et al. studied the transition from droplet to slug flow [13]. They conclude that interfacial forces and geometry are the dominant factors determining slug formation. Wetting properties of the channel are altered as a result of water accumulating (especially in the corners). Droplets can grow, deform and become films along the channel and GDL surface, with residual droplets and slugs acting

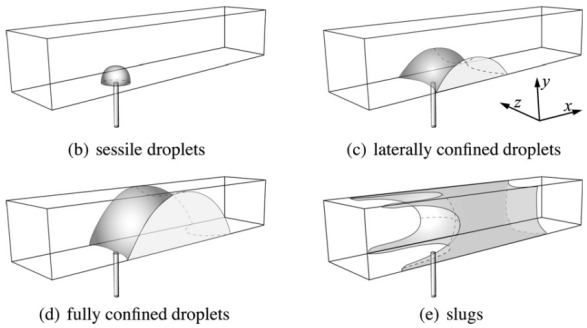

Figure 2.10: Droplet and Slug formation in gas flow channels [13].

as nucleating agents. Gravity was also found to influence deformation and slug behaviour, with smaller slugs resulting from pendant drops compared with sessile drops. They conclude that the orientation of the fuel cell is important, with cathode facing upwards encouraging the formation of liquid films that prevent the passage of gas through the diffusion media. Gravity also plays a role when the through-plane is orientated horizontally; channels that flow upwards tend to accumulate more water than those flowing downwards.

Corner geometry has been found to influence the accumulation of water in the channels as shown by Kim et al. [104]. The influence of rectangular and smooth circular corners was studied and it was found that hydrophobic smooth corners were the best for exhausting water through the channel. On the other hand, hydrophilic rectangular corners retained less water than hydrophilic smooth corners, due to the formation of longer continuous films in hydrophilic smooth corners. The tendency in hydrophobic channels is for water to form droplets which become more easily entrapped in a rectangular geometry, hence smoother geometry is preferable.

An interesting proposal is to fill the gas flow channels with porous media, in order to improve electrical and thermal conductivity and enhance channel design flexibility [105], [106]. One-dimensional analysis and CFD simulation showed that at low humidity performance was improved over conventional open channel design. In two-phase flow regimes the results were highly dependent on the relative permeability relation used. However, the impact of capillary action in the flow channel was found to be negligible. Instead flow was dominated by the interfacial

shear forces between gas and liquid phases. Saturation was found never to exceed 20%, which would not significantly block the reactant gases, making the proposed porous channel approach superior to open channel designs. Little research into this field has since been conducted and the two-phase analysis was conducted in one dimension only, so questions over the impact on cell performance remain unanswered.

2.3.5 Interfaces

Synchrotron X-ray tomography has shown that liquid water transport can be highly transient, and depends strongly on the interfaces between components. Hartnig et al. observed so called "Haines jumps" which are discrete drainage events (i.e. sudden changes in medium saturation), leading to compact cluster growth in the GDL, followed by eruption into the channel, and choke-off effects leaving portions of the GDL empty [107]. Gurau and Mann state that while the capillary pressure-saturation and relative permeability-saturation correlations determine the profile of the saturation field in the porous electrode, it is the liquid pressure in the pendant or sessile droplets which determine the boundary values and therefore the magnitude of the field [108]. More work is clearly needed on the treatment of interfaces between components, a topic which could be potentially aided by combining pore-scale models with continuum models and discussed later in Chapter 7.

2.3.6 Summary

From this brief overview of water transport and management in the various fuel cell components, one can appreciate the scale of investigative efforts into the broad topic. Water is present in some form in all of the fuel cell components and its management is critical to maintaining/improving fuel cell performance. On the one hand, water is needed in the membrane to aid proton conduction, but on the other hand, water is a nuisance in other parts of the cell, reducing the effective diffusivity of the porous components, and blocking convective transport in the gas channels. The GDL is possibly the most critical component for passive water management. Altering the characteristics such as structure and wettability of

the GDL or adjusting the pore size distribution by adding an MPL can have the greatest effect on water transport without external forcing. Whilst computational fluid dynamics and experimentation has now led to a fairly good understanding of the dynamics of water in the gas flow channels, understanding of the processes occurring within the GDL and how to manage them effectively under differing conditions is still lacking.

2.4 Modelling Two-phase Transport

Modelling is essential to understanding the transport phenomena occurring within the fuel cell. The polarisation curve can only give an indication of performance under various operating conditions, and cannot explain all the processes or present a picture of the distribution of various parameters within the cell. Imaging techniques have aided our understanding, but are often limited to observing the most exposed parts of the cell, or only present a two-dimensional picture. Amongst the different modelling techniques, CFD stands alone in presenting a full picture of the fuel cell, accounting for multi-dimensional, multi-component, multiphase phenomena. Other techniques such as Pore Network Modelling (PNM) and the Lattice-Boltzmann Method (LBM) have also been used extensively to study particular phenomenon and particular components in isolation, but have yet to be used to represent an entire fuel cell owing to computational complexity and resources. The various modelling approaches applied to studying multiphase flow in PEFC components are now reviewed.

2.4.1 Computational Fluid Dynamics

CFD encompasses a vast branch of modelling approaches and has evolved significantly with increasing resources. Three of the most widely used multiphase models implemented in CFD software over the last two decades are reviewed in this section, namely the mixture model, two-fluid model and volume of fluid (VOF) model.

Mixture Model (M^2)

The development of the fuel cell mixture model is credited to C Y Wang and his research group [109]. One set of governing equations is solved for all the species including a species representing a mixture of vapour and liquid water over the entire domain including the membrane. The density and dynamic viscosity of the mixture phase is calculated based on the respective volume fractions of each component using a saturation term in the following way:

$$\rho = \rho_l S + \rho_g (1 - S) \tag{2.4.1}$$

$$\mu = \frac{\rho_l S + \rho_g (1 - S)}{[(K_l/\nu_l) + (K_g/\nu_g)]/K_0} \tag{2.4.2}$$

where ρ_g and ρ_l are the densities, ν_g and ν_l are the kinematic viscosities, K_g and K_l are the permeabilities of the gas and liquid phases respectively, and K_0 is the absolute or intrinsic permeability of the medium. The liquid water volume fraction, or saturation, is determined by the partial pressure of the vapour phase relative to the saturation pressure. Wang et al. formulate it in terms of concentrations obtained by use of the ideal gas law in the following way:

$$S = \frac{C_{H_2O} - C_{sat}}{(\rho_l / M_{H_2O}) - C_{sat}} \tag{2.4.3}$$

A source term for each species is included as a divergence of the capillary flux ($J_{cap,l}$) which is treated as a diffusion term based on the relative mobilities of the gas and liquid phases, and the gradient of the capillary pressure.

$$J_{cap,l} = \frac{\Gamma_g \Gamma_l}{\mu} \rho K_0 \nabla P_C \tag{2.4.4}$$

where relative mobilities are related to relative permeabilities in the following way:

$$\Gamma_l = \frac{K_l/\nu_l}{(K_l/\nu_l) + (K_g/\nu_g)} \tag{2.4.5}$$

$$\Gamma_g = 1 - \Gamma_l \tag{2.4.6}$$

The individual phase velocities based on the open pore area rather than phase-occupied areas are then calculated from

$$\epsilon\rho_l u_l = J_{cap,l} + \Gamma_l \epsilon\rho u \quad (2.4.7)$$

$$\epsilon\rho_g u_g = -J_{cap,l} + \Gamma_g \epsilon\rho u \quad (2.4.8)$$

One of the earlier implementations of the mixture model describes flow in a straight cathode channel under isothermal conditions [110]. The polarisation curve obtained was in good agreement with experimental results, but with the on-set of mass transport effects due to two-phase flow occurring at higher than normal current density. The work describes an advancing evaporating front which approaches the channel from the reaction site of the cathode. When the front reaches the channel, the model can no longer predict the physical situation accurately, as water exists in liquid form in the channel. The gas phase behaviour in the porous media is dominated by diffusion, and the liquid saturation advancement is dominated by the capillary effect, with gravity having negligible effects and convective flow from interfacial drag between phases not accounted for.

One of the first three-dimensional implementations of the mixture model was carried out by Mazumder et al. who presented two papers modelling the same geometry where a base case neglects the effects of water [111] and the second includes it [112]. The model combined the mixture model with fast finite-rate phase transfer (i.e. approximate equilibrium conditions), and produced markedly different results to previous two-dimensional studies, which significantly over-predict fuel cell performance at high current density. Even with the inclusion of water in a 3D representative model the performance was over-predicted. The authors ascribe this result to several different reasons including: ignoring the electrical contact resistance between components, making simplified assumptions about the diffusion pathways such as a Bruggemann correlation for tortuosity, and ignoring the Knudsen diffusion, ignoring the blocking of active sites by liquid water, and crucially, setting the capillary diffusion coefficient to be two orders of magnitude lower in the open gas channels than in the GDL. This last reason is highlighted as being physically inappropriate, and was done as a compromise

between setting the diffusion co-efficient to zero and trying to properly model liquid water in the channel.

The mixture model is limited to predicting saturation profiles in the porous electrode regions and cannot be extended to liquid in the gas flow channels. Mist-flow is assumed in the channels, and a dirichlet boundary condition of zero saturation is imposed at the interface between channel and GDL.

Gurau and Mann [113] present a critical review of multiphase approaches to modelling fuel cells with CFD. They point out that the multiphase model is strictly only valid when:

i There is no mass transfer across inter-phase boundaries at sub-grid scale.

ii The momentum equation for each individual phase may be reducible to Darcy's law for multiphase flows

Gurau and Mann imply that ignoring the inter-phase momentum terms, and relying simply on Darcy's law to describe momentum loss constrains the validity of the results. For example when operating the fuel cell at limiting current, the oxygen is entirely consumed at the GDL/CL interface, which cannot be described by Darcy's law alone. A major limitation of the mixture model is its inability to capture complex fuel cell phenomena such as water transfer and saturation between the fuel cell components, and use of the model restricts it's application to cases where liquid water evaporates before exiting the diffusion media.

Wang states, in his review of fundamental models for fuel cell engineering [114], that all models describing liquid water transport through the GDL can be categorised into two approaches: the mixture model and Unsaturated Flow Theory (UFT). According to Wang, UFT assumes a constant gas phase pressure thus effectively decoupling the liquid water transport from gas flow. It is true that constant gas phase pressure is an assumption often made when modelling unsaturated flow, but it is not a pre-requisite. A more general description of the alternative modelling approach to the mixture model is a multi-fluid model or two-fluid model which will be covered in the next section.

Two-fluid Model

The two-fluid model solves a separate equation for liquid water transport, and does not couple the liquid and vapour phases into a single mixture, as the mixture model does. Phase equilibrium is always maintained in the mixture model whereby phase change happens instantaneously, whereas the two-fluid approach allows for non-equilibrium. When phase change is fast the two-fluid model produces fuel cell performance results comparable with the mixture model.

The gas and liquid phase velocities are both calculated according to Darcy's law as follows [115].

$$u_g = -\frac{K_0(1-S)}{\mu}\nabla P = -\frac{K_g}{\mu_g}\nabla P \tag{2.4.9}$$

$$u_l = \frac{K_l}{\mu_l}\nabla P_l \tag{2.4.10}$$

By using the capillary pressure the liquid phase velocity can be calculated as a function of the gas phase velocity and the saturation. This requires some constitutive relations between saturation and relative permeability, and between saturation and capillary pressure:

$$u_l = f u_g - D_c \nabla S \tag{2.4.11}$$

where f is an interfacial shear force defined as:

$$f = \frac{K_l \mu_g}{K_g \mu_l} \tag{2.4.12}$$

and D_C is a capillary diffusivity term defined as:

$$D_C = \frac{K_l}{\mu_l}\frac{dP_C}{dS} \tag{2.4.13}$$

Some of the relationships forming the constituent relations of Equation 2.4.13 were presented earlier in section 2.2 but are not an exclusive list. Wu et al. explore the effects of choosing the various empirical formulas for capillary pressure vs. saturation [95], and the effect of changing the exponent of the power law relation used for relative permeability. Wu et al. find that relations proposed by Kumbur

et al. [64], [116], [117] and Ye and Nguyen [54], who developed separate relations for CL and GDL, both result in a less uniform saturation distribution. Wu et al. also show that higher exponents in the power law relation for relative permeability result in worse water removal capability, and that this parameter is more influential on the overall saturation than the capillary pressure relation.

The study conducted by He et al. investigated an interdigitated flow field, concluding that products and reactants are transported through the porous electrodes by diffusion and convection [115]. Having enhanced the convective flow, the diffusion distance for gases is reduced, rwsulting in a better distribution underneath the ribs. Also, the shear force of the gas flow improves liquid water removal, thus reducing flooding effects. Not having the same phase equilibrium assumption as the mixture model allows a better estimation of the saturation profile along the length of the gas flow path. It is shown that when operating on un-humidified gas streams, a significant amount of water is removed by evaporation as the flow becomes more saturated with vapour towards the outlet.

Gurau et al. present a version of the two-fluid model to illustrate the importance of the interfacial saturation behaviour [118]. At interfaces between components of the fuel cell, the phase pressures of vapour and liquid water and in turn the capillary pressure, must be continuous. Therefore, as porosity changes so must saturation. By considering the force required to overcome the minimum surface tension of a droplet at the GDL/channel interface, the model predicts a related saturation profile in the GDL. Correspondingly a related saturation profile in the CL is also determined, which is linked to membrane water sorption/desorption, EOD and production from the ORR. Streamlines of liquid water transport from CL to channel show that, over time, water builds up in the section of GDL directly under the current collector ribs, then emerges into the channel at the corner of the rib where most streamlines converge. The level of saturation was also found to depend strongly on the permeability of each layer and the size of the pores at the GDL/channel interface which determine the size of the pending droplets, and therefore sets the upper limit for the capillary pressure profile.

One recently published two-fluid model attempts to couple the flow inside the GDL with the gas channels by assuming the channels are a porous zone with permeability 4 orders of magnitude higher than the GDL and porosity of 1.0 [119].

The results show that including saturation in the channel greatly influences the saturation in the GDL and the effects of immobile saturation also deteriorate performance slightly. The flow of liquid water in the channel was found to be insensitive to capillary action (as would be expected when there are no capillary walls) so physically the model is representative.

Volume of Fluid (VOF)

The VOF method is an Eulerian approach to two-phase flow which solves the Navier-Stokes equation for a mixture of the phases and the volume fractions of each phase determines the fluid density in the same manner as the mixture model. The advantage of the VOF model is the inclusion of a force term accounting for the surface tension between the phases and any geometrical boundaries such as walls. This allows the interface between phases to be tracked with precision, but means that geometry must be real or idealised rather than volume averaged, which would be almost impossible to implement for an entire fuel cell, due to the variety of scales as listed in Table 2.1. For this reason, the application of the VOF method is usually limited to single components, most typically the gas flow channels, where detailed water droplet behaviour can be studied. However, a recent study has utilised the method to study fluid drainage from a computationally constructed GDL geometry [120]. Another study modelling the GDL structure in two dimensions as a lattice of spherical fibres illustrates the interaction between GDL and gas flow channel [121]. The model shows that when cross flow is present in the GDL, considerably less saturation occurs, and droplets emerge from the GDL with higher frequency before detaching in the channel. Le et al. have implemented a VOF model for the entire fuel cell, and have published several papers examining the distribution of liquid water in various gas flow channel designs [122], [123]. They have also published some experimental results visualising the liquid water dynamics in the flow channel, showing good agreement with the model [124]. However, it is not clear from the publications how the interface between homogeneous porous zone and open channel zones are treated. To save time, the method developed was to run a single-phase simulation to generate a saturation profile in the porous media, then transpose liquid droplets inside the

fuel cell, or inject them through the inlet. Conclusions were then drawn about the intrusion of the liquid water from the channel into the GDL at certain points along the channel. These simulations do not capture the full physical behaviour of liquid water emerging from the GDL into the flow channel, which is an important factor determining the profile of saturation. In a review paper, Anderson criticises the findings further stating that it is not appropriate to apply the VOF method to a homogeneous porous region [125]. In a subsequent paper utilising the same model, liquid emergence from the GDL is studied but not implemented as part of the electrochemistry of the fuel cell [126]. The model shows liquid water emerging and accumulating preferentially at the intersection between rib and channel which agrees with experimental observations [127]. However, a constant flow rate is applied for the liquid at the catalyst layer, and the GDL appears to be fully saturated before any liquid water emerges into the flow channel. This behaviour is unrealistic and over simplified, and does not reflect the branching pattern that water takes when traversing the GDL. A recent and comprehensive review of the VOF model applied to studying fuel cells is given by Ferreira et al. [128], with suggestions for future work being the development of a model able to account for water transport from its formation on the CL to accumulation in the GDL and subsequent removal from the gas channels. Typically the VOF model is applied to fully resolved porous structures, and the construction of such a model for an entire fuel cell would be too intensive given the range of scales. Therefore simplifications have been made in the past assuming the GDL is a homogeneous medium. In the future it could be possible to combine the various modelling approaches with perhaps a mixture model in the CL and MPL, a pore scale model such as PNM or LBM for the GDL, and VOF model for the channel.

2.4.2 Pore Scale Modelling Overview

Pore scale models represent the actual geometry of the porous media and can be broadly categorised as being either rule-based or first-principle based. Rule-based simulations such as pore-network models (PNM) use re-constructed geometries based on idealised sets of rules, such as flow through inter-connected sets of cubes [129], or topologically equivalent skeletal structures representing connected pores

and throats [58]. First-principle models solve the governing equations, i.e. the Navier-Stokes equation, and can be classified as top-down which start from a macro-scale perspective and extrapolate towards finer length-scales, or bottom-up which consider molecular behaviour and extrapolate upwards. The biggest challenge facing the top-down approach is the discretisation of irregular and complex micro-structures. Bottom-up methods such as the Lattice-Boltzmann (LBM) method are able to treat these micro-structure with greater ease. Recently work has been undertaken by Chen et al. to utilise several different methods for different fuel cell components in a coupled fashion [130]. Much of the work required for this technique surrounds the interface between the domains (and models) where a statistical distribution must be converted into a physical parameter. So-called reconstruction operators are utilised for each property such as species concentration, velocity and temperature.

2.4.3 Pore Network Modelling

Pore-network models (PNMs) have been used to describe a wide range of properties, from capillary pressure characteristics to interfacial area and mass transfer coefficients. The void space of a porous material is described as a network of pores connected by throats as pictured in Figure 2.11. The pores and throats are assigned some idealized geometry, and rules are developed to determine the multiphase fluid configurations and transport in these elements. The rules are combined in the network to compute effective transport properties on a mesoscopic scale some tens to thousands of pores across.

PNMs are growing in popularity as tools for analysing the properties and transport characteristics of porous fuel cell components. They are especially useful for multiphase modelling, as simple percolation algorithms can be performed when transport is capillary dominated. The advantage of PNMs over the more widely used continuum models employed within Computational Fluid Dynamics software have been highlighted by Putz et al. [131]. They state that the discrepancy between observed saturation profiles and those predicted by continuum models are large and that transport calculations based on them are suspect. This is largely because percolation is not represented in the underlying physics.

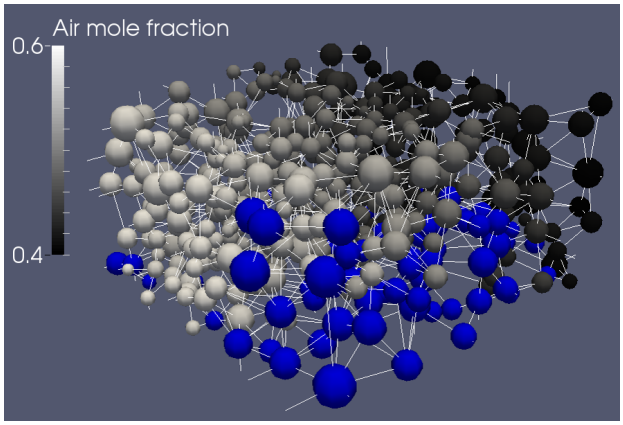

Figure 2.11: Pore Network Models (PNM) are a discretization of the void space in a porous material into larger pores connected by smaller throats.

PNMs help to understand the physics behind liquid water transport in porous media and have revealed that at extremely low capillary number, corresponding to a dominance of surface tension over viscous drag, liquid water transport is governed by fractal capillary fingering [58]. The resulting saturation distribution does not correspond to a Darcian flow regime, which would dictate a compact invasion pattern, whereby saturation is more uniformly distributed, and has a well defined evaporation front. A study comparing the effects of wettability on the liquid distribution reveals that hydrophobic media promote a fractal fingering pattern. This is beneficial to gas transport to the active sites, as liquid emergence (and therefore removal) at the surface of the GDL occurs at lower saturation compared with compact invasion [132].

Early PNMs focusing on fuel cell components were carried out on cubic networks with pores and throats represented by square or cylindrical geometry. The diameters of the pores and throats were set by a statistical distribution imposed upon the network in order to achieve the desired porosity and variation. Gostick et al. calibrated and spatially correlated their model to match two commercially available GDLs by generating realistic permeability and capillary pressure vs saturation (or drainage) curves [129]. Sinha and Wang constructed a network representing carbon paper composed of randomly stacked regular fibre screens, with pore and throat sizes assigned randomly according to a cut-off log normal

distribution [58]. Luo et al. constructed a topologically equivalent pore network (TEPN) by first reconstructing the fibrous geometry of a carbon paper and carbon cloth GDL by stochastic methods in 3D [133]. Then image analysis was used to extract the network, so pore and throat sizes determined by the geometry were mapped directly into the network, thus providing a topologically equivalent framework for the simulation. The two-phase characteristics of the two different materials were analysed and compared. It was found that the bi-modal distribution of throats and pores in the carbon-cloth led to two distinct regions of the capillary pressure and relative permeability curves, with the larger pores enabling much higher liquid transport capability. Recently Fazeli et al. have reported using X-ray micro-computed tomography (µCT) and image analysis to extract a 3D TEPN [134], a technique also reportedly used by others to exactly match saturation distributions and experimental drainage data gathered by tomography and network simulations [135].

A simpler method for constructing realistic networks is to use Delaunay and Voronoi tessellations [136], [137] and [69]. Thompson showed that random pore networks can give very good agreement with experiment for single phase permeability over a wide range of solid volume fraction [136]. Thompson also presents saturation profiles for imbibition at different flow rates, and images of drop spreading for models with differing morphological characteristics. Although the pore sizes studied are different to the average GDL relevant conclusions can still be drawn, particularly that the anisotropic network was found to favour drop spreading in the direction of greatest fibre alignment. Thompson used base-points to represent pore locations, and connections are defined by the Delaunay tesselation. The Voronoi diagram is used to construct the fibrous structure. Hinebaugh et al. [137] utilised µCT scans [138] to analyse the impact of heterogeneous porosity distributions on the percolation and breakthrough behaviour of water in a 2D random pore network. They found that water tended to accumulate in regions of high porosity, and that if a low porosity region was placed next to the inlet boundary the saturation at breakthrough was reduced (mimicking the function of an MPL). The Voronoi diagram was used directly to define pore connections, with the base points representing the circular fibres which were randomly located according to the desired porosity distribution. Gostick [69] developed Thompson's method to

study the diffusion through an anisotropic GDL, and also calibrated and validated the model by matching capillary pressure curves with experimental data obtained with mercury intrusion porosimetry [17]. Anisotropy was introduced by uniformly distributing pores throughout a domain with an initial height of 500 µm, and then scaling the pore coordinates and vertices generated by the Voronoi diagram by a factor of 0.5 in the through-plane direction only. The dry diffusivity tensor obtained from the anisotropic network corresponded very well with experimental data [139] and [140]. Gostick also calculated relative diffusivity, but agreement with the experimental data of Hwang and Weber [18] was not found. The difference between data sets was attributed to the difference in percolation process where numerical results were obtained with an Access Limited Ordinary Percolation (ALOP) algorithm and experimental results obtained by drying fully saturated samples to a desired weight which is more similar to air imbibition. Imbibition can create disconnected water clusters, as access is not limited and drying also occurs on all faces of the domain, whereas the simulation only allowed percolation from the bottom face. In addition to the overall saturation, the distribution and connectivity of saturated pores clearly affects the transport characteristics of the medium and warrants further investigation. Another factor contributing to the relative transport characteristics is directionality dependent throat sizes. In previous work, Gostick et al. simulated anisotropy by constricting throats oriented in the through-plane direction [129], which led to preferential in-plane liquid spreading, and thus further hindered through-plane gas transport. The throat sizes in the random network have far lesser directional dependence, yet in-plane liquid spreading is still observed as a result of the injection and percolation process.

Anisotropy in the heat, mass and electrical transport characteristics of GDLs has been observed by many researchers over many different commercially available samples [141], [47], [48]. Carbon paper GDLs in particular tend to have an in-plane alignment of fibres which increases in-plane transport compared with through-plane. Wu et al. constructed a series of 3D cubic pore networks representing GDLs to investigate the effects of structural parameters such as anisotropy, heterogeneity and coordination on the effective oxygen diffusivity [142]. The study was limited to a regular network topology with maximum coordination of

6 and throats aligned orthogonally. Pore and throat sizes were assigned using a uniform probability distribution over a set of fixed ranges, with larger ranges increasing the heterogeneity. Anisotropy was introduced by constricting throats aligned in the through-plane direction, and this was found to increase the exponent of the relative diffusivity function (see Equation 2.2.12). Computer aided pore-network design has also been implemented into a GDL fabrication process [143], and radial biasing has been shown to influence directional liquid water flow and reduce flooding significantly.

While cubic networks are useful for parametric studies they, do not necessarily best represent the disordered entangled fibrous structure of common GDLs as shown in Figure 2.2. The average coordination number of GDLs will be higher than that of a regular cubic network, and the orientation of throats will not be so orthogonal. The structural parameters such as anisotropy and homogeneity can be easily varied in a random network when using the Delaunay/Voronoi technique. The Voronoi regions surrounding each pore have vertices at the intersections of the fibres. These vertices can be scaled along with the pore coordinates to squash or stretch the pore space along a particular axis. This results in altered throat properties for throats aligned with that axis. The process results in connections that are not truly based on the Delaunay network of the final points, but is a simple and effective means of introducing anisotropy. Porosity distributions can also be introduced by choosing regions of higher or lower pore density. A higher density will result in a greater number of Voronoi facets which contribute to the fibrous structure and reduce porosity locally. The average coordination and degree of regularity can also be controlled to an extent with the configuration of the initial pore placement.

2.4.4 Full Morphology

Schulz et al. [144] and Zamel et al. [145] have used a technique known as full morphology (FM) which uses image analysis to determine the steady state liquid water distribution based on various wetting parameters. [69] also employs the technique and refers to it as morphological image opening (MIO). The technique takes a binary image of a porous material and uses a structuring element which is

typically a sphere (or voxelized approximation of a sphere) to "open up" the image. What this means is that sections of the image denoted as pore space are filled with the spherical elements, which can overlap each other, but not the solid space. This leaves a fraction of the pore space un-occupied by the structuring elements representing the residual wetting phase (air in the case of PEFC) and a fraction occupied representing the non-wetting phase, water. The water occupied sections can be further analysed and grouped into connected clusters, if a cluster reaches an inlet of the image domain it is kept and if not then it is returned back to pore space. In this way access limitations can be simulated and the capillary pressure related to the size of the structuring elements to generate a drainage curve. Schulz et al. [146] studied the effects of compression on the GDL by means of a finite element approach to reconstructing the geometry and a pore-morphology (PM) two-phase model. It was found that a compressed sample offered less resistance to liquid flow due to micro-structural changes in the percolation pathways. This observation agrees with experimental data gathered by Ramos-Alvarado et al. [147], where the relative permeability shifts from a high power law relation to a lower one, indicating a faster transition from the gas to liquid permeation regimes with increasing liquid saturation.

2.4.5 Lattice Boltzmann Method

Of the pore-scale methods, the LBM is by far the most computationally expensive but gives the most accurate representation of real fluid dynamics. The LBM evolved from the lattice gas automaton where particles resided on a lattice grid in discrete nodal locations. Particle interactions were described by collisions between neighbours and the method was able to simulate quite realistic fluid behaviour. However, the method suffered from numerical noise, requiring very large numbers of particles (or very small resolution), and computers turned out to be quite slow at working with discrete numbers, preferring floating point calculations. The LBM is based on a continuum description of molecules and combines the lattice approach with Kinetic Theory to solve a velocity distribution function (Maxwell-Boltzmann Distribution) at each node. The great advantage of the LBM is that macroscopic variables such as density, flow velocity, temperature and stress can be

calculated by summing individual terms of a truncated Hermite expansion of the velocity distribution function using Gaussian quadratures about the lattice points. In this way the details of the geometry can be treated very simply by applying a uniform lattice and fluid dynamics at wall boundaries can be accounted for by interpolating between lattice points. Another advantage is that the calculations scale very well with increased computational power and have also been adapted to run on GPU's as well as CPU's. The space-time dynamics of the LBM are governed by particle scattering and free transport between lattice points. All of the physics is contained within the scattering behaviour, so it must be chosen with care. The standard choice for a collision operator is the Bhatnagar-Gross-Krook (BGK) approximation [148] which is valid for ionized and neutral gases over a continuous range of pressures from the Knudsen limit to the high-pressure limit where aerodynamic equations are valid.

Two-phase flow in porous media can be simulated using the LBM [149] by solving a fluid-fluid interaction force and a fluid-solid interaction force accounting for surface tension and surface wetting properties. Koido et al. [150] used a microfocal X-Ray CT image of a carbon paper GDL to simulate liquid percolation, and measure relative permeability in the through-plane direction. The results were compared to experimental data collected for the relative permeability of the air phase, with good agreement found. Several simulations were performed to obtain the relative permeability characteristic dependence on saturation. Firstly two-phase LBM (TLBM) was performed, where liquid was introduced into the domain considering fluid-fluid, fluid-solid interactions and gravity. Secondly single-phase LBM (SLBM) was conducted for air, considering the liquid as a solid phase and, thirdly SLBM was conducted for water considering air as a solid-phase. Hao and Cheng also performed LBM simulations to calculate the relative permeability of GDL but used a stochastically generated structure as opposed to an image [151]. The dependence of permeability on saturation is different in the two studies: the exponent for relative gas permeability is 5 for Koido et al. and 3 for Hao and Cheng. This is perhaps due to the very planar nature of the Toray carbon fibre paper in the study of an actual image, giving a very anisotropic structure compared with the more isotropic structure that was computer generated. Wettability was also studied by Hao and Cheng and found not to affect the in-plane

or through-plane relative permeability, which also tend to show the same characteristics. Chen et al. use a cross-section of a 3D reconstructed GDL to simulate two-phase flow in an interdigitated flow field scenario, with pressure difference causing flow under a rib between two channels [152]. Anisotropy was introduced to the GDL with in-plane permeability double that of through-plane to simulate realistic GDLs. Electrochemistry terms were included in the simulation and the oxygen and water vapour concentrations were studied as a function of overpotential. The results show distinct minima and maxima in the concentrations, and therefore corresponding current densities, not seen with homogeneous GDL modelling. Liquid water dynamics were also investigated with droplets introduced into the section of GDL beneath the rib. Both capillary dominated creeping flow and shear induced flow were observed depending on the air flow in the local region of the GDL. Froning et al. use a stochastically generated fibre image to study the effects of compression on the GDL with the LBM [153]. The image is built up from stacking planar fibrous sheets and compression is simulated by merging neighbouring sheets. Their results agreed well with a Karman-Cozeny (K-C) model of permeability in the through-plane direction, but suffered from finite size effects when calculating the in-plane properties, and multiphase transport was not simulated. In later work Froning et al. simulated the flow through a partially compressed GDL in an HT-PEFC where water exists only in vapour form [154]. Entangled fibrous materials were simulated to simulate the structure of Freudenberg GDLs and this time a K-C model was not such a good fit.

Kim et al. [87] studied the effect of MPL thickness on the saturation of a combined MPL and GDL layer in 2D using the LBM. The results show that a thicker MPL region leads to lower over-all saturation. Transient saturation fluctuation was also observed at interfacial breakthrough of liquid clusters due to a temporary reduction in capillary pressure. Rosen et al. [155] combined X-ray tomography with the LBM to investigate the relative diffusivity in both in-plane and through-plane directions. Both rib and channel sections of the GDL were found to display similar characteristics, with relative transport exponents of 3 for through-plane and 2 for in-plane. García-Salaberri et al. [156] investigated the effective diffusivity in a partially saturated GDL reconstructed from tomographic images. The resistance of water to gas transport was found to depend strongly

on the local saturation, as bottle-necks can form in regions of high saturation which dominate the total resistance of the medium, and can be present even at relatively low total medium saturation. This brings into question the suitability of medium averaged properties and relations applied to homogeneous domains in continuum style modelling. The findings suggest that volume-averaged multiphase models explicitly solving local diffusion processes within finite sized porous media must incorporate constitutive relations obtained under conditions of no saturation gradient. The simplified methods (PNM and FM) suffer from systematic over-estimation of the water content, according to Vogel et al. [157] due to the required assumption that the wetting-nonwetting interface has a spherical shape. However, the simple network model is of great use when the relevant properties may be deduced from statistical descriptions of the pore structure.

2.4.6 Modelling Summary

The continuum models employed in computational fluid dynamics and the discrete pore network models are both useful for studying the details of multiphase transport in PEFCs. Volume averaged approximations are usually employed in continuum models to represent the porous regions to save on computational expense and to avoid complicated meshing. Pore-scale models offer greater details of the liquid distribution under different conditions, producing constitutive relations between capillary pressure and saturation and relative transport properties, but have yet to be applied to a full cell geometry. The application of the constitutive relations to continuum models for thin porous material where the GDL thickness is typically only 10-15 pores is questionable. Percolation processes in the flow regime encountered within PEFCs tend to produce non-uniform saturation profiles. This also brings into question the continuum approach which relies on average saturations, and produces diffusion like patterns for saturation, more similar to an invasive front than capillary fingering.

For the purposes of this investigation, the volume averaged continuum modelling approach is deemed unsuitable for studying the effects of compression on multiphase flow. Parametric studies of the different capillary pressure relations and relative permeability have already been performed showing that they have

great impact on the saturation in the porous media and therefore fuel cell performance. However, these relations are often fitted to experiment without deep knowledge of the material microstructure and solid-fluid interactions. A study of the effects of compression, which alters the microstructure, must therefore simulate and fully represent the morphological changes and fluid behaviour at the pore scale.

An ideal situation would be a coupling of an efficient pore-scale model to represent multiphase fluid dynamics with a continuum model which can solve the necessary equations to determine fuel cell performance over a larger domain size than the pore-scale model. This would also allow a better treatment of interfaces between components of differing porosity and pore size. Coupling models is out of the scope of this thesis but is addressed in the final chapter under the scope for future work.

2.5 Common Visualisation Techniques

Experimentation informs modelling and vice versa, and although visualization of liquid water is not included in this work, the techniques are outlined in this chapter to give further context. Liquid water formation and distribution is challenging to visualise in-situ due to the opaque nature of conventional materials such as graphite or metallic bipolar plates and carbon-based GDLs. The methods described here help validate the numerical models and enhance the understanding of pore-scale and cell-scale multiphase flow.

2.5.1 Nuclear Magnetic Resonance (NMR)

NMR is a physical phenomenon by which nuclei absorb and re-emit electromagnetic radiation in the presence of a magnetic field. The radiation emitted is detectable because it occurs only at specific resonant frequencies which depend on the strength of the magnetic field and the properties of the nuclei. Stable hydrogen isotopes are most commonly observed with NMR and several research groups have reported liquid water visualisation using this technique [158], [159], [160]. The technique has provided useful information about the water content in

the gas channel and membrane but is unable to resolve the GDL and other finer layers due to the limited spatial and temporal resolution provided, and rapid signal attenuation that occurs. Also, due to the restriction on magnetic properties, only limited materials (such as acrylic resin) can be studied, and often only very small cells may be tested [161].

2.5.2 Neutron Radiography

Neutron imaging involves measuring an attenuated signal from a beam of neutron particles and can produce two-dimensional images with a resolution of 25 µm, with a frequency up to 30 frames per second [162], [163]. The technique is particularly suited to visualising liquid water in fuel cells, because water carrying hydrogen atoms attenuate the signal but metals do not. The high resolution and frame rate make the technique suitable for transient analysis, but currently only a few institutions in the world have the necessary equipment. A trade-off between spatial and temporal resolution also occurs where high spatial resolution images need a longer exposure. Hatzell et al. used neutron imaging to investigate temperature driven flow [164]. Iranzo et al. incorporated saturation data from neutron imaging into a CFD model to calculate the effective diffusion through a GDL [165]. LaManna et al. used high resolution neutron (15 µm) imaging to investigate temperature, pressure and RH gradients on saturation in an asymmetrical cell [166]. The benefit of neutron radiography is its application to study larger cells made from standard fuel cell materials under realistic operating conditions. The draw-back is that average through-plane saturation profiles lose the details of water in individual pores, and the effects of certain in-plane geometrical features of the cell. Forner-Cuenca et al. have recently produced and studied a treatment technique that creates GDLs with a graded wettability which produces excellent phase separation, and has been visualized with neutron and synchrotron imaging [167], [168].

2.5.3 X-ray Radiography

Synchrotron X-ray sources typically have a much higher flux than neutron sources, and this makes them more suitable for investigating highly transient phenomena,

such as water droplet eruption from the GDL. The spatial resolution achievable with X-ray radiography is also about one order of magnitude finer than neutron radiography, but it is currently only possible to investigate relatively small sections of the fuel cell (typically a few square millimetres) [169]. Tomography techniques can be employed to render a pseudo three-dimensional image of the water distribution within the fuel cell [170]. During operation such studies have observed a swelling of the membrane by as much as 50%. As with NMR, the nature of the experimental technique limits the materials or design of the fuel cell being investigated to permit the X-rays to pass through the material. Some researchers have also found a degradation in performance after exposure to X-rays [171]. However, this technique is promising and growing in popularity as a tool for water visualisation and defect detection [172]. Eller et al. produced in-situ tomographic images with and without the presence of water [14]. Images were then processed to resolve liquid droplets in the GDL and flow channel of a working fuel cell. A spatial resolution of 2 µm was achieved and a temporal resolution of 1 second allowed very clear reconstruction of water in the GDL but slightly blurry reconstruction of water in the flow channels where movement occurred during the image capture. Never-the-less, the images produced are impressive and informative. Three main observations can be made from the results of the study which are shown in Figure 2.12:

i A high liquid saturation is observed under the ribs, in line with other observations. A common interpretation is that the area near the rib is cooler but is also shielded from high gas velocity.

ii A high liquid saturation is observed near the cathode catalyst layer.

iii In the bulk of the GDL water drops of different sizes are reconstructed, many of which are not connected by a liquid path to the channel interface or catalyst layer.

2.5.4 Electron Microscopy

Environmental Scanning Electron Microscopy (ESEM) has been used by Nam and Kaviany to visualise the formation and agglomeration of liquid water droplets in

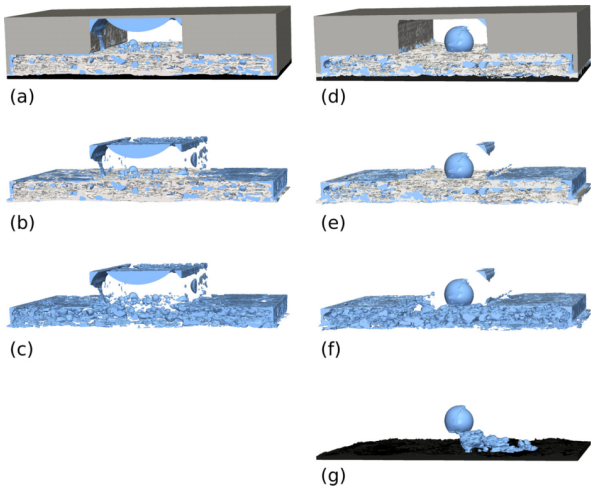

Figure 2.12: Smoothed surface rendering of phase segmented in-situ measured tomography data of cathode GDL (Toray TGP-H-060) of two different vertical cells; (a) and (d) flow field, GDL, CCM and liquid water; (b) and (e) GDL and liquid water; (c) and (f) liquid water; (g) surface droplet and water cluster connecting droplet to catalyst layer [14].

the GDL [15] and MPL [10]. The images gathered support Nam and Kaviany's branching tree hypothesis for liquid transport, but the configuration results from condensation processes only. Gurau et al. have also used SEM to visualise water droplets in the GDL in order to estimate the internal contact angle [173]. They conclude that conventional techniques for measuring contact angles do not provide accurate results, because the internal contact angle is more a function of surface roughness than material, so becomes a statistical property.

2.5.5 Optical Photography

By replacing the conventional current collector with a transparent one it is possible to view and record liquid flow in the gas flow channels and emergence from the GDL. Notable examples of this techniques include Tüber et al. who studied the effect of GDL coating and air flow velocity in a straight channel [174], Theodorakakos et al. who visualised droplet detachment from a side profile and validated a VOF model [102], and Bazylak et al. who performed an ex-situ experiment to

investigate the rapid emergence of liquid water from the GDL and also validated the results with CFD [175]. Kimball et al. conducted an ex-situ experiment with a controllable water mass-flux and an orientable fuel cell to investigate the effects of gravity on droplet formation and flow within the channels [176]. The study found that when droplets detach they collide with others downstream to form slugs, these slugs may become trapped if sufficient work is required to move them against gravity. They state that most CFD models ignore the effect of gravity and that a probabilistic approach to modelling the forces on liquid water in the flow channel may be more appropriate than any VOF method. Lu et al. studied the dynamic breakthrough and intermittent drainage characteristics of GDLs with and without applied MPLs [85]. The study found that the presence of the MPL increases the focus of droplet emergence to a few preferential sites and also pushes the slug-to-film flow regime to higher air velocities.

2.5.6 Fluorescence Microscopy

Fluorescence microscopy has been used by some groups in conjunction with optical photography to visualise transport through fibrous structures. Dye was injected into the GDL and was observed to follow different pathways in regions of higher compression [177]. This behaviour was attributed to the breaking of the hydrophobic coating and is suggested by Bazylak et al. to be potentially beneficial because the GDL could be strategically compressed in regions where water transport is preferred. Confocal fluorescence microscopy has been used to visualise unstable liquid transport through various GDL materials which was found to be largely random and similar to column flow in hydrophobic soils [178]. The samples tested were all carbon paper and had similar levels of PTFE treatment so strong conclusions cannot be drawn. However, the study does draw attention to the assumption made by some modellers, and rightly questions, that flow is uniform and stable.

2.6 Experimental Characterisation of Porous Components

Experimental characterisation of the porous components of the PEFC is important for understanding the dominant transport characteristics of the components, validating numerical models and also optimising the fuel cell performance. This section briefly overviews the experimental studies of both the single-phase effective properties of porous media used in PEFCs and multi-phase relative properties. An excellent review of the subject is presented by Zamel et al. [52].

2.6.1 Effective Properties

Effective Permeability

Permeability is typically measured by establishing a steady flow through a porous sample and measuring the flow rate and pressure drop then equating the two according to Darcy's Law (Equation 2.2.13). Darcy's Law assumes a linear dependence of the pressure drop on the flow rate and considers viscous forces only. At high flow rates inertial forces become more important and a non-linear term is added to the equation which becomes the Forchheimer equation (Equation 2.2.14). Ihonen et al. studied the permeability of GDLs and the parameter's effect on fuel cell performance [179]. They conclude that a permeability of 1E-12 m^2 should be sufficient and that it is more important to avoid flooding and loss of porosity under two-phase conditions than to maximize permeability under single-phase conditions. Feser et al. measured the in-plane permeability of three GDLs with a radial set-up and found that compressibility effects could not be ignored at high flow rates, and that the carbon cloth GDLs typically have a much higher permeability than carbon paper [180]. Gostick et al. measured the permeability of several common GDLs in three perpendicular directions showing that in-plane permeability in materials with strong alignment of fibres have higher permeability in the direction of alignment [141]. It was found that, for typical fuel cell operation, the error in using Darcy's law to calculate permeability due to inertial effects was about 5%. If convection can be enhanced in operating

fuel cells then these inertial effects will become non-negligible. The permeability dependence on compression was also investigated and found to fit quite well with a K-C model for materials with isotropic in-plane structure. However, a Tomadakis-Sotirchos (T-S) model [181] fitted completely anisotropic materials better. Gurau et al. calculated the coefficients of the Forcheimer equation for both in-plane and through-plane directions of GDLs with and without microporous layer, and with differing PTFE coatings [182]. It was found that samples with higher PTFE content in the MPL have higher viscous permeability coefficients compared to samples with lower PTFE content in the MPL. Analysis of PTFE-C structures reveals a bi-modal pore distributions of primary pores inside the carbon agglomerates (20 - 40 nm) and secondary pores between agglomerate (40 - 200 nm) [183]. It was found that increased PTFE loading increases the volume of the larger secondary pores (intra-agglomerates), therefore increasing permeability and also increases rigidity, enabling the material to maintain higher porosity under compression. Ismail et al. studied the through-plane permeability of GDLs without MPLs [184] and in-plane permeability of GDLs with MPLs [185]. The non-Darcy terms were found to be significant and the effect of the MPL on the in-plane permeability was to reduce it by up to an order of magnitude, implying significant levels of penetration into the GDL. The research group of Secanell present methods for simultaneously calculating the permeability and effective diffusivity of a GDL sample by means of a diffusion bridge with gas flow at different pressures on either side and an oxygen sensor [186] and [187]. The effect of PTFE content and compression on both parameters was investigated and found to decrease with porosity as expected. However, the method is limited to samples with an MPL in order to produce a suitable pressure gradient.

Effective Diffusivity

Arguably the most important transport characteristic of the porous media in PEFC is the diffusivity. Diffusion is the dominant transport process occurring within operating fuel cells for both reactant distribution and product water vapour removal. Therefore, a high diffusivity enables higher power density, as mass transport losses can be reduced. A standard technique for measuring the

diffusivity of porous media is to flood the material with an ionic solution and measure the conductivity to infer the formation factor: the ratio of the electrical resistance of the flooded porous sample to the bulk solution [188]. However, as the solid material of the GDL is conductive, the standard technique is inappropriate. The problem has been overcome by Kramer et al. by using electrochemical impedance spectroscopy to de-couple the electrical and ionic impedance [139], by making use of the fact that electrical conductivity is much higher than ionic conductivity. Therefore, when applying a high frequency sinusoidal current to the sample, the response is largely dependent on the material with lower conductivity. Fluckiger et al. also used the same technique to investigate the effect of the amount of PTFE binder and compression on the diffusivity [140]. It was found that the binder reduces the diffusivity of the samples and has an isotropic effect, whereas compression pronounces the in-plane orientation of the fibres.

Baker et al. used limiting current to characterize gas transport resistance and compared in-situ and ex-situ data to ascertain where the bulk of the transport losses occur within the cell [189], [190]. It was concluded that most of the diffusion resistance was Fickian and occurred in the GDL. Beuscher also carried out limiting current experiments and compared fuel cells with a single GDL and a stack of two GDLs on the cathode side of the cell [191]. Beuscher determined that GDL resistance accounts for about 26% of the total mass-transport resistance in the standard case of one layer of GDL by approximating the diffusional resistance of each component like resistors in series. Beuscher also concludes that Knudsen diffusion and film diffusion through ionomer and water films accounts for about half the total resistance.

Another technique is to use a Loschmidt cell to measure the transient concentrations within two chambers connected by the porous sample being characterised. Astrath at el. employed this technique to investigate the effect of relative humidity on binary gas diffusion [192], and Zamel at et al. later investigated the effects of applying PTFE to the GDL [193]. An oxygen sensor is placed inside one chamber at a distance from the sample and measures the equivalent diffusion coefficient by the transient response to a change in concentration. The equivalent diffusivity contains a contribution from the GDL and a contribution from the bulk diffusivity in open space. Unfortunately, due to the thin nature and high

porosity of GDLs, the overall contribution of the GDL is between 5 and 10%, using quoted values [193], which introduces large uncertainties in the results. The problem may be overcome by stacking several samples together for dry GDLs, but this would prove problematic for wet samples as water may wick and accumulate at the interfaces where porosity is higher. Chan et al. used a Loschmidt cell to measure the effective diffusion through a GDL with an MPL [194]. They determined that the diffusivity of the combined material was about 40% that of the bare substrate, and that Knudsen diffusion played an important role comprising roughly two thirds of the diffusive resistance in the MPL layer.

The effective water vapor diffusion coefficient has been determined by LaManna et al. for various unsaturated gas diffusion layers [80]. The experiment involved flowing a dry gas stream and a humidified gas stream in parallel with a GDL as the separator whilst measuring the humidity of the streams at the outlets to determine cross-over by diffusion. The back-pressure was carefully controlled to reduce convective transport across the sample, but uncertainty was inevitably quite high for samples without an MPL, which provides greater bulk resistance due to the lower permeability.

Rashapov et al. recently measured the effective in-plane diffusivity of a range of GDLs subject to compression [5]. The experiment utilised a sample holder containing a long thin strip of GDL placed between two metal plates and sealed with putty either side. Shims were used to control the level of compression and gas with varying oxygen concentrations was used to purge the samples establishing a constant initial concentration. Once purged, the samples were exposed to atmosphere either at both ends or one end, and the transient concentration was monitored at a fixed point along the sample's length. Fick's 2nd law was used to determine the effective diffusivity, and it was found to depend strongly on compression as the porosity reduced, and the tortuosity increased significantly. The method developed by Rashapov et al. is extended to measure the diffusive transport through partially saturated GDLs, i.e. relative diffusivity, in Chapter 5.

2.6.2 Relative Properties

As the power requirement of the fuel cell under certain operating conditions increases, saturation also increases if removal mechanisms are not in place such as purging or heating, or if sufficient vapour gradient is not established. Thus, the transport properties of the media are become significantly different from the dry conditions. An understanding of how gases transport through the saturated porous media is essential for predicting the behaviour and performance of the fuel cell, as a continual supply of reactant gas is required to sustain power production. The dependence of the effective transport properties on saturation is termed the relative permeability or diffusivity, and typically follows a power-law relation as discussed in Section 2.2.

Relative Permeability

Hussaini and Wang measured the through-plane and in-plane relative permeabilities of both the air and liquid water phases through a carbon paper and carbon cloth GDL [56]. Both phases were made to flow through the samples simultaneously and the pressure drop was measured for a given flow rate once steady-state was achieved. Darcy's law was then used to calculate permeability and saturation of the sample was measured by swiftly removing and weighing it. Samples were dried completely between experiments and different saturations were achieved by varying the ratio of the air and liquid flow rates. It was found that through-plane relative measurements suffered from high uncertainties, as the method relied on stacking samples. This could have resulted in liquid accumulation in the end layers creating bottlenecks. In-plane measurements were more reliable and a relative transport exponent of 4 was found to match the water data quite well for both carbon paper and cloth. Different relations were found to match the in-plane air data with:

$$K_{r,a} = (1 - S^2)^4 \tag{2.6.1}$$

for carbon paper and Equation 2.2.16 fitting the carbon cloth data with an exponent of 3.

Ramos-Alvarado et al. measured the relative permeability of the liquid phase in the through-plane direction for Toray090 samples with varying PTFE content

	Uncompressed	Compressed
Untreated	8	5
Treated	3	2

Table 2.2: Liquid Relative Permeability Exponents.

and varying compression [147], extending the work of Sole et al. [195]. Again the samples were stacked together, but unlike the experiment performed by Hussaini and Wang, the saturation of a central sample was measured. Values for the relative transport exponent used in Equation 2.2.17 are shown in Table 2.2. The fact that the untreated and uncompressed results have such a high exponent may be due to the uneven accumulation of liquid water in different samples along the stack of samples, and possible pooling of liquid at the interfaces between samples. Compression gives better contact between samples and could lead to better water transport along the stack, resulting in a lower transport exponent. Unfortunately, the relative transport behaviour of such thin and porous material is found by both Hussaini et al. and Ramos-Alvarado et al. to be very difficult to measure accurately. Wang et al. measured the in-plane permeability of both phases whilst using neutron imaging to calculate the saturation [196]. Results for the high and low saturation regions were difficult to measure because a percolating cluster in each phase is needed to establish a steady state. It was found that the power law relation was not a good fit to the data over the full range of saturations, and that saturation measured by the neutron and gravimetric methods can differ, possibly due to water imbibing when de-clamping the apparatus.

Relative Diffusivity

Electrochemical impedance spectroscopy, the diffusion bridge, and the Loschmidt cell techniques for measuring effective diffusivity, are rather difficult to use to measure the relative diffusivity. A carefully controlled environment is necessary and the uncertainties in the level of saturation would be high, due to the difficulty in localising the liquid, and maintaining a constant saturation through evaporation. Utaka et al. measured the diffusivity of GDLs by means of an oxygen sensor

based on a galvanic cell under both dry and wet conditions [197], [198]. The sensor itself consumed oxygen and established the concentration gradient necessary for diffusion to occur. The technique was used to investigate a novel GDL structure combining sections of different wettability. An uneven water distribution was created where water moved from the hydrophobic to the hydrophilic region, thus creating pathways for gas transport. At low saturations the effective oxygen diffusivity of the hybrid configuration was almost five times larger than that of the standard GDL with no wettability variation. Iwasaki et al. also used the method to measure the relative diffusivity through stacks of GDLs (comprised of around 130 individual samples) measuring 50 mm in through-plane thickness [199]. The relative transport exponent was found to be very high, however, the results are not representative of a single sample. Saturation was controlled by first vacuum flooding the stack and then drying it, but the two ends of the stack were subject to different conditions so dried at different rates, creating a saturation profile throughout the stack, with high saturation samples severely limiting diffusion at relatively low stack saturation. Koresawa et al. later improved the accuracy of the galvanic cell technique, citing improvements in uncertainty for single dry GDLs from 50% down to 20% [200]. However, the results presented still show a rapid decrease in diffusivity at low saturation indicative of a bottle-neck.

Hwang and Weber developed the limiting current method to investigate partially saturated GDLs in an ex-situ fashion using an electrochemical hydrogen-pump cell [18]. The method utilized a working and reference electrode separated by a proton conducting membrane to split hydrogen and then recombine it. The electro-kinetics were fast so that the limiting current was purely down to mass transport limitations caused by the flooding of the working electrode. The GDL was submerged in deionized water in a small container which was vacuum pumped in order to de-gas the sample, then saturation was controlled by drying the sample in ambient conditions until the desired weight was achieved. Some loss of water occurred during cell assembly but this was estimated to be no more than 10% at higher saturations. The size of the cell and portion of GDL open to the hydrogen gas stream was also minimized to ensure saturation remained constant and down-channel effects, such as variation in hydrogen concentration, were minimized. The experimental set-up was limited to measuring the through-plane

diffusivity but several different samples (Toray, SGL and Freudenberg) were all tested and found to produce similar results. The relative transport exponent was found to be around 3 in all cases. The results agree well with a PNM based on continuously connected water configurations in an ideal lattice [15]. It is expected that randomly filled water distributions lead to greater tortuosity in the gas phase and therefore higher exponents around 4 or 5, but a critical assumption of the PNM is how the gas phase conducts through partially filled pores. X-ray tomography has shown that partially water-filled pores still allow for gas flow, therefore the relative transport exponent might be expected to decrease. The effect of PTFE was also studied and found to reduce the relative transport exponent, thus improving diffusion. Hwang and Weber attribute the improvement to the PTFE creating good phase separation [18].

2.7 Influence of Structure and Compression

A major factor influencing water transport is the structure of the GDL and pore size distribution. The PTFE treatment reduces the number of large pores but is not able to penetrate smaller pores [201]. Macropores of radius 1 - 20 µm are found to be the most abundant, irrespective of PTFE loading. For hydrophobic porous media, liquid preferentially flows through larger pores because the capillary pressure is smaller; this results in a form of flow known as invasion percolation. Nam and Kaviany present a picture of liquid permeation [15] where many smaller flows through smaller pores converge into larger ones towards the gas channel side of the GDL forming a pattern likened to an "inverted-tree", shown in Figure 2.13.

Nam and Kaviany distinguish two forms of water transport, micro and macro. Near the catalyst layer a large number of condensation sites exist which encourage the formation of micro-droplets. These micro-droplets agglomerate when they come into contact with other droplets. This motion is largely random but has the effect of filling the pores and creating macro-droplets towards the lower saturation region nearer the flow channel. Macro-droplet flow will preferentially select larger pores, due the smaller capillary pressure required and lower flow resistance.

The inverted-tree hypothesis was supported by Pasaogullari and Wang [8] but Litster et al. present a slightly different scenario [16], shown in Figure 2.14.

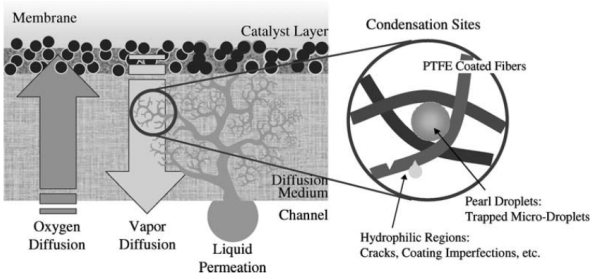

Figure 2.13: Nam and Kaviany's representation of the water transport model, showing the branching micro- to macro-transport. [15].

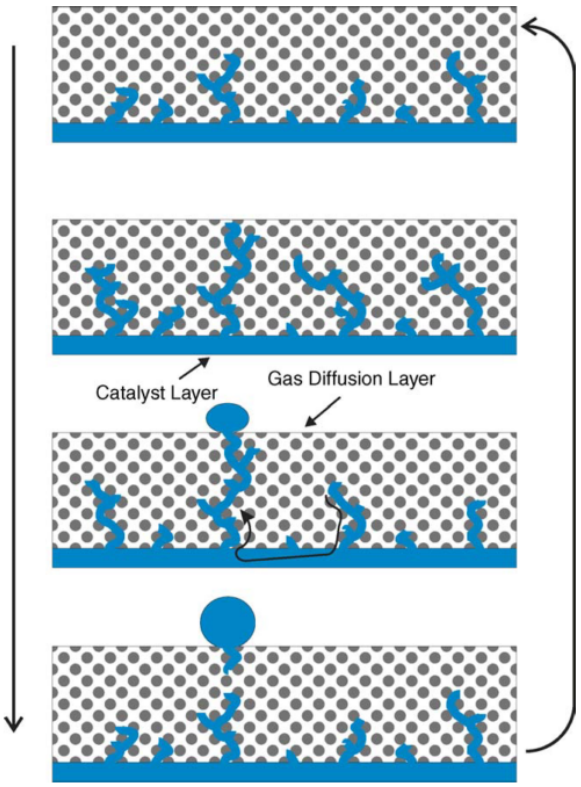

Figure 2.14: An alternative picture of water transport presented by Litster et al. [16].

Their study involved the ex-situ visualisation of liquid permeation through a carbon paper GDL with fluorescence microscopy, and produced a channelling and

fingering pattern. Distinct pathways were observed with some resulting in dead ends and others reaching the surface or converging. If pathways were hydraulically connected, the fate of one percolation affected the other, with a dominant pathway being established and others receding once breakthrough was achieved. The true pattern of liquid formation and percolation in an operating fuel cell GDL is most likely a combination of the two scenarios, and how closely each is resembled will depend on the operating conditions. Disconnected clusters may form when phase change is encouraged, and channelling clusters periodically reach the gas channels and produce droplets, if undisturbed by convective forces or phase change.

Jiao and Zhou proposed that conventional gas diffusion layers do not encourage a well organised liquid water flow from CL to flow channel [202]. Three examples of structured geometry were modelled representing the GDL near the CL region. It was concluded that the key property to consider, when designing the GDL, is to enhance air flow within the CL region. Jiao and Zhou also conclude that residual water inside the CL is unavoidable because it stops moving when all forces are balanced such as surface tension, wall adhesion, and contact with the membrane.

The structure of the GDL is, to an extent, dependant on the level of compression that each component is subject to, which is determined by the clamping pressure and the width of the gasket used to seal the fuel cell. Pressure due to compression occurs at varying levels throughout the cell and is highest beneath the ribs of the current collector, which form the contact points to the GDL. The following sections describe experimental and numerical investigations of the effects of compression on fuel cell performance:

2.7.1 Studies of Compression: Experimental

Experimental studies summarized in Table 2.3 have shown that the effects of compression cannot be ignored. The impacts on a number of performance factors such as electrical conductivity and gas permeability have been explored; the experimental results generally show a reduction in permeability by up to an order of magnitude when the GDL is compressed but thermal and electrical conductivity is increased as contact resistance is reduced.

Authors	Relevant Findings	Highest CR
Nitta et al. [203]	When compressed, sections of GDL beneath the channels remained at the same thickness and sections under the rib were compressed to the thickness of the gasket. In-plane permeability of the GDL decreased non-linearly by an order of magnitude in the compressed sections and the electrical conductivity increased linearly with compression.	35%
Ge et al. [204]	High compression reduces performance at high current density so contributes to greater mass transport losses. Losses occur sooner and the effect is more pronounced for carbon paper compared with carbon cloth. The decrease in contact resistance improved performance at low current densities but the amount is insignificant compared with mass transport loss.	39%
Gostick et al. [141]	Compressed GDL samples suffer a reduction in permeability by an order of magnitude in both in-plane and through-plane directions. Results compare well with Carmen-Kozeny and Tomadakis-Sotirchos models of permeability	50%
Bazylak et al. [177]	Ex-situ study using fluorescence microscopy showed that 80% of liquid breakthroughs occur in compressed regions which is greater than the proportion of GDL being compressed, thus illustrating that compression creates preferential liquid pathways. The effect is attributed to the hydrophobic PTFE coating being damaged leading to the creation of hydrophilic pathways.	Not stated
Ismail et al. [184]	The permeability in both in-plane and through-plane directions is reduced by up to an order of magnitude when the samples are compressed from 80% to 65% of the uncompressed thickness.	35%
Gao et al. [205]	Neutron radiography showed that the liquid water saturation in the GDL in the regions next to the ribs were lower than those in the regions next to the channels	12%
Sasabe et al. [206]	In-situ soft X-ray radiography study reveals in-plane and through plane visualisation of liquid water profiles. The majority of liquid water accumulates under the rib sections with one possible explanation given that the longer diffusion pathway for water vapour under the ribs amounts to a less effective removal and more condensation.	Not stated
Ramos-Alvarado et al. [147]	Compression shown to increase relative permeability for both wet-proof and non-wet-proof samples.	24%
James et al. [207]	X-ray computed tomography and numerical simulation based on pore-space shows that electrical conductivity doubles for compressed sections. Diffusion co-efficient decreases, however, through-plane diffusion coefficient increases relative to in-plane coefficient and both are significantly lower than the Bruggemann correlation.	40%
Mason et al. [208], [74]	Electrochemical Impedance Spectroscopy shows that with increasing compression, a significant reduction in net performance is observed, with the most significant differences occurring in the mass transport regions of the performance curves due to a reduction in GDL porosity. Periodic dimensional change is observed in the cell caused by membrane swelling which acts to compress the GDL, causing performance changes as the membrane becomes more hydrated and contact resistance decreases. Current spikes are also observed caused by liquid flooding and quick removal which temporally correspond to dimensional changes in the membrane but have a varied magnitude.	15%
Mortazavi and Tajiri [209]	Breakthrough pressure increases as GDL is compressed but the trend is non-linear and changes are slight for high compression. Breakthrough is only observed in 1 out of 5 cases when the sample is virtually uncompressed suggesting that compression is beneficial to breakthrough behaviour.	80%

Table 2.3: Experimental studies of the effects of compression on the GDL.

The non-uniform compression has been found to have implications for water distribution and performance throughout the cell, as shown by several different research groups [177], [210], [211]. For example, parallel flow channels in a serpentine design will have a pressure difference between them which forces the gas to flow beneath the ribs. This cross channel flow is crucial for interdigitated flow channels, but beneficial to mass transport in all cases. Park and Li conducted a numerical and experimental investigation into the effects of the cross channel flow and found that a considerable amount of cross-flow will occur for GDLs with high permeability, thus aiding water removal [212]. The pressure drop along the flow channel attached to a GDL was compared to a flow channel attached to an impermeable membrane, the drop was found to be significantly lower with the GDL which implies that less power is required to pump the reactant gases when GDL permeability is high. A novel fuel cell design employing parallel channels with induced pressure differences was introduced by Bachman et al., with the hypothesis that water will be forced to flow from high pressure towards low pressure channels [213]. The induced pressure gradient was found to be beneficial for water management, and also increased the oxygen concentrations under operation without saturation, thus improving overall current density. Santamaria et al. investigated the in-plane saturation distribution with neutron radiography in a cell with strong induced cross-flow [214]. Strong correlation between total GDL saturation and cross-flow was observed, with higher GDL permeability leading to lower saturation. Transport mechanisms similar to break-through pressure phenomena were found to exist for under-land transport. Compression decreases the permeability of the GDL, thus reduces this cross channel flow. Olesen et al. also determined that non-uniform compression decreased the reaction rates in the catalyst layer, as oxygen transport is also inhibited by highly compressed regions [215], an effect that is worsened by the tendency for liquid water to form and remain there.

2.7.2 Studies of Compression: Numerical

In a numerical study by Hottinen et al. [216] it was concluded that while mass transfer and overall cell performance was not significantly affected when consid-

ering compression effects, the in-plane current density profile shows significant variation, which in turn leads to an uneven temperature profile and the development of hotspots. However, the study was limited because the effects of two-phase transport were not considered, and it was conducted for a simple GDL without an MPL. Su et al. found that cell performance is controlled by transport under the channel area, but when a sufficient pressure difference exists between adjacent channels, cross-flow occurs and brings more reactant gas to the sections beneath the rib which improves performance [211]. Wang & Chen looked more closely at the water distribution inside compressed GDL and applied a spatially varying porosity in order to obtain a saturation profile which matched neutron radiography data [217].

Chi et al. compared two numerical models with a real fuel cell with the same dimensions and operating conditions [218]. One model took compression effects into account, the other assumed uniform GDL compression and porosity. It was found that the model with realistic compression effects matched the real data more closely in terms of limiting current and polarisation. Parametric analysis of the models revealed that heat flux and temperature distribution were underestimated in the uniform case. Hydrogen consumption was found to be greater in the non-uniform case nearer the inlet and becomes depleted significantly as the flow moves down stream. The uniform case allowed a more gradual consumption along the flow channel because the ribs do not present so much of a barrier to reaction and water removal. CFD has also been used to model the effects of non-uniform compression using a single channel geometry [219]. It was found that GDL compression and intrusion into the flow channels significantly alters the uniformity of saturation, oxygen concentration, membrane water content and consequently current density profiles. These effects have negative consequences for membrane durability and long term performance.

These studies were all performed using CFD incorporating models for liquid water that rely on empirical relations between saturation and liquid phase pressure. Another approach is to use pore network modelling which models the percolation process directly. Lee et al. constructed a pore network model by simulating a semi-random fibrous structure of short overlapping cylindrical rods located along the edges of a regular cubic lattice [220]. The lattice points at

the ends of the fibres were then randomized and the void space was analysed to extract the pore and throat sizes. Compression was simulated by scaling the coordinates of the lattice points in the through-plane direction, which had the effect of reducing the area of the throats orientated in the in-plane direction whilst leaving the through-plane throats unaffected. The consequence for liquid water was to promote through-plane transport which linearized the saturation profile through the domain.

The structural changes that occur under compression impact the fluid transport within the media as porosity is reduced, tortuosity is (generally) increased, hyrdophobicity may be lost as the PTFE may become cracked and break up, and greater inhomogeneity between compressed and uncompressed sections occurs. GDL compression has also been studied by Rebai and Pratt using a cubic PNM [221] where the sizes of pores and throats were simply scaled in compressed sections of the domain. It was found that the flow of water into uncompressed sections was promoted due to the decrease in pore volume in the compressed section. The results obtained were highly dependent on the location and nature of the liquid injection sites and also the scale of the model. The porous fuel cell components are very thin and have few pores spanning the through-plane direction, this makes them highly sensitive to boundary effects, and accordingly it is suggested that a study of percolation through the GDL must be accompanied by a study of the injection sites from adjacent layers e.g. MPL or CL.

2.8 Thermal Management

Water management in PEFCs is intricately coupled with thermal management. Weber and Newman modelled the coupled processes and investigated the influence of temperature magnitude and gradients on cell performance [222]. Comparing their non-isothermal models to the isothermal case the performance of the fuel cell is usually worse, except when the heat transfer co-efficient is high and average cell temperature is lower. This is due to the benefits gained from increased kinetics which outweigh the losses due to water management such as increased vapour pressure. A heat-pipe effect is described where a temperature difference of a few degrees between catalyst layer and channel can induce phase change and transport

water towards colder regions where it condenses. The exponential shape of the water vapour-pressure curves means that at higher temperatures reactant dilution from water vapour can cause significant losses.

Temperature dependent flow was also investigated by Kim and Mench [162] who found that it occurs in two primary modes: (i) Thermo-osmosis in the membrane and (ii) phase-change induced flow (PCI) occurring in the porous media when there is a temperature gradient. Hatzell used high-resolution neutron radiography to quantify the temperature driven flow in a single cell [164]. The change in liquid water distribution over time revealed two different water transport mechanisms: capillary driven percolation termed funicular due to the requirement of phase connectivity and PCI flow termed pendular due to the existence of discrete clusters of liquid connected by flow in the vapour phase. Saturation plateaux of around 30% were observed in most cases signifying that once percolation is possible liquid water is transported back to the evaporation sites by capillary transport creating an equilibrium between the two types of flow.

Wang and Wang developed a non-isothermal, two-phase 3D model of all the PEFC components along a single channel [223]. The thermal model accounts for irreversible heat and entropic heat generated due to electrochemical reactions, Joule heating due to protonic/electronic resistance, and latent heat of water condensation and/or evaporation. Their results show that water vapour transport via diffusion along thermal gradients plays a significant role in water transport, especially along the in-plane direction. Thomas et al. showed that temperature driven water flux between anode and cathode can occur under certain conditions [224]. Their experimental results show that water flux is highly dependent on temperature differences across the cell in the through-plane direction, proposing that the major contribution is through the vapour phase between membrane and gas channel, which can occur with differences as little as 2 °C.

Several reviews of heat and mass transfer at the cell level [225], stack level [226] and at component interfaces [227] are available for PEFCs. Whilst the considerations are very important for water management, the control strategies are largely dependent on the operating conditions of the cell, which is not the focus of this study. The dominant heat transfer mechanism is thought to be conduction through the solid components, with convection in the flow streams

accounting for up to around 20% [223]. The thermal conductivity of the fuel components, therefore, plays an important role in heat and water management with higher conductivity facilitating faster heat removal. This phenomena is fairly well understood from a fundamental point of view, and the impacts on fuel cell performance have also been studied [48], so engineering questions remain largely around material choice.

2.9 Concluding Remarks

CFD is a useful tool for investigating the design parameters and operating conditions affecting fuel cell performance. Once the physical models are established, changes to the design of the fuel cell may be easily tested against the benchmark geometry and materials, and improvements in performance can be made at a fraction of the cost of building a series of prototypes. Operating conditions can be changed and controlled with the click of a button enabling a greater depth of examination than any physical test-rig. However, understanding the fluid dynamics is central to understanding the overall behaviour of the fuel cell, and current CFD models based on volume averaged porous media are lacking in a realistic representation of liquid water transport. As the management of liquid water is critical to performance, a model must incorporate the production and distribution of liquid water with as much accuracy as possible, but also retain the greatest utility possible and be able to make predictions at a full cell and stack level.

The objective of this work is to investigate the liquid transport in porous media through modelling with a more realistic microstructure and through experimentation. The effects of structural changes induced by compression of the porous media will be investigated, and the influence on multiphase flow used to inform future modelling efforts by producing constitutive relations for continuum models. In future the work could be built upon to combine the various modelling approaches for different PEFC components to best utilize their respective strengths. As the relative transport relations are very important for modelling multiphase flow, these will be the focus of the study and the key objective will be to study their dependence upon compression. Non-isothermal effects and thermal

management considerations, though important, will be left for future work when integrating the findings of this study into larger full cell models.

Chapter 3

Multiphase CFD Model of Compression Effects on GDLs

3.1 Motivation

As discussed in Section 2.2, the gas diffusion layer (GDL) of a polymer electrolyte fuel cell (PEFC) is a crucial component and performs several functions simultaneously; it facilitates reactant gas transport towards the catalyst regions and also provides pathways for product water and electron transport. The GDL also helps protect the membrane when the membrane electrode assembly (MEA) is sealed between the current collector plates. Typically the current collectors will have gas channels, between 1 and 2 mm wide, which can be connected in a range of configurations [228]. This presents a series of channels and ribs or land areas that form the contact points with the GDL. It is necessary to clamp the fuel cell together using bolts and a gasket in order to seal the gases, and this can exert considerable pressure on the GDL, thus changing the material structure and properties of the medium with sections beneath the ribs subject to high compression, as shown in Figure 3.1.

Several experimental studies of the effect of compression on the GDL have been made and are summarised in Table 2.3. Compression is found to affect the liquid water profile in the GDL and the performance of the fuel cell, but no clear picture emerges about the mechanism by which compression affects multiphase transport or how this can be controlled.

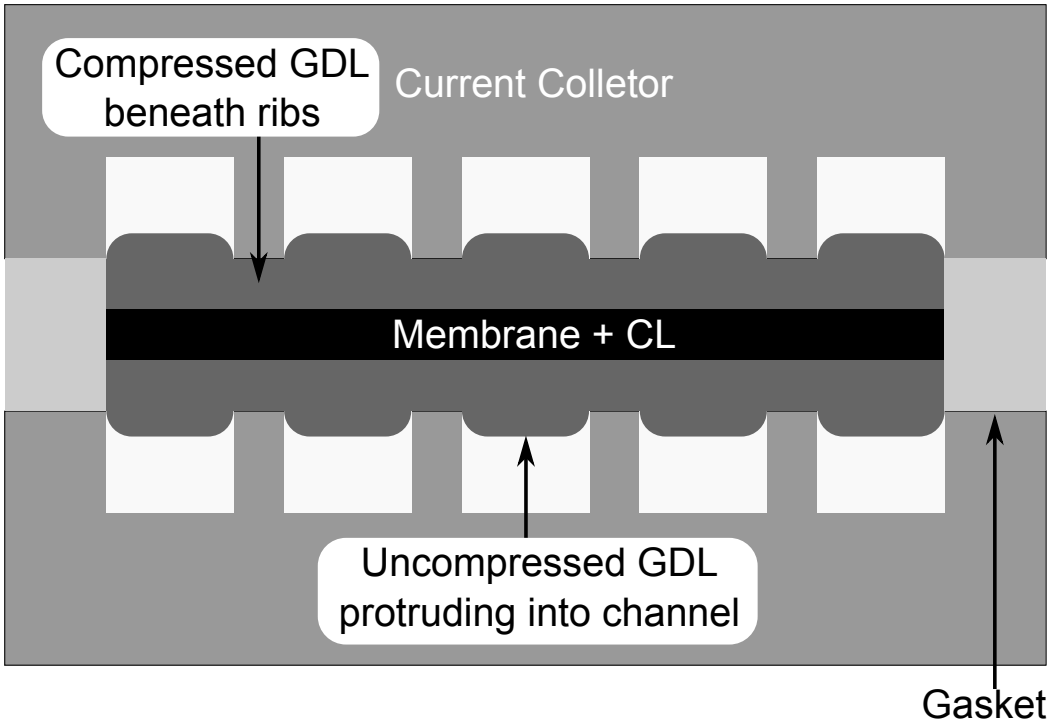

Figure 3.1: Schematic illustration of PEFC showing compression of GDL occurs up to the thickness of the gasket.

A review by Ferreira et al. [128] recently summarized the investigations of multiphase transport in PEFCs using the volume of fluid (VOF) method. Some 40 or so investigations have been conducted in recent years and nearly all focus on the dynamics of water in the gas flow channels of the bipolar plates (current collectors). The focus of the investigations, where the porous GDL is concerned, is usually on the detachment of droplets from the surface of the GDL. Park et al. [120] were, to the author's knowledge, the first to utilise the VOF method to capture liquid water dynamics inside a realistic 3D GDL structure. Drainage was simulated, and the pressure gradient from reactant flow and the contact angle were observed to be the most important parameters influencing the removal process. However, the domain was very small and the percolation process was not captured. Suresh and Jayanti [121] also modelled liquid transport through a representative GDL structure and the methods employed are the basis for the present chapter. A regular isotropic lattice of cylindrical fibres was created in 2D,

and liquid was allowed to emerge from inlets at the bottom of the domain. Cases where gas-flow is absent, present in the channel and present through the GDL were simulated to observe the effects of gas shearing on the liquid dynamics. The general pattern was that of channelling and fingering similar to the description of Litster et al. [16]. When gas-flow was present in the channel, liquid droplets emerging at the GDL-channel interface were removed from the surface, as observed by many experimenters and modellers [102], [13], [229]. Gas-flow in the GDL was also observed to influence the dynamics of liquid water, creating flow in the stream of the gases. This convective flow, however, is dependent on the permeability of the GDL medium, which reduces when the GDL is compressed, as shown by many of the experimental results in Table 2.3

In this chapter, an idealised 2-D lattice of fibres representing the GDL subject to compression in the through-plane direction is presented. Single phase and multiphase VOF simulations have been conducted to observe the effect of compression on the permeability and capillary flow which dominates the liquid transport process. A key finding is that whilst permeability is reduced by compression, liquid flow in the through-plane direction is actually positively affected leading to lower saturation of the GDL at breakthrough. Furthermore, the effect of the contact angle on the liquid dynamics in the most compressed case is investigated and reducing it is shown to have a detrimental effect on liquid water removal.

No previous study on the effects of GDL compression have been conducted using this technique. The advantage of the technique over other modelling approaches is the resolution of the discrete phases when compared to a mixture model and the solving of the full Navier-Stokes equations when compared to a pore network model, lattice Boltzmann or morphological technique.

3.2 Methodology

3.2.1 Modelling Domain

The modelling domain is a 2-D cross section of cylindrical fibres that are non-overlapping and equally spaced in a lattice configuration. This represents a small

section of the GDL and channel configuration, and is idealised to enable a sufficiently detailed parametric study of the effects of changing the fibre spacing in both the in-plane and through plane directions by means of compression. The model is most similar to a carbon paper type GDL. The modelling process involves the construction of five geometrical configurations representing different degrees of compression, details of which are found in Table 3.1. A channel section is later added to three of the modelling domains (cases A, C & E) which are used for the multiphase simulation. Figure 3.2 shows the unit cell with characteristic lengths.

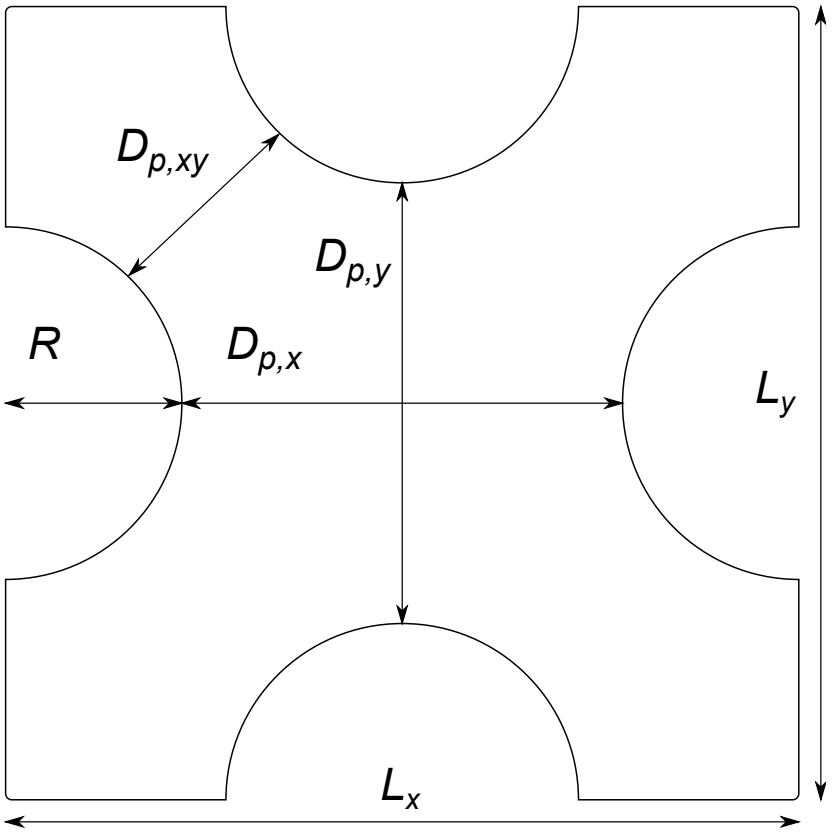

Figure 3.2: Unit cell with characteristic lengths for the modelling domain.

The change in important parameters are also summarised in Table 3.1, where ϵ is the porosity which can easily be calculated from the geometry and τ is the tortuosity which is commonly related to the porosity through Archie's Law: $\tau = \epsilon^{-n}$ where n is typically taken to be 0.5 when applying Bruggemann's correction

Case	CR	$D_{p,y}$ [µm]	$D_{p,xy}$ [µm]	ϵ	τ
A	0.00%	10.00	4.73	0.69	1.20
B	11.11%	8.00	4.04	0.65	1.24
C	22.22%	6.00	3.40	0.60	1.29
D	33.33%	4.00	2.82	0.53	1.37
E	44.44%	2.00	2.30	0.44	1.51

Table 3.1: Characteristic lengths and properties of the compressed geometry, $\tau = \epsilon^{-0.5}$.

to various transport properties [52].

Following the common assumptions that fibres are incompressible and that deformation only occurs in the direction of compression [141], the fibre radius (R) and pore diameter in the x-direction ($D_{p,x}$) are fixed at 4 and 10 µm respectively, for all cases. The compression ratio (CR) is defined as follows [219]:

$$CR = \frac{L_y^* - L_y}{L_y^*} = \frac{D_{p,y}^* - D_{p,y}}{D_{p,y}^* + 2R} \tag{3.2.1}$$

where * denotes the uncompressed value.

The modelling domains, which are 10 pores by 5, were created using ANSYS® ICEM CFD™ by constructing an ordered mesh surrounding a single fibre with an octagonal boundary which forms the interior connections. The single fibre mesh is translated diagonally, copied, and nodes are merged to form the modelling domain. Additional square sections between adjacent fibres in each row are also required but can easily be tessellated and merged in the same manner, providing the node spacing matches the vertical and horizontal node spacing of the octagonal mesh. A section of the final result is shown in Figure 3.3. Typical commercial GDLs can range in thickness between 110 and 420 µm as surveyed by El-kharouf and Mason [45], and the current collector's gas flow channels are usually between 1 and 2 mm in height. In the present study, the thickest uncompressed GDL section is approximately 90 µm thick which is close to the actual thickness of some GDLs, and allows for a good degree of variability in the liquid flow paths whilst minimising the computational expense of the simulation. We are not primarily concerned with channel droplet dynamics or the behaviour of

the liquid water after it has permeated through the GDL and merely include the channel as representative of an open space so only part of it is resolved.

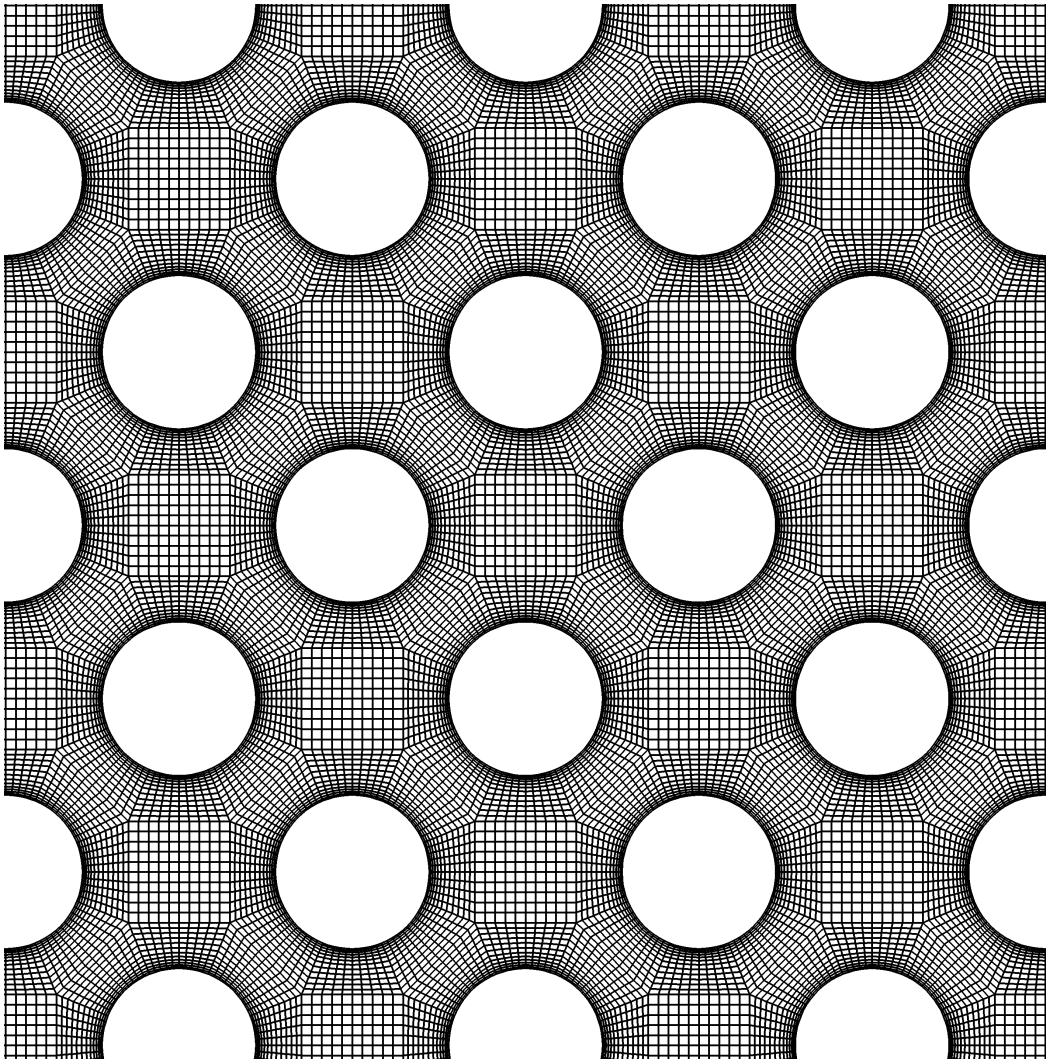

Figure 3.3: Tessellated Structured Mesh.

3.2.2 Governing Equations

Single-phase study

For the single-phase study, the top and bottom edges form the inlets and outlets to calculate through-plane permeability, and the sides are treated as no slip walls.

Free slip boundary conditions for the domain edges were not found to alter the results. For in-plane permeability, the boundary conditions are switched and the sides become the inlets and outlets. The circular boundaries around each fibre are treated as no slip walls in all cases. The simulation is isothermal and the full Navier-Stokes equations of motion are solved with zero gravity and other body forces owing to the dominance of viscous forces at these length scales. The fluid is modelled as incompressible air (but any Newtonian fluid could have been chosen) which is a valid assumption for low mass flow rates.

The continuity equation is given by:

$$\frac{\partial \rho}{\partial t} + \nabla.(\rho \vec{v}) = 0 \tag{3.2.2}$$

where ρ is the fluid density and $\vec{v}$ is the velocity. The momentum equation is given by:

$$\frac{\partial}{\partial t}(\rho \vec{v}) + \nabla.(\rho \vec{v}\vec{v}) = -\nabla p + \nabla.\mathbf{T} \tag{3.2.3}$$

where p is the pressure and $\mathbf{T}$ is the stress tensor given by:

$$\mathbf{T} = [\mu(\nabla \vec{v} + \nabla \vec{v}^{T}) - \frac{2}{3}\nabla.\vec{v}(\mathbf{I})] \tag{3.2.4}$$

where μ is the dynamic viscosity and $\mathbf{I}$ is the unit tensor.

Ismail et al. [230] have shown that, when calculating permeability, the Forchheimer or non-Darcy terms cannot be ignored for higher flow rates when inertial losses account for a significant proportion of the pressure drop across the medium. Ward [231] has shown that a smooth transition occurs between the linear Darcy regime and the non-linear Forchheimer regime when increasing the Reynolds number, defined as $Re = \rho \vec{v} K^{1/2}/\mu$ where K is the permeability, above 1. The simulations are all conducted for $Re < 1$ and so Darcy's law holds:

$$Q = K\frac{A}{\mu}\frac{\Delta p}{L} \tag{3.2.5}$$

where Q is the volumetric flow rate, A is the cross-sectional area of the medium open to flow and L is the length of the medium.

Multiphase study

For the multiphase study, the domain is initially filled with air, and three of the inter-fibre sections at the lower boundary are selected for water inlets with the rest being set to no slip walls. The inlet velocity is set to 0.01 ms^{-1} corresponding to a capillary number, $Ca = \mu_l v_l/\sigma$ where σ is the coefficient of surface tension, of the order 1E-04. This value is higher than those usually encountered in actual fuel cell operation, but is closest to the capillary fingering flow regime reported in the literature [58], whilst remaining computationally efficient and is also consistent with other studies [121],[232],[233]. A channel region above the GDL is included in the flow domain, with a pressure outlet at the top of the domain set to zero gauge pressure.

The VOF model is employed to simulate the multiphase behaviour, with the primary phase being air and the secondary phase being liquid water, thus simulating the environment within the GDL of the cathode side of a PEFC. The VOF model is a surface tracking technique where two immiscible fluids share a single set of momentum equations and the volume fraction of each fluid is tracked throughout each cell of the computational domain. The continuity equation for each phase becomes:

$$\frac{\partial}{\partial t}(\alpha_i \rho_i) + \nabla.(\alpha_i \rho_i \vec{v_i}) = 0 \tag{3.2.6}$$

and the momentum equation becomes dependent on each phase through the phase averaged density and viscosity terms:

$$\rho = \sum \alpha_i \rho_i \tag{3.2.7}$$

$$\mu = \sum \alpha_i \mu_i \tag{3.2.8}$$

where α_i is the volume fraction of the i^{th} phase. As for the single-phase simulations, the effects of gravity are ignored in the multiphase simulations. This is justified by considering the Eötvös number of the system, a dimensionless measure of the relative importance of gravity and surface tension:

$$E\ddot{o} = \frac{\Delta \rho g d^2}{\sigma} \tag{3.2.9}$$

which for droplets of diameter 30 µm (the largest possible in the simulation) is of the order 1E-04, therefore the surface tension is the dominant force.

3.2.3 Capillary Pressure Model

For simple straight capillary tubes, the capillary pressure, P_C, is determined by the curvature of the interface. The curvature is essentially governed by the contact angle, θ, between the phases at the solid boundaries constricting the flow, and can be expressed by the Washburn relation, as discussed in Section 6.2.1. The contact angle is a measure of how much a fluid wets ($\theta < 90°$) or doesn't wet ($\theta > 90°$) a particular surface and determines the direction of capillary flow, as the fluid filling the concave side of an interface will be at higher pressure. In the present study the contact angle is set to 130°, thus signifying a uniformly hydrophobic medium. This value has been shown by Fairweather et al. [234] to hold for a range of PTFE loadings. In reality, the PTFE coverage is not even, and fuel cell diffusion media do not possess uniform wettability. However, for the purposes of this study, which is more focused on the geometrical structure of the medium, it is best to eliminate the influence of other variables on the results, so each fibre has the same boundary conditions applied.

More generally the capillary pressure is defined as the difference between the phase pressures and is determined by the Young-Laplace equation [17] which makes use of the curvature of the interface (κ):

$$P_C = \sigma\kappa = \sigma\nabla.\hat{n} = P_l - P_g \tag{3.2.10}$$

where

$$\hat{n} = \frac{n}{|n|} \tag{3.2.11}$$

and

$$n = \nabla\alpha_q \tag{3.2.12}$$

where $P_C > 0$ is conventionally understood to mean that liquid is the non-wetting phase as is the case in a hydrophobic medium. Gostick [17] remarks that the Washburn relation's simple dependence on the contact angle erroneously predicts a switch in wettability for contact angle transitions across the value of

90°, when in fact a porous medium remains neutrally wettable across a wide range of contact angles from 75° to 105°. This suggests that wettability alone cannot determine the transport, but dependence on the structure, such as pore throat shapes and sizes, also plays an important role.

Surface tension is accounted for in this study by using the continuum surface force (CSF) model proposed by Brackbill et al. [235] based on the Young-Laplace equation. It is expressed as a volume force F_{vol} as part of the momentum equation where:

$$F_{vol} = \sigma_{pq} \frac{\rho \kappa \nabla \alpha_p}{1/2(\rho_p + \rho_q)} \tag{3.2.13}$$

In the present study, the surface tension coefficient between phases p and q (σ_{pq}) is taken to be 0.072 N/m which corresponds to room temperature.

3.2.4 Numerical Implementation

Roache's method for computing the grid convergence index (GCI) based on Richardson extrapolation [236], [237] is evaluated for the single-phase study by comparing the inlet pressure for constant mass flow rate with varying resolution of grid cell sizes. The results are presented in Table 3.2 for cases A and E. As the CGI is very low for all the cases investigated the largest cell sizes are selected to speed up the computations.

Further mesh convergence is established by observing the multiphase flow on a smaller section of the domain. A structured mesh is favoured to an unstructured approach, due to the recommendations that surface tension models are very sensitive to mesh uniformity and quadrilaterals and hexahedra should be used in regions where surface tension is important [238]. The resolution of the mesh can be controlled more easily with a structured approach with special attention paid to the node spacing normal to the fibre walls thus ensuring a smooth transition from smaller to larger cells. Two tessellation techniques were applied with one forming acute angles in the cells of adjoining units. These acute angles were observed to influence the direction of liquid permeation so the technique was abandoned in favour of the octagonal approach with adjoining square sections. The optimum number of cells was found to be about 200,000 for the uncompressed case and

	Case A	Case E
Number of Cells in Domain (N_1, N_2, N_3)	466400, 254150, 116600	525240, 300960, 168810
Average Cell Height Ratio (r_{21}, r_{32})	1.35, 1.48	1.34, 1.50
Average pressure at the Inlet (P_1, P_2, P_3)	49.58, 49.24, 47.90	237.71, 237.92, 232.32
Apparent Order (p)	3.17	11.37
Approximate Relative Error (e_{21}, e_{32})	0.68%, 2.72%	0.08%, 2.35%
Grid Convergence Index (GCI_{21}, GCI_{32})	0.5%, 1.4%	0.0%, 0.1%

Table 3.2: Parameters for the Grid Convergence Study

about 350,000 for the most compressed case. The governing equations are solved numerically in ANSYS FLUENT using a pressure-based solver and the explicit scheme-based VOF method is selected for the interface tracking. The SIMPLE scheme is used to obtain the pressure-velocity coupling and the PRESTO! scheme is used to interpolate the pressure field. The second-order upwind scheme is used to solve the momentum equation and the Geo-Reconstruct scheme to construct the interface between the two phases for the multiphase simulations. The transient formulation is first-order implicit and the time step is 1E-08 s with a maximum of 30 iterations per time step. This allows for residual convergence to less than 1E-05 for each time step, and keeps the Courant number below 1.

3.3 Results and Discussions

3.3.1 Single-Phase Study

The motivation for the single-phase study is partly to validate the modelling approach against published experimental results and theories of permeability, and partly to observe the effects on the flow to enable comparisons with the multiphase modelling. The geometry is idealised in this approach and has a limited range of pore and throat sizes but can be thought of as representing the average properties

of the medium. The 2D restriction is necessary for computational efficiency but imposes a level of order which is not commonly found in real GDL materials. Therefore, it is important to establish whether valid conclusions can be drawn from such a modelling approach. Comparisons made with established theory is the best way of doing this.

The most frequently used permeability relation in studies of porous medium is the Kozeny-Carman (K-C) equation, which is based on the idea of a porous medium being comprised of many tortuous capillary tubes [181]:

$$K = \frac{\epsilon}{k_c}\left(\frac{V_p}{A_p}\right)^2 = \frac{\epsilon \bar{r}^2}{4k_c} = \frac{\epsilon \bar{r}^2}{8\tau_v} \tag{3.3.1}$$

where V_p and A_p are the total volume and surface area of the pore space, k_c is the Kozeny constant and $\bar{r} = \bar{D}/2$ is the mean intercept half-length of the pore structure, a measure of the average pore radius. The tortuosity for viscous flow, τ_v, is not defined straight-forwardly for complicated geometry and is usually combined with the Kozeny constant as a fitting parameter for the medium and therefore:

$$K = C\frac{\epsilon \bar{D}^2}{32\tau_v} \tag{3.3.2}$$

Tomadakis and Sotirchos [239] showed that for random non-overlapping fibres $\bar{D}/R = 2\epsilon/(1-\epsilon)$ and therefore Equation (3.3.1) can be written:

$$K = \frac{\epsilon^3 R^2}{8\tau_v(1-\epsilon)^2} = \frac{\epsilon^3 R^2}{4k_c(1-\epsilon)^2} \tag{3.3.3}$$

where R is the fibre radius, however this equation does not account for orthotropic fibre spacing unless different constants are used for different directions so Equation (3.3.2) will be used.

Inspection of the velocity profile through the two extreme modelling domains in Figure 3.4 reveals that, as the geometry is compressed, the flow path becomes less tortuous and regions develop where flow is stagnant and unaffected by the bulk flow. A flow pattern emerges which is similar to a capillary tube, so fits well with the K-C model.

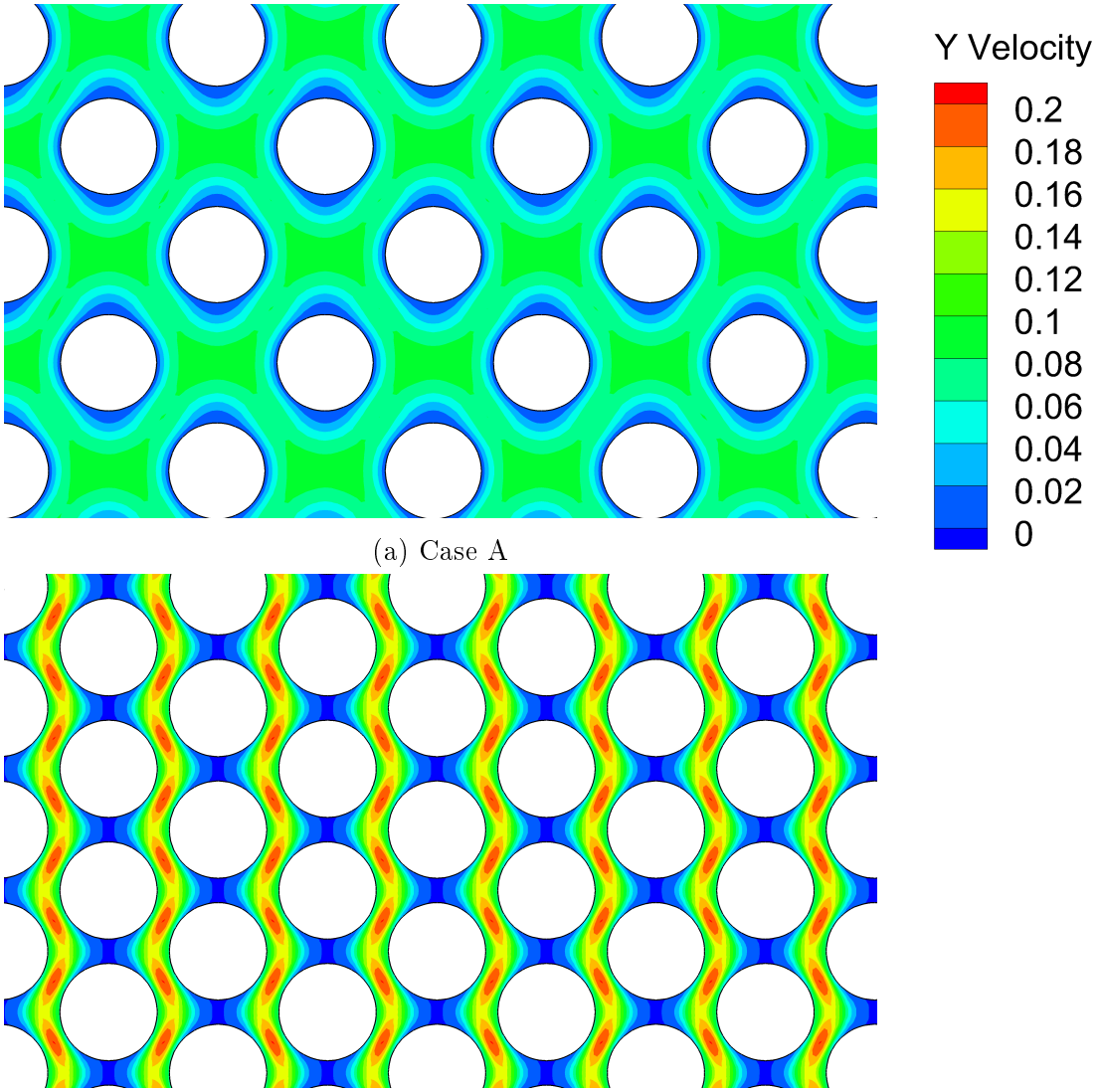

(a) Case A

(b) Case E

Figure 3.4: Comparison of the through-plane velocity profiles: Uncompressed case has uniform flow whereas most compressed case shows areas of low velocity and capillary tube like flow.

By analysing the pressure drop and tangential velocity along a stream line that passes through the mid-point of each throat, an effective capillary tube diameter can be derived using the following equation based on flow through a slowly varying channel [240]:

$$v = \frac{h^2}{2\mu}\frac{dp}{dx}\left(\frac{y^2}{h^2} - 1\right) \tag{3.3.4}$$

where h is the half channel height, similar to $\bar{r}$, in Equation (3.3.1), and y is the distance from the mid-point of the channel. Therefore, along the stream-line coinciding with $y = 0$, the effective capillary tube diameter that the fluid appears to pass through can be calculated as:

$$D_{eff} = 2\sqrt{\frac{2\mu v}{|dp/dx|}} \tag{3.3.5}$$

The flow parameters and effective capillary tube diameter along a streamline passing through the centre of each throat for the uncompressed case and the most compressed case are shown in Figure 3.5.

The pressure gradients in all cases oscillate between a regular minima and maxima when passing through pores and throats respectively. The minima and maxima lie within an order or magnitude of one-another, so to constrict the permeability calculation purely to a minimum length scale would be inaccurate. Excluding edge effects, the average effective capillary tube diameter is calculated for all cases in both in-plane (x) and through-plane (y) directions and plotted as a function of compression ratio in Figure 3.6.

Figure 3.7 shows the numerically calculated permeability according to Darcy's Law, plotted against compression ratio along with a simplified K-C type permeability utilising the average effective capillary tube diameter and Equation (3.3.1). Here a constant value of C = 2.31 is used, and the Bruggemann approximation ($\tau = \epsilon^{-0.5}$) is used for the tortuosity, for lack of a better approximation that holds over the compression range. It can be seen that the through-plane permeability becomes greater than the in-plane permeability under high compression. Equation (3.3.2), can be tuned with $k_c = 9.5$ to match the through-plane data quite

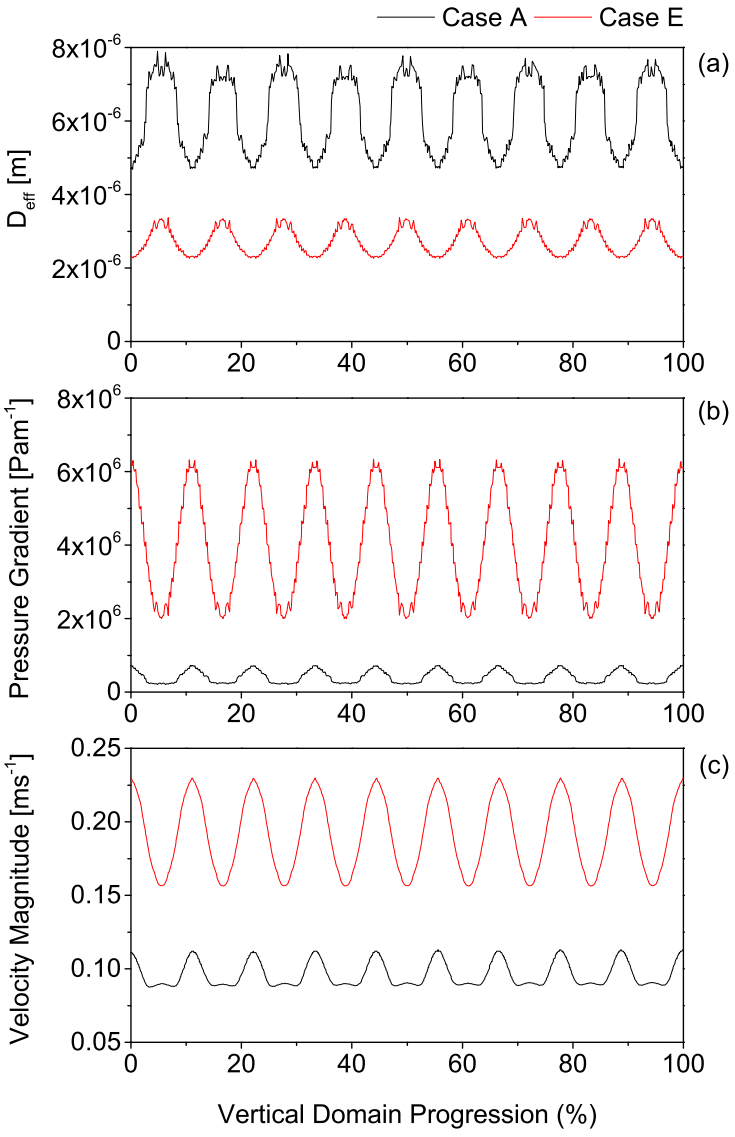

Figure 3.5: Comparison of key flow data for the uncompressed case (A) and most compressed case (E): (a) effective capillary tube diameter, (b) tangential pressure gradient along stream-line (c) tangential velocity along streamline.

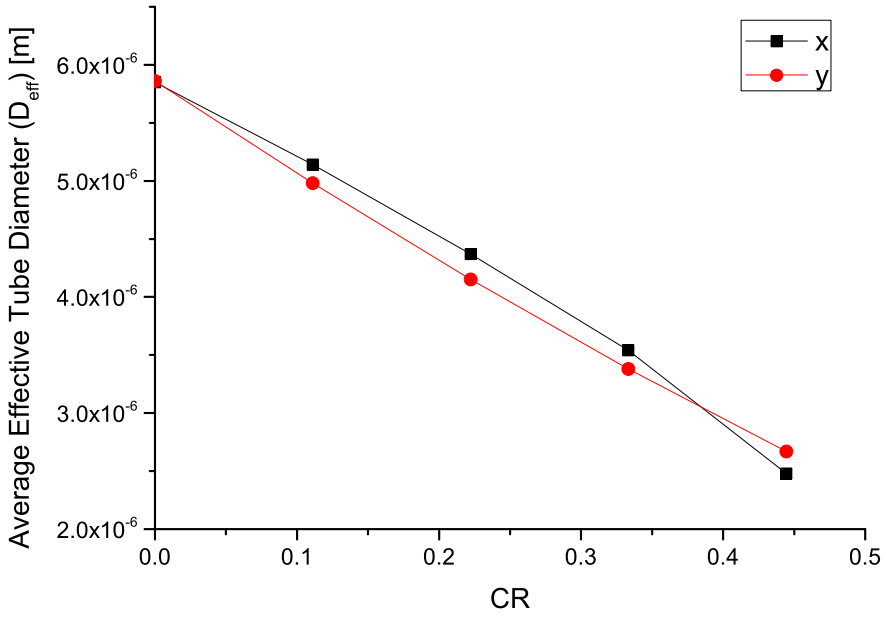

Figure 3.6: Average effective capillary tube diameter ($\bar{D}_{eff}$) for single-phase flow in the in-plane (x) and through-plane (y) directions.

well. A k_c value of 8.10 was found by Gostick et al. [141] to correspond well to the permeability of SGL-10BA with flow perpendicular to the fibre direction. Therefore, it can be concluded that the results are representative of carbon paper GDLs.

3.3.2 Multiphase Study - Low Compression

The results from the multiphase simulations for the uncompressed and middle cases are presented in Figures 3.8 and 3.9 respectively. The general pattern of evolution of the liquid phase through the GDL is similar for the uncompressed and mid-level compression cases, and again they are both similar to the work of Suresh and Jayanti's case without the presence of air flow [121]. Liquid flows from each inlet and, upon meeting a fibre wall, deforms and flows in one or both of two directions around it. As each row of fibres has its centres placed directly

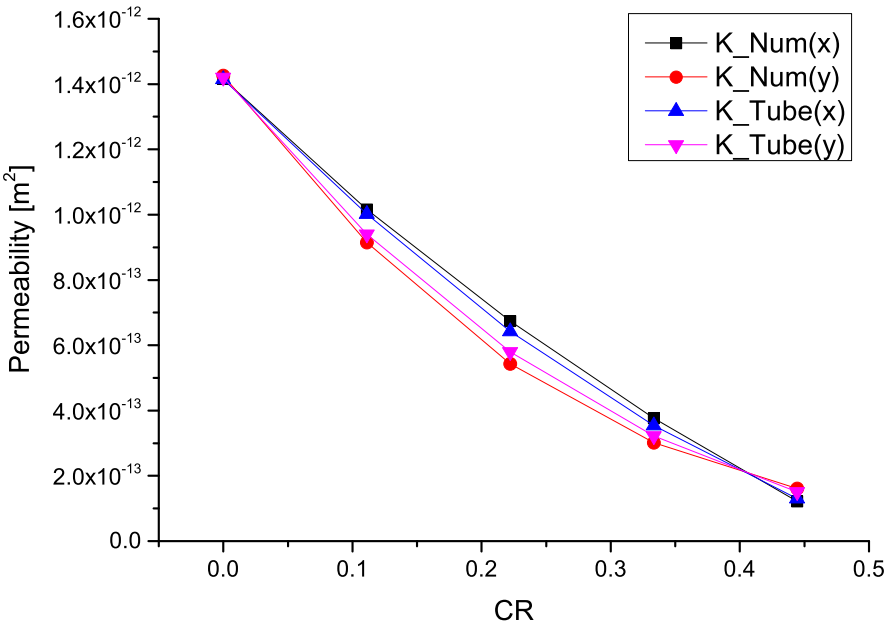

Figure 3.7: Absolute permeability as a function of compression ratio with simple Kozeny-Carman relationship.

between the fibres in the rows above and below, and there are no other deforming forces present. The direction of flow is largely random and subject to bifurcation. Due to the method of mesh creation, the conditions at each of the inlets should be identical, yet the individual pathways are not, because of the non-linearity in the governing equations.

Before the liquid front has reached the mid-point through the fibrous domain, the paths have converged and the pressure field is shared throughout the bulk of the liquid. As more liquid is added through the inlets, capillary pressure increases, and the interfaces penetrate the constricting throats between fibres further.

The flow pattern is that of a build up and quick release of pressure in the bulk fluid as surface tension restricts the flow simultaneously across the interfaces. Once a constriction is transitioned the bulk fluid is allowed to flow through the pore throat and it expands quite quickly to fill the pore space. Simultaneously, the other interfaces connected by the bulk recede owing to the drop in liquid phase

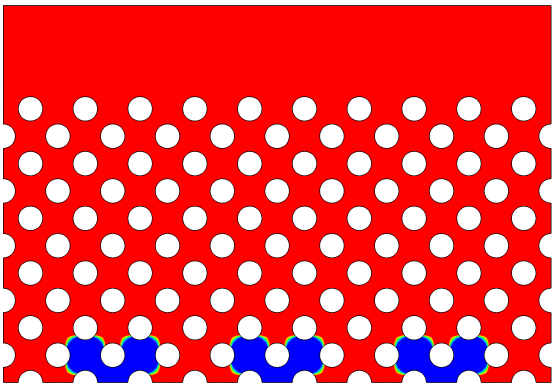

(a) 3 ms

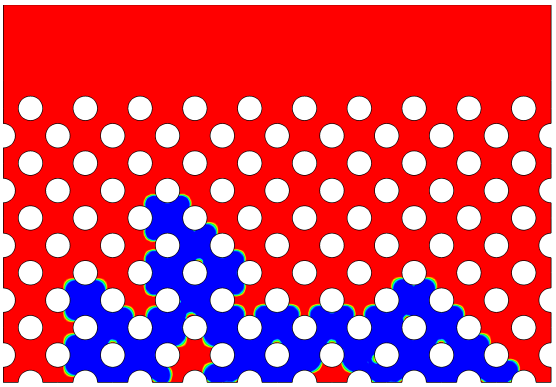

(b) 10 ms

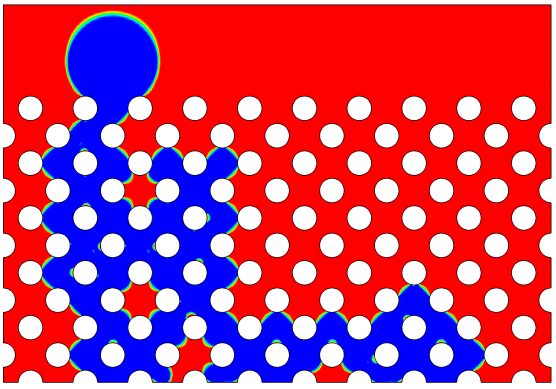

(c) 16 ms

Figure 3.8: Uncompressed geometry showing liquid permeation as a function of time from 3 inlets through the fibrous GDL and emerging as a droplet in the channel.

pressure. This effect is most obvious when the liquid reaches the GDL surface and expands rapidly to form a droplet, but does occur throughout the entire

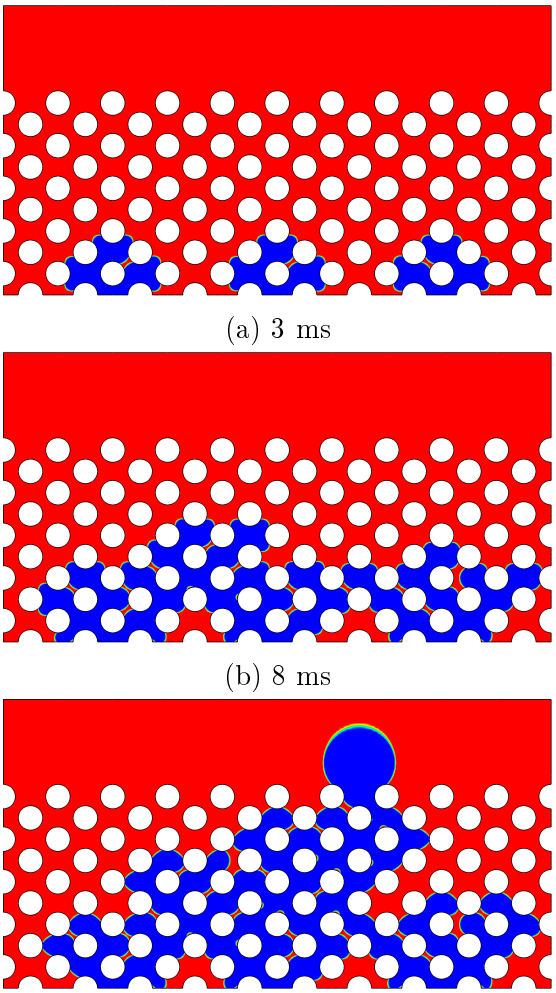

(a) 3 ms

(b) 8 ms

(c) 13 ms

Figure 3.9: Mid-level compression (CR = 22.22%) case showing liquid permeation as a function of time from 3 inlets through the fibrous GDL and emerging as a droplet in the channel.

process as shown in Figure 3.10. As the inlet velocity is maintained constant a periodic oscillation in the pressure at the inlets can be observed corresponding to mini-breakthroughs of the liquid front through the restricting pore throats.

Once a droplet is formed at the GDL surface a preferential pathway is established through the connected bulk fluid. The force required to expand the surface of the droplet is less than that required to penetrate through a constricting throat, so all other interfaces remain static until the droplet is removed.

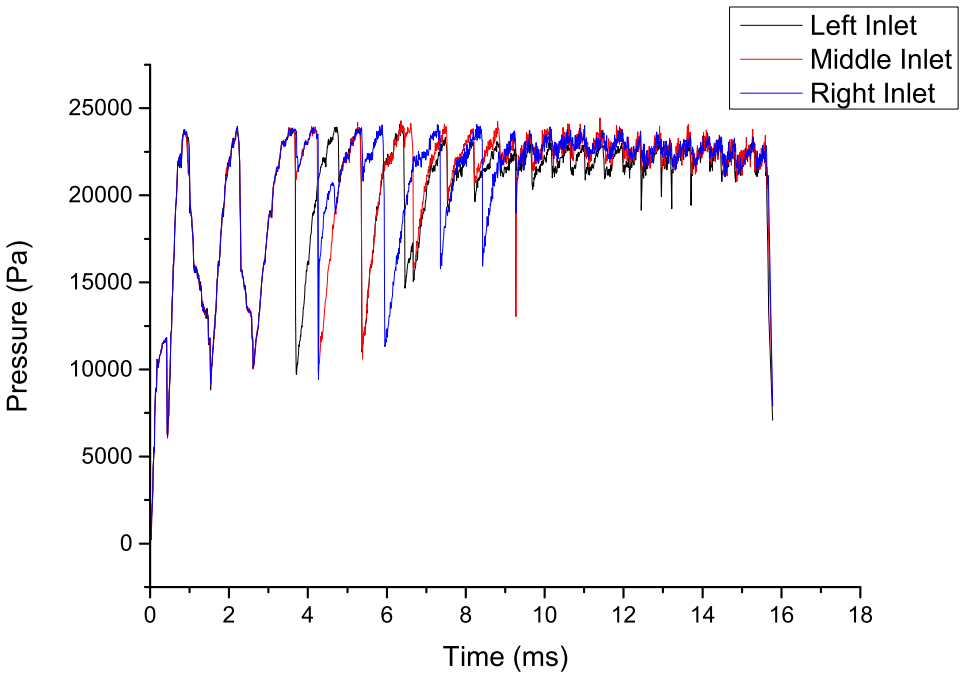

Figure 3.10: Time series of the pressure at each liquid inlet for case A.

Several researchers have investigated the dynamic percolation behaviour of liquid through GDLs with and without MPLs [175], [85], [241]. The results are qualitatively consistent with the pattern found here, although the time-scales and absolute pressure values are quite different. The initial pattern from 0 - 6 ms is that of three individual water clusters percolating through separate pathways. The highest pressure occurs when the leading meniscus approaches the smallest constrictions, and the lowest pressure occurs when a single meniscus occupies a single pore. Between 6 and 10 ms the left and middle clusters have merged, and the pressure for these inlets mirrors one another whilst the right is still independent and reaches lower pressure values throughout it's cycle. The difference in the magnitude of the pressure cycles is proportional to the number of connected menisci within each cluster, or in other words the number of throats the cluster has access to. As a pore is invaded, the meniscus making the transition advances and expands whilst others recede. The mass transfer that occurs when a pore is invaded is compensated by the recession which is shared evenly amongst the other menisci. Therefore, a greater number of menisci connected to the cluster results in a smaller recession, so the total pressure field shared amongst them reduces less, because the average curvature of the menisci is reduced by a smaller amount. Between 10 and 16 ms all the clusters have merged, and the pressure variation becomes smaller and repeats in a saw-tooth fashion as pores are invaded one at a time. Finally the cluster reaches the top surface and pressure can reduce dramatically as a large droplet is formed.

3.3.3 Multiphase Study - High Compression

The most compressed case, shown in Figure 3.11, differs greatly from the other multiphase cases investigated with the differences solely due to the change in minimum fibre spacing. All other flow parameters and wall contact angles remain the same. High compression of the medium creates anisotropy in the minimum fibre spacing normal to flow and this influences the evolution of the liquid path significantly. No lateral spreading is observed in the high compression case, and permeation occurs in a fraction of the time, indicating much higher relative permeability. As paths do not converge, multiple droplets form at the GDL surface.

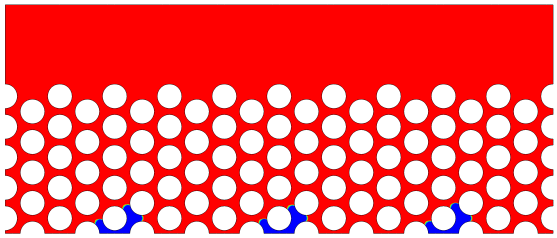

(a) 0.5 ms

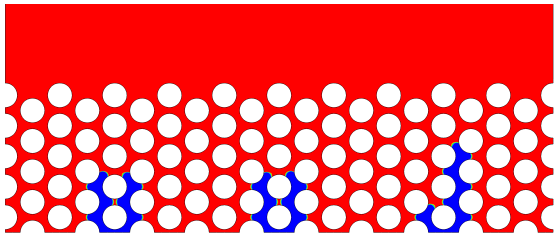

(b) 1.5 ms

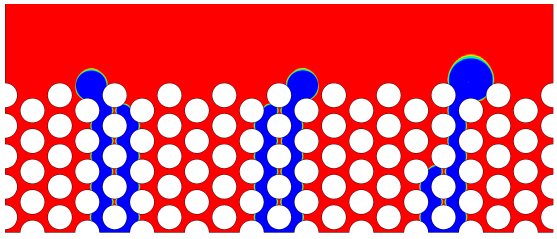

(c) 3.9 ms

Figure 3.11: Most compressed case (CR = 44.44%) showing liquid permeation as a function of time from 3 inlets through the fibrous GDL and emerging as 3 separate droplets in the channel with no lateral spreading of the paths.

For the lesser compressed cases, the minimum fibre spacing is the diagonal between successive displaced rows of fibres termed $D_{p,xy}$ in Figure 3.2, but for the most compressed case it is the vertical space between columns of fibres termed $D_{p,y}$. As flow in both the x and y directions must pass through $D_{p,xy}$, both are subject to the same resistive forces, and the flow is approximately uniform in both directions for the first two cases. However, because $D_{p,y}$ only restricts the flow in the direction normal to it, flow parallel to $D_{p,y}$ progresses and the liquid follows the path of least resistance. Due to the regularity of the geometry, the effect is perhaps accentuated as the liquid front is always presented with a wider throat to flow through in the same direction. The characteristic of the medium, which should reflect the anisotropy in the fibre spacing normal to flow, is the

permeability. A GDL which has higher through-plane permeability than in-plane permeability should give a preferentially directed liquid flow (and correspondingly a higher relative permeability) in the through-plane direction. Typically GDLs have higher in-plane permeability but compressed sections may experience a switch due to a smaller reduction in the average fibre spacing normal to the direction of compression (which is always through-plane).

Ramos-Alvarado et al. have experimentally determined the effect of compression on the absolute and relative permeability of Toray 090 carbon paper [147]. It was observed that whilst absolute permeability decreased with compression, relative permeability increased, which can now be explained by the relative change in fibre spacing.

3.3.4 Influence of contact angle

When the contact angle is 90°, Equation (2.2.23) shows that the capillary pressure is zero at the mid-point of the throat where the filling angle $\beta = 0$. This is also the point at which maximum curvature occurs (β^{max}). After the invading fluid passes through the mid-point, the sign of the capillary pressure becomes negative, indicating a switch in preferential wettability for the phases. For greater contact angles Equation (2.2.24) shows that the maximum curvature occurs after the point of maximum constriction with increasing β. This phenomenon explains why we observe interfaces that have penetrated past the mid-point but are unable to progress any further when the surface contact angle is greater than 90°. Once capillary pressure is great enough to push the interface past the point of maximum curvature the fluid flows uninhibited as surface tension decreases with expanding pore diameter.

Radhakrishnan and Haridoss have shown that compression can decrease the contact angle, or rather increase the wettability of GDLs, and with cyclic compression these changes may become permanent [242]. The most likely cause for this change in wettability is the damage and breakup of the PTFE coating. Equation (2.2.23) shows that for neutrally wettable media the capillary pressure is zero when the filling angle α is zero regardless of the width of the pore. Therefore, one would expect the effects of fibre spacing on multiphase flow to become less

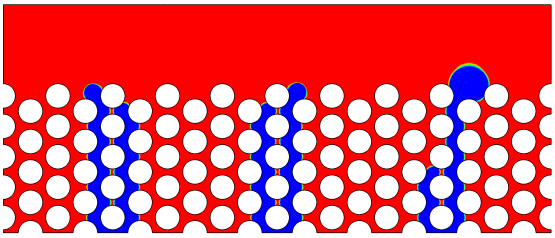

(a) Contact angle = 130°

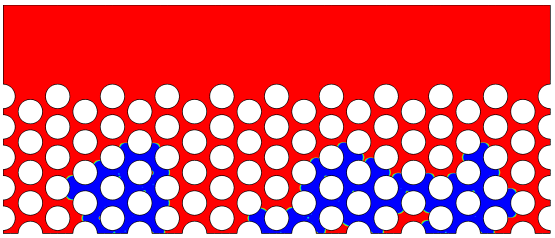

(b) Contact angle = 110°

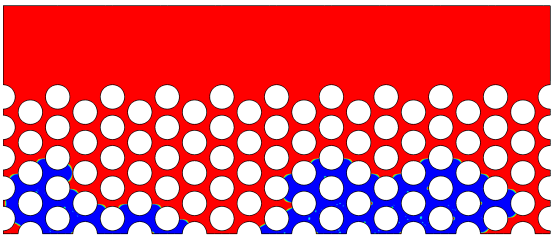

(c) Contact angle = 90°

Figure 3.12: Three snapshots at 3.5 ms for the most compressed case (E) with different contact angles.

CR	θ	*Saturation*
0.00%	130	0.34
22.22%	130	0.51
44.44%	130	0.25

Table 3.3: Saturation levels in the GDL for the multiphase simulations at breakthrough.

pronounced for neutrally wettable media. Two further simulations for the most compressed case with contact angle $\theta = 90°$ and $110°$ are presented in Figure 3.12, and do indeed show lesser directional flow and greater saturation with lesser contact angle. It is therefore important to increase the through-plane permeability and retain the hydrophobic nature of the GDL in order to direct flow. In other words, smaller hydrophobic throats are more effective at stopping liquid flow than neutrally wettable ones.

3.3.5 Saturation

The saturation is an important parameter when considering multiphase transport and is linked to capillary pressure and relative permeability by empirical relationships throughout fuel cell literature. The capillary pressure in these cases is that required for the liquid to penetrate the narrowest throat or constriction and overcome the greatest surface tension force. Saturation levels at breakthrough (i.e. when droplets begin to form at the surface of the GDL) for each case are presented in Table 3.3. At low compression, where the minimum fibre spacing is isotropic, the saturation is high and the variation between results is reflective of the non-linear nature of the governing equations. For high compression, where the minimum fibre spacing is anisotropic, the liquid is directed effectively in one direction towards the channel, and the saturation is much lower. When the contact angle is decreased, this lessens the effect of anisotropic surface tension forces and the lateral spreading increases. This leads to a greater saturation but breakthrough is not achieved in the same time-scale for the lesser contact angles, so they are not shown in Table 3.3.

The results agree with the observations of Bazylak et al. [177] who observe preferential liquid pathways under compressed sections of a GDL and also explain the results of Gao et al. [205] who observe a reduced saturation under compressed sections of a GDL before and after liquid breakthrough. The method of observation and experimental set-up is different in both of these experiments, with the key difference being the location of liquid water injection. Bazylak et al. allow water to absorb across the whole section of GDL (both compressed and uncompressed), whereas Gao et al. inject water only into the channel section. As there will be a negative porosity gradient from the uncompressed GDL adjacent to the channel to the compressed GDL in contact with the rib one would expect there to be limited lateral spreading and thus lower saturation under the rib. Bazylak et al. have also shown that GDLs can be fabricated to give biased directional transport to liquid water by altering the average throat spacing [143], which is the same mechanism observed in the present study.

Porosity gradients may in-fact play an important role in determining the liquid water distribution and overall saturation, as shown by Zhan et al. [243] and more recently Wang and Chen [217] and García-Salaberri et al. [244]. As porosity is directly linked to the local fibre spacing, the results presented in this study would also indicate that porosity grading plays an important role in directing liquid transport. However, it may be better to base relationships on fibre spacing directly, as porosity is a volume averaged parameter and may smooth out the local anisotropy introduced by compression.

Chi et al. have studied the effect of compression on the fuel cell performance using a continuum model of a single PEFC with a serpentine flow channel [218]. They find that saturation increases downstream when compression effects on the absolute permeability are accounted for. However, the effect of compression on the relative permeability or the capillary pressure is not mentioned. Further detailed investigation of how compression alters these key relationships is required for modelling purposes to understand the whole effect of compression on PEFC performance and flooding.

3.4 Concluding Remarks

The effect of compression on a representative PEFC gas diffusion layer has been modelled using computational fluid dynamics. Five geometries were meshed utilising a structured tessellation technique and a single-phase study revealed that a switch in permeability occurs at high compression, where the through-plane permeability becomes greater than the in-plane permeability. A simplified Kozeny-Carman relation using an effective capillary tube diameter is found to agree very well with the numerical data and reproduces the permeability switch at the correct level of compression.

Multiphase simulations using three of the geometries reveal that liquid transport is directed by compression, resulting in a lower saturation at breakthrough. The cases with mild or no compression display high levels of lateral spreading owing to the bifurcations in liquid flow path and uniform surface tension in both directions whereas the case with high compression exhibits preferential liquid pathways and fast water ejection. When the contact angle is reduced to represent a neutrally wettable media, the effect is also reduced signifying both the importance of structure and surface energy in determining the liquid flow.

These findings help to explain some of the previous experimental observations in Table 2.3 but further work is required to establish relations for the relative permeability as a function of compression ratio and saturation due to the expensive nature of the computations. This work can help to form the basis of future investigations using PNMs or other techniques, and highlights the need for further understanding on the topic of transport under compression. Moreover, a critical assumption highlighted by this study is how the fibre spacing changes in each direction under compression. The absolute in-plane and through-plane permeability of the medium could be used to determine whether tensorial relative permeability exists. From the findings it can also be concluded that increasing the through-plane permeability by other methods would have a beneficial impact on the liquid water transfer.

Chapter 4

Pore Network Modelling of the Compressed GDLs: Relative Transport Relations

4.1 Motivation

Many attempts to understand the multiphase processes occurring within the PEFC have been made over the years yet gaps in the knowledge still remain, owing largely to the unusual or atypical properties of the porous electrode components. With the exception of the current collectors the fuel cell components are all porous and vary in porosity, thickness, permeability, wettability and anisotropy, as shown in Table 2.1. One particular knowledge gap is how the multiphase transport processes throughout the porous media are affected by the morphological changes occurring with compression when assembling the fuel cell. An attempt to address this knowledge gap was made in the previous chapter, however, the modelling technique was limited to an idealized structure and was computationally expensive, so an extensive parametric study to determine constitutive relations was not possible.

Pore Network Models (PNMs) are useful tools for analyzing the properties and transport characteristics of porous fuel cell components, especially for multiphase modelling, as simple percolation algorithms can be performed when transport is capillary dominated. The general concept, as explained in Section 2.4.3, is to

map the pore space onto a discrete network of pores and connecting throats, then to conduct simulations using transport algorithms based upon a nodal balance of the transported fluids. In addition to speed and simplicity, PNMs have some advantages over the more widely used continuum models [131] as they can resolve realistic saturation profiles [129].

Greater attention is paid to the structure and topology of the porous material in contrast to volume averaging for continuum models. Topologically equivalent pore networks (TEPNs) can be generated using stochastic methods [133] or extracted from tomography images [134]. Another method for constructing realistic fibrous structures is to use Voronoi Diagrams [136], [137], [69] which are very useful for pore network modelling because the compliment to the Voronoi diagram is the Delaunay tessellation which directly defines the topology of the pore space i.e. connections between pores.

Anisotropy in the heat, mass and electrical transport characteristics of GDLs has been observed [141], [47], [48]. Carbon paper GDLs in particular tend to have an in-plane (IP) alignment of fibres which increases IP transport compared with through-plane (TP). PNMs representing GDLs have been used to investigate the effects of structural parameters such as anisotropy, heterogeneity and coordination on the effective oxygen diffusivity [142] and the effect of compression on the saturation profile [220], [221], however most studies employ cubic network topologies, so structural parameters can only be adjusted by directly altering pore and throat sizes in particular directions or regions.

While cubic networks are useful for parametric studies, they do not necessarily best represent the disordered entangled fibrous structure of common GDLs. The average coordination number of a GDL is higher than that of a regular cubic network and the orientation of throats is not orthogonal. Anisotropy and homogeneity can be easily varied in a random network when using a Voronoi diagram by scaling the coordinates and adjusting pore density. The average coordination and degree of regularity can also be controlled to an extent with the configuration of the initial pore placement. The effect of compression is also more realistic, because changes in the geometry and topology are intrinsically linked; as pores are moved closer together their throats become smaller and may close off, therefore coordination decreases.

Becker et al. have numerically investigated the effect of compression on multiphase transport using a tomography image of a Toray carbon paper GDL [245]. The image was compressed by shifting voxels designated as fibre and the GeoDict software was used to compute transport properties. Multiphase properties were calculated after filling the image with voxels designated as liquid according to a morphological image opening algorithm [246]. The liquid phase was then assumed to be static, therefore essentially treated as an additional solid phase with no-slip boundary conditions applied to the interfaces. The results show that hydraulic and diffusive transport is reduced with compression, with the reduction being more severe for the IP direction. The relative transport properties are not explicitly shown in normalized form, so it is hard to draw conclusions from the transport curves, although the shape of the curves appears to be unchanged with compression. Becker's study also focuses on uniform compression, so saturation distributions under non-uniform compression introduced by channel geometry are lacking.

In this chapter, PNMs are generated and compressed in an effort to study the effects on transport properties of the GDL. The MPL and CL regions are not modelled, as data about their structural changes under compression is lacking in the literature. The modelling approach is summarized, networks are validated with comparisons to experimental data, and light is shed on the effect of compression on single and multiphase flow. Uniform compression is simulated to systematically study the effects on the relative transport properties of the network. Non-uniform compression is simulated to mimic the impact of flow field compression by adjusting the IP porosity profile, and the effect on break-through saturation and limiting current within an operating fuel cell are investigated. The aim is to present the PNM approach with OpenPNM as a viable method for simulating realistic multiphase behavior over a broad range of compressions within a single modelling framework. In this way models can be built upon, incorporating more physical models, and investigating a range of materials and geometry scenarios such as the full membrane electrode assembly model recently published by Aghighi et al. [247].

4.2 OpenPNM: A Pore Network Modelling Package

4.2.1 Introduction

This section provides an overview of the OpenPNM package for pore network simulations to which the author has been a major contributor. The motivation behind OpenPNM was to provide an open source framework which was generic and flexible enough to tackle all the diverse porous media problems that exist across a range of disciplines. It is written in python and the code is freely available (under the MIT license) from PyPI, the python package index using or by downloading the source directly from github, the online code repository used for change management. The developers also maintain a website (www.openpnm.org) which contains information on the project, documentation and many examples for new users to become familiar with the package. Three main principles were kept in mind when developing the code: accessibility, generality and extensibility. The python language was chosen for it's growing popularity in the scientific community, it's ease of use, and open-source packages. Many of the functions in OpenPNM use NumPy [248] and SciPy [249] which combine to provide an extensive scientific computing toolkit comparable to commercial offerings such as Matlab. The full reference guide to OpenPNM has now been published [3] but a brief overview of the key software designs and class objects is provided here for reference.

4.2.2 Data Storage

OpenPNM stores all pore and throat data separately in NumPy ndarrays (multi-dimensional arrays) of length N_p or N_t for pores and throats respectively, giving each individual element an index specific to the network or related object. Each data array is stored in the objects dictionary with a key starting with "pore." or "throat." to denote the type of information stored. There are no restrictions on the data types stored in the arrays (such as floating point or integer) but boolean data is a special case and is treated as a "label" within OpenPNM. There are

routines to easily identify pores and throats by their labels. For example, all the pores on the bottom face of the network will have the label "pore.bottom" and net.pores("bottom") will return a list of their indices which is useful for applying boundary conditions and querying the data.

4.2.3 Implementation

The code is object oriented and the structure of the code follows a hierarchy with the python dictionary as the base class from which all others derive. Core methods are shared between all classes, giving the package an intuitive feel but no restrictions are imposed on customisation, as users can define their own functions to populate the object's data with various models. The core object has data handling and integrity methods and has five major subclasses designed to facilitate storage and manipulation of specific types of data. These are: Network, Geometry, Physics, Phase and Algorithms. Each of the objects has a *GenericObject* (i.e. *GenericNetwork*, *GenericGeometry* etc.) container class with the basic methods specific to each object and to which models are assigned in order to give the object increased functionality and information. More details of each object now follows.

Network

The network object contains topological information, namely the co-ordinates of the pores which are three-dimensional, and the connections between pores i.e. the throats. It is possible to simulate two-dimensional networks simply by defining a network that is one pore thick in a given direction. With generality in mind the connections of the network are stored in a sparse adjacency matrix which is a commonly used concept in graph theory. If the number of pores in the network is N_p then the adjacency matrix is a square array [N_p, N_p] with non-zero values at locations [i, j] indicating that pores i and j are connected. Throats are assumed to be bi-directional so the matrix is symmetric and also very sparse, as a pore will only be connected to a small subset of neighbours. An alternative but equivalent representation of the network connections is an incidence matrix where row numbers refer to pores (or vertices in graph theory)

and column numbers refer to throats (or edges in graph theory). Both formats are useful for querying the network to find connected throats or neighbour throats. Several network topologies are provided in the package, including *Cubic* which has pores distributed in a lattice formation and connected by faces, edges, and/or corners, and *Delaunay* which has pores distributed randomly or according to a probability distribution and connected by a Delaunay triangulation of nearest neighbours.

Geometry

The geometry object contains information on the physical properties and dimensions of the network elements (pores and throats). A distinction was made between topological and geometric information to enable networks to contain multiple geometries for modelling stratified or heterogeneous materials. Each geometry is defined by the models assigned to it, which can be taken from the code base or added by the user. For convenience, as with the network classes, a few custom subclasses of *GenericGeometry* are provided in the package as standard. The *Stick_and_Ball* geometry defines pores as spheres and throats as cylinders, with size distributions set randomly according to a statistical distribution, and is typically used with cubic networks. *Voronoi* is a geometry intrinsically linked to the *Delaunay* network subclass since they are derived from a Voronoi diagram and its dual, the Delaunay triangulation. Spatial correlation of geometric properties is inherent to the Voronoi diagram, but additional models must be applied to spatially correlate other types of geometry with a particular network. The *Voronoi* geometry object and associated models has been the author's main contribution to the OpenPNM project, and was developed in order to carry out the investigations presented in this chapter.

Phase

The phase objects are designed to contain and account for changes in the thermophysical properties of fluids in the network such as temperature, pressure, viscosity, surface tension etc. As algorithms progress, the fluids will typically move through the network, so phases are defined over the whole network, but

have an occupancy property between zero and one to account for the volume fraction of the pore or throat occupied by each phase. The phase objects will typically be passed to the algorithms and manipulated in order to gain information about the network such as the effective permeability. OpenPNM does not store units and every supplied model and algorithm assumes SI units. A small number of predefined *GenericPhase* subclasses are supplied, namely *Air*, *Water* and *Mercury*. Currently the package does not support mixtures, but development of this functionality is in progress.

Physics

The physics objects provide the means to define the transport properties of the network at the pore-scale by interaction of the phases with the geometry. As a pore network model is essentially a series of flow in pipe calculations, analytical models for diffusive and hydraulic flow in pipes are typically specified to calculate the pore-scale conductances. Physics objects therefore lie at the intersection of geometry and phase objects, where a pore-scale model for hydraulic conductance such as Hagen-Poiseuille requires a pore or throat diameter and a fluid viscosity. A *Standard* physics subclass is provided, containing common models for various transport properties such as the capillary entry pressure defined by the Washburn relation. As with the other objects, creating custom-models is encouraged, and is designed to be easy to implement.

Algorithms

The Algorithm objects are the key simulation tools for analysing the pore networks. Examples included are Fickian Diffusion, Stokes Flow, Invasion and Ordinary Percolation. The algorithms are the least standardised aspect of OpenPNM, but they can be broadly categorized as either Linear Transport or Percolation. Running an algorithm is typically a 3-step process: Firstly, the algorithm is instantiated by providing it with the appropriate network and relevant phase objects, as algorithms can be single or multiphase. Secondly, the necessary boundary conditions are applied, such as selecting pores as inlets for liquid invasion, or applying a fixed concentration for a diffusion calculation. Lastly, the algorithm's

run method is called, which if solving an unknown variable such as concentration or pressure, handles the building of a coefficient matrix and then calls the matrix inversion routine (*scipy.sparse.linalg.spsolve* as standard).

4.3 Methodology

The development of random pore networks using Voronoi diagrams and Delaunay tessellations was undertaken as part of the collaborative open source project OpenPNM (www.openpnm.org) [3]. The project is written in Python, which is also open source, and makes use of many of the functions for graph theory, computational geometry, and image analysis found in Python's SciPy module [249].

This section first describes the process of creating and compressing a disordered network, then describes the percolation algorithm and image analysis approach taken to investigate the effect of compression on multiphase flow. The next part of the section describes how the networks were validated against a morphological approach and experimental drainage data, and how the pore scale models that determine the saturation were set. Finally the transport algorithms used to calculate the relative transport characteristics of compressed GDLs are explained.

4.3.1 Network Creation

The steps involved in creating the pore network model from a Voronoi diagram are shown pictorially in Figure 4.1 in 2D for clarity. The details of the steps for constructing the networks are as follows:

i Randomly distribute pores in space as shown in Figure 4.1a. For the uncompressed network a domain size of 750x750x375 µm filled with approximately 5000 pores is used. Pores are distributed uniformly but with increased density at the domain edges to counteract the naturally arising higher porosity introduced by the Voronoi method, as explained by Gostick [69]. The land-channel results are conducted for networks with a domain size of 1000x1000x580 µm

populated with approximately 6000 pores and have a spatially varying porosity in the IP x-direction. The domain is bound within a rectangular box, and boundary pores that have no volume are created at the boundary faces by reflecting the internal pores about the 6 faces of the box before generating the Voronoi diagram. The reflection about a plane creates Voronoi vertices and facets aligned with the plane, and afterwards all pores with connections solely outside the initial domain bounding box are deleted. The network could have been formed with non-planar faces by removing unbounded pores at the domain edges but for transport calculations planar faces are very useful.

ii Create throats by connecting nearest neighbour pores according to the Delaunay triangulation [250] and saving the connections in a sparse adjacency matrix as shown in Figure 4.1b. The Delaunay triangulation identifies pore triplets in 2D that lie on the circumference of a circle that encircles no other pore. In 3D the triangulation identifies groups of 4 pores lying on the circumsphere enclosing no other pore and connects them with non-overlapping tetrahedra.

iii Define the fibrous geometry with a Voronoi diagram [251], the mathematical dual of the Delaunay triangulation. This partitions the domain into proximal regions surrounding each pore defined by sets of vertices connected by edges forming a cage-like structure. This cage is known mathematically as the "convex hull" of the set of Voronoi vertices. The diagram is shown in Figure 4.1c and in 2D the edges of the Voronoi cells completely surround each pore. In 3D the cells become open cages but a slice of the 3D diagram is similar to the 2D figure presented. A full 3D structure is shown later.

iv Introduce anisotropy by scaling vertices and pore coordinates. The domain is initially scaled in the z-direction by a factor of 0.82 for uniform compression, and 0.5 for the land-channel model to align fibres along the IP direction and reduce domain height to 307 and 290 µm respectively. For uniform compression, this scaling was chosen to match porosity and single-phase permeability data for an uncompressed Toray 090 GDL [141]

v Create the fibres by populating a binary 3D voxel image with a skeletal frame using a Bresenham line algorithm on the Voronoi vertices (zero defines a voxel containing fibre and one defines pore space). Distance transforms of the voxel image are then performed and re-binarized using a fibre radius of 5 µm as a threshold to expand the skeleton and fill the voxel image with thicker fibres, shown in Figure 4.2. The 2D equivalent process is shown in Figures 4.1d to 4.1f.

vi Populate a similar "hull image" and use this in combination with the fibre image to extract pore and throat sizes by through image analysis. We make use of the convex hull to accurately determine pore volumes, as described in detail by Gostick [69]. Throat areas are also extracted from the images by identifying those lying on the intersections between neighboring pores. An additional distance transform of the fibre image is used to identify those "pore voxels" adjacent to "fibre voxels" in order to calculate pore and throat perimeter lengths.

vii Compression is simulated by a manipulation of the fibre image to shift fibre voxels according to their TP position as described by Schulz et al. [144], [245], [252]. Compression ratio (CR) is defined as percentage reduction in domain height from the 307 µm baseline as per Equation 3.2.1. Five levels of compression are simulated in 10% step increases from 0% to 50%, the maximal level likely to be experienced within a fuel cell. The land-channel networks remain compressed at 290 µm but contain different pore densities for the different sections.

Geometry Models

This section details a few of the important geometry models developed to create the PNM from the Voronoi diagram. The diagram is created with a voxel length of 1 µm, so voxel volumes represent 1E-18 m^3 and voxel areas 1E-12 m^2. Many of the methods rely on Scipy's Euclidean distance transform method [249], which is a voxel map where voxels are assigned values according to the smallest distance from an obstacle voxel.

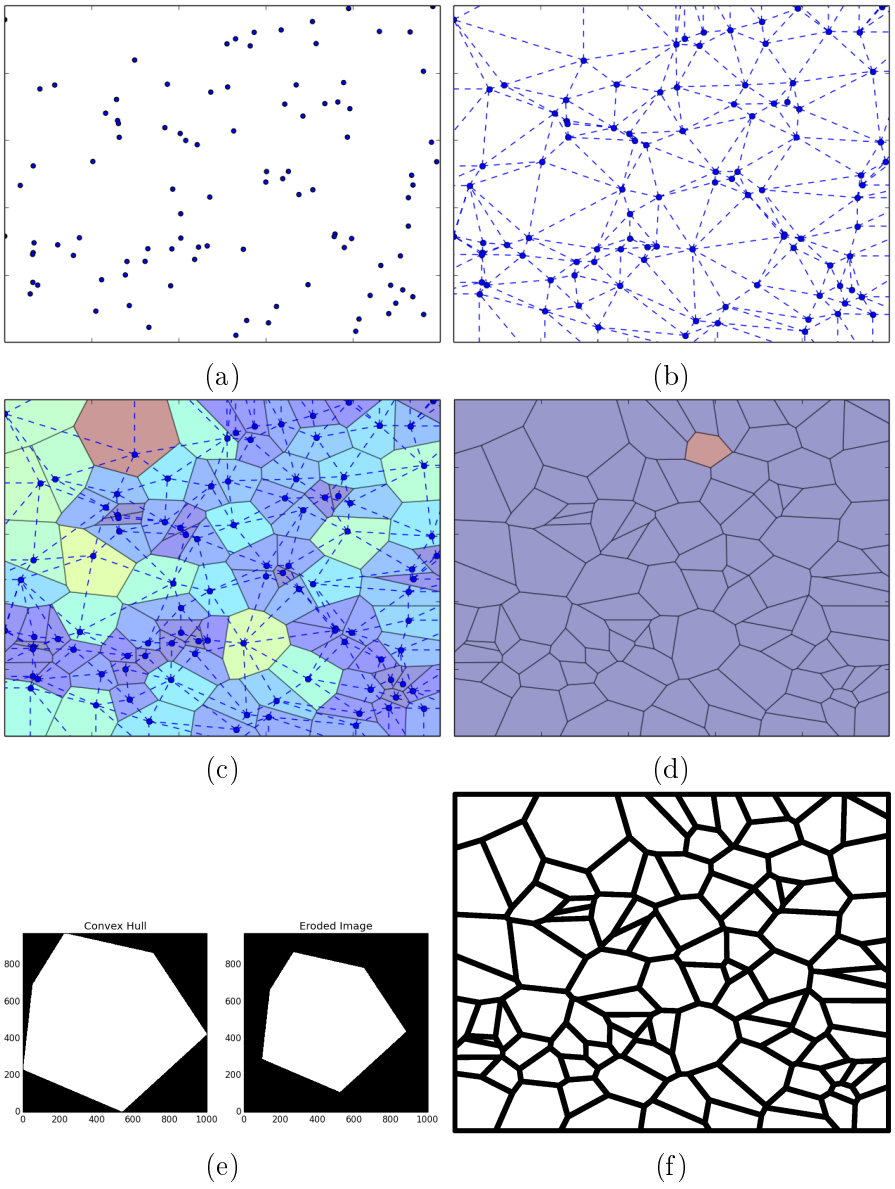

Figure 4.1: The various steps for creating a fibrous image and PNM: a) Placement of pores, b) Throat connections defined with Delaunay Triangulation, c) Pore sizes assigned with Voronoi Diagram, d) Single pore highlighted, e) Solid volume added by expanding fibres, f) Final solid structure for all pores

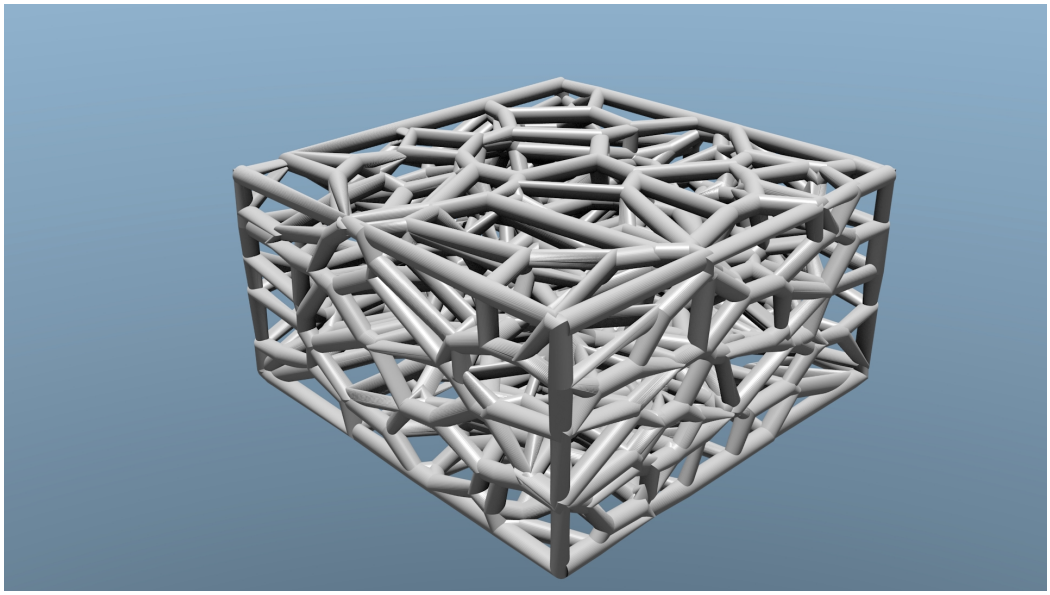

Figure 4.2: Example fibrous structure generated from Voronoi diagram.

- Pore Volume: A hull image is created using an adapted version of the "inhull" method [253]. For each set of vertices defining the intersection of the hyperplanes forming the cage around each pore the plane normal ($\vec{n}$) is computed and made to point inwards. Incidentally before compression this is also the throat normal vector. Then taking one plane at a time, for every voxel within a bounding box of each pore the vector from the voxel coordinate to one of the plane vertices ($\vec{x}$) is computed in vectorized form. The dot products of the voxel vectors with the plane normal are then compared to the dot product of any plane vertex ($\vec{a}$) with the plane normal. If ($\vec{x}.\vec{n} - \vec{a}.\vec{n} >= 0$) within some small tolerance, one is added to a running tally assigned to each voxel. After performing the steps for each plane if the tally is equal to the number of planes then the voxel is within the convex hull of the pore. This calculation and population of the convex hull image is the most time-consuming part of generating the network. For an image of 1000 x 1000 x 300 voxels the process takes about 20 minutes on a 3.40 GHz 16.0 GB desktop. Images much larger than this begin to run into memory issues and a chunking procedure has been implemented which

divides the domain into smaller, slightly overlapping chunks. The chunks overlap to ensure that every pores near the edges is fully calculated as the process requires that all the Voronoi vertices be present for each calculation.

- Pore Diameter: This is calculated from the Pore Volume using an equivalent sphere approximation.

- Throat Area: Using the convex hull image, throat areas are calculated by identifying voxels belonging to the perimeter of each pore by performing a distance transform in the local space around each pore. A binary image is created for the distance transform with voxels belonging to the pore assigned zero and those outside the convex hull one. The distance transform is then used to identify all the voxels less than 2 voxel lengths away from the pore convex hull. These voxels are used as a mask to inspect the convex hull image as they overlap neighbour pores and are summed after subtracting the voxels assigned to fibres.

- Throat Perimeter: A process similar to the above is used to identify those voxels lying on the perimeter of the throats. The pore space of the fibre image is eroded by one additional voxel (again with a distance transform), effectively expanding all the fibres and those in the new expansion zone overlapping voxels identified as belonging to the throat area are summed to get the perimeter length.

- Throat Volume: The fibre diameter is used as the throat length for volume calculation which is a simple extrusion of the throat area.

- Pore and Throat Centroids: A distance transform of the entire pore space is performed on the fibre image, and local maxima for voxels assigned to each pore and throat are used to identify the positions of the centroids. This represents the point furthest away from any fibre within each space, and the maximum value is also equal to the radius of an inscribed circle or sphere. The centroids are then used to calculate centre-centre lengths for transport calculations.

Network Porosity

Several methods were investigated to generate and compress the fibrous geometry resulting from the Voronoi diagram. At first a method which did not generate a voxel image was tried. Instead, vertex points located at the fibre intersections were offset in the plane of the throat facets to a point equidistant from the facet edges by a distance equal to the fibre radius. This in itself was not trivial and again several methods were tried to obtain the offset vertex points. The most reliable method is based on image analysis, where a 2D image is created for each throat, and binary erosion of the convex hull of the vertices is used to reduce the throat area to represent the fibres (as pictured in Figure 4.1e). Once the offset throat vertices were produced, they were then used to calculate pore volumes by computing the convex hull of all the offset vertices associated with all the throats belonging to each pore. This method was very fast, but resulted in larger pore volumes that are bound by cages of polygonal rather than circular fibres. For reasonably round shaped pores, this over-simplification may have been acceptable as the aspect ratio of the polygonal fibres was fairly close to unity. However, as the domain is compressed the offset vertices also compress and this results in fibres with high aspect ratio and smaller volumes than spherical un-deformed fibres. Therefore, the approach was abandoned in favour of a completely imaged based approach, as detailed previously, primarily to preserve fibre volume under compression.

In order to achieve fibre volume preservation, voxels were not allowed to overlap, so regions of low porosity have solid voxels stacked on top of one another. This technique distorts the fibres and throats slightly, and results in non-planar throats and concave pore shapes. This presents a problem, as the method of pore volume calculation relies on the pore shapes being convex. The problem was overcome by assigning voxels in another image with identical dimensions to the "fibre image" to a pore before compression by assessing which convex hull they lie within using the Voronoi vertices. This builds a non-overlapping hull image with voxels labelled with the original uncompressed pore index called the "hull image", and includes all the voxels in positions labelled as fibres in the fibre image. On compression, the hull image is simply scaled by the compression ratio,

and pore index labels are mapped according to their respective height in the TP direction. Combining the two images, retaining hull voxels that only lie within the pore-space of the fibre image, then gives the new pore volumes by summing the surviving hull image voxels for each pore.

A simpler method of simulating compression is to scale the vertices of the uncompressed Voronoi diagram and regenerate the image, but this does not preserve fibre volume and was found to introduce significant porosity errors at high compression levels. Without generating and scaling the hull image, the pore and throat sizes could have been extracted directly from the fibre image through image analysis. This approach was also tried using a maximal ball technique [254], and software available from the Imperial College research group of Blunt [255]. However, the resulting networks tended to lose their anisotropy, which is a key feature of the GDLs being simulated, due to the spherical filling of the pore space. Other techniques using skeletonization are possible [256] and probably more suitable for network extraction on fibrous material, but the current approach worked well. Although the centre of the fibres does not always lie entirely on the boundaries of the convex hulls associated with each pore, closer inspection of the image for a number of pores revealed that these errors are not important, as the fibre volume covers enough voxels either side of the boundary to still partition effectively. Some pores may have slightly larger volumes, but this is always balanced by neighbouring pores having slightly smaller volumes and overall porosity is always accurate. The methods described here could form the basis of a generic network extraction tool for fibrous media by creating a series of convex hulls and merging those that are not completely bounded by fibres but, this is left for future work.

4.3.2 Percolation Algorithms

Two percolation algorithms are developed in this study: invasion percolation using the generated pore networks and a morphological image analysis performed directly on the fibre image.

Invasion Percolation

The percolation algorithm used to determine the placement of liquid water in the network is a modified version of the invasion percolation algorithm first described by Wilkinson and Willemsen [257], as discussed in the context of fuel cells by Gostick et al. [258]. The algorithm represents drainage of a wetting phase by invasion of a non-wetting phase. This corresponds to the percolation of water in the fuel cell from the catalyst layer at the bottom of the domain to the bipolar plate land or gas channel at the top. This process is typically simulated by starting with an initially dry network and sequentially invading accessible throats belonging to the path of least resistance. Resistance is based on the capillary entry pressure, determined by the Washburn equation, details of which are given in section 4.3.3. The algorithm continues until the entire network is filled. Trapping of air is not considered, as the wetting phase is assumed to form thin films which can always percolate. In the general case of invasion percolation, when a throat is invaded, the pores it connects are assumed to also be filled, since pores are larger than throats by definition. In the present case of highly porous anisotropic media with compression, however, some pores were rather flattened and an inscribed sphere was often smaller than some or all of the throats. Consequently, the general invasion percolation algorithm was altered such that the entry pressure of both throats and pores, collectively referred to here as elements, were considered when seeking the path of least resistance.

Invasion percolation progresses one element at a time by tracking a list of un-invaded elements connected to the invading cluster, and invading the one with smallest entry pressure. This enables an invasion sequence to be produced which allows the precise determination of saturation at the point of breakthrough. Liquid cluster breakthrough is the point at which an outlet pore at the top of the domain first becomes invaded. A percolating pathway is formed if the cluster of invaded pores spans the network, the significance of which is discussed by Gostick et al. [259]. In operating fuel cells, the percolating pathways offer less resistance to fluid flow, as less pressure is required to inflate a droplet interface growing in the fuel cell gas channels, than to invade smaller pores inside the GDL. Therefore, once a pathway is established, the breakthrough pattern is often

repeated and liquid droplets can be seen forming at the same positions over and over, as modelled in Chapter 3, and observed experimentally by Quesnel et al. [241]. Saturation at breakthrough is therefore a good indication of average medium saturation during fuel cell operation.

Python's *heapq* module, provided as part of the standard library, is used to manage the list of accessible un-invaded pores and throats efficiently. The heaps are sorted data structures representing a priority queue where the first element always has the smallest value. When a pore is invaded, its newly accessible connecting throats are all added to the queue and sorted by capillary entry pressure automatically. Similarly, when a throat is invaded, its connecting pore is added to the queue. The algorithm progresses sequentially removing the most easily accessible pore or throat from the queue, marking the element as invaded with a sequence and cluster number, and adding neighbours until the queue is empty and all elements are invaded. The algorithm is a combination of site and bond percolation, as pores and throats are treated equally and invaded separately, as opposed to assuming that once a throat is invaded, its connecting pores are also invaded.

For the uniform compression study individual inlet pores are designated for fluid invasion. The inlets are assumed to share the same pressure as if connected to a common external reservoir. We randomly designate 50% of the pores along the bottom face of the network as inlets. Fazeli et al. present a detailed discussion of the different inlet conditions for fuel cell modelling [260], and we consider this to be a fair representation in order to match ex-situ drainage experiments. As Fazeli et al. suggest, percolation through the GDL of operating fuel cells may occur differently, with separate liquid clusters growing at different rates. To calculate the breakthrough saturations, in Section 4.4.3 we apply a cluster inlet condition that groups neighbouring inlet pores together. Clusters progress individually, but are allowed to merge together, and have their own termination condition at the outlet. We randomly choose a number of cluster invasion sites with random grouping radii for our inlet condition. The effect of cluster size is not investigated, but 100 realizations are made for each simulation to ensure statistical representation, and the simulations are repeated for an inlet condition of 10 and 20 clusters.

Once an element is invaded, the volume fraction of each phase is determined heuristically by a late pore filling (LPF) model, described in section 4.3.3. This decreases the residual air phase fraction with increasing capillary pressure. A drainage curve can be produced as a post-processing step by summing the volume of the elements with invasion sequence less than a critical step. The critical step corresponds to the first element to be invaded with entry pressure above a critical value. This critical value is incremented from zero to a maximum of 30 MPa in sequence to produce the curves.

In addition to the general compression and transport studies, this chapter also looks at some fuel-cell specific arrangements. The influence of the fuel cell bipolar plate's land to channel ratio, pictured in Figure 2.9, is investigated by applying an IP porosity gradient to sections of varying size determined by a channel area fraction. The invasion percolation algorithm is run for each network, selecting clusters of pores in the bottom face across the entire domain for liquid water inlets, and all of the pores in the channel section of the top face as outlets. Percolation of each cluster continues until reaching an outlet pore and the total saturation is recorded once all clusters have either reached an outlet pore to form a percolating cluster, or have merged with another cluster.

To investigate the influence of the saturation on the fuel cell performance, the limiting current is calculated by simultaneously performing a percolation and diffusion algorithm, described in Section 4.3.4. A channel boundary condition is set at 10% for oxygen concentration and 0% at the bottom face. The total rate of diffusive flux, Q, is then calculated by summing the rates of the bottom face pores and converted to a limiting current using Faraday's law:

$$I_{limit} = 4FQ/A \tag{4.3.1}$$

where F is Faraday's constant and A is the area of the bottom face of the network (1 mm x 1 mm). The boundary conditions reflect the environment in the cathode of an operating fuel cell running at high current density with humidified gas streams [258].

Morphological Image Opening

As part of the model validation process, a morphological image opening (MIO) algorithm is performed on the binary image of the fibrous structure. A brief overview of Full Morphology techniques for analysing porous material was given in Section 2.4.4. The general method is outlined by Hilpert and Miller [246] and has been applied to fuel cells several times by Schulz et al. [144], more recently with varying contact angles surrounding the fibres [261] and Gostick [69]. The steps taken are broadly the same as that of Gostick except that routines from SciPy's multi-dimensional image processing tool (*ndimage*) are used as opposed to Matlab:

i Using the fibre image produced by OpenPNM's *Voronoi* geometry module as described in Section 4.3.1, a Euclidean distance transform (dt_1) is performed using the *distance_transform_edt* function. This enables the identification of voxels in portions of the pore space at least distance r from any voxel designated as solid thus creating a skeletal image for the liquid phase.

ii Next identify connected clusters of skeletal voxels using the measurements.label function on the distance transformed image. Address access limitations by only retaining clusters connected to inlet voxels on the bottom face

iii Perform a second distance transform (dt_2) on the remaining skeletal clusters using the same radius again to expand the liquid phase.

iv Sum the voxels in each phase and correlate this with capillary pressure using the Washburn relation (Equation 2.2.22): 0 is solid, $dt_2 <= r$ is water and $dt_2 > r$ is air.

v Decrease r (i.e. increase capillary pressure) and repeat steps (i) to (iv) until r is just one voxel length. With a smaller radius the spherical liquid interfaces are able to penetrate smaller features of the voxel image and saturation increases.

MIO naturally accounts for LPF and is used to determine the LPF parameters for the PNM, thus accounting for sub pore-scale features.

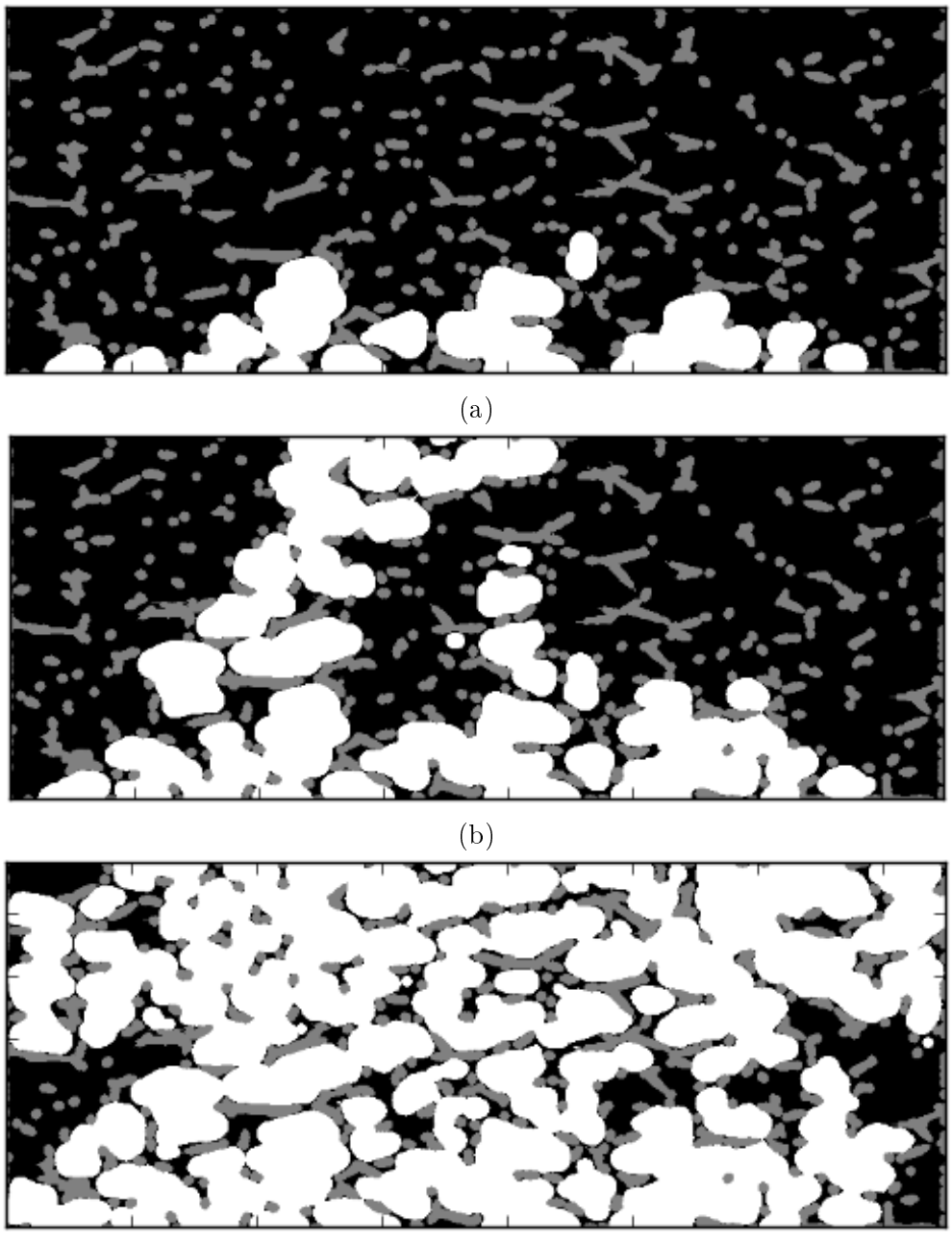

(a)

(b)

(c)

Figure 4.3: Sections of the fibre image at various stages of the MIO algorithm with decreasing r and increasing P_C. Black represents pore space, grey is fibre and white is liquid water.

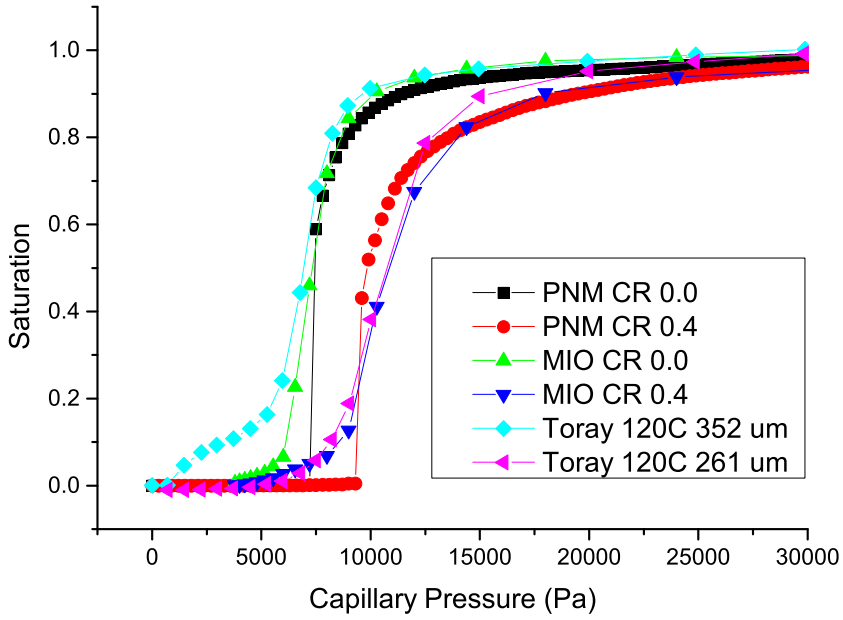

Figure 4.4: Comparison of drainage curves generated from PNM and MIO simulations and experiment for GDL under compression.

4.3.3 Model Validation

To ensure that the PNM is a realistic representation of a GDL, several steps were taken to validate the modelling approach. To check that pore and throat sizes are being extracted correctly, a drainage simulation is performed using both percolation algorithms described in Section 4.3.2 and the results are shown in Figure 4.4 along with experimental data collected by Gostick et al. [17].

MIO erodes the pore space with spherical elements of decreasing diameter representing the liquid phase. The capillary pressure is related to the radius, r, of the element with the Washburn relation stated previously as Equation 2.2.22. A contact angle, θ, of 110° and surface tension, σ, of 0.072 Nm^{-1} was used. The radius chosen for the pore network calculation was half the diameter of an inscribed circle for throats gathered by image analysis, as this best matches the MIO process. As the PNM percolation algorithm progresses, the volume of the

Compression Ratio	S'_{WP}	η
0.0	0.312	4.00
0.1	0.317	3.30
0.2	0.321	2.87
0.3	0.333	2.56
0.4	0.370	2.35
0.5	0.421	2.08

Table 4.1: The late pore filling parameters for different compression ratios determined from morphological image analysis.

wetting phase in each pore ($S_{WP,i}$) is determined by a heuristic relation accounting for LPF as follows [262]:

$$S_{WP,i} = S'_{WP} \left(\frac{P'_{C,i}}{P_C} \right)^{\eta} \tag{4.3.2}$$

where S'_{WP} is a fitting parameter representing the volume fraction of the wetting phase remaining in the pore upon initial invasion at capillary pressure $P_{C,i}$, and η is another fitting parameter which determines how quickly the residual wetting phase occupancy decreases inside the pore when increasing capillary pressure. MIO is used to calculate the average fitting parameters for all the pores at each compression ratio by matching Equation 4.3.2 to the fraction of occupied voxels inside the pores at each pressure. The fitting parameters are shown in Table 4.1.

The LPF parameters show that the residual wetting phase upon initial invasion is quite high, and increases with compression. On initial invasion of the pore, the invading phase (if non-wetting) resembles a spherical volume similar in size to an inscribed sphere, although this may bulge out of the pore in reality. As capillary pressure increases, the invading phase will push further into the crevices of the pore space and corners of the pore, shown in Figure 4.5. As the geometry is compressed, the pore volumes become more skewed, and an inscribed sphere occupies less of the total pore volume fraction, leading to higher wetting phase saturation upon initial pore invasion. The results presented in Figure 4.4 show close agreement between the two numerical approaches, giving confidence to use the generated pore and throat sizes for further pore network modelling.

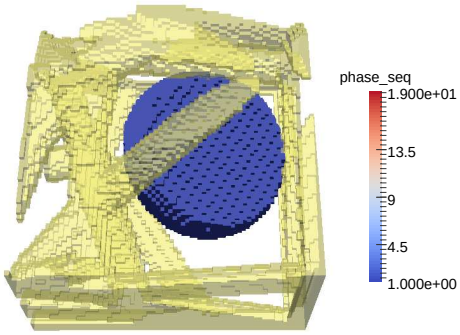

(a) Initial invasion, liquid has spherical shape inside pore.

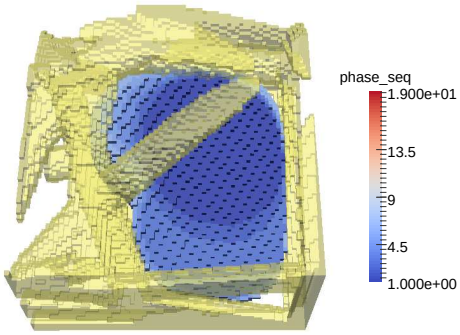

(b) Pore partially filled at invasion sequence 5.

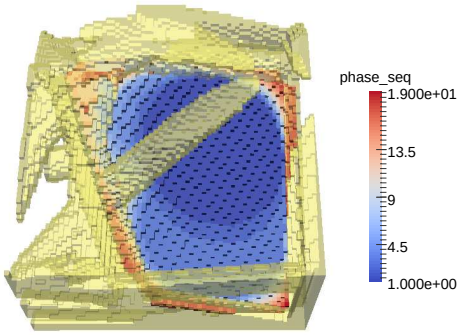

(c) Pore fully filled at highest capillary pressure.

Figure 4.5: A section of the voxel image produced with MIO demonstrating the late pore filling (LPF) effect.

The uncompressed experimental data shows higher saturation at low capillary pressures compared with the simulations, but this is most likely due to experimental artifacts such as water pooling at the GDL surface due to imperfect contact between the GDL and water injection source. The compressed PNM curve in Figure 4.4 shows a steeper increase in saturation at around 10,000 Pa than the experimental data, which is most likely due to a narrower distribution in pore and throat sizes used in the model. In reality, fibres may deform and break under compression, leading to the bisection of pores and creation of micro-pores within fibres leading to a larger number of smaller pores. This behavior is beyond the scope of the modelling approach however, and a satisfying level of agreement between datasets is achieved. The MIO results also agree better with experiment when compared with the PNM at low saturations. This is because interfaces are allowed to bulge through the inlet pores without fully invading the pores, and because the medium is thin this effect can contribute to a significant level of saturation.

4.3.4 Transport Algorithms

In addition to percolation algorithms, the single phase and multiphase characteristics of porous media can be studied with PNMs. This is achieved by employing 1D linear transport equations and nodal balances to each set of neighbouring pores, then solving the system of equations over the 2D or 3D network. PNMs are therefore similar to resistor networks where hydraulic and diffusive conductivities used to solve Stokes flow and Fickian diffusion are analogous to electrical conductivity used to solve Ohm's Law.

The governing equations for mass and species conservation used in this study are presented in this section. For the conductance values we assume an equivalent spherical and cylindrical shape for pores and throats respectively.

Permeability

The mass flow rate corresponding to a pressure drop across the medium is determined according to the hydraulic conductance, g_h, of the set of pores spanning the

medium. Conservation of mass is ensured by obeying the conservation between each pore, i and it's neighbour, j, with the following equation:

$$\sum_{j=1}^{n} q_{ij} = \sum_{j=1}^{n} g_{h,ij}(P_j - P_i) = 0 \tag{4.3.3}$$

The hydraulic conductivity is calculated assuming Hagen-Poiseuille flow through a straight cylindrical conduit:

$$g_h = \frac{\pi d_i^4}{128 l_i \mu} \tag{4.3.4}$$

where d is the diameter of the conduit, μ is the dynamic viscosity of the flowing fluid and l_i is the length of the conduit. The total hydraulic conductivity for a pore-throat-pore assembly or conduit is found by combining the individual conductances like resistors in series, taking the centre to centre length of the pore centroids and throat centroid as an appropriate length scale.

$$\frac{1}{g_{ij}} = \frac{1}{g_{pi}} + \frac{1}{g_t} + \frac{1}{g_{pj}} \tag{4.3.5}$$

Solving the set of linear algebraic equations in the form of Equation (4.3.3) for the network yields a total flow rate, Q, which can be used with the prescribed pressure drop across the boundaries $(P_{in} - P_{out})$ to calculate the absolute permeability, K_0, of the medium using Darcy's Law:

$$Q = \frac{K_0 A(P_{in} - P_{out})}{L\mu} \tag{4.3.6}$$

where A is the network cross-sectional area normal to flow and L is the physical length of the domain across which flow occurs.

Diffusivity

Similarly to mass conservation and permeability calculation, a species conservation and diffusivity calculation can be done using the same principal of 1D nodal balances. Fick's law is used to calculate the diffusive transport of each species

between pores:

$$\sum_{j=1}^{n} n_{a,ij} = \sum_{j=1}^{n} g_{d,ij}(lnx_{a,j} - lnx_{a,i}) = 0 \tag{4.3.7}$$

where $n_{a,ij}$ is the molar flow rate of species a between pores, x_a is the mole fraction of species a and $g_{d,ij}$ is the diffusive conductivity, which is analogous to the hydraulic conductivity, and is defined as:

$$g_d = \frac{cD_{ab}A_i}{l_i} \tag{4.3.8}$$

where c is the molecular density of the gas, D_{ab} is the diffusion co-efficient of the mixture in open space and A_i is the cross-sectional area of the conduit. At a network level, the solution of the set of species conservation equations yields a total molar flux:

$$N_a = \frac{cD_{eff}A}{L}(lnx_{a,in} - lnx_{a,out}) \tag{4.3.9}$$

Both algorithms are implemented in OpenPNM (*StokesFlow*, *FickianDiffusion*) and inherit from a *GenericLinearTransport* object which builds a coefficient matrix based on the supplied conductance models and boundary conditions, then solves it using the standard matrix inversion routines within SciPy. The effective permeability and diffusivity which are intrinsic properties of the networks (K_0 and D_{eff}) are then extracted from the predicted flow rates, known domain dimensions, and applied boundary conditions.

Relative Transport

Multiphase flow is simulated by effectively solving the equations in each phase separately, where the conductivity of one phase is severely reduced in pores and throats occupied by the other. This is accomplished by multiplying the single-phase conductance values by a factor of 1E-06. In this way relative transport characteristics can be determined by running transport algorithms at successive stages of the percolation algorithm. A further study of the validity of this conductance assumption could be undertaken, as MIO has revealed that a significant fraction of residual wetting phase exists upon initial invasion which could be conducting. However, this is not the focus of the present study, so it is assumed that

corner-filled pockets of air do not effectively conduct.

A general relative transport property, Φ_r, which represents either permeability or diffusivity, is calculated as the dimensionless fractional change in the effective transport of each phase, i, as a result of the presence of other phases. Relative transport is often related to the volume fraction of the pore space occupied by that phase, V_i, by a power law relation.

$$\Phi_{r,i} = \frac{\Phi_i}{\Phi_0} = V_i^n \tag{4.3.10}$$

When modelling fuel cells, as water is generally the non-wetting phase, saturation by water of the pore space, S, is used to express the relative transport of both phases, the sum of the relative transport relations is generally taken to be unity and $n = 3$ is usually assumed [7].

$$\Phi_{r,air} = (1 - S)^n \tag{4.3.11}$$

$$\Phi_{r,water} = S^n \tag{4.3.12}$$

where S is defined as the volume fraction of the pore space occupied by water. Relative phase transport, $\Phi_{r,i}$, is calculated by effectively only solving the conservation equations over the subset of pores occupied by phase i. Pores and throats occupied by other phases are knocked out of the network by having their conductances severely reduced by a factor of 1 million. However, network conservation laws are still applied to the dimensions of the medium as a whole. The exponent used for the relative relations is therefore a reflection of the percolation process. If taken to be a linear relationship between domain volume fraction and phase effective permeability, this would imply that all percolating pathways progress straight through the medium with no trapping of the other phase between pathways. This is an ideal case, deviations from which result in increased flow tortuosity and higher power law relations for relative transport. In addition, the more tortuous the pathway and the more dispersed the phases, the higher the overall saturation at percolation breakthrough.

4.4 Results and Discussion

4.4.1 Size distributions and single phase transport

The key geometric properties of the networks under compression are shown below and tabulated in Appendix A with fitting parameters to a log normal distribution:

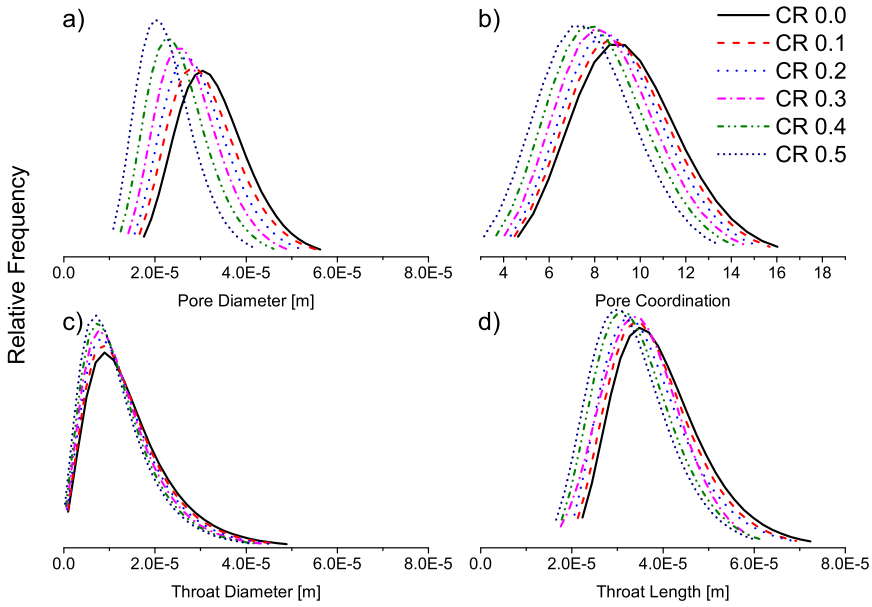

Figure 4.6: Key network size distributions for all levels of compression.

The general trend is a decrease in all key properties with compression although some changes are more significant than others. Pore diameter is an effective calculation based on the volume of an equivalent sphere. Throat diameter is also an effective calculation based on the area of an equivalent circle. Throat length is the total conduit length used in transport calculations from the centroid of pore i to the throat center to the centroid of pore j. Volumes and therefore equivalent diameters of pores reduce the most under compression, whereas only a relatively small change in throat lengths is seen. However, as discussed later the change in throat length is different for different directions. Other properties of the network

such as surface wetting contact angle are assumed to remain unchanged with compression. A very recent study by Zenyuk et al. analyses the changes in pore size distribution (PSD) for several different GDLs under compression [263]. The general shift in shape from a more normally distributed range of sizes to a skew towards smaller sizes is observed, as one would expect, and in agreement with the simulated results presented here.

By also using the throat vector, it is possible to see how the key throat properties that influence the transport change with compression in the different directions. The angle between the throat vector and the TP axis is used to group throats, and their average properties are normalized by the maximum value in each data set, and are plotted with compression below in Figure (4).

Figure 4.7a shows that in general the throats aligned with the TP direction have the largest area, and Figure 4.7b shows they have shortest length. The throat area changes significantly for throats aligned with the IP direction, and not significantly for throats aligned TP. In contrast, the throat length does not change significantly with compression in the IP direction. On average IP throat length reduces by about 20% at most, which in-turn reduces IP tortuosity slightly. Through-plane throat length scales proportionally with compression ratio as pores are moved closer together, so TP tortuosity will remain constant.

Figure 4.8a shows the effective permeability of the compressed networks for IP and TP directions. Reasonable agreement is found between the simulated data and a Kozeny-Carman (K-C) relation given as:

$$\frac{K}{d_f^2} = \frac{\epsilon^3}{16k_C(1-\epsilon)^2} \tag{4.4.1}$$

where ϵ is porosity and k_C is a fitting parameter which is equivalent to Equation 3.3.3 which used the fibre radius, R, instead of the fibre diameter, d_f. Here a value of 4.07 for k_C is used as this was found to be in good agreement for IP data collected for Toray090 GDL [141]. Data from a study by Becker et al. conducted on samples of Toray 060 GDL [252] is also included for comparison. The datasets are similar, but the effect of compression on the IP permeability seems to be more severe in Becker's study. Toray 060 may have a greater anisotropy than Toray 090 or the differences between the extracted and generated structures

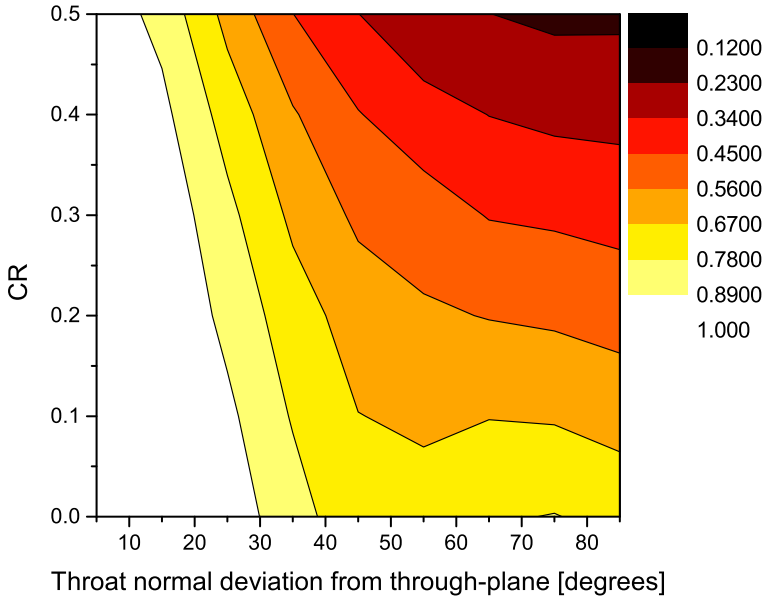

(a) Throat Area

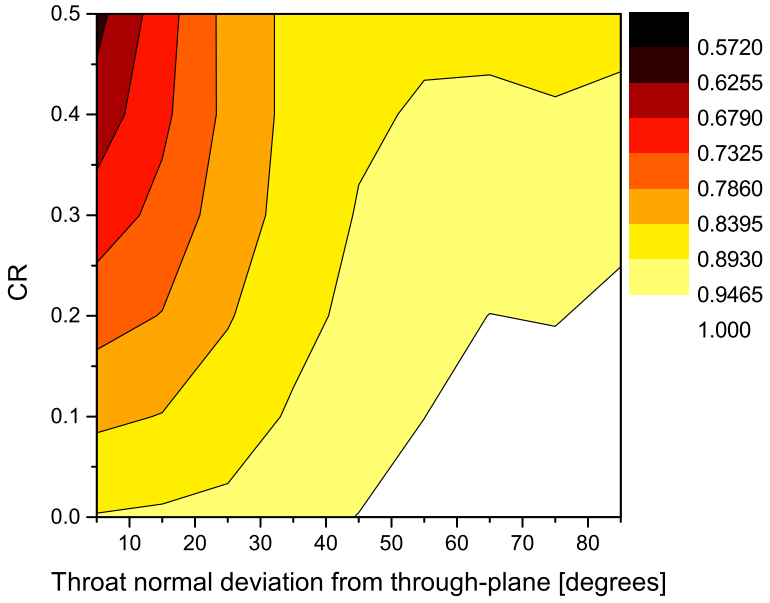

(b) Throat Length

Figure 4.7: Normalized throat properties averaged by throat normal vector and compression ratio.

or modelling approaches may lead to the difference. For simplicity, we do not include the influence of a shape factor in our hydraulic conductivity, which will also change anisotropically with compression, but is not expected to have a great bearing on the results.

Figure 4.8b shows the effective diffusivity of the compressed networks for IP and TP directions normalized by the diffusivity of air in open space. The simulated IP data is again compared with Becker et al. and with recently obtained experimental IP data for Toray090 [46]. Encouragingly, good agreement is found between all data-sets.

Both single-phase simulations clearly show the anisotropy in the structures, with IP values typically double that of TP values. As noted by Becker et al., the influence of compression is more greatly felt by the permeability than the diffusivity, because permeability depends on the square of the effective pore/throat radius, whereas diffusivity is more dependent on the tortuosity which is not found to change significantly.

4.4.2 Multiphase transport under uniform compression

The relative transport properties of each phase are normalized by the transport property with full phase occupancy, and are expressed as functions of the liquid phase domain volume fraction i.e. the saturation including late pore filling. In the present study, where percolation thresholds are a feature of the network approach, the simple power relation Equation 4.3.10 does not fit the data very well. The relative transport of mass and species within the air phase is expressed as a function of both saturation and a critical saturation or percolation threshold, S_c, above which no percolating clusters of pores occupied by air are found [264]:

$$K_a = D_a = \begin{cases} (1-S)^n \left((S_c - S)/S_c\right), & \text{if } S < S_c \\ 0, & \text{otherwise} \end{cases} \tag{4.4.2}$$

The relative permeability of water was found to fit a log normal expression similar to that presented by Hwang & Weber [18] for relative air diffusivity:

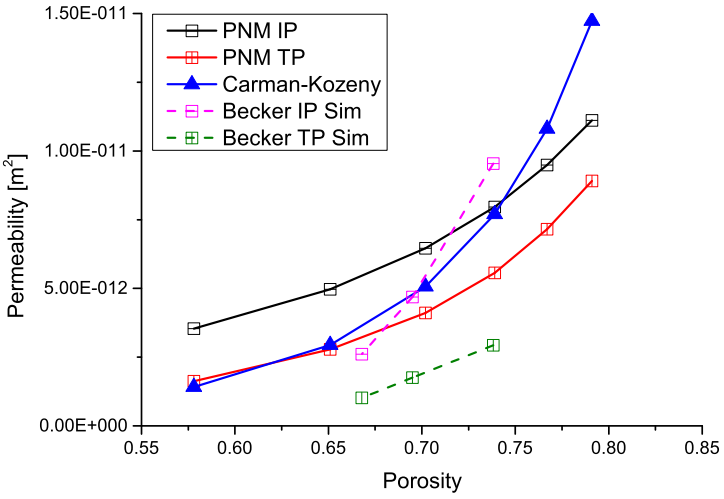

(a) Single phase effective permeability

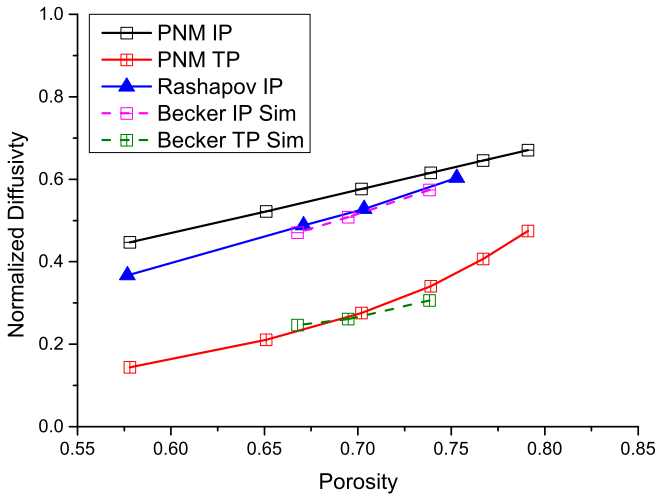

(b) Normalized single phase effective diffusivity

Figure 4.8: Comparison of the single phase transport properties under uniform compression.

$$K_w = \frac{1}{2}\left[1 + erf\left(-\frac{ln(1-S)+a}{b}\right)\right] \tag{4.4.3}$$

where a and b are simply fitting parameters. 100 realizations of each relative property simulation were performed using different randomizations of the inlet boundary pores for percolation.

Figure 4.9 shows the dependence of the fitted relative transport expressions on compression of the networks. The pattern for relative air diffusivity is similar to relative air permeability but with slightly lower values. For IP relative air transport, the percolation threshold appears to decrease with compression, signifying that transport in the air phase is impeded more significantly at lower saturations under compression. Compression has the opposite effect on TP relative air transport which is less impeded at higher saturations compared with IP. With increasing compression, the difference between IP and TP relative air transport widens, as saturation would appear to hamper IP transport more significantly. Our results show that an average medium saturation of 0.35 for compressed GDL would result in highly reduced air phase transport in the IP direction. Our generated fibrous structures have IP fibre alignment but no preferential alignment within the IP direction. It is expected that compression would hamper "cross-fibre" transport much more severely than "along-fibre" transport. It would be possible to construct fully 3-dimensionally anisotropic networks using the Voronoi approach through scaling of the vertices but this is left for future work.

For liquid permeability we see a decrease in the IP relative transport, and comparatively little change in the TP transport. Given the initial anisotropy in the networks, which show IP conductance typically twice that of TP, the multiphase results suggest that, as networks start becoming saturated, this anisotropy is assuaged and the effect increases with compression. The reason for this rebalancing of TP and IP transport can be explained by the relative change in throat area for the different directions shown in Figure 4.7. Throats that are orientated more towards IP close off quicker than those orientated though-plane, and therefore capillary pressure increases and the path of least resistance points more towards the TP direction.

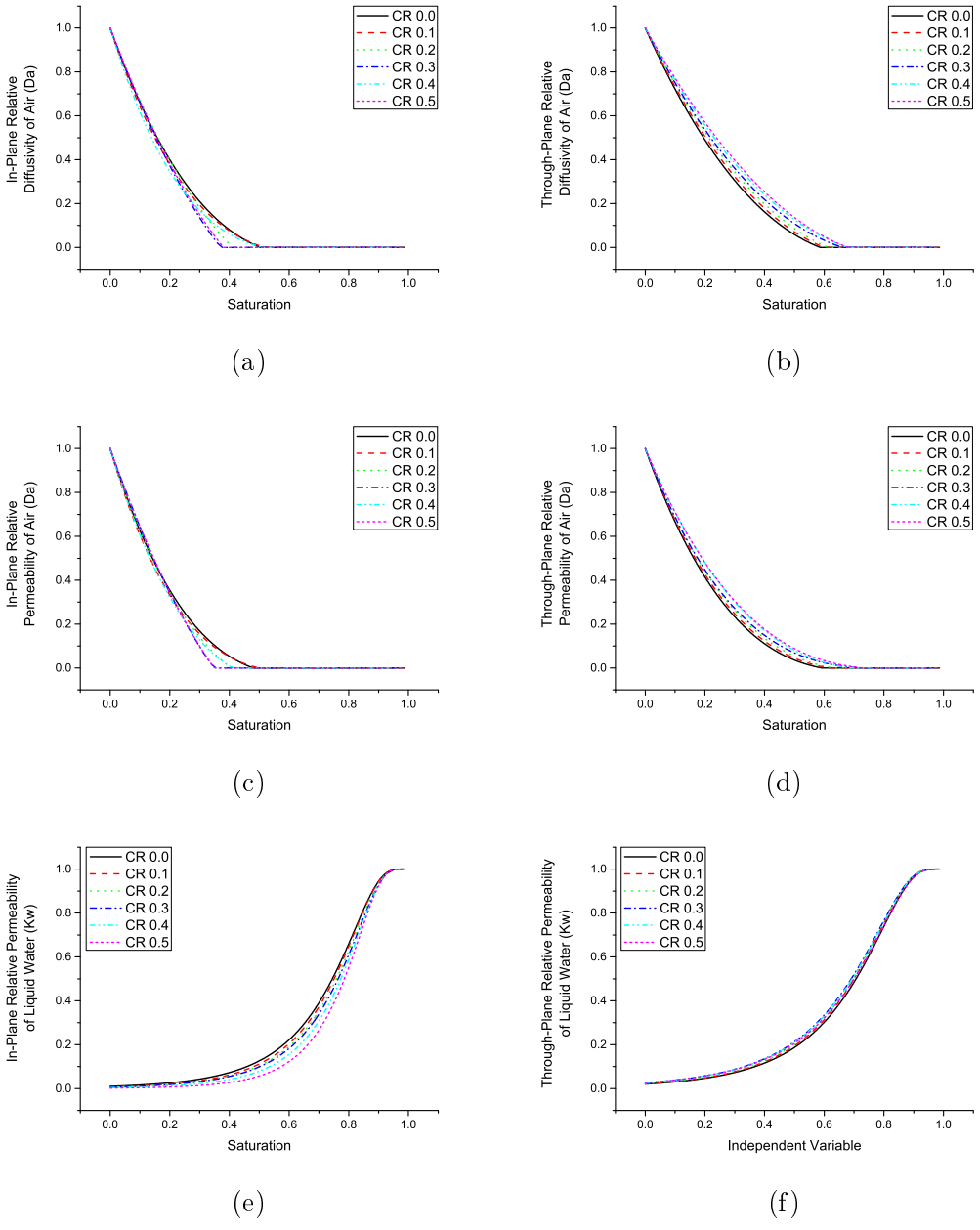

Figure 4.9: All relative transport relations and their dependence on uniform compression ratio.

	Da IP		Da TP	
CR	S_c	n	S_c	n
0.00	0.50	1.84	0.59	1.32
0.10	0.52	2.17	0.60	1.23
0.20	0.41	1.11	0.61	1.11
0.30	0.37	0.95	0.66	1.17
0.40	0.51	2.53	0.68	1.05
0.50	0.38	0.95	0.68	0.95

Table 4.2: Fitted parameters for the relative diffusivity of the air phase in both IP and TP directions using Equation 4.4.2.

	Ka IP		Ka TP	
CR	S_c	n	S_c	n
0.00	0.48	2.23	0.59	2.09
0.10	0.50	2.63	0.61	2.04
0.20	0.41	1.71	0.63	1.93
0.30	0.35	0.96	0.71	2.13
0.40	0.41	2.07	0.69	1.75
0.50	0.35	0.95	0.73	1.84

Table 4.3: Fitted parameters for the relative permeability of the air phase in both IP and TP directions using Equation 4.4.2.

	Kw IP		Kw TP	
CR	a	b	a	b
0.00	1.37	0.83	1.23	0.85
0.10	1.39	0.81	1.20	0.84
0.20	1.42	0.82	1.19	0.83
0.30	1.45	0.83	1.17	0.85
0.40	1.49	0.80	1.18	0.86
0.50	1.54	0.76	1.20	0.88

Table 4.4: Fitted parameters for the relative permeability of the liquid water phase in both IP and TP directions using Equation 4.4.3.

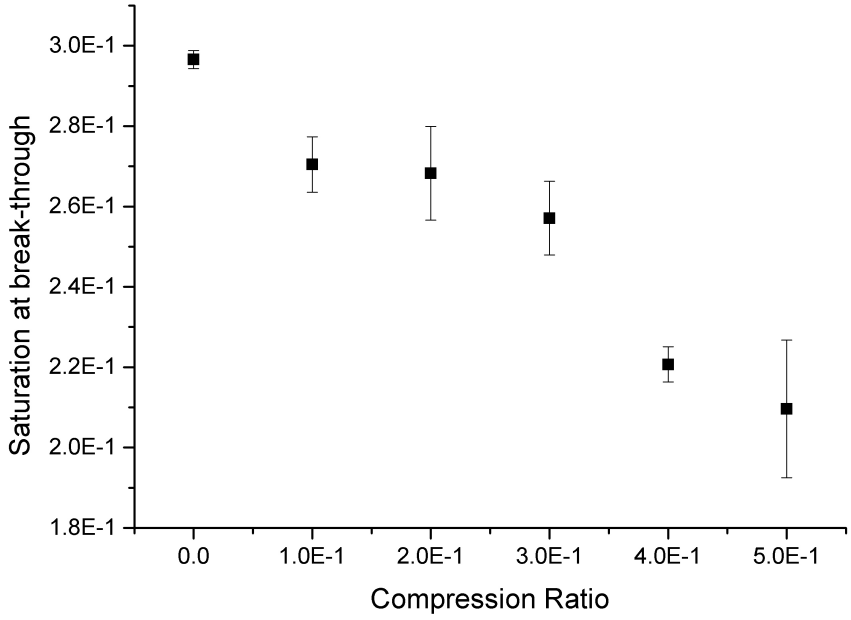

Figure 4.10: Domain saturation at break-through for compressed networks, with error bars of one standard deviation.

If compression induces preferential TP liquid fingering, one would expect lower domain saturation at the point of break-through (i.e. when a liquid cluster reaches the top of the domain), as investigated in Chapter 3. Using the invasion percolation algorithm, which sequentially records each successive pore and throat invasion, it is possible to record the invasion sequence when an outlet pore is first invaded and stop the algorithm to obtain the saturation of the domain at break-through. Figure 4.10 shows the average breakthrough saturation as a function of compression ratio over five realizations randomly selecting 50% of the bottom face pores as liquid inlets. It is clear that the compression of the medium does in-fact reduce the break-through saturation which could enhance air transport, although this effect is counteracted by a general reduction in porosity.

4.4.3 Multiphase transport with IP porosity gradient

The results shown in the previous two sections were produced using uniformly compressed networks. The GDL is not generally compressed uniformly when assembling the fuel cell, as current collector flow fields are grooved and present a series of channels and lands as reviewed by Hamilton and Pollet [12]. The lands make contact with the GDL and reduce the porosity, creating IP porosity gradients. Networks are created with lowered pore density in a central region of the domain with varying width, representing the GDL beneath a channel in the bipolar plate of a fuel cell. The land width to channel width ratio is set at 3:1, 2:1, 1:1, 1:2 & 1:3 and is expressed in the following figures as a channel area fraction. Pores in the channel region are further apart and consequently have larger volumes, so the region has higher porosity.

The influence of the channel area fraction on the breakthrough saturation is shown in Figure 4.11a. There is no discernible pattern and little variation with channel area fraction. There also appears to be little difference in the total saturation of the medium when varying the number of inlet clusters. No attempt to correlate the inlet cluster positions with the position of the lands is made, and only percolation from the bottom face is considered. The reason for the lack of pattern is possibly that two influencing factors are mitigating one another: increasing channel area fraction increases the size of the outlet and so a percolating cluster is more likely to reach the outlet quicker so reduces overall saturation, whereas at the same time the total porosity of the domain also increases and so more water can accumulate in the area below the channel.

The IP saturation profiles produced by our simulations agree well with x-ray computed tomography data collected by Zenyuk et al. [265], conducted ex-situ under isothermal conditions. An example is shown in Figure 4.11b. The bulk of the liquid tends to collect in the higher porosity section of GDL beneath the channel. However, under non-isothermal conditions such as those typically encountered within a fuel cell, the liquid may condense under the cooler rib sections and evaporate where convection is strongest under the channels [266], [155]. Two recent pore network studies that investigated phase change phenomena support

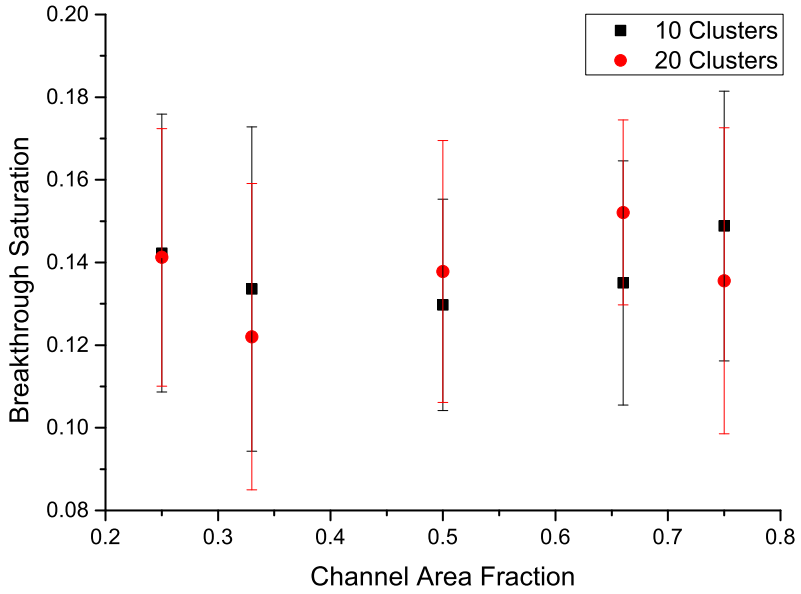

(a) Break-through saturation for non-uniform compression with land-channel boundary conditions and different numbers of clusters. Error bars are one standard deviation.

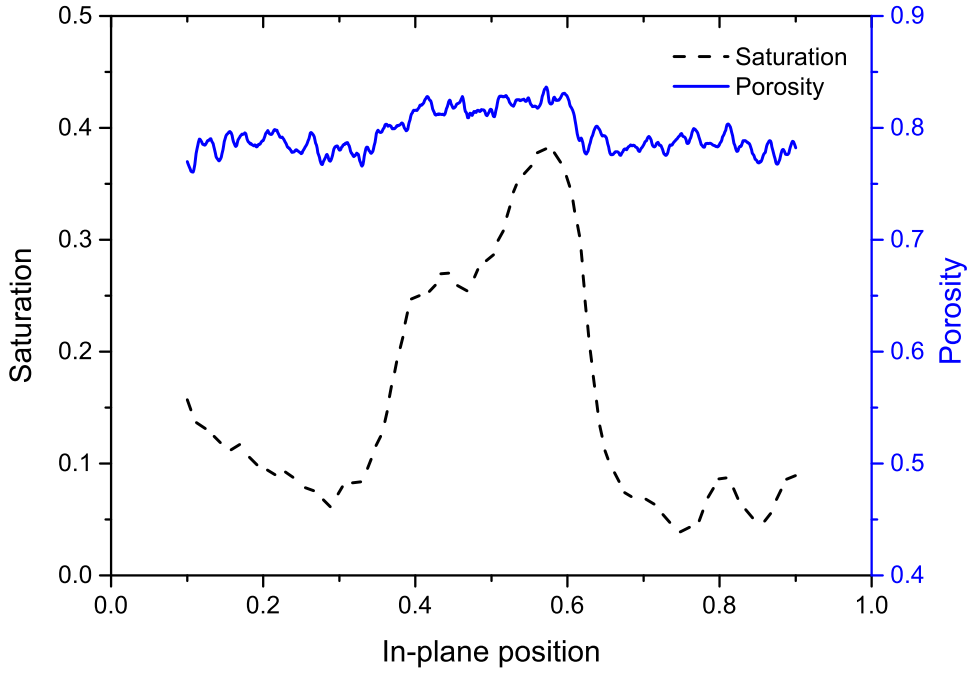

(b) In-plane variation of porosity and saturation for the 1:1 land-channel ratio case.

Figure 4.11: Multiphase plots for non-uniform compression cases.

this hypothesis, but did not account for porosity variation or local pore structure changes due to compression [267], [268]. Further work is required to assess the relative importance of the competing transport effects on the liquid percolation under different operating fuel cell conditions, including realistic porosity distributions.

Figure 4.12 shows the influence of both the channel area fraction and number of inlet clusters on the limiting current. The dry results with no water in the network show that, as the channel area fraction is increased, the limiting current also increases. This result is intuitive, as the area open to flow is increasing, so diffusive flux is greater. Introducing water reduces the diffusive conductivity of the network, as shown in the previous section, but the influence of the saturation distribution also becomes clearer.

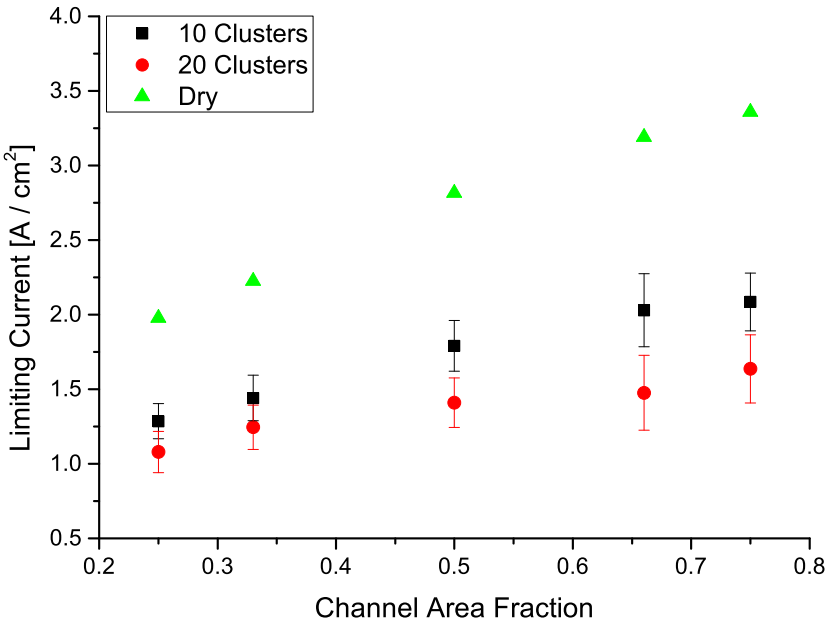

Figure 4.12: Limiting current for non-uniform compression with land-channel boundary conditions and different numbers of clusters. Error bars are one standard deviation

Although the total domain saturation at break-through is relatively similar

for the 10 and 20 cluster inlet conditions, the distribution of saturation is skewed more towards the inlets at the bottom face for the 20 cluster condition, as shown in Figure 4.13. This in turn creates more of a bottleneck for diffusive transport and reduces the rate at which oxygen can flow to the bottom face. Hence the limiting current is reduced compared with the 10 cluster simulations. This situation demonstrates one of the effects of introducing an MPL to the bottom face of the GDL, which acts to reduce the number of percolating clusters, and therefore reduces the bottleneck effect. A recent study by García-Salaberri et al. using the Lattice Boltzmann technique also supports these findings [156]. It would seem that peak saturation is a stronger indicator of fuel cell performance than average saturation, and modelling techniques that can accurately re-produce saturation profiles should be used to predict fuel cell performance. Although our inlet condition is not dependent on the level of compression or position within the domain, one might expect the entry points into the GDL to depend on cracks in the MPL which are more likely to occur beneath the land. Compression is also important for the contact between layers which, if poor, will result in liquid pooling at interfaces leading to severe bottle-necks for air transport as discussed by [269].

4.5 Concluding Remarks

A series of PNMs subject to compression are presented, with good agreement with experimental drainage and single phase transport data. Effective and relative transport simulations are performed, and the effect of compression is shown to reduce effective transport but increase some relative transport, depending on the direction and phase. It is found that compression has a more adverse effect on the IP transport than TP and this can be explained by considering the different structural changes to constrictions between fibres.

In-plane porosity variation under a land-channel-land scenario is shown to affect the liquid percolation pathway with a strong correlation between saturation and porosity. This in turn affects the limiting current achievable with a fuel cell which increases proportionally with the channel area fraction, and decreases with the number of inlet clusters. PNMs are demonstrated as powerful tools capable of characterizing porous materials with great efficiency and accuracy.

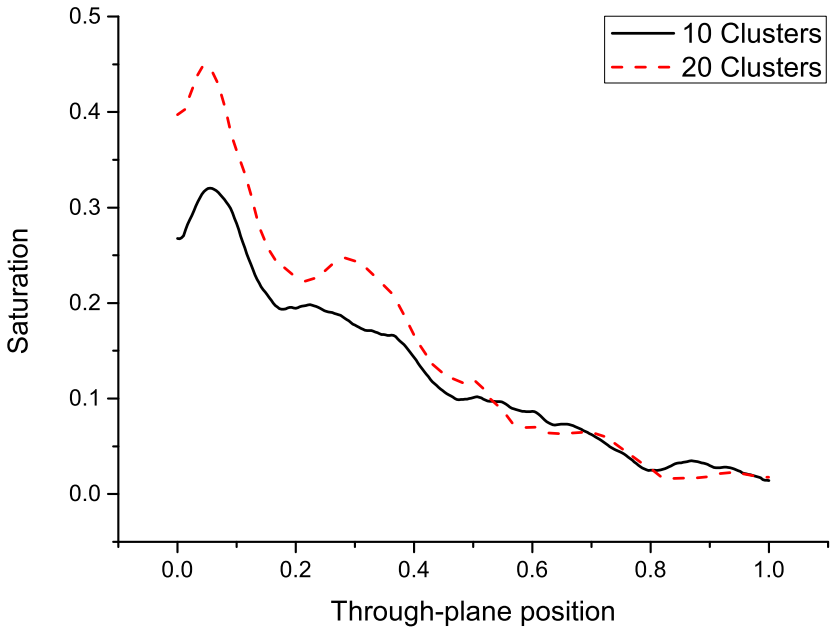

Figure 4.13: Through-plane saturation profile for the different cluster conditions with a channel area fraction of 0.5.

It is recommended that further investigation into the land-channel influence on transport in the GDL is conducted combining the topological considerations presented here and the phase change considerations presented elsewhere. It is hoped that performing simulations with OpenPNM, an open source framework developed as part of this work, will aid future investigations.

Chapter 5

Measuring the Relative In-Plane Diffusivity of Partially Saturated GDLs

5.1 Motivation

Transport in thin saturated porous media is of interest to fuel cell engineers due to the use of thin porous materials known as gas diffusion layers (GDL) in polymer electrolyte fuel cells (PEFC). As described in Section 2.3, water produced by the reaction on the cathode side of the PEFC can form liquid which percolates throughout the GDL, blocking reactant gases and reducing performance through mass transport limitations. The topic of water management in PEFC has been extensively reviewed by Jiao and Li [7]. The GDL has been intensively studied to date, but mostly with respect to single-phase transport properties, [189], [191], [140], [139] and [270]. To reduce stack costs, cell manufacturers aim to increase power density, which in turn increases water production within the cell. Under these conditions, the GDL can become partially filled with liquid water, owing to the percolation from the reaction sites and condensation of water vapour if the relative humidity exceeds the saturation point. If ameliorating mechanisms are not in place, such as purging or heating, the reactant diffusion through the media becomes significantly hindered compared to dry conditions. An understanding of the relative diffusivity, i.e. how gases diffuse through the partially water-filled

porous media, is essential for understanding and improving the performance of the fuel cell. The focus of the previous research chapters has been numerical investigations of the effects of compression on multiphase flow in PEFC GDL. The present chapter aims to provide a method for experimentally investigating the relative diffusivity of such materials, and aims to help validate the modelling work.

In Section 2.6.1 the atypical properties of common GDLs, compared with traditionally studied porous material such as rock and soil, were introduced. The most common material used for GDLs is a carbon fibre paper that exhibits highly anisotropic transport characteristics. Fibres have a high degree of in-plane (IP) alignment, increasing transport in this direction compared with through-plane (TP). The TP direction tends to be the focus of studies, as this is the principle direction of transport within the PEFC between the gas distributor plates and the reaction sites. However, IP transport is also important for distributing gases beneath the flow-field ribs, facilitating a more uniform current-density across the cell, and increased durability [216], [210]. To make the GDLs more hydrophobic, and therefore improve water management, they are often treated with a coating of PTFE. Flückiger et al. showed that PTFE treatments reduce diffusive transport by occupying and blocking the pore pathways [140], but this reduction is a worthwhile trade-off since it prevents liquid water from spreading within the GDL where it would completely block gas diffusion.

A review of the experimental and modelling techniques used to characterize the diffusive transport in PEFC materials is presented by Ismail et al. [53]. Numerous techniques have been employed to measure the dry diffusivity in both IP and TP directions. Researchers have used electrochemical impedance spectroscopy (EIS) to measure the ionic transport in an electrolyte soaked GDL, and by analogy diffusive transport [271], [139], [208]. In-situ techniques can also be applied to diagnose mass transfer in running fuel cells, including EIS and limiting current measurements [190]. However, knowledge and/or control of the water saturation becomes very difficult. The EIS technique can also be applied to partially saturated porous media, as demonstrated by Chevalier et al. [272], in a fashion similar to limiting current. The liquid content was measured with x-ray radiography, then modelling was used to determine the contributions of each component

to mass transfer resistance. Another method for measuring effective diffusivity is the Loschmidt cell, which measures the transient concentrations of a mixture within two chambers separated by a porous sample or controllable barrier [273], [192]. This method has not been applied in the IP direction, although the approach presented by Rashapov et al. [5] is similar, where a step change in oxygen concentration boundary conditions is applied, and the transient response along the sample is measured. This is the method adapted for studying the IP relative diffusivity of partially saturated GDLs in this chapter.

To date, only a few other studies have succeeded in measuring the diffusivity in GDLs under conditions of variable water saturation [18], [198], [200], and employ an oxygen sensor that creates the concentration gradient itself by consuming the oxygen. These studies all focused on the TP direction and are unsuitable for IP measurements since they require the use of a reactive layer on one face of the GDL to consume the transferring species resulting in a TP diffusive flux. Due to the very thin nature of the GDL, it would be impractical to coat such a layer onto the IP face. Numerous studies have approached the problem by modelling transport using direct numerical simulation on images of the GDL microstructure. Becker et al. obtained tomographic images of dry GDL, then simulated water invasion using morphological image opening, followed by diffusion calculations in the remaining gas space [252]. The problem with this approach is that simulating water invasion in mixed wettability, fibrous, anisotropic media is not trivial, and usually relies on the use of spherical elements. García-Salaberri et al. performed Lattice-Boltzmann simulations on tomographic images with water injected during imaging, hence providing realistic invasion patterns [156]. A key finding of that work and the subsequent work [274] was that global average water saturation was not a good indicator of diffusive resistance, a conclusion also supported by the findings of Chapter 4. García-Salaberri et al. found that the presence of saturation gradients undermined any attempts to extract generalized trends about relative diffusivity and also recommends that diffusion measurements, for use in continuum models, are made under conditions of uniform saturation profile.

The aim of the present chapter is to demonstrate an experimental methodology, which could be applied to any thin porous media, to evaluate the relative IP diffusive transport in the presence of water-filled pores. The method utilizes

an oxygen sensor placed inside a custom-built sample holder that enables the control of temperature and oxygen concentrations at the outer boundaries of the samples. Saturation is carefully controlled and regulated by keeping the water in a state close to freezing. The transient response to a step-change in oxygen concentration at the boundaries is used to calculate diffusivity using Fick's second law. The present study is the first to experimentally examine the IP diffusive transport through the GDL as a function of water saturation.

5.2 Method

5.2.1 Experimental Set-up

The method for measuring the diffusivity of the porous material is based on that of Rashapov et al. [5], [46]. The transient response to a step change in oxygen concentration at the boundaries of the sample is monitored at a fixed point in the sample with an optical oxygen sensor (OceanOptics FOXY-Neofox®).

The previous method set the initial oxygen concentration throughout the sample to zero by purging it with nitrogen and then removing the gas supply, thereby manually returning the boundary conditions to atmospheric concentration of 20.9%. This method was avoided in the present work because the pressure from the purging would possibly disturb the liquid configuration and cause evaporation, thus adding uncertainty to the calculated saturation values. Instead, slow purging was used by flowing gases past the ends of the sample at a low flow rate (50 sccm) and waiting for the sample interior to equilibrate with the end conditions via diffusion. A sample holder with small chambers next to the sample ends was constructed for this purpose, and a schematic diagram of the experimental set-up is shown in Figure 5.1.

Boundary conditions were controlled by combining nitrogen and air with mass flow controllers and flowing the gas mixture past the end(s) of the sample. The holder was partially constructed with a 3D printer (B9Creator) to enable the design to include a serpentine cooling channel. This was required for more precise temperature control to ensure that samples retained their saturation throughout the experiment. The cooling channel design is shown in Figure 5.2a. The

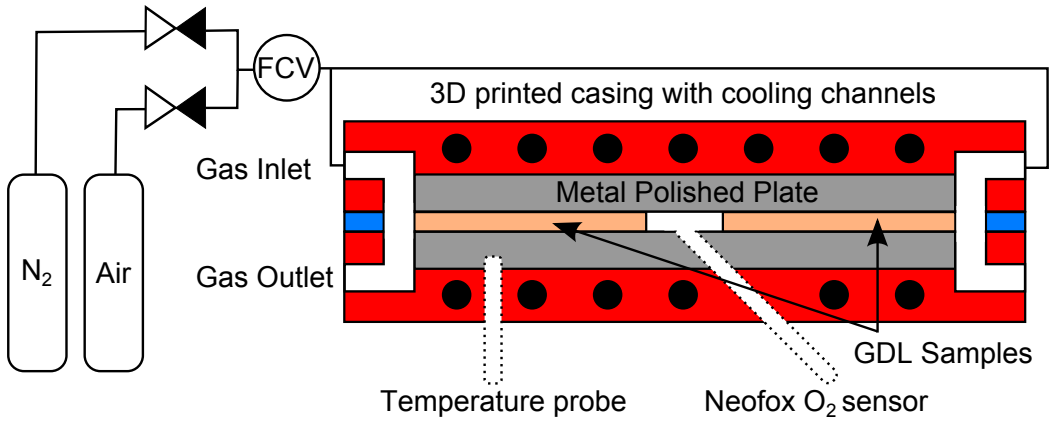

Figure 5.1: Schematic Diagram of Experimental Setup.

temperature was regulated by constantly pumping cooling fluid with a Fisher Scientific Isotemp 3006D refrigerated circulator set to $-10°C$. With the apparatus exposed to the laboratory atmosphere at room temperature, it was necessary to measure the temperature of the holder as close to the sample as possible. A hole was drilled into the under-side of the sample holder to a depth 1mm from the inner surface, and a mineral insulated thermocouple was inserted and fastened with epoxy resin. The temperature recorded was between $-1°C$ and $+2°C$ at all times. The longest experiments lasting over an hour, with several changes of oxygen concentration, were found to have transient responses that remained constant, proving that sample saturation was maintained. The state of water could not be verified visually, however, the temperature range measured for the holder meant that water was either in a frozen state, or very cold with a small vapour pressure.

The samples were sealed between two steel plates with the printed cooling plates sandwiched on each side. The steel plates were polished to a mirror finish to eliminate surface roughness and any bowing of the surfaces of the plates. This ensured that even contact was made with the sample surfaces. Rough or uneven surfaces would have allowed additional diffusional pathways and introduced systematic errors. Pliable putty was used to encircle the samples and the boundary gas chambers as a sealant, and was rolled by hand to a thickness of about 1 mm. Care was taken to ensure that the putty was rolled evenly and was placed

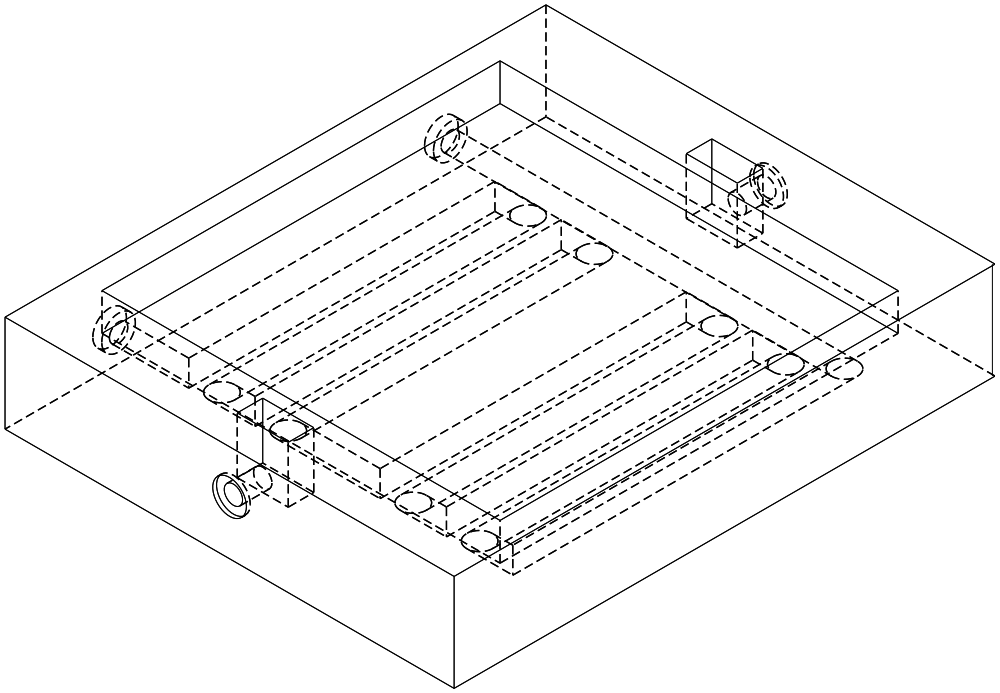

(a) Isometric view of 3D printed holder part with cooling channels.

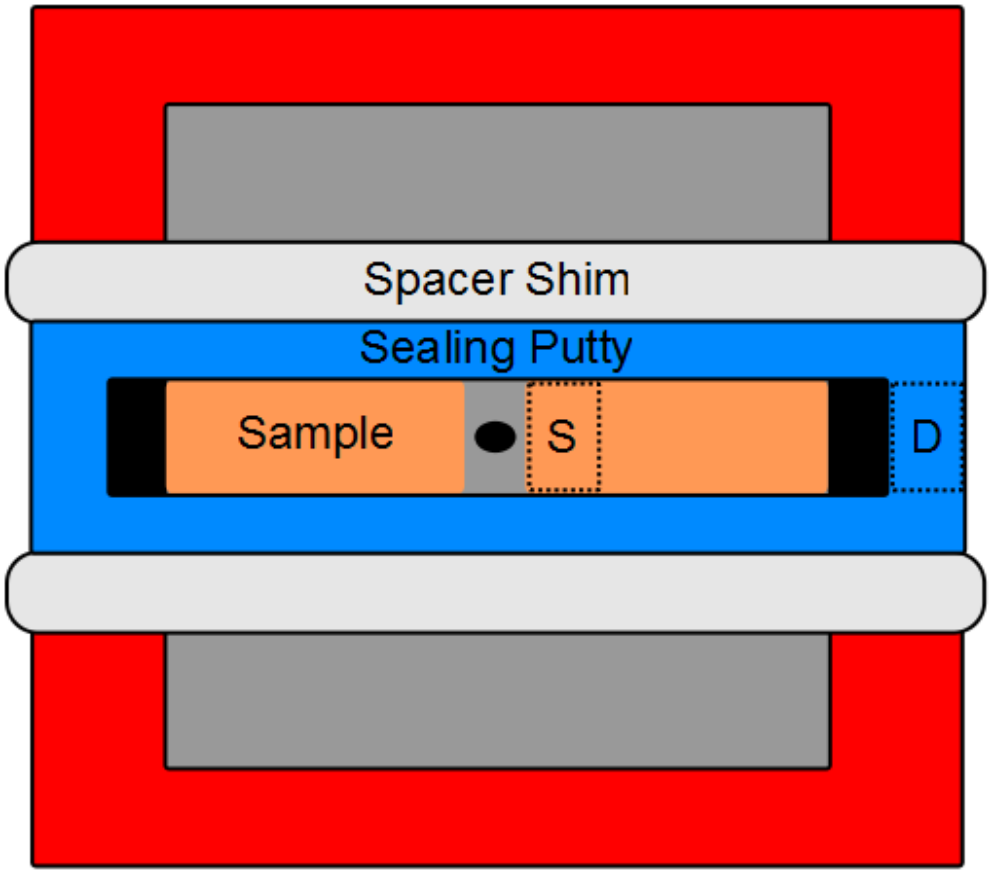

(b) Top-down view of the bottom plate of the sample holder.

Figure 5.2: Views of the custom sample holder

as close to the samples as possible to prevent air gaps along the sample length. The putty was found to be a more reliable sealing material than a gasket which needed to be cut with high precision and did not provide easy variation in height when samples of different thickness were tested.

5.2.2 Sample Preparation

Samples were cut to a length of either 35 or 70 mm, for the single or double-ended set-up, and weighed while dry. They were then submerged in a beaker of de-ionized water (18 MΩ) and vacuum pumped for several minutes to remove any trapped gas. The samples were then dried on a mass balance to a predetermined target weight to achieve the desired saturation (S), defined by the following expression:

$$S = (M_{wet} - M_{dry})/(\epsilon V \rho_{water}) \tag{5.2.1}$$

where M_{wet} and M_{dry} are the mass of the samples when wet and dry, ϵ is the sample porosity which were measured in a previous study [46], V is the volume of the sample when compressed by the holder and ρ_{water} is the density of water. The process of drying water from a hydrophobic media is equivalent to air imbibition, which is known to be less influenced by surface effects and access limitations due to the formation of thin films by the wetting fluid [9]. Consequently, this water configuration within the GDLs is expected to be more uniform, and is preferred over injecting liquid water from the surface, as pointed out by García-Salaberri et al. [156], [274]. The effect of compression on the flow behaviour of the samples was not investigated in this work and is left for a future study, so the spacer shims were chosen with a thickness similar to that of the samples to avoid any reduction in pore space when clamping and sealing the experiment.

A top-down view of the sample sitting on one of the holder plates is shown in Figure 5.2b. The shims were placed about 10 mm from the samples in order to let the putty expand away and not intrude into the sample. Samples were not placed directly on top of the sensor to prevent the formation of ice on the tip which would have impeded the measurements. The experiments were conducted in one of two equivalent (i.e. symmetrical) arrangements. These are single and double-ended, with the position of the putty marked with an 'S' and 'D' in Figure

5.2b, respectively. For the double-ended arrangement, gas was flowed past both ends of the sample, which was cut in half and placed on each side of the sensor. Alternatively, gas was only flowed past one end of the sample while the other was blocked, in which case the sample was only placed on one side of the sensor. In both cases the sensor was located at the no flux position in the domain, and the mathematical treatment was identical, with minor differences in the domain length and relative position of the sensor. The advantage of the single-ended arrangement is to ensure that pressure differentials do not exist across the sample, so that all transport can be attributed to diffusion. Results repeated for both scenarios yielded similar diffusive coefficients, giving confidence that convective flow does not occur in either case. In future, the double-ended set-up could be used to simultaneously measure diffusivity and permeability with the appropriate sensors.

5.2.3 Calculation of the Effective Diffusion Coefficient

The following analytical solution to Fick's Second Law, given by Crank [275], was used previously to find the effective diffusion coefficient, D, of the GDL by fitting the following equation to the experimental data using D as the only fitting parameter [5]:

$$\frac{C(t)-C_0}{C_1-C_0} = \sum_{n=0}^{\inf}(-1)^n \frac{(2n+1)l-x}{2\sqrt{Dt}} + \sum_{n=0}^{\inf}(-1)^n \frac{(2n+1)l+x}{2\sqrt{Dt}} \tag{5.2.2}$$

with initial and boundary conditions

$$C(t=0) = C_0 \tag{5.2.3}$$

$$C(x=\pm l) = C_1 \tag{5.2.4}$$

Equation 5.2.2 is valid for homogeneous samples which was the case with the previous experiment [5] as the GDL filled the entire sample space. However, this approach was not valid for the present study, due to the composite domain created by the air gap around the sensor. Instead the experiment was modelled

as a one-dimensional diffusion process through each section using finite element analysis with FiPy [276]. In the air gap around the sensor the bulk diffusivity of oxygen in air was used as the diffusion coefficient. The surrounding section(s) containing sample were assigned an initial guess for the diffusivity of the GDL, and the SciPy optimize package [249] was used to find the effective diffusivity for the sample by minimizing the square of the residuals of the error between the experimental and transient response simulated by the finite element code. The sensor captures data every second and the longest experiment typically lasts for around 1000 seconds. The transient diffusion equation was solved implicitly with a time-step of 0.25 seconds, so the longest simulations must solve the equation up to 4000 times per iteration. The optimization always converged within 15 iterations to an R^2 value of greater than 0.995 and the whole solving process lasted no longer than 2 minutes per data set. The code used for the fitting process is detailed in Appendix B.

Other studies monitoring transient diffusion through multiple layered materials or inhomogeneous spaces have employed an equivalent resistance assumption. Diffusivity of the individual components is then extracted through a resistors in series calculation [277]. This assumption introduces significant error to the calculation of the component diffusion coefficients, especially when the diffusivity of the different sections differs significantly, or the lengths of the different sections are comparable, so that no one material dominates the process. The problem is highlighted by observing the difference between the numerical and analytical solutions for transient diffusion using an equivalent resistance in Figure 5.3. Figure 5.3a shows that, for a homogeneous domain, the solutions match each other, and Figure 5.3b shows that there is a significant difference between the solutions when modelling a composite domain. The model is representative of the double-ended arrangement with a central section with higher diffusivity than the surrounding sections. Transient diffusion through composite material is a tricky subject, summarized by Crank [275], where elaborate equations describing the time lag for concentration changes have been provided for special circumstances. Other forms of analytical solution are available such as those using eigenfunctions [278]. However, given the computational efficiency of the current procedure it seems

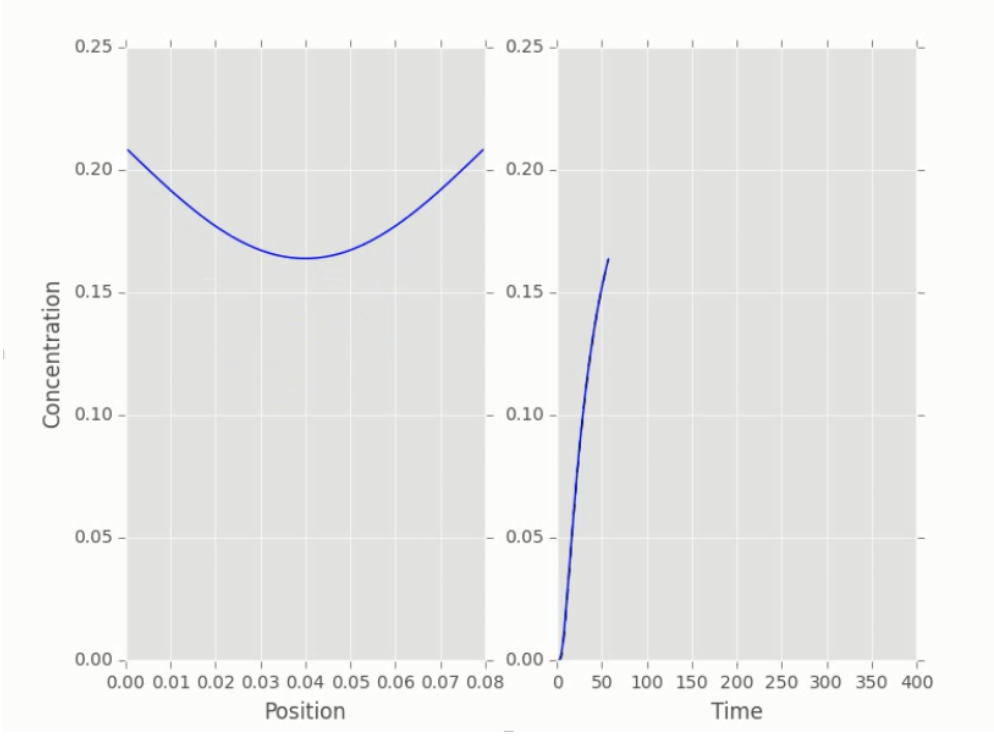

(a) Numercial and analytical solution for homogeneous domain.

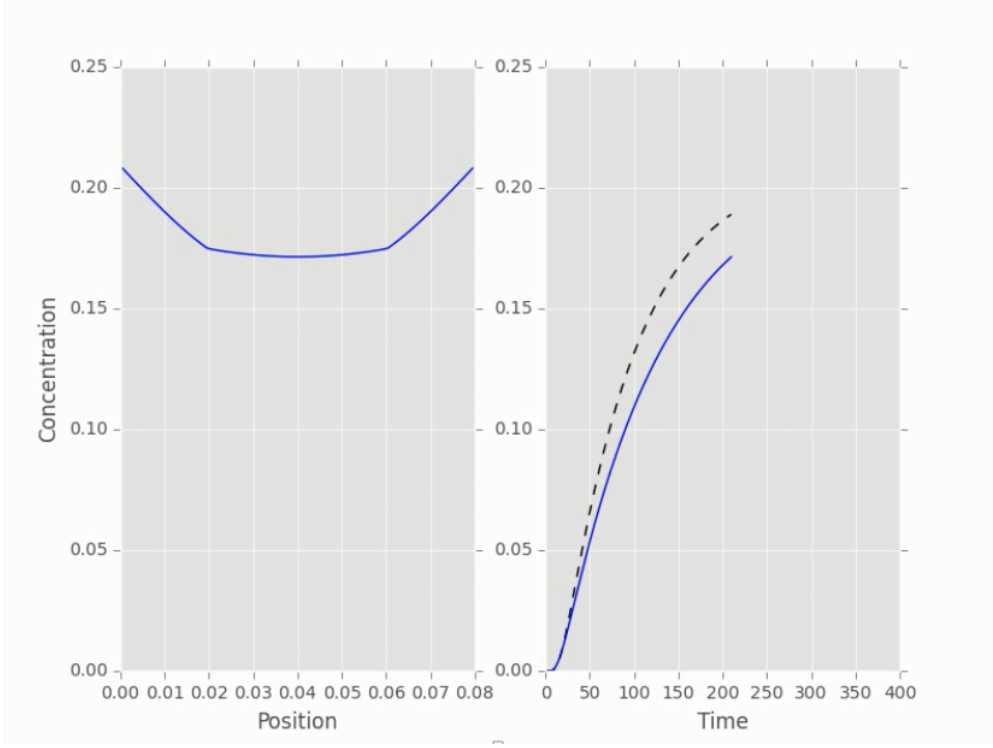

(b) Numercial and analytical solution for composite domain with different diffusion coefficients.

Figure 5.3: Comparison of the numerical and analytical solutions for transient diffusion in a 1D domain with homogeneous (a) and composite varied diffusivity (b). Concentration across the sample is shown on the left and the transient change at the sensor is shown on the right.

to be adequate. The script used to fit the data is provided as supplementary material.

The bulk diffusion coefficient can be calculated at any temperature, given that it is known for one temperature by the following relation [279]:

$$D_{T_2} = D_{T_1}(T_1/T_2)^{1.75} \tag{5.2.5}$$

As it was not possible to conduct each experiment at exactly the same temperature, due to fluctuations in room temperature and exposure to the atmosphere when changing samples, the temperature of the holder was monitored, and the calculated diffusion coefficients were adjusted for temperature. However, the uncertainty due to temperature fluctuations, and the possibility that the temperature of the flowing gases is not equilibrated with the sample holder, is likely to be very small, and also systematically cancelled out by normalizing the results under the same conditions.

Where previously the holder was fastened together using screws with a controlled torque, for this experiment a framework was constructed with a hydraulic piston that pressed the pieces together, as shown in Figure 5.4. This was primarily done to avoid screwing into the 3D printed plastic which could fracture, but also sped up the changing of samples. The outer surfaces of the sample holder were also sanded to ensure good contact and even compression. However, some fine adjustment was sometimes needed by placing additional material between piston and holder. The firmness of the seal was assessed by trying to move the shims which protruded from either end of the holder. If good even compression was achieved then neither shim would move. An additional gas-tight test was conducted by running nitrogen past the sample until zero oxygen concentration was established, then closing the outlets at both ends. Any increase in oxygen reading indicated the presence of a leak. Unfortunately a very slow leak was present for all the tests which was established to be from the fittings for the gases into the printed holder parts. Although useful for prototyping and fast production, the 3D printed material was not ideal for tapping and fastening gas fittings due to its brittle nature. This meant that permeability tests were not possible with the current apparatus, but diffusion tests that are normalized by the dry result

effectively have the systematic error cancelled out, so are still valid providing that the flow rate is kept constant throughout each experiment. The apparatus leak also meant that a truly zero oxygen concentration could not be established at the boundaries. However, the diffusivity is calculated from the transient change in concentration, and this is independent of the actual boundary values, which simply serve to scale the concentration at any given point in space or time according to Equation 5.2.2.

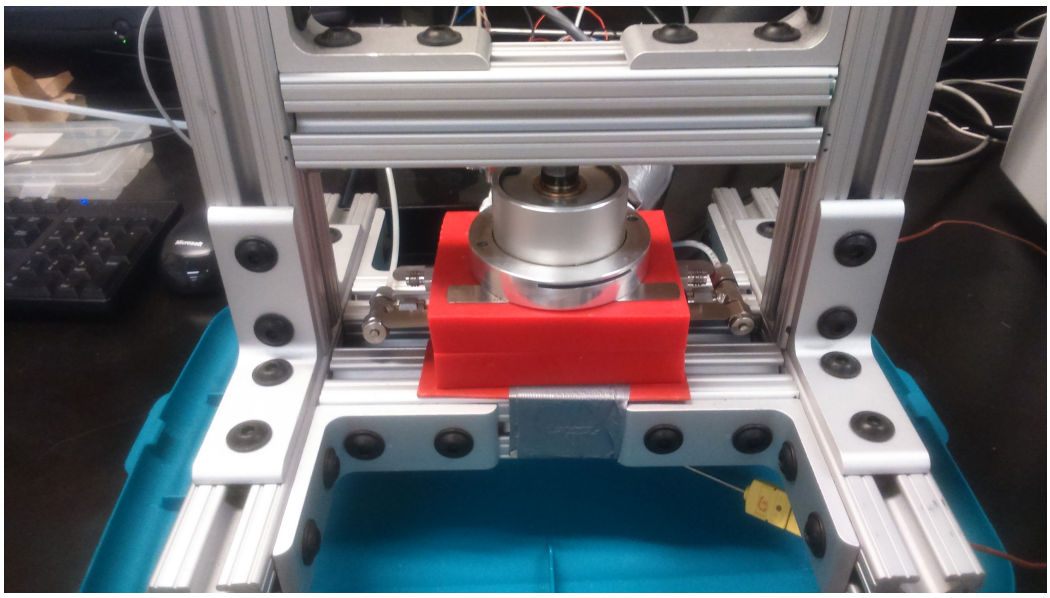

Figure 5.4: Picture of the apparatus including framework and piston for compression sealing the sample holder.

5.3 Results and Discussion

Five different GDL materials were investigated to assess whether structural differences and PTFE coating made a significant difference to the relative diffusivity. The characteristics of the samples, as measured by Rashapov et al. [46], and fitted relative diffusivity data are shown in Table 5.1. Figures 5.5, 5.6 and 5.7 show the normalised fitted diffusion coefficients for the various samples. The data is multiplied by a factor of $(1 - S)$, to account for volume reduction, and

resulting saturation functions are fitted to both Equation 2.2.12 and the following expression, commonly used in the literature:

$$g(S) = 1/2(1 + erf[(-ln(S) + a)/b]) \tag{5.3.1}$$

The data presented is the average result for a number of experiments on a single sample collected with different boundary condition changes. In each case, the mass flow rates of the gases were altered to change the concentration of oxygen flowing past the sample ends and the system was left to reach steady state. The purpose of repeated measurements on the same sample was two-fold. Firstly, the sensor does not measure concentration directly but a phase-shift in a fluorescent response of the coating material on the sensor tip to a pulsed excitation. This phase shift is temperature dependent, so in-situ calibration was possible using the various steady-state concentration values. Secondly, for some cases, the calculated diffusivity was found to be different when switching from high to low oxygen concentration boundary conditions and vice versa. This was an indication of a leak, with atmospheric oxygen penetrating the sample holder, thus providing additional diffusion pathways to the sensor. These anomalies were due to inadequate positioning of the sealing putty and results with inconsistent diffusivity were discarded. The raw data for SGL 10 BA and Toray 120 was collected by Pavel Stogornyuk, an undergraduate at McGill University, under the present author's guidance. However, development of the methodology and the collection of all other datasets and interpretation of every dataset was entirely the work of the present author. In all cases the error bar on saturation is an estimated uncertainty based on the propagated uncertainty in sample dimensions and uncertainty in porosity from [46].

The material properties of the uncompressed materials are presented in Table 5.1. During the experiment it was necessary to compress the materials slightly to seal the gases and the compressed properties are shown in Table 5.2. Also included in Table 5.2 is the dry diffusivity values and a comparison to the same manufacturers samples in the literature. The results for this experimental setup agree well with those collected by Rashapov et al. [5], [280] using a similar setup where the sample ends were exposed to the atmosphere rather than flowing gases.

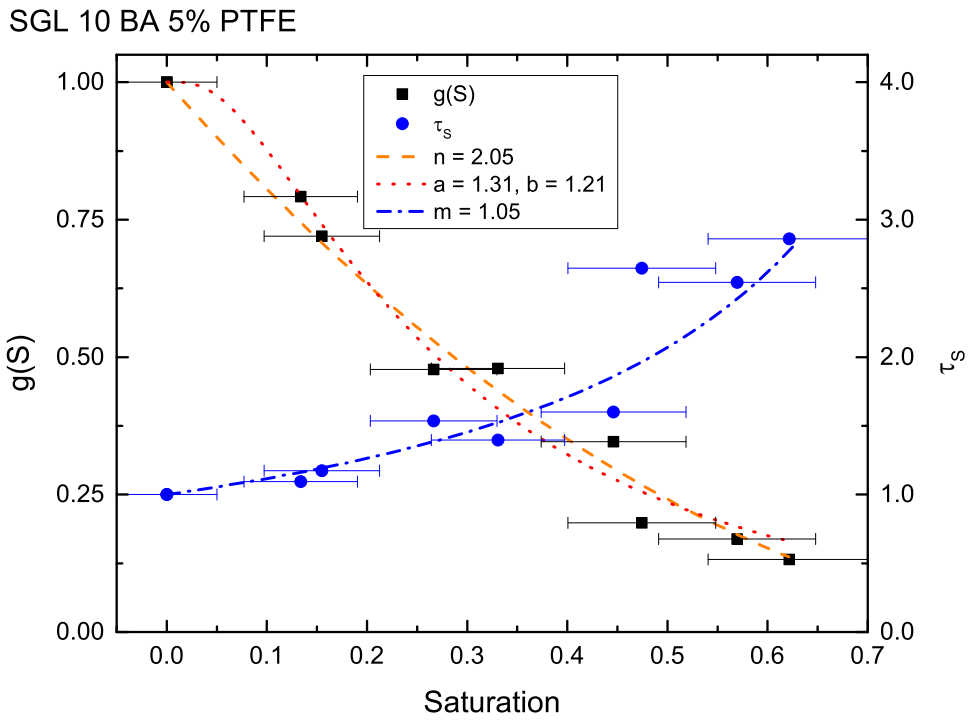

(a)

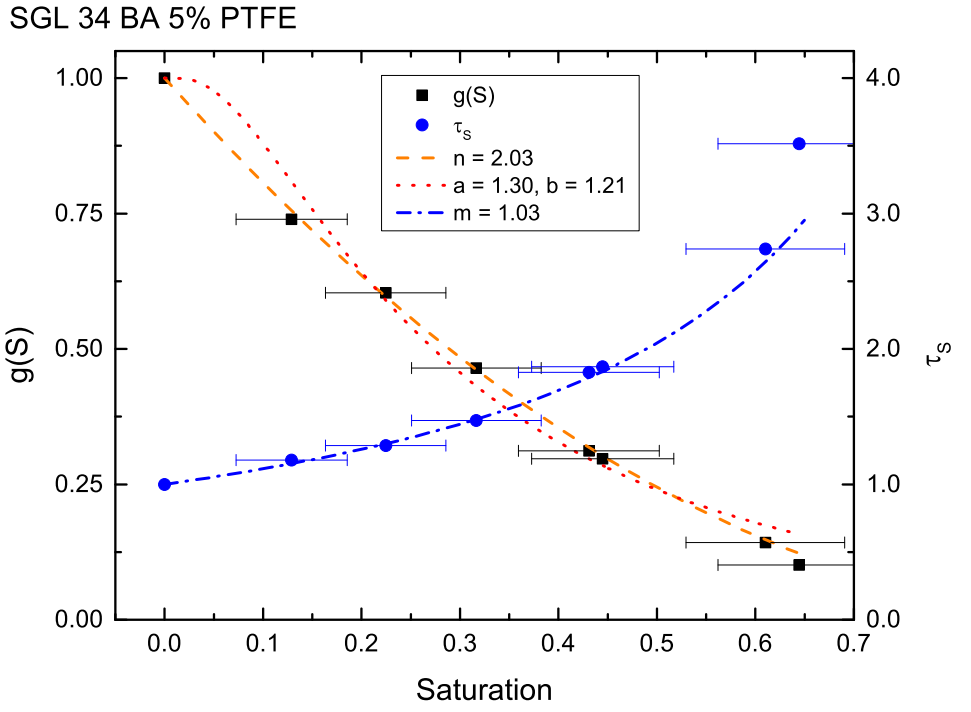

(b)

Figure 5.5: Results for the SGL GDLs showing $g(S)$ data fit to both equations 2.2.12 and 5.3.1 and τ_S.

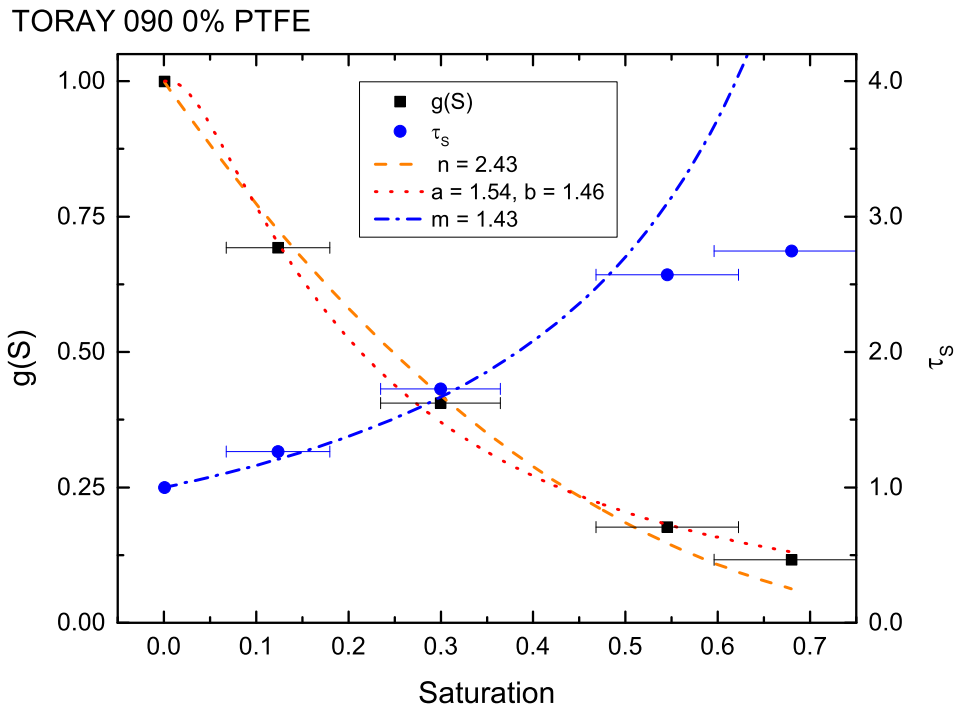

(a)

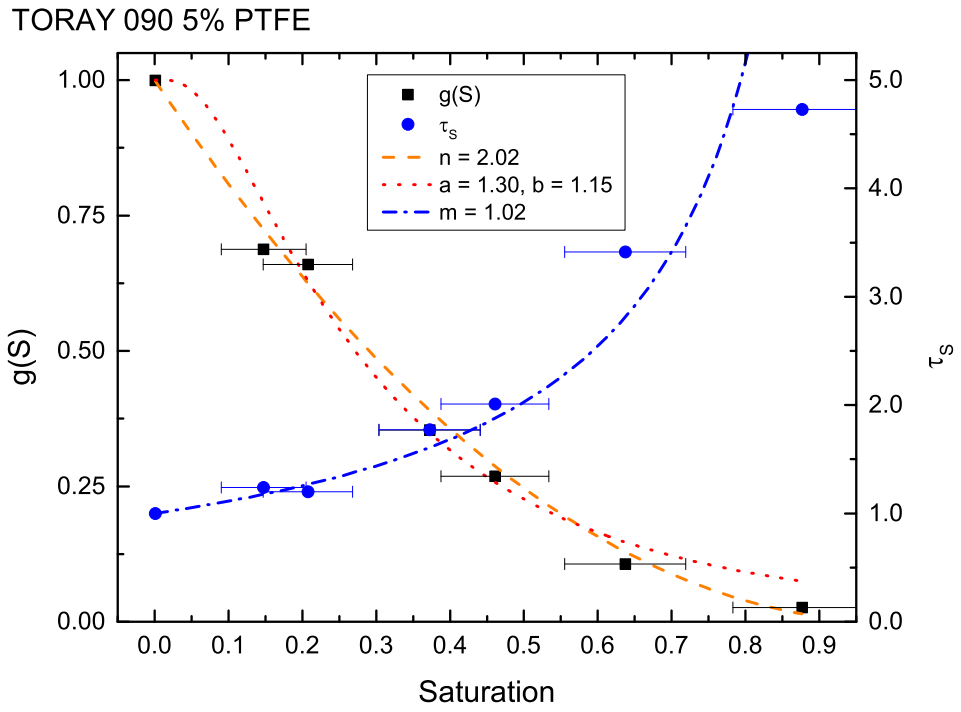

(b)

Figure 5.6: Results for the Toray 090 GDLs showing $g(S)$ data fit to both equations 2.2.12 and 5.3.1 and τ_S.

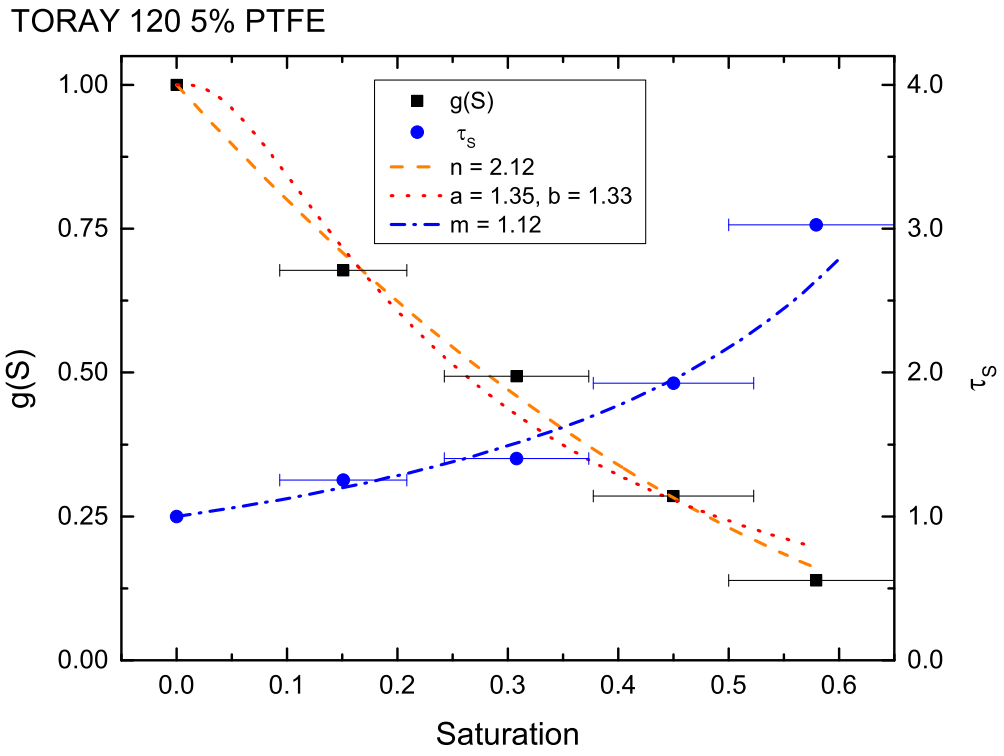

Figure 5.7: Results for the Toray 120 GDL showing $g(S)$ data fit to both equations 2.2.12 and 5.3.1 and τ_S.

However, a study by Mangal et al. [187] reports values for dry diffusivity for Toray 090 which are about 40% lower, when comparing values using the compressed porosity. The reported sample thickness and uncompressed porosity values differ between studies and so the reported compressed porosity corresponds to different compression ratios which may account for some of the difference, as well as sample variation and possible material degradation. The SGL values reported in the present study agree well with the literature. However, the present Toray 120 value agrees well with the study of Hwang and Weber [18], who recorded through-plane values, but less well with Rashapov et al. [280], who reported in-plane values. This is a somewhat puzzling result, given that the Toray 090 results agreed so well. We can, at this time, only attribute the difference to material variability.

A summary of the fitted parameters for all the results is also shown in Table 5.3. Overall, there is little difference between PTFE treated samples with power-law exponents all close to 2. The results agree with simulated results from both pore network models (PNM) [15], [69] and Lattice Boltzmann models (LBM) [155], [156], as well as theoretical predictions [281], [282]. The exception is the sample with no PTFE added (Toray 090), which has a higher exponent, signifying decreased transport with higher saturation. The observed difference between treated and untreated samples, though modest, might indicate the partial filling of pores in the more hydrophobic samples, allowing air to diffuse around the water through the interstitial space in the unfilled corners.

Sample	Name	PTFE Content	Porosity	Thickness
A	SGL 10 BA	5.0	0.871 ± 0.006	423 ± 13.7
B	SGL 34 BA	5.0	0.827 ± 0.008	284 ± 12.0
C	Toray 090	0.0	0.745 ± 0.008	280 ± 9.0
D	Toray 090	5.0	0.719 ± 0.010	262 ± 9.6
E	Toray 120	5.0	0.746 ± 0.007	364 ± 8.5

Table 5.1: Uncompressed material properties.

Material	Shim Thickness	Compressed Porosity	Dry Normalized Diffusivity	Literature Value(s)
A	406	0.866 ± 0.039	0.47 ± 0.03	0.463 [18]
B	254	0.807 ± 0.036	0.54 ± 0.04	0.53 [280]
C	254	0.719 ± 0.032	0.52 ± 0.04	0.54 [280], 0.31 [187]
D	254	0.710 ± 0.032	0.51 ± 0.04	0.56 [280]
E	305	0.697 ± 0.031	0.34 ± 0.02	0.49 [280], 0.325 [18]

Table 5.2: Compressed properties and dry diffusivity normalized by open air value with comparison to literature.

Material	n	a	b
A	2.05	1.31	1.21
B	2.03	1.30	1.21
C	2.43	1.54	1.46
D	2.02	1.30	1.15
E	2.12	1.35	1.33

Table 5.3: Materials used in this study with fitted exponents using the g(S) relations.

5.3.1 Comparison to Literature

The relative diffusivity power-law exponents measured in this chapter are similar to the PNM of Nam and Kaviany [15] constructed from overlapping squares. The PNM considers edge and face diffusion and the connectivity of liquid water clusters. As porosity reduces, edge diffusion between adjacent fibres becomes more important, but liquid connectivity does not appear to affect the IP diffusion as saturation increases. The TP flow is shown to be less than the IP flow with increasing saturation, with an exponent of 3 or 4 depending on the cluster connectivity. This is because the fibre alignment in the IP direction reduces tortuosity. Nam and Kaviany described the connectivity of the liquid phase as being a mixture of randomly dispersed and correlated pillar-like shapes, where a fully correlated scenario would result in straight pillars and a linear relationship between transport and saturation. The PNM of Gostick [69] predicts that, as saturation increases, TP diffusional transport will become more hindered than

IP transport, and utilises a random network generated from a Voronoi Diagram that generates a realistic fibrous structure. The structure is scaled so that fibres have some IP alignment which appears to promote IP liquid spreading. Liquid is invaded from the bottom face and appears to stratify, so that the saturation distribution is skewed towards the bottom face in the TP direction, but relatively uniform in the IP direction. The spreading of water into a liquid plane impedes transport through that plane and this increases the relative diffusivity exponent. The Lattice Boltzmann simulation of García-Salaberri [156] highlights the influence of saturation distributions on the TP transport where bottlenecks can be created by liquid planing along the fibre direction. This results in different transport regimes for different levels of saturation, so that the relative diffusivity exponent actually depends on, and increases with, average local saturation. The study highlights the problems involved with using an average saturation to calculate the transport properties. The IP relative diffusion, however, does not suffer as badly as the TP and remains with exponents between 2 and 3 for all local saturation values. This is possibly because bottle-necks in the IP direction are less likely when the domain is not subject to compression or IP porosity gradients.

The results for a TP study of relative diffusivity conducted by Hwang and Weber tend to fit well with Equation 2.2.12 using an exponent of 3 for samples without any PTFE treatment [18]. However, in PTFE treated samples, Equation 5.3.1 was a better fit to their data, as it accounted for an initial region at low saturation where the normalized effective diffusivity remained close to 1. The explanation given by them is that PTFE coating hinders liquid transport, leading to good phase separation and better gas phase conductivity. Their data show large scatter between samples coated with different amounts of PTFE. However, a significant variation is consistently observed between samples with and without PTFE, indicating that PTFE does indeed improve gas phase transport at a given saturation level. The impact of PTFE was not nearly as substantial for the present study. Equation 2.2.12 fits both treated and untreated materials equally well and no delayed onset of diffusion resistance was observed at low saturations. The exponent for Equation 2.2.12 was slightly higher for the untreated sample (n=2.43 compared to n=2.01), so PTFE does seem to improve IP relative diffusivity slightly.

The added material tend to form planar structures along the fibre direction collecting at fibre intersections, which are more common for Toray papers in the IP direction as has been shown [140], [277]. Also, depending on the drying method the distribution of PTFE can be concentrated at the TP surfaces leaving the bulk of the material free of PTFE [283], [284], [285]. The results suggest that the morphology of the binder and PTFE and its tendency to form planar structures influences the liquid transport and cluster formation differently for TP and IP transport.

Modelling of the single-phase transport properties of GDLs with binder and PTFE structures has been conducted by El Hannach and Kjeang [286]. Stochastically generated non-overlapping cylinders were used as the base structure and binder was built up from sections of the pore space next to fibrous intersections. PTFE was added in a similar manner but was only applied to the top and bottom surface regions of the domain. Three sub-domains are generated with low, average and high porosity with the low porosity displaying strong fibre alignment due to the condition that fibres are non-overlapping. The authors state that the impact of PTFE loading on IP properties is almost negligible, whereas TP properties (diffusivity and permeability) decrease by 10% to 40% depending on the initial porosity of the base structure. To the authors knowledge, no multi-phase simulations have been conducted that incorporate the different material types and structures present within a PTFE treated GDL but the experimental results presented in this study and by Hwang and Weber [18] would suggest that PTFE influences liquid transport in the TP direction creating good phase separation but does not influence the IP transport in the same manner, possibly due to the banding of the PTFE at the surfaces or the fact that PTFE aligns with the predominant fibre alignment. It would therefore be interesting to investigate the multiphase transport properties of treated GDLs further, both over a wider range of materials with different structures. Some having fibre alignment and some not, and with different heat treatments that affect the penetration of the PTFE.

5.4 Concluding Remarks

A new method for measuring the relative IP diffusivity of partially saturated thin porous material has been created. Several GDL samples were investigated, with little difference found between data-sets, except for a slight decrease in relative diffusivity for untreated samples compared with treated. However, behaviour observed by other researchers investigating TP relative diffusivity for varying hydrophobic treatment levels was not found in the current data, suggesting that the treatment affects transport differently in different directions. The method was found to produce the expected relation between relative diffusivity and saturation for homogeneous three-dimensional media: a power law dependence with exponent around 2. Where other techniques for measuring effective properties of dry material are not suitable for measuring partially saturated material, this method has proved successful. Future work could utilise the same set-up with minor modification to measure the relative permeability and also study the effect of compression and inhomogeneity on the relative transport properties. In addition the bottom plate may be modified to allow for in-situ liquid injection, to investigate the effect of differing saturation distributions.

Chapter 6

Capillary Hysteresis in Neutrally Wettable PEFC GDLs

6.1 Motivation

Modelling porous media requires an understanding of the topology and geometry of the pore space in order to make appropriate simplifications to predict fluid interactions and behaviour. A fundamental relationship when characterizing porous media regarding multiphase flow is how the saturation depends upon the capillary pressure, here termed the $S(P_C)$ relation. For a medium occupied by air and water that is non-water wetting the saturation, S, is defined as the volume fraction of the pore space occupied by water. The capillary pressure, P_C, is then defined as the pressure in the non-wetting phase minus the pressure in the wetting phase ($P_C = P_{NW} - P_W$). The relationship largely depends on how well the pores are connected by throats i.e. topology, the size distribution of the pores and throats i.e. geometry, the history of the fluid flow and the physical laws applied to the algorithms for solving the fluid flow and interaction. The latter is the main subject of this chapter, specifically the impact of the chosen pore-scale capillary pressure relation in determining pertinent size information and percolation characteristics and consequently, the distribution of the phases and their relative transport properties.

The material of interest, SGL 10 BA carbon paper, is typically employed as a gas diffusion layer (GDL) in polymer electrolyte fuel cells (PEFCs) and serves

to distribute reactant gases, conduct electricity and also aid the removal of liquid water. To serve these functional requirements GDLs have high porosity (0.75 - 0.85) and are often coated with a wet-proofing material, PTFE, which also binds the fibres of the material together. However, the coating is not evenly applied and the carbon fibre substrate, as well as the PTFE, are considered neutrally wettable, with average contact angle between 60° and 120° [287]. The contact angle is defined as the interface angle between phases when measured through the non-wetting phase at solid boundaries, therefore a non-wetting fluid is generally understood to have a contact angle greater than 90°. The capillary pressure characteristics of fuel cell GDLs have been studied by several research groups [66], [288], [289], [290], [17]. These studies found strong hysteresis in the $S(P_C)$ curves for intrusion of water, termed drainage (referring to the wetting phase, air), and extrusion, termed imbibition. This is surprising at first, as the material appears to switch wettability where positive capillary pressure is required to force water in, signifying air wetting, and negative capillary pressure is required to withdraw it, signifying water wetting. Despite this apparent ambiguity about the wetting properties of the GDL, the convention in the fuel cell community is to consider liquid water to be non-wetting and define the capillary pressure as: $(P_C = P_l - P_g)$.

Amongst studies where hysteresis is observed there is apparently no consistent explanation as to why the phenomenon occurs. Schwartz and co-workers attribute the hysteresis in $S(P_C)$ to hysteresis in the contact angle [289], [291], described and illustrated by Bear as the "rain-drop" effect [292], but later acknowledge that their contact angles should be viewed as effective ones that are not a direct result of the surface wettability [234]. The "rain-drop" effect is so-called as one can imagine a rain-drop sliding down a surface under the influence of gravity. The bulk of the fluid forms a bulge at the advancing contact point, whereas a tail-like shape forms at the receding contact point, creating different contact angles. The advancing and receding contact angle is used, when modelling drainage and imbibition through fibrous media, as a fitting parameter without direct physical reasoning, and serves to account for more complex geometrical effects that cannot be explained by a simple capillary tube analogy. Gostick et al. conclude that the hysteresis in their experimental results highlight the fact that capillary

behaviour in such materials is highly influenced by pore structure [17], a theory also supported by many of the findings of Harkness et al. [290].

Another cause of capillary pressure hysteresis is the so called "ink-bottle" effect, where drainage of the wetting fluid is controlled by the size of the pore necks (or throats), and imbibition is controlled by the pore bodies, as illustrated by Dullien [188]. But Harkness et al. point out that observing water withdrawal at negative capillary pressure (without contact angle hysteresis) implies having negative pore bodies, so this cannot be the only explanation.

Pore network models studying transport, and topological features of fibrous diffusion media (DM) are numerous in recent years [157], [58], [293], [129], [132], [221], [294], [295], [296], [297], [298], [299], [247]. The assumption that capillary pressure should be calculated based on straight capillary tubes is common and implemented using the Washburn equation. It is shown in this chapter that this assumption leads to erroneous results concerning the pore size distribution and characteristic capillary flow.

Making use of a three-dimensional cubic pore network model (PNM) it is shown that, when fitting a specific geometry and topology, good agreement between experimental data using air and water collected for fibrous carbon paper material and numerical data can be obtained. However, the hysteresis observed in the capillary pressure when observing percolation and imbibition is only seen when considering the constrictions between data to be of a toroidal shape, rather than straight capillary tubes, therefore accounting for the influence of pore structure. Furthermore, the model does not require that contact angle hysteresis occurs for drainage and imbibition, but arises naturally from the requirement of positive pressure in the invading phase.

6.2 Method

6.2.1 Capillary Pressure Model

A common model for capillary pressure in a straight cylindrical capillary tube of radius r, between phases with surface tension σ, is the Washburn equation. Switches in wettability can be explained using the contact angle, θ, between

phases because the sign of the capillary pressure changes when the contact angle passes through 90°:

$$P_C = -\frac{2\sigma cos\theta}{r} \qquad \text{(2.2.22 revisited)}$$

However, the capillary pressure is actually determined by the curvature of the interface where the contact angle only forms part of the boundary condition [9]. Equation 2.2.22 is only valid for straight cylindrical capillary tubes as a solution of the more general Young-Laplace equation:

$$P_C = \sigma \nabla . \vec{n} \qquad (6.2.1)$$

where $\vec{n}$ is the solid surface unit normal vector at which the three-phase contact line between wetting fluid, non-wetting fluid and solid forms. Dullien illustrates that the capillary pressure is very sensitive to the geometry of the solid structure when the surface exhibits contact angles in the neutrally wettable region [188], rendering strict application of the Washburn equation invalid.

The Purcell model for capillary pressure accounts for the converging-diverging nature of fibrous material structures by imagining the meniscus passing through the centre of a torus as follows:

$$P_C = \frac{(-2\sigma)}{r} \frac{(cos(\theta - \beta))}{(1 + R/r(1 - cos\beta))} \qquad \text{(2.2.23 revisited)}$$

where r is half the minimum fibre spacing or pore/throat radius, R is the fibre radius (set at 5 µm for our study) and β is the filling angle, defined as zero when the interface reaches the smallest constriction. At this point Equation 2.2.23 reduces to Equation 2.2.22, but critically, this is not the point at which maximum interface curvature occurs. The model was first proposed by Purcell [68] and is discussed in detail by Kim and Harriott [300] and Mason and Morrow [62]. The filling angle at which the maximum meniscus curvature occurs was shown by Mason and Morrow to be:

$$\beta^{max} = \theta - \pi + arcsin[sin(\theta)/(1 + r/R)] \qquad \text{(2.2.24 revisited)}$$

The maximum curvature corresponds to maximum capillary pressure, used in

Case (uncompressed & compressed)	Capillary Pressure Model	Mean Contact Angle (Water / Air)
A & D	Purcell	(110° / 70°)
B & E	Washburn	(110° / 70°)
C & F	Washburn	(110° / 110°)

Table 6.1: Details of the capillary pressure models for each numerical case.

network modeling as a threshold entry-pressure for the invading phase, and is higher than that predicted by the Washburn equation. By substituting Equation 2.2.24 directly into Equation 2.2.23 and using this value for the threshold entry pressure, Gostick was able to create a PNM simulating drainage of air from a typical GDL [69]. The same method is used in the present chapter for cases employing the Purcell model, and is applied to both drainage and imbibition.

Figure 6.1 shows the shapes of the interface for different contact angles, where water is pushing upwards through a straight capillary tube on the left, and the centre of a toroid on the right. For the straight tube, the sign of the pressure in each phase is determined by the contact angle, with positive pressure required to maintain a convex interface shape. For the toroidal geometry, we observe an inflection of the interface from concave to convex in all cases, irrespective of intrinsic surface wettability. This signifies that positive pressure is always required in the invading phase to transition through the constriction, regardless of the wetting angle. For very strongly wetting or non-wetting fluid-surface interactions, this inflection is not expected to happen. However, for neutrally wettable surfaces the effect of geometry dominates the capillary behaviour.

Six numerical cases are investigated: three matching experimental $S(P_C)$ data for an uncompressed material sample and three for the compressed material to demonstrate the applicability of the method to different scenarios and investigate the effect of compression. The Purcell model is used as the pore scale capillary pressure model without applying contact angle hysteresis for the first of the cases for each compression level. The Washburn model is used without applying contact angle hysteresis and with contact angle hysteresis for the second and third cases, respectively. The details of each case are summarized in Table 6.1.

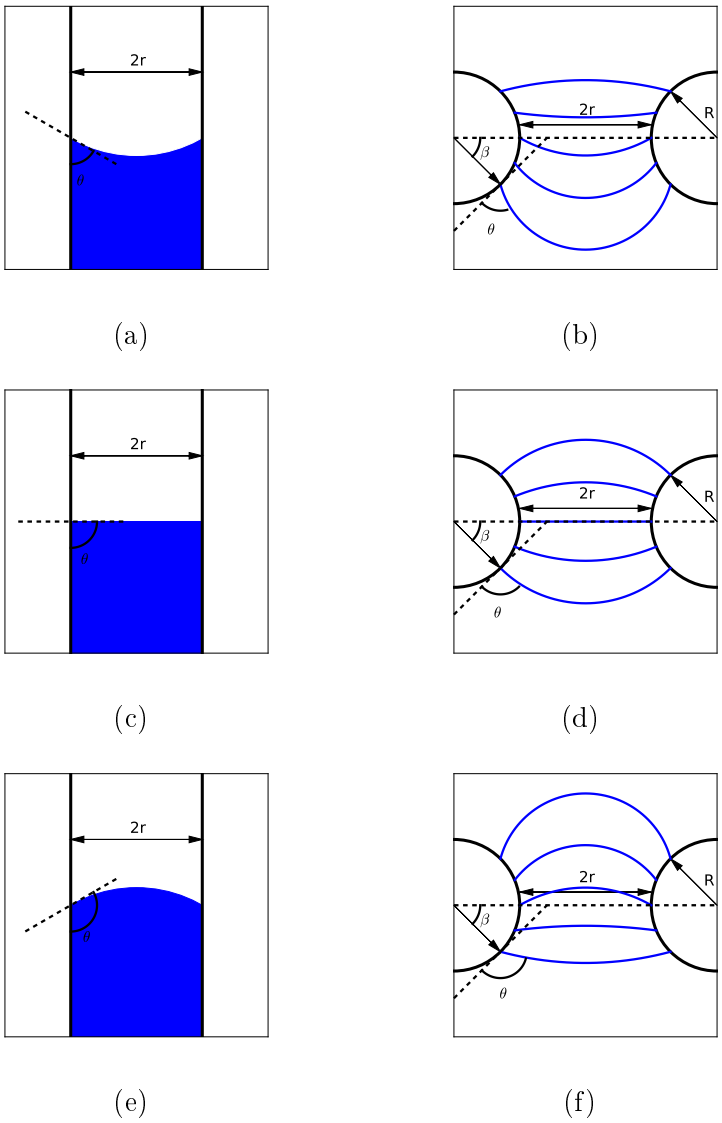

Figure 6.1: Shape of the interface using the different pore-scale capillary pressure models for different contact angle (θ) and different filling angle (β).

Thickness [µm]	Porosity	Permeability [m^2]
350 (Uncompressed)	0.88	2E-11
167 (Compressed)	0.75	5E-12

Table 6.2: SGL 10 BA experimental attributes [141].

A normal contact angle distribution, CAD, with mean value as per Table 6.1 and standard deviation of 10° is applied randomly to the pores and throats in the network. This simulates the mixed, but generally air wetting, material properties and accounts for the surface roughness of the fibres, which tends to increase the effective contact angle. The threshold entry pressure in the percolation algorithm is always calculated for the invading phase, so for imbibition of air, a contact angle of $180° - \theta$, where θ is the contact angle measured through the liquid, is used when not applying contact angle hysteresis. This signifies that the intrinsic wettability of the phases remains unchanged. For comparison, $S(P_C)$ curves using the Washburn model with contact angle hysteresis are also generated. In these cases (C & E) identical contact angles are applied to the invading phases: water during drainage and air during imbibition. This signifies that the intrinsic wettability of the phases have switched for drainage and imbibition, and that contact angle hysteresis has occurred with respect to each phase.

6.2.2 Genetic Algorithm

A genetic algorithm is implemented using the DEAP python package [301] to optimise a PNM by sizing the pores and throats to match the capillary pressure data obtained by Gostick et al. [17]. The SCOOP python package [302] is also used to run the genetic algorithm in parallel. A sample of SGL 10 BA is chosen for the fitting procedure in both the uncompressed state and also the compressed state with physical attributes shown in Table 6.2.

OpenPNM is used to generate a 3D cubic network consisting of regularly spaced pores with a lattice spacing equal in each direction, and initial connectivity or coordination of 12. This coordination is achieved by representing pores as cubes and connecting neighbours with throats diagonally by shared edge association. After generating the network topology, roughly 25% of the throats are removed

Genetic Attribute	Minimum	Maximum
Shape (s)	0.5	3.0
Location	1E-8	1E-4
Scale	1E-6	1E-4
Lattice Spacing	1E-5	1E-4

Table 6.3: Limits of the attributes of the genetic algorithm.

from the network at random to introduce variability in coordination. A log normal distribution is applied to the pore sizes (using the *scipy.stats.lognorm* function) without spatial correlation defined with probability density function (PDF):

$$PDF(X, s) = 1/(sX\sqrt{2\pi})exp[(-ln(X)^2)/(2s^2)] \tag{6.2.2}$$

where X is a random variable assigned to pores with value between 0 and 1 used as a seed and s is a shape parameter. To shift the location and scale of the distribution the "loc" and "scale" parameters are also used as genetic attributes to set the distribution's minima and range.

The parameters of the pore-size distribution (PSD) and the lattice spacing of the network form the genes of the genetic algorithm, and an initial population is randomly assigned values for each attribute between bounds with uniform probability according to Table 6.3.

The genetic algorithm consists of the following steps:

i Define an individual or chromosome by assigning the genetic attributes (i.e. genes).

ii Create an initial population of 100 individuals and assign values randomly to each gene within the bounds of the parameter space (Table 6.3).

iii Create a phenotype in the form of a PNM for each genotype, detailed in Section 6.2.3.

iv For each capillary pressure case, assess the fitness of individuals by generating drainage and imbibition $S(P_C)$ curves using OpenPNM's Ordinary Percolation algorithm, and comparing the results to experimental data for SGL 10

BA. Porosity and permeability are also used as part of the multi-objective fitting process with the desired results shown in Table 6.2. For each data set, the mean of the square of the residuals is used as the fitting function, and all objectives are given equal weighting.

v Iterate the population creating new generations of the same size until the best individual is found according to a minimisation of fitness functions. The following principles are employed to evolve the population from generation to generation:

a Cross over: two individuals are selected for mating according to fitness in a tournament style and elements of the genetic attributes are shared producing children which are included in the next generation.

b Mutation: an individual is selected at random and its genetic attributes are randomly changed according to the initial bounds of the genetic parameters.

c Reproduction: an individual is simply reproduced entirely in the next generation.

It was decided to include the porosity as part of the fitting process of the genetic algorithm as this helps to restrict the lattice spacing parameter which in turn restricts the throat lengths and volumes. Without sensible porosity the $S(P_C)$ curves could be fit using only pore sizes but then throat volumes would have to be ignored. The domain could then take on an arbitrary shape and size which would render effective transport properties meaningless. Similarly, permeability was also chosen as a fitting parameter, because it is highly dependent on throat sizes which contribute little volume, so do not influence the porosity too much, but are important for transport calculations. Matching permeability helps to strike the right balance between the pore and throat contributions to both volume and saturation during the percolation simulations.

Each generation contained 100 individual networks in each generation that is successively optimized to find a fitting PSD. The finishing criteria was that each fitting parameter was within 10% of the experimental value or no significant improvement could be achieved across the multiple objectives. With a cross-over

probability of 0.65 and mutation probability of 0.25, 200 generations was sufficient to converge and select a well-fitted individual.

6.2.3 Network Specifications

The genetic algorithm was run using cubic networks consisting of 32,000 pores arranged in a [40, 40, 20] configuration, excluding boundary pores. This size is deemed to be representative as the material is very thin in the through-plane direction. The pore diameters are assigned directly using the genetic attributes to obtain each individual PSD. Some pores are removed during the network creation process when they become merged, as will now be explained.

Throat diameters are set equal to the minimum pore diameter to which they are connected. The throat lengths are dependent on the topology by taking the Euclidean distance between pore coordinates, and subtracting both pore radii. As the radii are randomly applied, this can sometimes result in non-physical overlapping of pores, which artificially increases the porosity and results in negative throat lengths. To create a more realistic network, overlapping pores are merged together, and the connections to neighbouring pores are assigned to the newly created larger pore. This means that larger pores tend to have higher coordination number, which is physically realistic. Very large pores that overlap more than one set of neighbouring pores are merged with their primary neighbours, then are shrunk to the largest size that does not result in negative throat lengths. This process limits the maximum pore diameter to less than 4 lattice spacing lengths, but still allows for a wide range of pore sizes.

For volume calculation the pores are considered to be cubic in shape and throats are considered to be cylindrical. Critically however, when calculating the capillary pressure required to invade the throats using the Purcell model their shape is assumed to be toroidal as discussed in Section 6.2.1. Using cubic shapes for pores allows for a higher porosity than using spheres, which was found to be necessary for matching a realistic porosity.

Feature	Drainage	Imbibition
Invading Phase	Water	Air
Boundary Pores	Bottom Face	All Faces
Defender Trapping	No	Yes
Percolation Method	Bond	Site
Access Limited	Yes	Yes

Table 6.4: Adjustable features of the ordinary percolation algorithm and their configuration for each percolation simulation.

6.2.4 Effective Transport Properties

The same transport models are applied in this chapter as previously detailed in Section 4.3.4, with the exception that late pore filling (LPF) is not applied to the saturation calculations. LPF may be important for matching porosimetry data obtained for various different fluids such as mercury and water, but in this case would only complicate the fitting process and, as air-phase conductance is assumed to be severely reduced in water filled pores, LPF has little bearing on the results.

6.2.5 Percolation Model

Both drainage and imbibition of the wetting phase (in this case air) are simulated with a OpenPNM's ordinary percolation algorithm as detailed elsewhere [3]. The key adjustable parameters are summarized in Table 6.4.

Drainage is simulated with bond percolation (controlled by throat sizes) and imbibition is simulated with site percolation (controlled by pore sizes). Defending and invading phases are determined, and the domain is initially filled with the defending phase. Inlets are defined according to Table 6.4 and filled with the invading phase. In each case half the boundary pores in the selected faces of the domain are designated as inlets. Pressure in the invading phase is incremented at intervals matching the experimental data-set. At each step, connected clusters of elements with entry pressure below the current threshold are invaded. For bond percolation, the throats are evaluated to identify clusters, and for site percolation the pores are evaluated. Access limitations are considered for drainage of air (or

invasion of water), as the liquid interface will only invade pores connected to the invading cluster. For imbibition of air, the access is unlimited when beginning from a partially liquid saturated state, as air will reside in the crevices of highly porous materials. However, in the case of primary imbibition, the medium is assumed to be completely filled with water initially, and invasion is also considered to be access limited.

Trapping of the non-wetting phase may occur when the wetting phase completely encircles a pore or collection of connected pores currently occupied by the non-wetting phase. As the liquid water is considered incompressible, further increases in air pressure cannot reduce the volume of the trapped fluid. As there is no escape route, because surface tension does not allow for films of non-wetting phase to develop and travel, there will be a residual saturation, which is assumed not to evaporate. The wetting phase does not normally remain trapped, as it retains high connectivity, so the trapping model is applied to imbibition only. Trapping is calculated as a post-process, identifying clusters of pores and throats that are not invaded and not connected to any pores at the outer faces of the domain.

6.3 Results and Discussion

6.3.1 Pore Size Distribution (PSD)

The optimized genetic attributes for each case investigated are summarized in Table 6.5. The resulting network size distributions after the pore-merging process are shown in Figure 6.2.

It is clear from Figure 6.2 that the choice of pore-scale capillary pressure model affects the sizing of pores and throats significantly; as the predicted capillary entry pressure is higher for the Purcell model for a pore or throat of given size, to match the experimental curves larger pores are selected compared to the cases where the Washburn model is used. The magnitude of the capillary pressure for the Washburn model is less than that of the Purcell model because the converging-diverging nature of the fibrous constrictions increases the maximum curvature of the meniscus and increases capillary pressure. This fact should serve as a caution

	Uncompressed		Compressed	
Genetic Attribute	Purcell (A)	Washburn (B & C)	Purcell (D)	Washburn (E & F)
Shape (s)	0.950	0.953	0.855	0.962
Location	3.50E-6	1.38E-6	2.79E-7	1.94E-6
Scale	5.72E-5	2.01E-5	2.83E-5	1.43E-5
Lattice Spacing	1.02E-4	7.70E-5	9.08E-5	4.05E-5
Porosity	0.755	0.588	0.495	0.636
Permeability $[m^2]$	1.05E-11	3.11E-12	2.73E-12	7.6E-13

Table 6.5: Optimised attributes for the pore network model giving best fit to experimental drainage data.

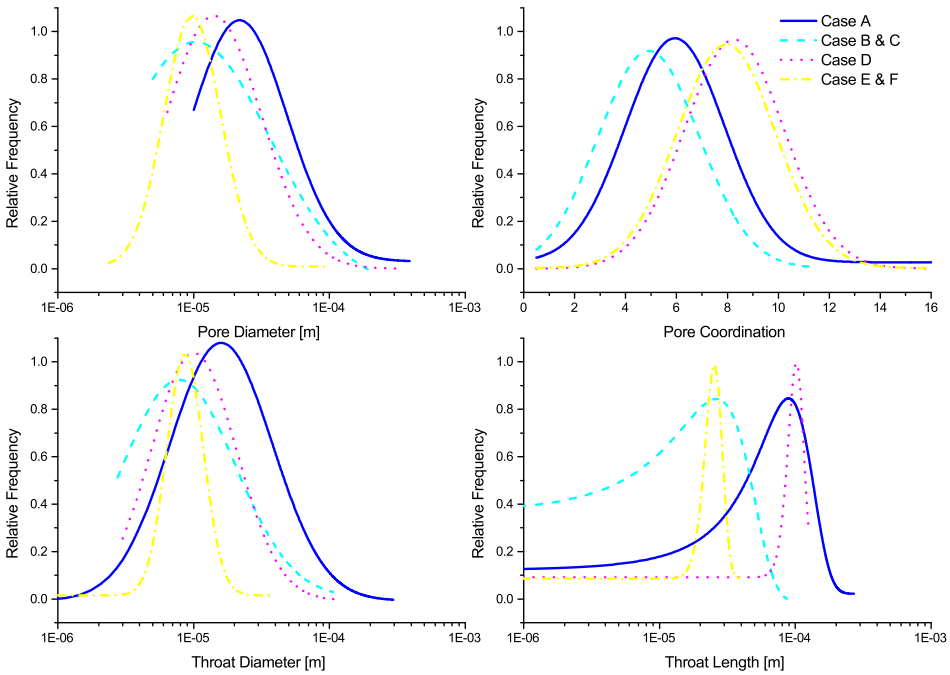

Figure 6.2: Various size distributions for the networks generated from the optimization process.

to those wishing to extract pore size information from capillary pressure data that the correct interpretation of the local capillary pressure should be made otherwise sizes are likely to be incorrect.

The topology of a cubic lattice is less representative of the fibrous GDL in the present study than that of the random networks described in Section 4.3.1 of Chapter 4, but was chosen to serve the optimisation process, and provide a constant base from which to compare the capillary pressure models. Generating images of fibrous structures from random networks is also computationally time-consuming, whereas applying sizes to pores and throats from statistical distributions is very quick. As a result of this compromise in topological representation the simulated porosity and permeability of all the networks, shown in Table 6.5, is lower than the real material. This is because the cubic packing of the pores is less efficient than that achievable with other methods, such as a Voronoi diagram. However, values for porosity and permeability within 50% of those stated in Table 6.2 were achieved when using the Purcell model. In contrast, the network permeability is much lower than the desired result (about a factor of 10) when using the Washburn model, due to the smaller sizes, but porosity is in reasonable agreement as lattice spacing is also reduced.

It is also worth mentioning that the networks are isotropic, and no effort to resolve porosity distributions or differences in transport properties in the principle directions of the real media are made, such as those observed by Fishman and Bazylak [59] and modelled in Chapter 4. This could potentially be implemented as a secondary optimisation process, but is not necessary for the purposes of this study. As drainage progresses in the through plane direction for the experimental data, the network characteristic transport curves represent this direction of transport.

Figure 6.3 is an example visualisation of the generated network with invaded pores and throats shown in blue for a capillary pressure of 7000 Pa and un-invaded shown in red.

6.3.2 Capillary Pressure Hysteresis

The following section compares numerical results generated for each case, using the two capillary pressure models with experimental data collected by Gostick et al. for both the compressed and uncompressed SGL 10 BA samples [17].

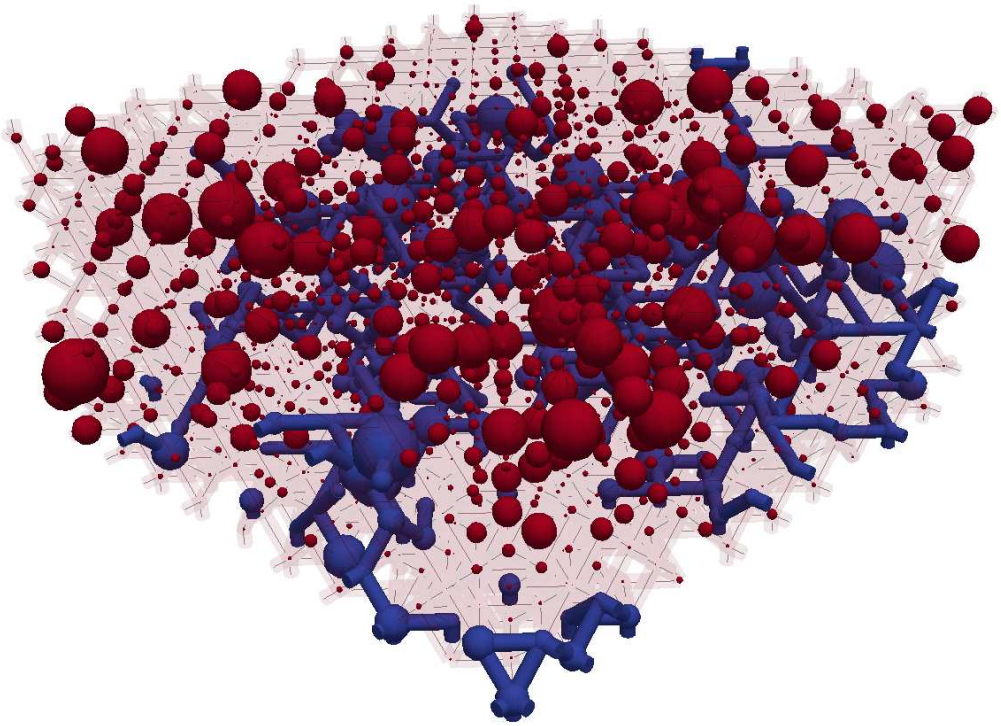

Figure 6.3: Visualisation of the partially saturated network at capillary pressure of 7000 Pa.

The genetic algorithm was used to match the drainage data, represented with solid symbols at positive capillary pressure, and good agreement is obtained between simulation and experiment when using either pore-scale capillary pressure model. The algorithm achieves a better match for the compressed sample data at low saturations because the experimental data, unlike the uncompressed data, does not show signs of a shoulder. This most likely arises from bad contact between sample and injection source under low compressive force. Encouragingly, a match is achieved for both the drainage and imbibition data, represented with open symbols, in both compression cases when using the Purcell model (Cases A & D). However, imbibition data for the Washburn model without contact angle hysteresis (Cases B & E) is a poor match. Some hysteresis is visible for these cases due to the "ink-bottle" effect but the model predicts that virtually all water is evacuated from the network at the point that capillary pressure is reduced to

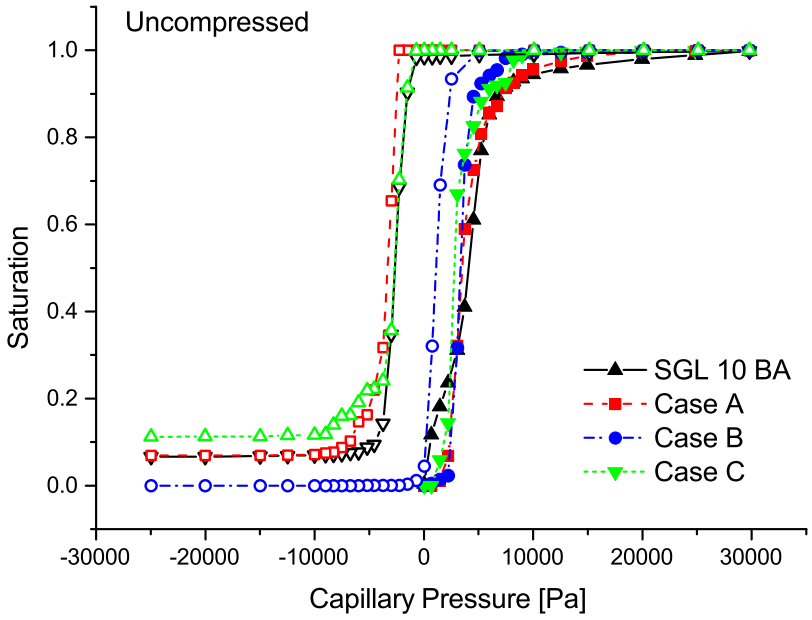

(a) Uncompressed

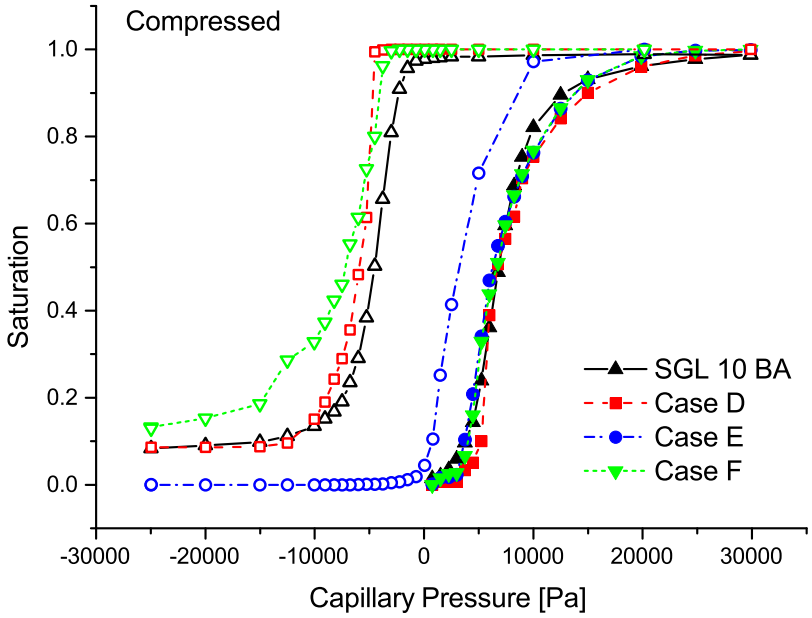

(b) Compressed

Figure 6.4: Saturation vs Capillary Pressure generated by the optimised PNM calculated with the Washburn and Purcell models for capillary entry pressure and experimental data for SGL 10 BA, Figure (9b) [17], with minimal and high compression to different thickness.

zero. This is the critical difference between the two models, and is the primary reason for invoking an explanation of contact angle hysteresis when using the Washburn model. To match capillary pressure data using the Washburn model, contact angle hysteresis must be employed (Cases C & F). Without contact angle hysteresis the volume of water trapped is also close to zero when using the Washburn model.

As discussed by Gostick et al. the wettability of fibrous media is not solely determined by the contact angle, but also the pore-scale geometry [17]. As explained in section 6.2.1, a positive pressure is always required in the invading phase to penetrate the constriction of a torus irrespective of the contact angle. This means that hysteresis in the capillary pressure data does not result purely from contact angle hysteresis, and also explains why spontaneous uptake of water or air is not seen at the beginning of each experiment. In-fact there is no explanation given for contact angle hysteresis inside the porous structure of a GDL, especially one that would give rise to such drastic differences as those predicted by Schwarz et al., who fit their data to a mean contact angle of 92° for liquid intrusion and 52° for gas intrusion [291]. Weber also chooses to use a distribution of contact angles centred around very different mean values for liquid intrusion and withdrawal in his bundle of capillaries model [303].

Contact angle hysteresis is generally understood as a surface phenomenon, observed in droplets under stress where the advancing contact angle is greater than the receding, and can be attributed to pinning of the trailing contact line [304]. The situation inside a GDL is very different. Firstly, the gravitational force is small compared with surface tension, as the size of the droplets are constrained to the maximum pore size. Secondly, phases are often not droplets but continua connected throughout multiple pores. Thirdly, the geometry of the intertwined fibres are not flat surfaces, so water may impinge at any number of angles in an irregular way. This makes it difficult to argue why significant contact angle hysteresis should occur and it is therefore unlikely to be the primary cause of the capillary pressure hysteresis observed in GDLs. Furthermore, Gostick has already shown that the Purcell model fits very well with drainage data, when used in a random PNM constructed with a Voronoi diagram representing the fibres of the GDL, and a Delaunay tessellation defining the throat connections [69]. Gostick

found that unrealistically high contact angles must be used to fit drainage data using the Washburn equation with a realistic PSD. It has now been shown in this chapter that the Purcell model may be used to fit drainage and imbibition data, without any need to invoke contact angle hysteresis.

The Purcell model matches the capillary pressure hysteresis in the experimental data very well in the present study, and also agrees reasonably well with residual saturation at low capillary pressures caused by the trapping of water. In practice, the residual saturation is found to vary quite significantly from sample to sample, so lesser importance should be placed on this result. No contact angle hysteresis is applied and some hysteresis can be attributed to the "ink-bottle" effect, where the critical entry pressure is calculated for throats during drainage, and pores during imbibition. It is clear that the Washburn equation cannot be used to model the capillary pressure hysteresis without employing assumptions about contact angle hysteresis. Alternatively, when using the Washburn model to simulate imbibition, one can view the contact angle as an effective angle that incorporates both wetting and geometrical effects. However, this does not resolve the pore sizing problems discussed in Section 6.3.1. The Purcell model is physically satisfying, as the constrictions between fibres found in the GDL are much more like the constriction of a torus rather than a straight capillary tube, and the hysteresis in phase pressure is a natural consequence of the local solid geometry.

The importance placed on the capillary pressure hysteresis is questioned by Weber several times in the context of operating fuel cells [303], [60]. It is noted that only the liquid intrusion data is important, as this is the main method by which water is introduced into the GDL when injected from the catalyst layer. Liquid withdrawal characteristics are important when drying occurs, and the liquid distribution may be significantly different in this case. As discussed in Section 2.8, under certain operating conditions, drying is the main method of water management in fuel cells, so it is necessary to understand both processes. Also for validation, experiments utilising a drying technique to obtain saturated samples for multiphase characterisation, such as those conducted by Hwang and Weber [18], may have had different results if the liquid had been injected. Pore network modelling is used in the next section to elaborate on these differences.

6.3.3 Relative Diffusivity

The following section presents the numerical results of a Fickian diffusivity algorithm at varying levels of saturation, as calculated by the percolation algorithms. Trapping of the liquid phase is not considered for the following simulations to enable results over the entire range of saturation. The absolute effective diffusivity of the dry network is calculated with 100% air phase occupancy, and this value is then used to normalize the results for partial occupancy at each stage of the percolation algorithm, so that relative air diffusivity can be calculated.

The relative diffusivity is an important parameter for multiphase characterisation of porous media and is indicative of how well phases are separated. A linear relation between effective diffusivity and saturation indicates well separated phases, as the connected pathways open to the flow of each phase are not tortuous, and depend in number only on the volume fraction of each phase. A power law dependence is more common, where the higher the power the more tortuous the flow paths and the more intermingled the phases become.

Figure 6.5 shows that the relative diffusivity can be represented as a function of saturation, $g(S)$, and tends to follow a power law for drainage (originally presented as Equation 2.2.12), and a log normal relation for imbibition (originally presented as Equation 5.3.1), where fitted parameters are included in the figure legends:

$$g(S) = \begin{cases} (1-S)^n & \text{if drainage} \\ 1/2(1+erf[(-ln(S)+a)/b]) & \text{if imbibition} \end{cases}$$

The present finding, that the relative diffusivity for phase distributions obtained by drainage follows a power law with exponent between 3 and 4 is consistent with other studies on this type of porous media [15], [156] for the through-plane direction of transport. The exponent decreases slightly with compression, which is consistent with the results presented in Chapter 4. The imbibition results are compared to the experimental data for SGL 10 BA obtained by Hwang and Weber [18] who controlled the saturation by drying fully saturated samples to a desired weight. This process is air imbibition so it is encouraging that we

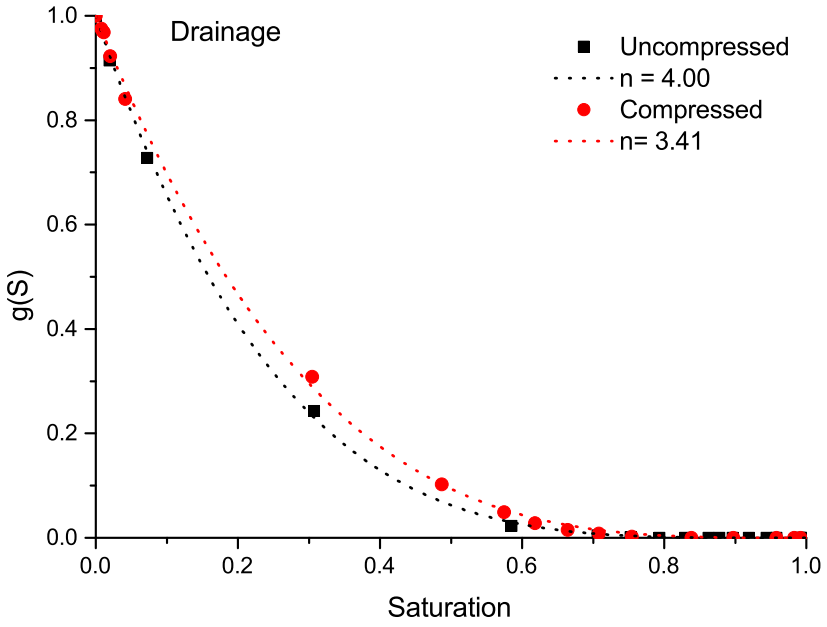

(a)

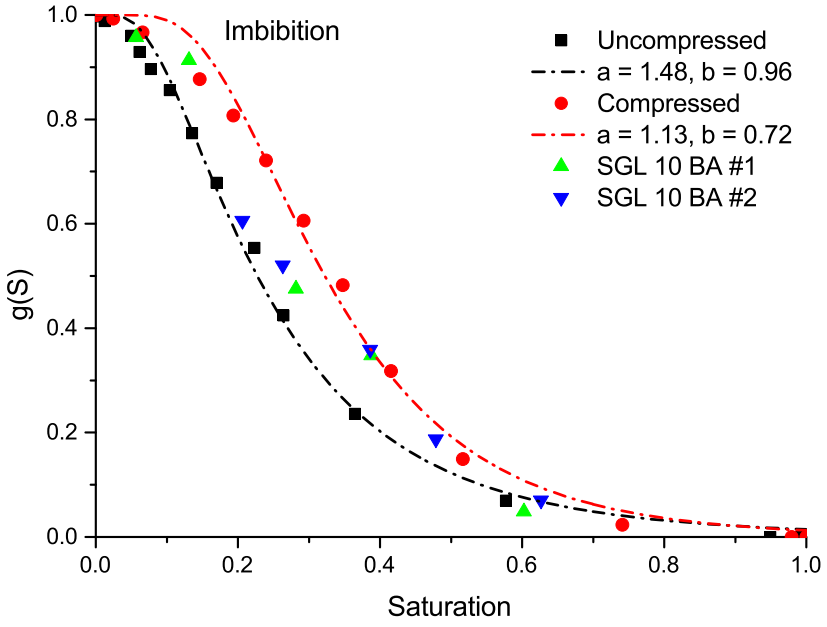

(b)

Figure 6.5: Relative diffusivity of air plotted against saturation (water volume fraction in the pore space) as calculated from the phase distributions determined by (a) drainage and (b) imbibition algorithms. Experimental data from Hwang & Weber [18] is also shown.

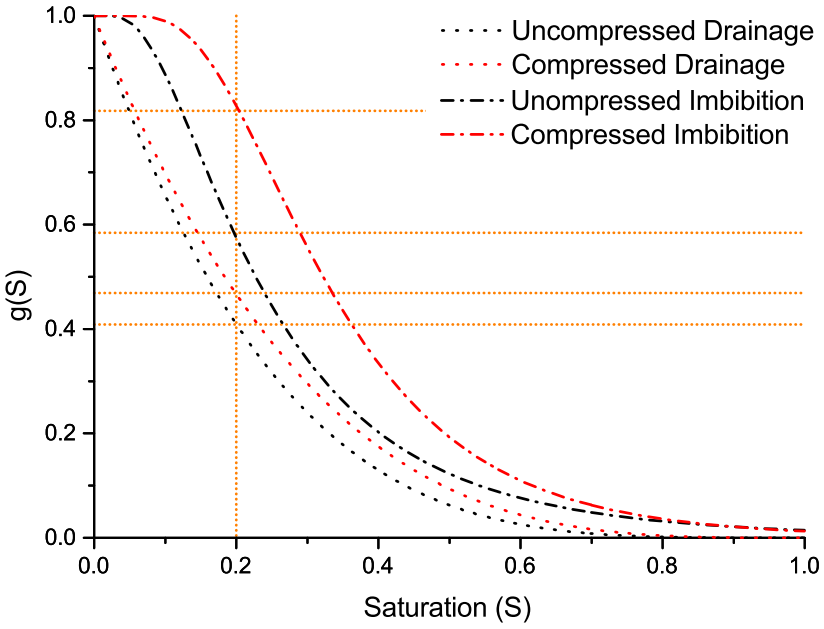

Figure 6.6: Comparison of the relative diffusivity $g(S)$ relations for saturation distributions obtained under drainage and imbibition for both compressed and uncompressed samples.

find good agreement. The experimental data lies mostly between our numerical data sets for uncompressed and compressed samples, which is expected as Hwang & Weber used a gasket of 320 µm to seal their sample GDLs, giving a level of compression between our modelled samples.

Interestingly, at intermediate saturation, $g(S)$ under drainage saturation distribution is significantly different from $g(S)$ under imbibition conditions, as shown in Figure 6.6. The imbibition relative diffusivity data differs from the drainage data in several ways, and this is largely a feature of the conducting phase taking on different roles for each data-set. Beginning with imbibition scanning back along the curve from high saturation to low: air is the invading phase and has poor network-level connectivity at high saturations in both cases, in fact closer inspection of Figure 6.5 reveals that the data seems identical, and very close to zero, above saturations of 0.8, and Equation 5.3.1 tends to over-predict the dif-

fusivity in this region. As more air enters the network, clusters of pores invaded with air begin to merge, and conductivity within the phase steeply increases to a near maximum dry level. At low saturation, relatively few clusters of liquid exist and none appear to span the entire network or block air diffusion significantly, which is why the flat region exists in $g(S)$ at low saturation for imbibition (between 0.0 and 0.1).

With drainage scanning from low saturation to high: at low saturation when water has just begun to invade the network we observe a steeper decrease in air diffusivity than with the imbibition data. This is because the invasion of water is concentrated in one region of the network near the bottom face where the inlets are designated. The liquid phase is spread in a planar fashion along the bottom face and creates a bottle neck for air transport in the through-plane direction. This has a significant effect, as shown by evaluating the different $g(S)$ relations for a saturation of 0.2 (a value typical for an operating fuel cell), shown graphically in Figure 6.6 with the yellow dashed lines. At a saturation of 0.2 under a drainage configuration of phases, the relative diffusivity is between 0.4 and 0.5 of the dry value, whereas it lies be between 0.6 and 0.8 with an imbibition configuration, depending on the level of compression. With increasing saturation air again has poor network conductivity, and above saturations of 0.6 there is little difference between the liquid configurations and resulting relations.

6.4 Concluding Remarks

The genetic algorithm approach has been successfully applied to the optimization of a pore network model in matching the drainage data of a typical fuel cell gas diffusion layer. Selecting the correct pore-scale model for capillary entry pressure is shown to be critical for matching both drainage and imbibition data for fibrous media, thus improving the reliability of the pore size distribution and transport characteristics. Relative diffusivity of the networks is also shown to match well with the literature under different percolation scenarios, and it is demonstrated that care should be taken when using constitutional relations to consider the effects of phase configuration, especially when modelling compressed materials. One constitutive relation may not be sufficient to cover all operating scenarios

when continuum modelling fuel cells, and it is recommended to use pore network modelling to establish the phase configuration using the Purcell model.

6. CAPILLARY HYSTERESIS IN NEUTRALLY WETTABLE PEFC GDLS

Chapter 7

Conclusion

7.1 Foreword to the Conclusion

Water plays a key role in two of the performance loss mechanisms associated with PEFCs, as water is needed to hydrate the membrane in order to increase proton conductivity, but liquid water trapped in the GDL blocks reactant gases, thus leading to greater mass transport losses. This problem of water management, i.e. striking the right balance, is well documented and has received much attention in the last few decades. Jiao & Li [7] provide an excellent review of water management for PEFCs and highlight the areas needing further research, including the need for a fundamental understanding of the multiphase processes occurring at the micro-scale. In Chapter 2 a literature review was presented covering a diverse range of topics relating to the more general theme of water management in PEFCs. A simple google scholar search of the words "water management polymer electrolyte fuel cells" returns 52,000 results with roughly 18,000 occurring within the last 10 years. So formulating a plan to research a topic within this broader theme was quite a challenge in itself and required extensive research into the state of fuel cell science in order to identify gaps in the knowledge. Having a background in physics with specific interest in fluid dynamics it was decided to pursue a modelling approach and first construct a working model of a single cell. The subsequent work then pursued a narrower focus analysing the transport of water within the GDL component under compression, as this seemed to be an important yet incomplete part of the body of knowledge.

Using the commercial CFD software ANSYS Fluent, a single-cell model was developed to simulate the polarization curves of the fuel cell previously built by Dr. Masli Rosli and Dr. Mohammed Ismail, which at the time, was available in the department labs for testing. This task was completed in the first year of study, using the built-in fuel cell model provided with the software. However, it became clear that to really investigate the multiphase flow inside a fuel cell, the continuum approach, where porous media are modelled as homogeneous volume averaged regions, would be insufficient. The simplistic Leverett-J function relating saturation and capillary pressure was originally developed for sand and does not capture the capillary processes occurring in fibrous fuel cell diffusion media. Also, the requirement that liquid saturation become zero in the flow channels sets the boundary condition, and therefore saturation profile, within the diffusion media, and is an oversimplification. The discrete percolation processes resulting in capillary fingering are also misrepresented and smoothed out due to the approximate treatment of the liquid transport as a diffusion process. Overall, the treatment of liquid water within the CFD model was too simplistic, and led to an over-prediction of fuel cell performance.

The modelling process did provide an opportunity to learn the CFD approach and become familiar with the challenges of operating fuel cells, so was not a wasted exercise, but the results are not published or included within this thesis. George Box is credited with the aphorism "all models are wrong, some are useful", and whilst the CFD model was useful for parametric analysis of engineering design parameters, the treatment of multiphase flow was insufficient for the complex processes that became the focus of this study. The polarization curve produced by the continuum model is also not a particularly helpful representation of fuel cell performance in terms of deducing cause and effect. Fuel cell models suffer from over-parameterization, so any number of factors can be adjusted to achieve the same result.

An understanding of the fluid dynamics is central to understanding the overall behaviour of PEFC and current CFD models based on volume averaged porous media are lacking in a realistic representation of liquid water transport. As the management of liquid water is critical to performance, a model must incorporate the production and distribution of liquid water with as much fidelity as possible,

but also retain the greatest utility possible. The objective of this work was to investigate the liquid transport in porous media through modelling with a more realistic microstructure, and through experimentation. The effects of structural changes induced by compression of the porous media have been investigated and the influence on multiphase flow can be used to inform future modelling efforts. In addition the OpenPNM framework co-developed as part of this work can be built upon directly, incorporating additional physical models and increasing the utility of the pore network approach. A promising area of research now is to combine models appropriate for different scales, and a few open source CFD packages are already being used for this purpose. What now follows is a summary of the work completed in this study and suggestions for future work.

7.2 Summary of Work Completed and Final Conclusions

7.2.1 Modelling Work

In Chapter 3 the effect of compression of a 2D model structure representing the PEFC gas diffusion layer was modelled using computational fluid dynamics. Rather than constructing a homogeneous volume averaged porous domain, an effort to replicate features of the actual microstructure was made. This approach had several advantages: the multiphase interface could be resolved in high detail, therefore factors influencing its progression through the modelling domain could be studied in greater depth. However, the approach also had disadvantages: the structures were perhaps oversimplified and did not incorporate enough statistical variation to fully represent the real microstructure. Also, the computationally intensive solving process employed by the volume of fluid method meant that only a domain of limited size could be investigated, and the dimensionality was restricted to 2. However, the model did produce some interesting behaviour and the simplifications could still be considered representative of the average properties of the media. Five geometries were meshed utilising a structured tessellation technique, and a single-phase study revealed that a switch in permeability occurs at high compression, where the through-plane value becomes greater than the

in-plane. A simplified Kozeny-Carman relation using an effective capillary tube diameter was found to agree very well with the numerical data and reproduces the permeability switch at the correct level of compression.

Multiphase simulations using three of the geometries revealed that liquid transport is directed by compression, resulting in a lower saturation at breakthrough. The cases with mild or no compression display high levels of lateral spreading owing to the bifurcations in liquid flow path and uniform surface tension in both directions, whereas the case with high compression exhibits preferential liquid pathways and faster water ejection. When the contact angle is reduced to represent a neutrally wettable medium the effect is also reduced, signifying both the importance of structure and surface energy in determining the liquid flow.

These initial findings were published [1] and helped to explain some of the previous experimental observations, such as why saturation distribution follows porosity distribution, but further work was required to establish relations for the relative permeability as a function of compression ratio, due to the expensive nature of the computations. Moreover, a critical assumption highlighted by this study is how the fibre spacing changes in each direction under compression. From the findings it can also be concluded that increasing the through-plane permeability by other methods would have a beneficial impact on the liquid water transfer, as laser perforation has demonstrated.

The work presented in Chapter 3 helped to form the basis of future investigations using pore network models (PNMs) and highlighted the need for further understanding on the topic of transport under compression. In Chapter 4 a series of PNMs subject to compression were presented. The work was carried out as part of the development of a collaborative open source modelling project called OpenPNM [3]. Much of the focus of the author's contribution was on the development of random network geometry and topology models, but also included percolation algorithm development and multiphase model development. The project was initially started by Professor Jeff Gostick and his PhD student Mahmoud Aghighi at the University of McGill, with Professor Aimy Bazylak and post-doctoral fellow James Hinebaugh at the University of Toronto, under the guidance and funding of Andreas Putz at AFCC. After finding information

about the project on the internet, the author contacted the development team and became part of the core developing group, participating in weekly teleconferences, and helping shape the architecture and solving problems. At the time of writing the author's overall contribution, visible on github (the development tool used for code-change management), is ranked 4$^{\text{th}}$ with approximately 3,000 lines of net additional code. To date the OpenPNM project has garnered international popularity with several European and North American institutions adopting it and numerous research papers have been published utilising it: [260], [305], [306], [247], [272].

The numerical results presented in Chapter 4 have also been published [2], and are in good agreement with experimental drainage and single phase transport data. Effective and relative transport simulations were performed, and the effect of compression was shown to reduce effective transport, but increase some relative transport, depending on the direction and phase. It was found that compression has a more adverse effect on the in-plane transport than through-plane, and this can be explained by considering the different structural changes to constrictions between fibres. The results are an extension of the work presented in Chapter 3, and demonstrate the power of the simple pore network modelling approach. To obtain the relative transport curves required running the transport algorithms for at least 20 different saturation points, and to obtain a statistically valid set of results the process was repeated 100 times. There are 6 different transport curves presented and a total of 6 levels of compression were investigated including the uncompressed model. In total, around 72,000 simulations were performed in order to produce the results for Sections 4.4.1 and 4.4.2. With each simulation taking just a matter of seconds to complete, the entire modelling process could be completed in a day once the network topology and geometry had been generated. In contrast, one multiphase simulation (from Chapter 3), performed with CFD solving the full Navier-Stokes equations and resolving the liquid interface with the VOF model using 32 cores each with 2GB ram took up to 4 days to finish. The PNM approach enables a speed increase over the CFD model of about 6 orders of magnitude and allows for better representation of the microstructure. The sacrifice comes with a less rigorous treatment of the fluid dynamics, as transport is modelled as a series of flow-in-pipe calculations, and liquid is assumed to follow

the path of least resistance. When flow is capillary dominated, these assumptions are valid, and in the majority of fuel cell operating conditions this is the case. When purging the fuel cell, and in situations where there may be large pressure differences between adjacent channels, convection plays a more important role, so PNM modelling is an oversimplification in these cases. However, the benefits of the PNM approach in providing the speed and efficiency to be able to calculate relative transport curves, far outweighs the negatives.

Also presented in Chapter 4 were results based on having a GDL with an in-plane porosity variation. This simulated the effect of compression on percolation and diffusive transport under a land-channel-land scenario. In-plane porosity gradients were shown to affect the liquid percolation pathway, with a strong correlation between saturation and porosity. Using a simple limiting current calculation based on the diffusive flux, it was shown that the saturation distribution affects the limiting current achievable with a fuel cell, which increases proportionally with the channel area fraction, and decreases with the number of inlet clusters. Physically this represents the liquid entry points into the GDL and can be controlled with the inclusion of a microporous layer, lending weight to the argument that this is the primary role of the MPL. Where other studies have focused on through-plane porosity gradients and the impact of an MPL, this work has highlighted the importance of in-plane gradients induced by compression. This is a factor which should not be ignored from future modelling and one which can easily be controlled.

When considering water management in fuel cell GDLs, one also has to account for drying processes. In Chapter 6, a genetic algorithm approach was successfully applied to optimizing a standard cubic PNM to match the drainage data of an SGL GDL with differing amounts of compression. The aim of the chapter was to highlight the importance of selecting the correct pore-scale model for capillary entry pressure, and also to investigate the effect of saturation distribution under conditions of drainage (invasion) and imbibition (drying). The toroidal-based Purcell model, which accounts for the converging-diverging nature of fibrous constrictions, is capable of matching both drainage and imbibition data for fibrous media, thus improving the reliability of the pore size distribution and multiphase behaviour. The model accounts for the hysteresis observed in drainage

and imbibition, without the need to include contact angle hysteresis. The use of the Purcell model to infer size information from porosimetry is therefore highly recommended for fibrous media.

The saturation distribution or phase configuration obtained by drying materials fully saturated with the non-wetting phase are shown to be significantly different from those obtained from invasion of the non-wetting phase. Relative diffusivity of the networks is also shown to match well with the literature under different percolation scenarios, and it is demonstrated that care should be taken when using constitutional relations to consider the effects of phase configuration, especially when modelling compressed materials. One constitutive relation may not be sufficient to cover all operating scenarios when continuum modelling fuel cells and it is recommended to use pore network modelling to establish the phase configuration using the Purcell model.

7.2.2 Experimental Work

The experiment performed and detailed in Chapter 5 extended work performed by Rinat Rashpov [5], a former Masters student of Professor Gostick's, on dry materials to investigate the effect of saturation on relative in-plane diffusivity through GDLs.

A new method for measuring the relative IP diffusivity of partially saturated thin porous material has been created. This was primarily accomplished by thermally encasing a custom-designed sample holder, which was built in-house by the author partly with a 3D printer. The holder encompassed cooling channels in order to maintain constant saturation through-out the experiments which could last up to an hour. Several GDL samples were investigated, with little difference found between data-sets, except for a slight decrease in relative diffusivity for untreated samples compared with treated. However, behaviour observed by other researchers investigating TP relative diffusivity for varying hydrophobic treatment levels was not found in the current data, suggesting that the treatment affects transport differently in different directions. The method was found to produce the expected relation between relative diffusivity and saturation for homogeneous three-dimensional media: a power law dependence with exponent

around 2. Where other techniques for measuring effective properties of dry material are not suitable for measuring partially saturated material, this method has proved successful.

7.3 Scope for Future Work

It is recommended that further investigation into the land-channel influence on transport in the GDL is conducted, combining the topological considerations presented here, and the phase change considerations presented elsewhere. It is hoped that performing simulations with OpenPNM, an open source framework developed as part of this work, will aid future investigations. The work has highlighted the importance of choosing the appropriate pore-scale capillary pressure model in predicting the phase configurations under differing percolation scenarios. An assumption of the current work is that thin films of wetting fluid present in sub-pore-scale features such as cracks and corners do not effectively conduct. The morphological image opening technique used to establish the late pore filling relations has revealed that upon initial invasion, the residual wetting pore volume fraction is quite high. Therefore, future work could focus on the validity of the assumption that film conduction is very low. However, the PNM framework is not best suited to conduct this further investigation, and instead Lattice Boltzmann or other techniques resolving the microstructures with higher resolution would be required. An area where further investigation is warranted is the uniformity of PTFE treatment and its impact on multiphase flow, as highlighted by the experimental results. If PTFE inherently hinders through-plane transport and not in-plane transport, because of its interaction with the base fibrous structure, then alternative treatments that do not display this tendency may be more beneficial to fuel cell performance.

A very promising avenue for future modelling research is the combination of PNMs with other techniques and a few examples have already been published in the fuel cell literature [307], [308]. Whilst PNMs offer speedy calculations and simple algorithms for water placement, they are not readily applicable to models of single cells or stacks as not all components are porous and the length scales

involved in representing the various components mean that continuum approximations must be made when the pore size is much greater than or smaller than a suitable elementary volume. Therefore, coupling PNM's with CFD could be resource effective and illuminating. However, the nature of the coupling is critical and as yet not fully explored.

Extension of the experimental work could include investigation of the in-plane relative diffusivity under differing compression, with differing injection methods, and for different fuel cell layers. Due to time constraints, it was not possible to perform any of these additional investigations, and work focused solely on the method. Future work could utilise the same set-up with minor modification to measure the relative permeability and also study the effect of saturation and porosity inhomogeneity on the relative transport properties. In addition the bottom plate may be modified to allow for in-situ liquid injection, to investigate the effect of differing saturation distributions.

Appendices

Appendix A

Tabulated fitting parameters for compressed PNMs

CR	Shape	Location	Scale
0.0	0.217	-4.667E-06	3.678E-05
0.1	0.269	8.266E-07	2.956E-05
0.2	0.255	-8.112E-07	2.954E-05
0.3	0.234	-3.453E-06	3.032E-05
0.4	0.249	-2.876E-06	2.741E-05
0.5	0.260	-2.414E-06	2.429E-05

Table A.1: Pore diameter fitted parameters under compression using the lognorm distribution from SciPy's statistics routines.

CR	Shape	Location	Scale
0.0	0.152	-6.494	15.830
0.1	0.156	-6.019	15.105
0.2	0.151	-6.384	15.205
0.3	0.148	-6.743	15.212
0.4	0.142	-7.515	15.588
0.5	0.121	-10.483	18.076

Table A.2: Pore coordination fitted parameters under compression using the lognorm distribution from SciPy's statistics routines.

CR	Shape	Location	Scale
0.0	0.489	-4.521E-6	1.712E-5
0.1	0.489	-4.416E-6	1.649E-5
0.2	0.485	-4.462E-6	1.601E-5
0.3	0.484	-4.399E-6	1.549E-5
0.4	0.491	-4.271E-6	1.480E-5
0.5	0.502	-4.119E-6	1.409E-5

Table A.3: Throat diameter fitted parameters under compression using the lognorm distribution from SciPy's statistics routines.

CR	Shape	Location	Scale
0.0	0.332	8.769E-6	2.934E-5
0.1	0.312	6.689E-6	3.023E-5
0.2	0.352	8.829E-6	2.662E-5
0.3	0.145	-2.590E-5	6.094E-5
0.4	0.261	-7.59E-7	3.398E-5
0.5	0.256	-2.328E-6	3.431E-5

Table A.4: Throat length fitted parameters under compression using the lognorm distribution from SciPy's statistics routines.

Appendix B

Python code used to fit transient diffusion

```
import matplotlib.pyplot as plt
from matplotlib import style
from fipy import *
import numpy as np
import math
from scipy.optimize import minimize

style.use("ggplot")

#####################
#Experimental Data
times, O2 = bespoke_data_load_method(your_data)
#####################
#Constants

Dgdl_guess = 1.0e-5 # initial guess
num_iter = 15
nx = 380
dx = 1e-4
start_conc = O2[:3].mean()
end_conc= O2[len(O2)-20:].mean()
c0 = start_conc
c1 = end_conc
```

```
l = (nx)*dx
z = 10e-3
nmax = 100
s_l = 2.5e-2 # sample length
t_l = nx*dx #total length
Dbulk = 1.79e-5
timeStepDuration = 1
steps = np.int(len(times)/timeStepDuration)
best_sol = None
import time
st = time.time()
sim_count=0
####################
def run_simulation(Dgdl):
        global times
        global Dbulk
        global nx
        global dx
        global c0
        global c1
        global timeStepDuration
        global steps

        mesh = Grid1D(nx=nx, dx=dx)
        phi = CellVariable(name="O2 Concentration",
                           mesh=mesh,
                           value=c0)
        diff = CellVariable(name="diffusion coefficient",
                            mesh=mesh,
                            value=Dbulk)
        x = mesh.cellCenters[0]
        diff.setValue(Dgdl, where= x <= s_l)
        valueLeft = c1
        phi.constrain(valueLeft, mesh.facesLeft)
        # Explicit finite difference
        eqI = TransientTerm() == DiffusionTerm(coeff=diff)

        eq = eqI
        ct = np.zeros([steps,nx])
        solution = []
        solution.append(c0)
```

```
        sensor = np.int(nx-(z/dx))
        for step in range(steps-1):
        eq.solve(var=phi,dt=timeStepDuration)
        ct[step,:] = phi.value
        if np.remainder(step*timeStepDuration,1)==0:
        #print(phi.value[np.int(z*nx)])
        solution.append(ct[step,sensor])
        solution = np.asarray(solution)

        return solution
####################
#Analytical Solution
def sum_terms(D,l,z,nmax,t):
        my_sum = 0
        for n in range(nmax):
        my_sum+= ( (-1)**n * math.erfc( ((2*n+1)*l-z)
                / (2*np.sqrt(D*t)) ) )
        my_sum+= ( (-1)**n * math.erfc( ((2*n+1)*l+z)
                / (2*np.sqrt(D*t)) ) )
        return my_sum

####################
#Analytical Solution for all times
def run_d(D):
        global l
        global z
        global nmax
        global times
        global c1
        global c0

        c_t_test = np.zeros(len(times))
        for step, t in enumerate(times):
        c_t_test[step] = sum_terms(D,l,z,nmax,t)

        return (c1 - c0)*c_t_test + c0
####################
#Assess deviation from analytical solution
def evaluate_d(D, sol):
        global sim_count
        global st
```

```
        c_t = run_d(D)
        sq_diff = np.sum((c_t - sol)**2)
        sim_count +=1
        return sq_diff
####################
#Assess deviation from analytical solution
def evaluate_d_sim(D):
        global st
        global sim_count
        global O2
        global best_sol
        sol = run_simulation(D)
        best_sol = sol
        sq_diff = np.sum((sol - O2)**2)
        sim_count +=1
        return sq_diff
####################
#solution = run_simulation(Dgdl)
ig = t_l/((s_l/Dgdl_guess)+((t_l - s_l)/Dbulk)) # initial guess
#Crank Fit
print("Starting Crank fit, time: " +str(time.time()-st))
result1 = minimize(fun=evaluate_d,
x0=(ig,),
args=(O2,),
bounds=((ig*0.5,ig*1.5),),
method = 'L-BFGS-B',
options={'ftol':1e-99, 'gtol':1e-99, 'maxfun':num_iter})
Dcrank = result1.x[0]
Dres = s_l/((t_l/Dcrank)-((t_l - s_l)/Dbulk))
#Fipy simulation fit
ig = Dcrank
sim_count=0
print("Starting Simulation fit, time: " +str(time.time()-st))
result2 = minimize(fun=evaluate_d_sim,
x0=(ig,),
bounds=((ig*0.5,ig*1.5),),
method = 'L-BFGS-B',
options={'ftol':1e-99, 'gtol':1e-99, 'maxfun':num_iter})
Dsim = result2.x[0]
print("Start conc",start_conc,"End conc",end_conc)
print('----------------------')
```

```
print("D Sim Fitted: "+str(Dsim))
print("D Crank Fitted: "+str(Dcrank))
print("D Resistors: " +str(Dres))
print("Error: "+str(np.around(100*np.abs(Dres-Dsim)/Dsim))+"%")

plt.figure()
plt.plot(times,best_sol,'b-', label="Sim Fitted")
plt.plot(times,run_d(Dcrank),'r-', label="Crank")
plt.plot(times,O2,'g-', label="Experiment")
plt.legend(bbox_to_anchor=(0,1.02,1,0.102),
           loc=3,
           ncol=5,
           borderaxespad=0)
```

References

[1] T. G. Tranter, A. D. Burns, D. B. Ingham, and M. Pourkashanian, "The effects of compression on single and multiphase flow in a model polymer electrolyte membrane fuel cell gas diffusion layer," *International Journal of Hydrogen Energy*, vol. 40, pp. 652–664, dec 2014.

[2] T. G. Tranter, J. T. Gostick, A. D. Burns, and W. F. Gale, "Pore Network Modeling of Compressed Fuel Cell Components with OpenPNM," *Fuel Cells*, vol. 16, no. 4, pp. 504–515, 2016.

[3] J. T. Gostick, M. Aghighi, J. Hinebaugh, T. G. Tranter, M. Höh, H. Day, A. Bazylak, A. D. Burns, W. Lehnert, and A. Putz, "Openpnm: A pore network modeling package," *CISE*, vol. 18, pp. 60 – 74, 2016.

[4] BP, "BP Statistical Review of World Energy, 2013," 2013.

[5] R. Rashapov, F. Imami, and J. T. Gostick, "A method for measuring in-plane effective diffusivity in thin porous media," *International Journal of Heat and Mass Transfer*, vol. 85, pp. 367–374, June 2015.

[6] F. Barbir, *PEM fuel cells: theory and practice*. Academic Press, 2012.

[7] K. Jiao and X. Li, "Water transport in polymer electrolyte membrane fuel cells," *Progress in Energy and Combustion Science*, vol. 37, pp. 221–291, June 2011.

[8] U. Pasaogullari and C. Y. Wang, "Liquid Water Transport in Gas Diffusion Layer of Polymer Electrolyte Fuel Cells," *Journal of The Electrochemical Society*, vol. 151, no. 3, p. A399, 2004.

[9] J. T. Gostick, M. a. Ioannidis, W. Fowler, and M. D. Pritzker, "Characterization of the Capillary Properties of Gas Diffusion Media," *Modeling and Diagnostics of Polymer Electrolyte Fuel Cells in Modern Aspects of Electrochemistry*, pp. 225–254, 2010.

[10] J. H. Nam, K.-J. Lee, G.-S. Hwang, C.-J. Kim, and M. Kaviany, "Microporous layer for water morphology control in PEMFC," *International Journal of Heat and Mass Transfer*, vol. 52, pp. 2779–2791, may 2009.

[11] C. Xu and T. S. Zhao, "A new flow field design for polymer electrolyte-based fuel cells," *Electrochemistry Communications*, vol. 9, pp. 497–503, Mar. 2007.

[12] P. J. Hamilton and B. G. Pollet, "Polymer Electrolyte Membrane Fuel Cell (PEMFC) Flow Field Plate: Design, Materials and Characterisation," *Fuel Cells*, vol. 10, pp. 489–509, May 2010.

[13] C. E. Colosqui, M. J. Cheah, I. G. Kevrekidis, and J. B. Benziger, "Droplet and slug formation in polymer electrolyte membrane fuel cell flow channels: The role of interfacial forces," *Journal of Power Sources*, vol. 196, pp. 10057–10068, Dec. 2011.

[14] J. Eller, T. Rosén, F. Marone, M. Stampanoni, A. Wokaun, and F. N. Büchi, "Progress in in situ x-ray tomographic microscopy of liquid water in gas diffusion layers of pefc," *Journal of The Electrochemical Society*, vol. 158, no. 8, pp. B963–B970, 2011.

[15] J. H. Nam and M. Kaviany, "Effective diffusivity and water-saturation distribution in single- and two-layer PEMFC diffusion medium," *International Journal of Heat and Mass Transfer*, vol. 46, pp. 4595–4611, Nov. 2003.

[16] S. Litster, D. Sinton, and N. Djilali, "Ex situ visualization of liquid water transport in PEM fuel cell gas diffusion layers," *Journal of Power Sources*, vol. 154, pp. 95–105, Mar. 2006.

[17] J. T. Gostick, M. A. Ioannidis, M. W. Fowler, and M. D. Pritzker, "Wettability and capillary behavior of fibrous gas diffusion media for polymer electrolyte membrane fuel cells," *Journal of Power Sources*, vol. 194, pp. 433–444, Oct. 2009.

[18] G. S. Hwang and A. Z. Weber, "Effective-Diffusivity Measurement of Partially-Saturated Fuel-Cell Gas-Diffusion Layers," *Journal of the Electrochemical Society*, vol. 159, pp. F683–F692, Aug. 2012.

[19] G. Meehl and T. Karl, "An Introduction to Trends in Extreme Weather and Climate Events: Observations, Socioeconomic Impacts, Terrestrial Ecological Impacts, and Model Projections," *Bulletin of the American Meteorological Society*, pp. 413–416, 2000.

[20] IPCC, "IPCC Fourth Assessment Report: Climate Change 2007," 2007.

[21] R. K. Pachauri, M. R. Allen, V. R. Barros, J. Broome, W. Cramer, R. Christ, J. A. Church, L. Clarke, Q. Dahe, P. Dasgupta, *et al.*, "Climate change 2014: Synthesis report. contribution of working groups i, ii and iii to the fifth assessment report of the intergovernmental panel on climate change," 2014.

[22] H. Ibrahim, A. Ilinca, and J. Perron, "Energy storage systems - Characteristics and comparisons," *Renewable and Sustainable Energy Reviews*, vol. 12, pp. 1221–1250, June 2008.

[23] M. H. Albadi and E. F. El-Saadany, "Overview of wind power intermittency impacts on power systems," *Electric Power Systems Research*, vol. 80, no. 6, pp. 627–632, 2010.

[24] H. Chen, T. N. Cong, W. Yang, C. Tan, Y. Li, and Y. Ding, "Progress in electrical energy storage system: A critical review," *Progress in Natural Science*, vol. 19, no. 3, pp. 291–312, 2009.

[25] Z. Yang, J. Zhang, M. C. W. Kintner-meyer, X. Lu, D. Choi, and J. P. Lemmon, "Electrochemical energy storage for green grid.pdf," *Chemical reviews*, pp. 3577–3613, 2011.

[26] J. Andrews and B. Shabani, "Re-envisioning the role of hydrogen in a sustainable energy economy," *International Journal of Hydrogen Energy*, vol. 37, no. 2, pp. 1184–1203, 2012.

[27] M. Ball and M. Weeda, "The hydrogen economy - Vision or reality?," *International Journal of Hydrogen Energy*, vol. 40, no. 25, pp. 7903–7919, 2015.

[28] N. Konno, S. Mizuno, H. Nakaji, and Y. Ishikawa, "Development of compact and high-performance fuel cell stack," *SAE International Journal of Alternative Powertrains*, vol. 4, no. 2015-01-1175, pp. 123–129, 2015.

[29] G. Hoogers, *Fuel Cell Technology Handbook*. CRC, 2002.

[30] A. B. Stambouli, "Fuel cells: The expectations for an environmental-friendly and sustainable source of energy," *Renewable and Sustainable Energy Reviews*, vol. 15, pp. 4507–4520, Dec. 2011.

[31] A. Kraytsberg and Y. Ein-Eli, "Review on Li-air batteries - Opportunities, limitations and perspective," *Journal of Power Sources*, vol. 196, pp. 886–893, Feb. 2011.

[32] A. Z. Weber, M. M. Mench, J. P. Meyers, P. N. Ross, J. T. Gostick, and Q. Liu, "Redox flow batteries: A review," *Journal of Applied Electrochemistry*, vol. 41, no. 10, pp. 1137–1164, 2011.

[33] P. Jena, "Materials for hydrogen storage: Past, present, and future," *Journal of Physical Chemistry Letters*, vol. 2, no. 3, pp. 206–211, 2011.

[34] B. Sørensen, *Hydrogen and Fuel Cells: Emerging Technologies and Applications*. Academic Press, 2005.

[35] J. R. Bartels, M. B. Pate, and N. K. Olson, "An economic survey of hydrogen production from conventional and alternative energy sources," *International Journal of Hydrogen Energy*, vol. 35, no. 16, pp. 8371–8384, 2010.

[36] A. Kirubakaran, S. Jain, and R. K. Nema, "A review on fuel cell technologies and power electronic interface," *Renewable and Sustainable Energy Reviews*, vol. 13, no. 9, pp. 2430–2440, 2009.

[37] M. M. Mench, *Fuel Cell Engines*. John Wiley & Sons, 2008.

[38] UKH2, "UK H2 Mobility, Phase 1 Results." `https://www.gov.uk/government/uploads/system/uploads/attachment_data/file/192440/13-799-uk-h2-mobility-phase-1-results.pdf`, 2013.

[39] T. E. Springer, "Polymer Electrolyte Fuel Cell Model," *Journal of The Electrochemical Society*, vol. 138, no. 8, p. 2334, 1991.

[40] M. Ji and Z. Wei, "A Review of Water Management in Polymer Electrolyte Membrane Fuel Cells," *Energies*, vol. 2, pp. 1057–1106, Nov. 2009.

[41] Z. Chen, D. Higgins, A. Yu, L. Zhang, and J. Zhang, "A review on non-precious metal electrocatalysts for PEM fuel cells," *Energy & Environmental Science*, vol. 4, no. 9, p. 3167, 2011.

[42] M. K. Debe, "Electrocatalyst approaches and challenges for automotive fuel cells," *Nature*, vol. 486, no. 7401, pp. 43–51, 2012.

[43] S. Park, J.-W. Lee, and B. N. Popov, "A review of gas diffusion layer in PEM fuel cells: Materials and designs," *International Journal of Hydrogen Energy*, vol. 37, pp. 5850–5865, Apr. 2012.

[44] S. Park and B. N. Popov, "Effect of a GDL based on carbon paper or carbon cloth on PEM fuel cell performance," *Fuel*, vol. 90, no. 1, pp. 436–440, 2011.

[45] A. El-Kharouf, T. J. Mason, D. J. L. Brett, and B. G. Pollet, "Ex-situ characterisation of gas diffusion layers for proton exchange membrane fuel cells," *Journal of Power Sources*, vol. 218, pp. 393–404, Nov. 2012.

[46] R. R. Rashapov, J. Unno, and J. T. Gostick, "Characterization of pemfc gas diffusion layer porosity," *Journal of The Electrochemical Society*, vol. 162, no. 6, pp. F603–F612, 2015.

[47] M. S. Ismail, K. J. Hughes, D. B. Ingham, L. Ma, and M. Pourkashanian, "Effects of anisotropic permeability and electrical conductivity of gas diffusion layers on the performance of proton exchange membrane fuel cells," *Applied Energy*, vol. 95, pp. 50–63, July 2012.

[48] N. Alhazmi, D. B. Ingham, M. S. Ismail, K. J. Hughes, L. Ma, and M. Pourkashanian, "Effect of the anisotropic thermal conductivity of GDL on the performance of PEM fuel cells," *International Journal of Hydrogen Energy*, vol. 38, pp. 603–611, Jan. 2013.

[49] L. Shen and Z. Chen, "Critical review of the impact of tortuosity on diffusion," *Chemical Engineering Science*, vol. 62, no. 14, pp. 3748–3755, 2007.

[50] N. Epstein, "On tortuosity and the tortuosity factor in flow and diffusion through porous media," *Chemical Engineering Science*, pp. 3–5, 1989.

[51] D. A. G. Bruggeman, "Calculation of various physical constants of heterogenous substances. ii. dielectricity constants and conductivity of non regular multi crystal systems," *Annalen Der Physik*, vol. 25, no. 7, pp. 0645–0672, 1936.

[52] N. Zamel and X. Li, "Effective transport properties for polymer electrolyte membrane fuel cells - With a focus on the gas diffusion layer," *Progress in Energy and Combustion Science*, vol. 39, pp. 111–146, Feb. 2013.

[53] M. S. Ismail, D. B. Ingham, K. J. Hughes, L. Ma, and M. Pourkashanian, "Effective diffusivity of polymer electrolyte fuel cell gas diffusion layers: An overview and numerical study," *International Journal of Hydrogen Energy*, vol. 40, no. 34, pp. 10994–11010, 2015.

[54] Q. Ye and T. V. Nguyen, "Three-Dimensional Simulation of Liquid Water Distribution in a PEMFC with Experimentally Measured Capillary Functions," *Journal of The Electrochemical Society*, vol. 154, no. 12, p. B1242, 2007.

[55] J. T. Gostick, M. W. Fowler, M. A. Ioannidis, M. D. Pritzker, Y. M. Volfkovich, and A. Sakars, "Capillary pressure and hydrophilic porosity in gas diffusion layers for polymer electrolyte fuel cells," *Journal of Power Sources*, vol. 156, pp. 375–387, June 2006.

[56] I. S. Hussaini and C. Y. Wang, "Measurement of relative permeability of fuel cell diffusion media," *Journal of Power Sources*, vol. 195, no. 12, pp. 3830–3840, 2010.

[57] M. Kaviany, *Principles of Heat Transfer in Porous Media*. Springer-Verlag, New York, 1995.

[58] P. K. Sinha and C.-Y. Wang, "Pore-network modeling of liquid water transport in gas diffusion layer of a polymer electrolyte fuel cell," *Electrochimica Acta*, vol. 52, pp. 7936–7945, Nov. 2007.

[59] Z. Fishman and A. Bazylak, "Heterogeneous through-plane distributions of tortuosity, effective diffusivity, and permeability for pemfc gdls," *Journal of The Electrochemical Society*, vol. 158, no. 2, pp. B247–B252, 2011.

[60] A. Z. Weber, R. L. Borup, R. M. Darling, P. K. Das, T. J. Dursch, W. Gu, D. Harvey, A. Kusoglu, S. Litster, M. M. Mench, R. Mukundan, J. P. Owejan, J. G. Pharoah, M. Secanell, and I. V. Zenyuk, "A Critical Review of Modeling Transport Phenomena in Polymer-Electrolyte Fuel Cells," *Journal of the Electrochemical Society*, vol. 161, pp. F1254–F1299, sep 2014.

[61] E. W. Washburn, "The dynamics of capillary flow," *Physical Review*, vol. 17, no. 3, pp. 273–283, 1921.

[62] G. Mason and N. R. Morrow, "Effect of contact angle on capillary displacement curvatures in pore throats formed by spheres," *Journal of Colloid and Interface Science*, 1994.

[63] K. S. Udell, "Heat transfer in porous media considering phase change and capillarity - the heat pipe effect," *International Journal of Heat and Mass Transfer*, vol. 28, pp. 485–495, Feb. 1985.

[64] E. C. Kumbur, K. V. Sharp, and M. M. Mench, "Validated Leverett Approach for Multiphase Flow in PEFC Diffusion Media I. Hydrophobicity Effect," *Journal of The Electrochemical Society*, vol. 154, no. 12, p. B1295, 2007.

[65] X. Liu, F. Peng, G. Lou, and Z. Wen, "Liquid water transport characteristics of porous diffusion media in polymer electrolyte membrane fuel cells: A review," *Journal of Power Sources*, vol. 299, pp. 85–96, 2015.

[66] J. Benziger, J. Nehlsen, D. Blackwell, T. Brennan, and J. Itescu, "Water flow in the gas diffusion layer of PEM fuel cells," *Journal of Membrane Science*, vol. 261, pp. 98–106, Sept. 2005.

[67] J. T. Gostick, M. A. Ioannidis, M. W. Fowler, and M. D. Pritzker, "Direct measurement of the capillary pressure characteristics of water-air-gas diffusion layer systems for PEM fuel cells," *Electrochemistry Communications*, vol. 10, pp. 1520–1523, oct 2008.

[68] W. R. Purcell, "Interpretation of capillary pressure data," *Journal of Petroleum Technology*, vol. 189, pp. 369–371, 1950.

[69] J. T. Gostick, "Random Pore Network Modeling of Fibrous PEMFC Gas Diffusion Media Using Voronoi and Delaunay Tessellations," *Journal of the Electrochemical Society*, vol. 160, pp. F731–F743, Apr. 2013.

[70] S. Motupally, A. J. Becker, and J. W. Weidner, "Diffusion of Water in Nafion 115 Membranes," *Journal of The Electrochemical Society*, vol. 147, no. 9, pp. 3171–3177, 2000.

[71] H. Zhang and P. K. Shen, "Recent development of polymer electrolyte membranes for fuel cells," *Chemical Reviews*, vol. 112, no. 5, pp. 2780–2832, 2012.

[72] T. J. P. Freire and E. R. Gonzalez, "Effect of membrane characteristics and humidification conditions on the impedance response of polymer electrolyte fuel cells," *Journal of Electroanalytical Chemistry*, vol. 503, no. 1, pp. 57–68, 2001.

[73] S. Tsushima, T. Ikeda, T. Koido, and S. Hirai, "Investigation of Water Distribution in a Membrane in an Operating PEMFC by Environmental MRI," *Journal of The Electrochemical Society*, vol. 157, no. 12, p. B1814, 2010.

[74] T. J. Mason, J. Millichamp, T. P. Neville, P. R. Shearing, S. Simons, and D. J. L. Brett, "A study of the effect of water management and electrode flooding onÂăthe dimensional change of polymer electrolyte fuel cells," *Journal of Power Sources*, vol. 242, pp. 70–77, nov 2013.

[75] T. Berning, D. M. Lu, and N. Djilali, "Three-dimensional computational analysis of transport phenomena in a PEM fuel cell," *Journal of power sources*, vol. 106, no. 1, pp. 284–294, 2002.

[76] A. Z. Weber and J. Newman, "Transport in polymer-electrolyte membranes I. Physical model," *Journal of the Electrochemical Society*, vol. 150, no. 7, pp. A1008–A1015, 2003.

[77] J. Zhang, Z. Xie, J. Zhang, Y. Tang, C. Song, T. Navessin, Z. Shi, D. Song, H. Wang, D. P. Wilkinson, Z.-S. Liu, and S. Holdcroft, "High temperature PEM fuel cells," *Journal of Power Sources*, vol. 160, pp. 872–891, Oct. 2006.

[78] A. Z. Weber and J. Newman, "Effects of Microporous Layers in Polymer Electrolyte Fuel Cells," *Journal of The Electrochemical Society*, vol. 152, no. 4, p. A677, 2005.

[79] U. Pasaogullari, C.-Y. Wang, and K. S. Chen, "Two-phase transport in polymer electrolyte fuel cells with bilayer cathode gas diffusion media," *Journal of The Electrochemical Society*, vol. 152, no. 8, pp. A1574–A1582, 2005.

[80] J. M. LaManna and S. G. Kandlikar, "Determination of effective water vapor diffusion coefficient in pemfc gas diffusion layers," *International Journal of Hydrogen Energy*, vol. 36, pp. 5021–5029, Apr. 2011.

[81] J. Becker, C. Wieser, S. Fell, and K. Steiner, "A multi-scale approach to material modeling of fuel cell diffusion media," *International Journal of Heat and Mass Transfer*, vol. 54, pp. 1360–1368, Mar. 2011.

[82] M. V. Williams, E. Begg, L. Bonville, H. R. Kunz, and J. M. Fenton, "Characterization of Gas Diffusion Layers for PEMFC," *Journal of The Electrochemical Society*, vol. 151, no. 8, p. A1173, 2004.

[83] J. T. Gostick, M. A. Ioannidis, M. W. Fowler, and M. D. Pritzker, "On the role of the microporous layer in PEMFC operation," *Electrochemistry Communications*, vol. 11, pp. 576–579, Mar. 2009.

[84] Z. Lu, S. G. Kandlikar, C. Rath, M. Grimm, W. Domigan, A. D. White, M. Hardbarger, J. P. Owejan, and T. A. Trabold, "Water management studies in pem fuel cells, part ii: Ex situ investigation of flow maldistribution, pressure drop and two-phase flow pattern in gas channels," *International Journal of Hydrogen Energy*, vol. 34, no. 8, pp. 3445–3456, 2009.

[85] Z. Lu, M. M. Daino, C. Rath, and S. G. Kandlikar, "Water management studies in PEM fuel cells, part III: Dynamic breakthrough and intermittent drainage characteristics from GDLs with and without MPLs," *International Journal of Hydrogen Energy*, vol. 35, pp. 4222–4233, May 2010.

[86] J. H. Kang, K.-J. Lee, S. H. Yu, J. H. Nam, and C.-J. Kim, "Demonstration of water management role of microporous layer by similarity model experiments," *International Journal of Hydrogen Energy*, vol. 35, pp. 4264–4269, May 2010.

[87] K. N. Kim, J. H. Kang, S. G. Lee, J. H. Nam, and C.-J. Kim, "Lattice Boltzmann simulation of liquid water transport in microporous and gas diffusion layers of polymer electrolyte membrane fuel cells," *Journal of Power Sources*, vol. 278, pp. 703–717, Mar. 2015.

[88] J. P. Owejan, J. E. Owejan, W. Gu, T. A. Trabold, T. W. Tighe, and M. F. Mathias, "Water Transport Mechanisms in PEMFC Gas Diffusion Layers," *Journal of The Electrochemical Society*, vol. 157, no. 10, p. B1456, 2010.

[89] X. Wang, H. Zhang, J. Zhang, H. Xu, X. Zhu, J. Chen, and B. Yi, "A bi-functional micro-porous layer with composite carbon black for PEM fuel cells," *Journal of Power Sources*, vol. 162, pp. 474–479, Nov. 2006.

[90] C. S. Kong, D.-Y. Kim, H.-K. Lee, Y.-G. Shul, and T.-H. Lee, "Influence of pore-size distribution of diffusion layer on mass-transport problems of proton exchange membrane fuel cells," *Journal of Power Sources*, vol. 108, no. 1, pp. 185–191, 2002.

[91] Q. Duan, B. Wang, J. Wang, H. Wang, and Y. Lu, "Fabrication of a carbon nanofiber sheet as a micro-porous layer for proton exchange membrane fuel cells," *Journal of Power Sources*, vol. 195, pp. 8189–8193, Dec. 2010.

[92] M. Uchida, Y. Fukuoka, Y. Sugawara, N. Eda, and A. Ohta, "Effects of microstructure of carbon support in the catalyst layer on the performance of polymer-electrolyte fuel cells," *Journal of The Electrochemical Society*, vol. 143, no. 7, pp. 2245–2252, 1996.

[93] P. K. Das, "Liquid-Water Uptake and Removal in PEM Fuel-Cell Components," *Berkeley Lab Online Publication*, 2013.

[94] F.-Y. Zhang, D. Spernjak, A. K. Prasad, and S. G. Advani, "In Situ Characterization of the Catalyst Layer in a Polymer Electrolyte Membrane Fuel Cell," *Journal of The Electrochemical Society*, vol. 154, no. 11, p. B1152, 2007.

[95] H. Wu, X. Li, and P. Berg, "On the modeling of water transport in polymer electrolyte membrane fuel cells," *Electrochimica Acta*, vol. 54, pp. 6913–6927, Nov. 2009.

[96] M. B. Ji, Z. D. Wei, S. G. Chen, and L. Li, "A Novel Antiflooding Electrode for Proton Exchange Membrane Fuel Cells," *The Journal of Physical Chemistry C*, vol. 113, pp. 765–771, Jan. 2009.

[97] J. E. Steinbrenner, E. S. Lee, C. H. Hidrovo, J. K. Eaton, and K. E. Goodson, "Impact of channel geometry on two-phase flow in fuel cell microchannels," *Journal of Power Sources*, vol. 196, pp. 5012–5020, June 2011.

[98] A. Arvay, J. French, J.-C. Wang, X.-H. Peng, and A. M. Kannan, "Nature inspired flow field designs for proton exchange membrane fuel cell," *international journal of hydrogen energy*, vol. 38, no. 9, pp. 3717–3726, 2013.

[99] J. Scholta, G. Escher, W. Zhang, L. Küppers, L. Jörissen, and W. Lehnert, "Investigation on the influence of channel geometries on PEMFC performance," *Journal of Power Sources*, vol. 155, pp. 66–71, Apr. 2006.

[100] J. Owejan, T. Trabold, D. Jacobson, M. Arif, and S. Kandlikar, "Effects of flow field and diffusion layer properties on water accumulation in a PEM fuel cell," *International Journal of Hydrogen Energy*, vol. 32, pp. 4489–4502, Dec. 2007.

[101] S. C. Cho, Y. Wang, and K. S. Chen, "Droplet dynamics in a polymer electrolyte fuel cell gas flow channel: Forces, Deformation and detachment. II: Comparisons of analytical solution with numerical and experimental results," *Journal of Power Sources*, vol. 210, pp. 191–197, July 2012.

[102] A. Theodorakakos, T. Ous, M. Gavaises, J. M. Nouri, N. Nikolopoulos, and H. Yanagihara, "Dynamics of water droplets detached from porous surfaces of relevance to PEM fuel cells.," *Journal of Colloid and Interface Science*, vol. 300, pp. 673–87, Aug. 2006.

[103] L. Chen, Y.-L. He, and W.-Q. Tao, "Effects of surface microstructures of gas diffusion layer on water droplet dynamic behaviors in a micro gas channel of proton exchange membrane fuel cells," *International Journal of Heat and Mass Transfer*, vol. 60, pp. 252–262, May 2013.

[104] H.-i. Kim, J. H. Nam, D. Shin, T.-Y. Chung, and Y.-G. Kim, "A numerical study on liquid water exhaust capabilities of flow channels in polymer electrolyte membrane fuel cells," *Current Applied Physics*, vol. 10, pp. S91–S96, Mar. 2010.

[105] Y. Wang, "Porous-Media Flow Fields for Polymer Electrolyte Fuel Cells : I. Low Humidity Operation," *Journal of The Electrochemical Society*, vol. 156, no. 10, pp. B1124–B1133, 2009.

[106] Y. Wang, "Porous-Media Flow Fields for Polymer Electrolyte Fuel Cells: II. Analysis of Channel Two-Phase Flow," *Journal of The Electrochemical Society*, vol. 156, no. 10, pp. B1134–B1141, 2009.

[107] C. Hartnig, I. Manke, R. Kuhn, S. Kleinau, J. Goebbels, and J. Banhart, "High-resolution in-plane investigation of the water evolution and transport in PEM fuel cells," *Journal of Power Sources*, vol. 188, no. 2, pp. 468–474, 2009.

[108] V. Gurau and J. A. Mann, "Effect of Interfacial Phenomena at the Gas Diffusion Layer-Channel Interface on the Water Evolution in a PEMFC," *Journal of The Electrochemical Society*, vol. 157, no. 4, p. B512, 2010.

[109] C. Y. Wang and P. Cheng, "Multiphase flow and heat transfer in porous media," *Advances in Heat Transfer*, vol. 30, pp. 93–196, 1997.

[110] Z. H. Wang, C. Y. Wang, and K. S. Chen, "Two-phase flow and transport in the air cathode of proton exchange membrane fuel cells," *Journal of Power Sources*, vol. 94, pp. 40–50, 2001.

[111] S. Mazumder and J. V. Cole, "Rigorous 3-D Mathematical Modeling of PEM Fuel Cells: I. Model Predictions without Liquid Water Transport," *Journal of The Electrochemical Society*, vol. 150, no. 11, p. A1503, 2003.

[112] S. Mazumder and J. V. Cole, "Rigorous 3-D Mathematical Modeling of PEM Fuel Cells: II. Model Predictions with Liquid Water Transport," *Journal of The Electrochemical Society*, vol. 150, no. 11, pp. A1510–A1517, 2003.

[113] V. Gurau and J. A. Mann Jr, "A critical overview of computational fluid dynamics multiphase models for proton exchange membrane fuel cells," *SIAM Journal on Applied Mathematics*, vol. 70, no. 2, pp. 410–454, 2009.

[114] C.-Y. Wang, "Fundamental models for fuel cell engineering.," *Chemical Reviews*, vol. 104, pp. 4727–65, Oct. 2004.

[115] W. He, J. S. Yi, and T. V. Nguyen, "Two-phase flow model of the cathode of PEM fuel cells using interdigitated flow fields," *AIChE Journal*, vol. 46, pp. 2053–2064, Oct. 2000.

[116] E. C. Kumbur, K. V. Sharp, and M. M. Mench, "Validated Leverett Approach for Multiphase Flow in PEFC Diffusion Media II. Compression Effect," *Journal of The Electrochemical Society*, vol. 154, no. 12, p. B1305, 2007.

[117] E. C. Kumbur, K. V. Sharp, and M. M. Mench, "Validated Leverett Approach for Multiphase Flow in PEFC Diffusion Media III. Temperature Effect and Unified Approach," *Journal of The Electrochemical Society*, vol. 154, no. 12, p. B1315, 2007.

[118] V. Gurau, T. A. Zawodzinski, and J. A. Mann, "Two-Phase Transport in PEM Fuel Cell Cathodes," *Journal of Fuel Cell Science and Technology*, vol. 5, no. 2, p. 021009, 2008.

[119] C. Qin, D. Rensink, S. Fell, and S. Majid Hassanizadeh, "Two-phase flow modeling for the cathode side of a polymer electrolyte fuel cell," *Journal of Power Sources*, vol. 197, pp. 136–144, Jan. 2012.

[120] J. W. Park, K. Jiao, and X. Li, "Numerical investigations on liquid water removal from the porous gas diffusion layer by reactant flow," *Applied Energy*, vol. 87, no. 7, pp. 2180–2186, 2010.

[121] P. V. Suresh and S. Jayanti, "Effect of air flow on liquid water transport through a hydrophobic gas diffusion layer of a polymer electrolyte membrane fuel cell," *International Journal of Hydrogen Energy*, vol. 35, pp. 6872–6886, July 2010.

[122] A. D. Le and B. Zhou, "A general model of proton exchange membrane fuel cell," *Journal of Power Sources*, vol. 182, pp. 197–222, July 2008.

[123] A. D. Le and B. Zhou, "A generalized numerical model for liquid water in a proton exchange membrane fuel cell with interdigitated design," *Journal of Power Sources*, vol. 193, pp. 665–683, Sept. 2009.

[124] A. D. Le, B. Zhou, H.-R. Shiu, C.-I. Lee, and W.-C. Chang, "Numerical simulation and experimental validation of liquid water behaviors in a proton

exchange membrane fuel cell cathode with serpentine channels," *Journal of Power Sources*, vol. 195, pp. 7302–7315, Nov. 2010.

[125] R. Anderson, L. Zhang, Y. Ding, M. Blanco, X. Bi, and D. P. Wilkinson, "A critical review of two-phase flow in gas flow channels of proton exchange membrane fuel cells," *Journal of Power Sources*, vol. 195, pp. 4531–4553, Aug. 2010.

[126] X. Wang and B. Zhou, "Liquid water flooding process in proton exchange membrane fuel cell cathode with straight parallel channels and porous layer," *Journal of Power Sources*, vol. 196, pp. 1776–1794, Feb. 2011.

[127] M. I. Rosli, D. J. Borman, D. B. Ingham, M. S. Ismail, L. Ma, and M. Pourkashanian, "Transparent PEM Fuel Cells for Direct Visualization Experiments," *Journal of Fuel Cell Science and Technology*, vol. 7, no. 6, p. 061015, 2010.

[128] R. B. Ferreira, D. Falcão, V. Oliveira, and A. Pinto, "Numerical simulations of two-phase flow in proton exchange membrane fuel cells using the volume of fluid method–a review," *Journal of Power Sources*, vol. 277, pp. 329–342, 2015.

[129] J. T. Gostick, M. A. Ioannidis, M. W. Fowler, and M. D. Pritzker, "Pore network modeling of fibrous gas diffusion layers for polymer electrolyte membrane fuel cells," *Journal of Power Sources*, vol. 173, no. 1, pp. 277–290, 2007.

[130] L. Chen, Y.-L. Feng, C.-X. Song, L. Chen, Y.-L. He, and W.-Q. Tao, "Multi-scale modeling of proton exchange membrane fuel cell by coupling finite volume method and lattice boltzmann method," *International Journal of Heat and Mass Transfer*, vol. 63, pp. 268–283, 2013.

[131] A. Putz, J. Hinebaugh, M. Aghighi, H. Day, A. Bazylak, and J. T. Gostick, "Introducing OpenPNM: An Open Source Pore Network Modeling Software Package," *ECS Transactions*, vol. 58, no. 1, pp. 79–86, 2013.

[132] O. Chapuis, M. Prat, M. Quintard, E. Chane-Kane, O. Guillot, and N. Mayer, "Two-phase flow and evaporation in model fibrous media," *Journal of Power Sources*, vol. 178, pp. 258–268, Mar. 2008.

[133] G. Luo, Y. Ji, C.-Y. Wang, and P. K. Sinha, "Modeling liquid water transport in gas diffusion layers by topologically equivalent pore network," *Electrochimica Acta*, vol. 55, pp. 5332–5341, July 2010.

[134] M. Fazeli, J. Hinebaugh, and A. Bazylak, "Investigating Inlet Condition Effects on PEMFC GDL Liquid Water Transport through Pore Network Modeling," *ECS Transactions*, vol. 64, no. 3, pp. 593–602, 2014.

[135] T. Agaesse, A. Lamibrac, F. Büchii, J. Pauchet, M. Marcoux, and M. Prat, "A comparison between x-ray tomography images of water distribution in a gas diffusion layer and pore network simulations," *Submitted for publication*, 2015.

[136] K. E. Thompson, "Pore-scale modeling of fluid transport in disordered fibrous materials," *AIChE Journal*, vol. 48, pp. 1369–1389, July 2002.

[137] J. Hinebaugh, Z. Fishman, and A. Bazylak, "Unstructured Pore Network Modeling with Heterogeneous PEMFC GDL Porosity Distributions," *Journal of The Electrochemical Society*, vol. 157, no. 11, p. B1651, 2010.

[138] Z. Fishman, J. Hinebaugh, and A. Bazylak, "Microscale Tomography Investigations of Heterogeneous Porosity Distributions of PEMFC GDLs," *Journal of The Electrochemical Society*, vol. 157, no. 11, p. B1643, 2010.

[139] D. Kramer, S. A. Freunberger, R. Flückiger, I. A. Schneider, A. Wokaun, F. N. Büchi, and G. G. Scherer, "Electrochemical diffusimetry of fuel cell gas diffusion layers," *Journal of Electroanalytical Chemistry*, vol. 612, no. 1, pp. 63–77, 2008.

[140] R. Flückiger, S. A. Freunberger, D. Kramer, A. Wokaun, G. G. Scherer, and F. N. Büchi, "Anisotropic, effective diffusivity of porous gas diffusion layer materials for PEFC," *Electrochimica Acta*, vol. 54, pp. 551–559, Dec. 2008.

[141] J. T. Gostick, M. W. Fowler, M. D. Pritzker, M. A. Ioannidis, and L. M. Behra, "In-plane and through-plane gas permeability of carbon fiber electrode backing layers," *Journal of Power Sources*, vol. 162, pp. 228–238, Nov. 2006.

[142] R. Wu, X. Zhu, Q. Liao, H. Wang, Y.-d. Ding, J. Li, and D.-d. Ye, "Determination of oxygen effective diffusivity in porous gas diffusion layer using a three-dimensional pore network model," *Electrochimica Acta*, vol. 55, pp. 7394–7403, Oct. 2010.

[143] A. Bazylak, V. Berejnov, B. Markicevic, D. Sinton, and N. Djilali, "Numerical and microfluidic pore networks: Towards designs for directed water transport in GDLs," *Electrochimica Acta*, vol. 53, pp. 7630–7637, Nov. 2008.

[144] V. P. Schulz, J. Becker, A. Wiegmann, P. P. Mukherjee, and C.-Y. Wang, "Modeling of Two-Phase Behavior in the Gas Diffusion Medium of PEFCs via Full Morphology Approach," *Journal of The Electrochemical Society*, vol. 154, no. 4, p. B419, 2007.

[145] N. Zamel, X. Li, J. Becker, and A. Wiegmann, "Effect of liquid water on transport properties of the gas diffusion layer of polymer electrolyte membrane fuel cells," *International Journal of Hydrogen Energy*, vol. 36, no. 9, pp. 5466–5478, 2011.

[146] V. P. Schulz, P. P. Mukherjee, and H. AndraÌĹ, "Compression Modeling and Transport Characterization of the PEM Fuel Cell Diffusion Medium," in *ASME 2011 9th International Conference on Fuel Cell Science, Engineering and Technology collocated with ASME 2011 5th International Conference on Energy Sustainability*, pp. 623–627, American Society of Mechanical Engineers, 2011.

[147] B. Ramos-Alvarado, J. D. Sole, A. Hernandez-Guerrero, and M. W. Ellis, "Experimental characterization of the water transport properties of PEM fuel cells diffusion media," *Journal of Power Sources*, vol. 218, pp. 221–232, Nov. 2012.

[148] M. K. P. L Bhatnagar, E. P. Gross, "A model for Collision Processes in Gases. I. Small Amplitude Processes in Charged and Neutral One-Component Systems," *Physical Review*, vol. 94, no. 3, pp. 511 – 525, 1954.

[149] C. Pan, M. Hilpert, and C. T. Miller, "Lattice-Boltzmann simulation of two-phase flow in porous media," *Water Resources Research*, vol. 40, Jan. 2004.

[150] T. Koido, T. Furusawa, and K. Moriyama, "An approach to modeling two-phase transport in the gas diffusion layer of a proton exchange membrane fuel cell," *Journal of Power Sources*, vol. 175, pp. 127–136, Jan. 2008.

[151] L. Hao and P. Cheng, "Pore-scale simulations on relative permeabilities of porous media by lattice Boltzmann method," *International Journal of Heat and Mass Transfer*, vol. 53, pp. 1908–1913, Apr. 2010.

[152] L. Chen, H.-B. Luan, Y.-L. He, and W.-Q. Tao, "Pore-scale flow and mass transport in gas diffusion layer of proton exchange membrane fuel cell with interdigitated flow fields," *International Journal of Thermal Sciences*, vol. 51, pp. 132–144, Jan. 2012.

[153] D. Froning, J. Brinkmann, U. Reimer, V. Schmidt, W. Lehnert, and D. Stolten, "3D analysis, modeling and simulation of transport processes in compressed fibrous microstructures, using the Lattice Boltzmann method," *Electrochimica Acta*, vol. 110, pp. 325–334, 2013.

[154] D. Froning, J. Yu, G. Gaiselmann, U. Reimer, I. Manke, V. Schmidt, and W. Lehnert, "Impact of compression on gas transport in non-woven gas diffusion layers of high temperature polymer electrolyte fuel cells," *Journal of Power Sources*, vol. 318, pp. 26–34, 2016.

[155] T. Rosen, J. Eller, J. Kang, N. I. Prasianakis, J. Mantzaras, and F. N. Büchii, "Saturation Dependent Effective Transport Properties of PEFC Gas Diffusion Layers," *Journal of the Electrochemical Society*, vol. 159, pp. F536–F544, Aug. 2012.

[156] P. A. García-Salaberri, G. Hwang, M. Vera, A. Z. Weber, and J. T. Gostick, "Effective diffusivity in partially-saturated carbon-fiber gas diffusion layers: Effect of through-plane saturation distribution," *International Journal of Heat and Mass Transfer*, vol. 86, pp. 319–333, July 2015.

[157] H.-J. Vogel, J. Tölke, V. P. Schulz, M. Krafczyk, and K. Roth, "Comparison of a Lattice-Boltzmann Model, a Full-Morphology Model, and a Pore Network Model for Determining Capillary Pressure-Saturation Relationships," *Vadose Zone Journal*, vol. 4, no. 2, p. 380, 2005.

[158] S. Tsushima, K. Teranishi, and S. Hirai, "Magnetic resonance imaging of the water distribution within a polymer electrolyte membrane in fuel cells," *Electrochemical and Solid-State Letters*, vol. 7, no. 9, pp. A269–A272, 2004.

[159] K. R. Minard, V. V. Viswanathan, P. D. Majors, L.-Q. Wang, and P. C. Rieke, "Magnetic resonance imaging (MRI) of PEM dehydration and gas manifold flooding during continuous fuel cell operation," *Journal of power sources*, vol. 161, no. 2, pp. 856–863, 2006.

[160] K. W. Feindel, S. H. Bergens, and R. E. Wasylishen, "The influence of membrane electrode assembly water content on the performance of a polymer electrolyte membrane fuel cell as investigated by 1h nmr microscopy," *Physical Chemistry Chemical Physics*, vol. 9, no. 15, pp. 1850–1857, 2007.

[161] A. Bazylak, "Liquid water visualization in PEM fuel cells: A review," *International Journal of Hydrogen Energy*, vol. 34, pp. 3845–3857, May 2009.

[162] S. Kim and M. M. Mench, "Investigation of Temperature-Driven Water Transport in Polymer Electrolyte Fuel Cell: Phase-Change-Induced Flow," *Journal of The Electrochemical Society*, vol. 156, no. 3, p. B353, 2009.

[163] N. Pekula, K. Heller, P. A. Chuang, A. Turhan, M. M. Mench, J. S. Brenizer, and K. Ünlü, "Study of water distribution and transport in a polymer electrolyte fuel cell using neutron imaging," *Nuclear Instruments and Methods in Physics Research Section A: Accelerators, Spectrometers, Detectors and Associated Equipment*, vol. 542, pp. 134–141, Apr. 2005.

[164] M. C. Hatzell, A. Turhan, S. Kim, D. S. Hussey, D. L. Jacobson, and M. M. Mench, "Quantification of Temperature Driven Flow in a Polymer Electrolyte Fuel Cell Using High-Resolution Neutron Radiography," *Journal of The Electrochemical Society*, vol. 158, no. 6, p. B717, 2011.

[165] A. Iranzo, P. Boillat, P. Oberholzer, and J. Guerra, "A novel approach coupling neutron imaging and numerical modelling for the analysis of the impact of water on fuel cell performance," *Energy*, vol. 68, pp. 971–981, 2014.

[166] J. M. Lamanna, S. Chakraborty, J. J. Gagliardo, and M. M. Mench, "Isolation of transport mechanisms in PEFCs using high resolution neutron imaging," *International Journal of Hydrogen Energy*, vol. 39, no. 7, pp. 3387–3396, 2014.

[167] A. Forner-Cuenca, V. Manzi-orezzoli, J. Biesdorf, E. Kazzi, D. Streich, L. Gubler, T. J. Schmidt, and P. Boillat, "Advanced Water Management in PEFCs: Diffusion Layers with Patterned Wettability I. Synthetic Routes, Wettability Tuning and Thermal Stability," *Journal of The Electrochemical Society*, vol. 163, no. 8, pp. 788–801, 2016.

[168] A. Forner-Cuenca, J. Biesdorf, A. Lamibrac, V. Manzi-Orezzoli, F. N. Büchi, L. Gubler, T. J. Schmidt, and P. Boillat, "Advanced Water Management in PEFCs: Diffusion Layers with Patterned Wettability II. Measurement of Capillary Pressure Characteristic with Neutron and Synchrotron Imaging," *Journal of The Electrochemical Society*, vol. 163, no. 9, pp. F1038–F1048, 2016.

[169] I. Manke, C. Hartnig, N. Kardjilov, H. Riesemeier, J. Goebbels, R. Kuhn, P. Krüger, and J. Banhart, "In situ Synchrotron X-ray Radiography Investigations of Water Transport in PEM Fuel Cells," *Fuel Cells*, vol. 10, no. 1, pp. 26–34, 2010.

[170] P. Krüger, H. Markötter, J. Haußmann, M. Klages, T. Arlt, J. Banhart, C. Hartnig, I. Manke, and J. Scholta, "Synchrotron x-ray tomography for

investigations of water distribution in polymer electrolyte membrane fuel cells," *Journal of Power Sources*, vol. 196, no. 12, pp. 5250–5255, 2011.

[171] A. Schneider, C. Wieser, J. Roth, and L. Helfen, "Impact of synchrotron radiation on fuel cell operation in imaging experiments," *Journal of Power Sources*, vol. 195, no. 19, pp. 6349–6355, 2010.

[172] T. Mukaide, S. Mogi, J. Yamamoto, A. Morita, S. Koji, K. Takada, K. Uesugi, K. Kajiwara, and T. Noma, "*In situ* observation of water distribution and behaviour in a polymer electrolyte fuel cell by synchrotron X-ray imaging," *Journal of Synchrotron Radiation*, vol. 15, pp. 329–334, Jul 2008.

[173] V. Gurau, M. J. Bluemle, E. S. De Castro, Y.-M. Tsou, J. A. Mann, and T. A. Zawodzinski, "Characterization of transport properties in gas diffusion layers for proton exchange membrane fuel cells 1. Wettability," *Journal of Power Sources*, vol. 160, pp. 1156–1162, Oct. 2006.

[174] K. Tüber, D. Pócza, and C. Hebling, "Visualization of water buildup in the cathode of a transparent pem fuel cell," *Journal of Power Sources*, vol. 124, no. 2, pp. 403–414, 2003.

[175] A. Bazylak, D. Sinton, and N. Djilali, "Dynamic water transport and droplet emergence in pemfc gas diffusion layers," *Journal of Power Sources*, vol. 176, no. 1, pp. 240–246, 2008.

[176] E. Kimball, T. Whitaker, Y. G. Kevrekidis, and J. B. Benziger, "Drops, slugs, and flooding in polymer electrolyte membrane fuel cells," *AIChE Journal*, vol. 54, no. 5, pp. 1313–1332, 2008.

[177] A. Bazylak, D. Sinton, Z.-S. Liu, and N. Djilali, "Effect of compression on liquid water transport and microstructure of PEMFC gas diffusion layers," *Journal of Power Sources*, vol. 163, pp. 784–792, Jan. 2007.

[178] B. Gao, T. S. Steenhuis, Y. Zevi, J. Parlange, R. N. Carter, T. A. Trabold, *et al.*, "Visualization of unstable water flow in a fuel cell gas diffusion layer," *Journal of Power Sources*, vol. 190, no. 2, pp. 493–498, 2009.

[179] J. Ihonen, M. Mikkola, and G. Lindbergh, "Flooding of Gas Diffusion Backing in PEFCs," *Journal of The Electrochemical Society*, vol. 151, no. 8, p. A1152, 2004.

[180] J. P. Feser, A. K. Prasad, and S. G. Advani, "Experimental characterization of in-plane permeability of gas diffusion layers," *Journal of Power Sources*, vol. 162, pp. 1226–1231, Nov. 2006.

[181] M. M. Tomadakis and T. J. Robertson, "Viscous permeability of random fiber structures: comparison of electrical and diffusional estimates with experimental and analytical results," *Journal of Composite Materials*, vol. 39, no. 2, pp. 163–188, 2005.

[182] V. Gurau, M. J. Bluemle, E. S. De Castro, Y.-M. Tsou, T. A. Zawodzinski, and J. A. Mann, "Characterization of transport properties in gas diffusion layers for proton exchange membrane fuel cells 2. Absolute Permeability," *Journal of Power Sources*, vol. 165, pp. 793–802, Mar. 2007.

[183] M. Uchida, Y. Aoyama, N. Eda, and A. Ohta, "Investigation of the Microstructure in the Catalyst Layer and Effects of Both Perfluorosulfonate Ionomer and PTFE-Loaded Carbon on the Catalyst Layer of Polymer Electrolyte Fuel Cells," *Journal of The Electrochemical Society*, vol. 142, no. 12, p. 4143, 1995.

[184] M. S. Ismail, T. Damjanovic, K. Hughes, D. B. Ingham, L. Ma, M. Pourkashanian, and M. Rosli, "Through-plane permeability for untreated and ptfe-treated gas diffusion layers in proton exchange membrane fuel cells," *Journal of fuel cell science and technology*, vol. 7, no. 5, 2010.

[185] M. S. Ismail, T. Damjanovic, D. B. Ingham, L. Ma, and M. Pourkashanian, "Effect of polytetrafluoroethylene-treatment and microporous layer-coating on the in-plane permeability of gas diffusion layers used in proton exchange membrane fuel cells," *Journal of Power Sources*, vol. 195, pp. 6619–6628, Oct. 2010.

[186] L. M. Pant, S. K. Mitra, and M. Secanell, "Absolute permeability and Knudsen diffusivity measurements in PEMFC gas diffusion layers and micro porous layers," *Journal of Power Sources*, vol. 206, pp. 153–160, May 2012.

[187] P. Mangal, M. Dumontier, N. Carrigy, and M. Secanell, "Measurements of permeability and effective in-plane gas diffusivity of gas diffusion media under compression," *ECS Transactions*, vol. 64, no. 3, pp. 487–499, 2014.

[188] F. A. Dullien, *Porous media: fluid transport and pore structure*. Academic press, 1991.

[189] D. R. Baker, C. Wieser, K. C. Neyerlin, and M. W. Murphy, "The use of limiting current to determine transport resistance in PEM fuel cells," *ECS Transactions*, vol. 3, no. 1, pp. 989–999, 2006.

[190] D. R. Baker, D. A. Caulk, K. C. Neyerlin, and M. W. Murphy, "Measurement of Oxygen Transport Resistance in PEM Fuel Cells by Limiting Current Methods," *Journal of The Electrochemical Society*, vol. 156, no. 9, p. B991, 2009.

[191] U. Beuscher, "Experimental Method to Determine the Mass Transport Resistance of a Polymer Electrolyte Fuel Cell," *Journal of The Electrochemical Society*, vol. 153, no. 9, p. A1788, 2006.

[192] N. G. C. Astrath, J. Shen, D. Song, J. H. Rohling, F. B. G. Astrath, J. Zhou, T. Navessin, Z. S. Liu, C. E. Gu, and X. Zhao, "The effect of relative humidity on binary gas diffusion," *The Journal of Physical Chemistry B*, vol. 113, no. 24, pp. 8369–8374, 2009.

[193] N. Zamel, N. G. C. Astrath, X. Li, J. Shen, J. Zhou, F. B. G. Astrath, H. Wang, and Z.-S. Liu, "Experimental measurements of effective diffusion coefficient of oxygen-nitrogen mixture in PEM fuel cell diffusion media," *Chemical Engineering Science*, vol. 65, pp. 931–937, Jan. 2010.

[194] C. Chan, N. Zamel, X. Li, and J. Shen, "Experimental measurement of effective diffusion coefficient of gas diffusion layer/microporous layer in PEM fuel cells," *Electrochimica Acta*, vol. 65, pp. 13–21, 2012.

[195] J. D. Sole, *Investigation of water transport parameters and processes in the gas diffusion layer of PEM fuel cells*. PhD thesis, Virginia Tech, 2008.

[196] X. Wang, T. V. Nguyen, D. S. Hussey, and D. L. Jacobson, "An Experimental Study of Relative Permeability of Porous Media Used in Proton Exchange Membrane Fuel Cells," *Journal of The Electrochemical Society*, vol. 157, no. 12, p. B1777, 2010.

[197] Y. Utaka, Y. Tasaki, S. Wang, T. Ishiji, and S. Uchikoshi, "Method of measuring oxygen diffusivity in microporous media," *International Journal of Heat and Mass Transfer*, vol. 52, pp. 3685–3692, July 2009.

[198] Y. Utaka, I. Hirose, and Y. Tasaki, "Characteristics of oxygen diffusivity and water distribution by X-ray radiography in microporous media in alternate porous layers of different wettability for moisture control in gas diffusion layer of PEFC," *International Journal of Hydrogen Energy*, vol. 36, pp. 9128–9138, July 2011.

[199] D. Iwasaki, Y. Utaka, Y. Tasaki, and S. Wang, "Oxygen diffusion characteristics of gas diffusion layers with moisture," in *ASME 2008 6th International Conference on Nanochannels, Microchannels, and Minichannels*, pp. 1279–1284, American Society of Mechanical Engineers, 2008.

[200] R. Koresawa and Y. Utaka, "Precise measurement of effective oxygen diffusivity for microporous media containing moisture by review of galvanic cell oxygen absorber configuration," *International Journal of Heat and Mass Transfer*, vol. 76, pp. 549–558, Sept. 2014.

[201] N. Zamel, E. Litovsky, S. Shakhshir, X. Li, and J. Kleiman, "Measurement of in-plane thermal conductivity of carbon paper diffusion media in the temperature range of -20°C to +120°C," *Applied Energy*, vol. 88, pp. 3042–3050, Sept. 2011.

[202] K. Jiao and B. Zhou, "Innovative gas diffusion layers and their water removal characteristics in PEM fuel cell cathode," *Journal of Power Sources*, vol. 169, pp. 296–314, June 2007.

[203] I. Nitta, T. Hottinen, O. Himanen, and M. Mikkola, "Inhomogeneous compression of PEMFC gas diffusion layer," *Journal of Power Sources*, vol. 171, pp. 26–36, Sept. 2007.

[204] J. Ge, A. Higier, and H. Liu, "Effect of gas diffusion layer compression on PEM fuel cell performance," *Journal of Power Sources*, vol. 159, pp. 922–927, Sept. 2006.

[205] Y. Gao, T. V. Nguyen, D. S. Hussey, and D. Jacobson, "In Situ Imaging of Water Distribution in a Gas Diffusion Layer by Neutron Radiography," *ECS Transactions*, vol. 33, no. 1, pp. 1435–1441, 2010.

[206] T. Sasabe, S. Tsushima, and S. Hirai, "In-situ visualization of liquid water in an operating PEMFC by soft X-ray radiography," *International Journal of Hydrogen Energy*, vol. 35, pp. 11119–11128, Oct. 2010.

[207] J. P. James, H.-W. Choi, and J. G. Pharoah, "X-ray computed tomography reconstruction and analysis of polymer electrolyte membrane fuel cell porous transport layers," *International Journal of Hydrogen Energy*, vol. 37, pp. 18216–18230, Dec. 2012.

[208] T. J. Mason, J. Millichamp, P. R. Shearing, and D. J. L. Brett, "A study of the effect of compression on the performance of polymer electrolyte fuel cells using electrochemical impedance spectroscopy and dimensional change analysis," *International Journal of Hydrogen Energy*, vol. 38, pp. 7414–7422, June 2013.

[209] M. Mortazavi and K. Tajiri, "Liquid water breakthrough pressure through gas diffusion layer of proton exchange membrane fuel cell," *International Journal of Hydrogen Energy*, vol. 39, pp. 9409–9419, June 2014.

[210] I. Nitta, S. Karvonen, O. Himanen, and M. Mikkola, "Modelling the Effect of Inhomogeneous Compression of GDL on Local Transport Phenomena in a PEM Fuel Cell," *Fuel Cells*, vol. 8, pp. 410–421, Dec. 2008.

[211] Z. Y. Su, C. T. Liu, H. P. Chang, C. H. Li, K. J. Huang, and P. C. Sui, "A numerical investigation of the effects of compression force on PEM fuel cell performance," *Journal of Power Sources*, vol. 183, pp. 182–192, Aug. 2008.

[212] J. Park and X. Li, "An experimental and numerical investigation on the cross flow through gas diffusion layer in a PEM fuel cell with a serpentine flow channel," *Journal of Power Sources*, vol. 163, pp. 853–863, Jan. 2007.

[213] J. Bachman, A. Santamaria, H.-Y. Tang, and J. W. Park, "Investigation of polymer electrolyte membrane fuel cell parallel flow field with induced cross flow," *Journal of Power Sources*, vol. 198, pp. 143–148, 2012.

[214] A. D. Santamaria, M. K. Becton, N. J. Cooper, A. Z. Weber, and J. W. Park, "Effect of cross-flow on PEFC liquid-water distribution: An in-situ high-resolution neutron radiography study," *Journal of Power Sources*, vol. 293, pp. 162–169, 2015.

[215] A. C. Olesen, T. Berning, and S. K. Kaer, "The Effect of Inhomogeneous Compression on Water Transport in the Cathode of a Proton Exchange Membrane Fuel Cell," *Journal of Fuel Cell Science and Technology*, vol. 9, no. 3, p. 031010, 2012.

[216] T. Hottinen, O. Himanen, S. Karvonen, and I. Nitta, "Inhomogeneous compression of PEMFC gas diffusion layer," *Journal of Power Sources*, vol. 171, pp. 113–121, Sept. 2007.

[217] Y. Wang and K. S. Chen, "Effect of Spatially-Varying GDL Properties and Land Compression on Water Distribution in PEM Fuel Cells," *Journal of The Electrochemical Society*, vol. 158, no. 11, p. B1292, 2011.

[218] P. H. Chi, S. H. Chan, F. B. Weng, A. Su, P. C. Sui, and N. Djilali, "On the effects of non-uniform property distribution due to compression in the gas diffusion layer of a PEMFC," *International Journal of Hydrogen Energy*, vol. 35, pp. 2936–2948, Apr. 2010.

[219] P. Chippar, O. Kyeongmin, K. Kang, and H. Ju, "A numerical investigation of the effects of gdl compression and intrusion in polymer electrolyte fuel cells (pefcs)," *international journal of hydrogen energy*, vol. 37, no. 7, pp. 6326–6338, 2012.

[220] K.-J. Lee, J. H. Nam, and C.-J. Kim, "Pore-network analysis of two-phase water transport in gas diffusion layers of polymer electrolyte membrane fuel cells," *Electrochimica Acta*, vol. 54, pp. 1166–1176, Jan. 2009.

[221] M. Rebai and M. Prat, "Scale effect and two-phase flow in a thin hydrophobic porous layer. Application to water transport in gas diffusion layers of proton exchange membrane fuel cells," *Journal of Power Sources*, vol. 192, pp. 534–543, July 2009.

[222] A. Z. Weber and J. Newman, "Coupled Thermal and Water Management in Polymer Electrolyte Fuel Cells," *Journal of The Electrochemical Society*, vol. 153, no. 12, p. A2205, 2006.

[223] Y. Wang and C.-y. Wang, "A Nonisothermal, Two-Phase Model for Polymer Electrolyte Fuel Cells," *Journal of The Electrochemical Society*, vol. 153, no. 6, p. A1193, 2006.

[224] A. Thomas, G. Maranzana, S. Didierjean, J. Dillet, and O. Lottin, "Thermal effect on water transport in proton exchange membrane fuel cell," *Fuel Cells*, vol. 12, no. 2, pp. 212–224, 2012.

[225] S. K. Das and A. S. Bansode, "Heat and mass transport in proton exchange membrane fuel cells - A review," *Heat Transfer Engineering*, vol. 30, no. 9, pp. 691–719, 2009.

[226] S. G. Kandlikar and Z. Lu, "Thermal management issues in a PEMFC stack âĂŞ A brief review of current status," *Applied Thermal Engineering*, vol. 29, pp. 1276–1280, may 2009.

[227] J. X. Liu, H. Guo, F. Ye, C.-F. Ma, *et al.*, "Interfacial phenomena and heat transfer in proton exchange membrane fuel cells," *Interfacial Phenomena and Heat Transfer*, vol. 3, no. 3, 2015.

[228] X. Li and I. Sabir, "Review of bipolar plates in PEM fuel cells: Flow-field designs," *International Journal of Hydrogen Energy*, vol. 30, pp. 359–371, Mar. 2005.

[229] Z. Zhan, C. Wang, W. Fu, and M. Pan, "Visualization of water transport in a transparent PEMFC," *International Journal of Hydrogen Energy*, vol. 37, pp. 1094–1105, Jan. 2012.

[230] M. S. Ismail, D. Borman, T. Damjanovic, D. B. Ingham, and M. Pourkashanian, "On the through-plane permeability of microporous layer-coated gas diffusion layers used in proton exchange membrane fuel cells," *International Journal of Hydrogen Energy*, vol. 36, pp. 10392–10402, Aug. 2011.

[231] J. Ward, *Turbulent flow in porous media*. University of Arkansas, Engineering Experiment Station, 1965.

[232] Y. Tabe, Y. Lee, T. Chikahisa, and M. Kozakai, "Numerical simulation of liquid water and gas flow in a channel and a simplified gas diffusion layer model of polymer electrolyte membrane fuel cells using the lattice Boltzmann method," *Journal of Power Sources*, vol. 193, pp. 24–31, Aug. 2009.

[233] Z. Y. Ahmad, S. Didari, J. Moon, and T. A. Harris, "Computational fluid dynamics of water droplet formation and detachment from gas diffusion layer," *ECS Transactions*, vol. 45, no. 23, pp. 89–100, 2013.

[234] J. D. Fairweather, P. Cheung, and D. T. Schwartz, "The effects of wetproofing on the capillary properties of proton exchange membrane fuel cell gas diffusion layers," *Journal of Power Sources*, vol. 195, pp. 787–793, Feb. 2010.

[235] J. U. Brackbill, D. B. Kothe, and C. Zemach, "A continuum method for modeling surface tension," *Journal of Computational Physics*, vol. 100, pp. 335–354, 1992.

[236] P. J. Roache, *Verification and validation in computational science and engineering*. Hermosa, 1998.

[237] I. B. Celik, U. Ghia, P. J. Roache, C. J. Freitas, H. Coleman, and P. E. Raad, "Procedure for Estimation and Reporting of Uncertainty Due to Discretization in CFD Applications," *Journal of Fluids Engineering*, vol. 130, no. 7, p. 078001, 2008.

[238] Ansys, "14.0 theory guide," *Ansys Documentation, Release 14*, 2011.

[239] M. M. Tomadakis and S. V. Sotirchos, "Effective kundsen diffusivities in structures of randomly overlapping fibers," *AIChE journal*, vol. 37, no. 1, pp. 74–86, 1991.

[240] B. R. Gebart, "Permeability of Unidirectional Reinforcements for RTM," *Journal of Composite Materials*, vol. 26, pp. 1100–1133, Jan. 1992.

[241] C. Quesnel, R. Cao, J. Lehr, A.-M. Kietzig, A. Z. Weber, and J. T. Gostick, "Dynamic Percolation and Droplet Growth Behavior in Porous Electrodes of Polymer Electrolyte Fuel Cells," *The Journal of Physical Chemistry C*, vol. 119, no. 40, pp. 22934–22944, 2015.

[242] V. Radhakrishnan and P. Haridoss, "Effect of cyclic compression on structure and properties of a Gas Diffusion Layer used in PEM fuel cells," *International Journal of Hydrogen Energy*, vol. 35, pp. 11107–11118, Oct. 2010.

[243] Z. Zhan, J. Xiao, Y. Zhang, M. Pan, and R. Yuan, "Gas diffusion through differently structured gas diffusion layers of PEM fuel cells," *International Journal of Hydrogen Energy*, vol. 32, pp. 4443–4451, Dec. 2007.

[244] P. A. García-Salaberri, M. Vera, and I. Iglesias, "Modeling of the anode of a liquid-feed DMFC: Inhomogeneous compression effects and two-phase transport phenomena," *Journal of Power Sources*, vol. 246, pp. 239–252, Jan. 2014.

[245] J. Becker, V. Schulz, and A. Wiegmann, "Numerical determination of two-phase material parameters of a gas diffusion layer using tomography images," *Journal of fuel cell science and ...*, 2008.

[246] M. Hilpert and C. T. Miller, "Pore-morphology-based simulation of drainage in totally wetting porous media," *Advances in Water Resources*, vol. 24, no. 3, pp. 243–255, 2001.

[247] M. Aghighi, M. A. Höh, W. Lehnert, G. Merle, and J. Gostick, "Simulation of a full fuel cell membrane electrode assembly using pore network modeling," *Journal of The Electrochemical Society*, vol. 163, no. 5, pp. F384–F392, 2016.

[248] S. Van Der Walt, S. C. Colbert, and G. Varoquaux, "The NumPy array: A structure for efficient numerical computation," *Computing in Science and Engineering*, vol. 13, no. 2, pp. 22–30, 2011.

[249] E. Jones, T. Oliphant, P. Peterson, *et al.*, "SciPy: Open source scientific tools for Python," 2001. [Online; accessed 2015-11-09].

[250] B. Delaunay, "Sur la sphere vide," *Izv. Akad. Nauk SSSR, Otdelenie Matematicheskii i Estestvennyka Nauk*, vol. 7, no. 793-800, pp. 1–2, 1934.

[251] G. Voronoï, "Nouvelles applications des paramètres continus à la théorie des formes quadratiques. deuxième mémoire. recherches sur les parallélloèdres primitifs.," *Journal für die reine und angewandte Mathematik*, vol. 134, pp. 198–287, 1908.

[252] J. Becker, R. Flückiger, M. Reum, F. N. Büchi, F. Marone, and M. Stampanoni, "Determination of material properties of gas diffusion layers: experiments and simulations using phase contrast tomographic microscopy," *Journal of The Electrochemical Society*, vol. 156, no. 10, pp. B1175–B1181, 2009.

[253] J. D'Errico, "Inhull efficient test for points inside a convex hull in n dimensions." `http://uk.mathworks.com/matlabcentral/fileexchange/10226-inhull`, 2012. Accessed: 2012-09-06.

[254] D. Silin and T. Patzek, "Pore space morphology analysis using maximal inscribed spheres," *Physica A: Statistical Mechanics and its Applications*, vol. 371, no. 2, pp. 336–360, 2006.

[255] H. Dong and M. J. Blunt, "Pore-network extraction from micro-computerized-tomography images," *Physical review E*, vol. 80, no. 3, p. 036307, 2009.

[256] Z. Liang, M. A. Ioannidis, and I. Chatzis, "Geometric and topological analysis of three-dimensional porous media: pore space partitioning based on morphological skeletonization," *Journal of colloid and interface science*, vol. 221, no. 1, pp. 13–24, 2000.

[257] D. Wilkinson and J. F. Willemsen, "Invasion percolation: a new form of percolation theory," *Journal of Physics A: Mathematical and General*, vol. 16, no. 14, p. 3365, 1983.

[258] J. T. Gostick, M. A. Ioannidis, M. D. Pritzker, and M. W. Fowler, "Impact of liquid water on reactant mass transfer in pem fuel cell electrodes," *Journal of the Electrochemical Society*, vol. 157, no. 4, pp. B563–B571, 2010.

[259] J. T. Gostick, M. A. Ioannidis, M. W. Fowler, and M. D. Pritzker, "Characterization of the capillary properties of gas diffusion media," in *Modeling and Diagnostics of Polymer Electrolyte Fuel Cells*, pp. 225–254, Springer, 2009.

[260] M. Fazeli, J. Hinebaugh, and A. Bazylak, "Investigating inlet condition effects on pemfc gdl liquid water transport through pore network modeling," *Journal of The Electrochemical Society*, vol. 162, no. 7, pp. F661–F668, 2015.

[261] V. P. Schulz, E. A. Wargo, and E. C. Kumbur, "Pore-morphology-based simulation of drainage in porous media featuring a locally variable contact angle," *Transport in Porous Media*, vol. 107, no. 1, pp. 13–25, 2015.

[262] D. Chang and M. A. Ioannidis, "Magnetization evolution in network models of porous rock under conditions of drainage and imbibition," *Journal of colloid and interface science*, vol. 253, no. 1, pp. 159–170, 2002.

[263] I. V. Zenyuk, D. Y. Parkinson, L. G. Connolly, and A. Z. Weber, "Gas-diffusion-layer structural properties under compression via x-ray tomography," *Journal of Power Sources*, vol. 328, pp. 364–376, 2016.

[264] N. S. Martys, "Diffusion in partially-saturated porous materials," *Materials and Structures*, vol. 32, no. 8, pp. 555–562, 1999.

[265] I. V. Zenyuk, D. Y. Parkinson, G. Hwang, and A. Z. Weber, "Probing water distribution in compressed fuel-cell gas-diffusion layers using X-ray computed tomography," *Electrochemistry Communications*, vol. 53, pp. 24–28, Apr. 2015.

[266] Y. Tabuchi, T. Shiomi, O. Aoki, N. Kubo, and K. Shinohara, "Effects of heat and water transport on the performance of polymer electrolyte membrane fuel cell under high current density operation," *Electrochimica Acta*, vol. 56, pp. 352–360, dec 2010.

[267] B. Straubhaar, J. Pauchet, and M. Prat, "Water transport in gas diffusion layer of a polymer electrolyte fuel cell in the presence of a temperature gradient. Phase change effect," *International Journal of Hydrogen Energy*, pp. 2–9, apr 2015.

[268] C. Qin, "Water transport in the gas diffusion layer of a polymer electrolyte fuel cell: Dynamic pore-network modeling," *Journal of The Electrochemical Society*, vol. 162, no. 9, pp. F1036–F1046, 2015.

[269] C. Simon, F. Hasché, D. Müller, and H. A. Gasteiger, "Influence of the gas diffusion layer compression on the oxygen mass transport in pem fuel cells," *ECS Transactions*, vol. 69, no. 17, pp. 1293–1302, 2015.

[270] C. Quick, D. Ritzinger, W. Lehnert, and C. Hartnig, "Characterization of water transport in gas diffusion media," *Journal of Power Sources*, vol. 190, pp. 110–120, May 2009.

[271] M. Ciureanu and R. Roberge, "Electrochemical impedance study of pem fuel cells. experimental diagnostics and modeling of air cathodes," *The Journal of Physical Chemistry B*, vol. 105, no. 17, pp. 3531–3539, 2001.

[272] S. Chevalier, J. Lee, N. Ge, R. Yip, P. Antonacci, Y. Tabuchi, T. Kotaka, and A. Bazylak, "In operando measurements of liquid water saturation distributions and effective diffusivities of polymer electrolyte membrane fuel cell gas diffusion layers," *Electrochimica Acta*, 2016.

[273] J. H. Rohling, J. Shen, C. Wang, J. Zhou, and C. E. Gu, "Determination of binary diffusion coefficients of gases using photothermal deflection technique," *Applied Physics B*, vol. 87, no. 2, pp. 355–362, 2007.

[274] P. A. García-Salaberri, J. T. Gostick, G. Hwang, A. Z. Weber, and M. Vera, "Effective diffusivity in partially-saturated carbon-fiber gas diffusion layers: Effect of local saturation and application to macroscopic continuum models," *Journal of Power Sources*, vol. 296, pp. 440–453, 2015.

[275] J. Crank, *The mathematics of diffusion*. Oxford university press, 1979.

[276] J. E. Guyer, D. Wheeler, and J. A. Warren, "FiPy : Partial Differential Equations with Python," *Computing in Science & Engineering*, vol. 11, no. 3, pp. 6–15, 2009.

[277] N. Zamel, X. Li, and J. Shen, "Correlation for the Effective Gas Diffusion Coefficient in Carbon Paper Diffusion Media," *Energy & Fuels*, vol. 23, pp. 6070–6078, Dec. 2009.

[278] Y. Sun and I. S. Wichman, "On transient heat conduction in a one-dimensional composite slab," *International Journal of Heat and Mass Transfer*, vol. 47, no. 6-7, pp. 1555–1559, 2004.

[279] J. A. Currie, "Gaseous diffusion in porous media part 1.-a non-steady state method," *British Journal of Applied Physics*, vol. 11, no. 8, p. 314, 1960.

[280] R. R. Rashapov and J. T. Gostick, "In-Plane Effective Diffusivity in PEMFC Gas Diffusion Layers," *Transport in Porous Media*, 2016.

[281] M. Sahimi, B. D. Hughes, L. E. Scriven, and H. T. Davis, "Critical exponent of percolation conductivity by finite- size scaling," *Journal of Physics C: Solid State Physics*, vol. 16, pp. L521–L527, 1983.

[282] R. B. Pandey, D. Stauffer, A. Margolina, and J. G. Zabolitzky, "Diffusion on random systems above, below, and at their percolation threshold in two and three dimensions," *Journal of Statistical Physics*, vol. 34, no. 3-4, pp. 427–450, 1984.

[283] N. Khajeh-Hosseini-Dalasm, T. Sasabe, T. Tokumasu, and U. Pasaogullari, "Effects of polytetrafluoroethylene treatment and compression on gas diffusion layer microstructure using high-resolution X-ray computed tomography," *Journal of Power Sources*, vol. 266, pp. 213–221, nov 2014.

[284] T. Sasabe, G. Inoue, S. Tsushima, S. Hirai, T. Tokumasu, and U. Pasaogullari, "Investigation on effect of ptfe treatment on gdl microstructure by high-resolution x-ray ct," *ECS Transactions*, vol. 50, no. 2, pp. 735–744, 2012.

[285] A. Rofaiel, J. S. Ellis, P. R. Challa, and A. Bazylak, "Heterogeneous through-plane distributions of polytetrafluoroethylene in polymer electrolyte membrane fuel cell gas diffusion layers," *Journal of Power Sources*, vol. 201, pp. 219–225, mar 2012.

[286] M. El Hannach and E. Kjeang, "Stochastic Microstructural Modeling of PEFC Gas Diffusion Media," *Journal of the Electrochemical Society*, vol. 161, no. 9, pp. F951–F960, 2014.

[287] W. Anderson, "Wettability Literature Survey- Part 2: Wettability Measurement," *Journal of Petroleum Technology*, vol. 38, no. 11, pp. 1246–1262, 1986.

[288] T. Koido, T. Furusawa, K. Moriyama, and K. Takato, "Two-phase Transport Properties and Transport Simulation of the Gas Diffusion Layer of a PEFC," *ECS Transactions*, vol. 3, no. 1, pp. 425–434, 2006.

[289] J. D. Fairweather, P. Cheung, J. St-Pierre, and D. T. Schwartz, "A microfluidic approach for measuring capillary pressure in PEMFC gas diffusion layers," *Electrochemistry Communications*, vol. 9, no. 9, pp. 2340–2345, 2007.

[290] I. R. Harkness, N. Hussain, L. Smith, and J. D. B. Sharman, "The use of a novel water porosimeter to predict the water handling behaviour of gas diffusion media used in polymer electrolyte fuel cells," *Journal of Power Sources*, vol. 193, no. 1, pp. 122–129, 2009.

[291] P. Cheung, J. D. Fairweather, and D. T. Schwartz, "Characterization of internal wetting in polymer electrolyte membrane gas diffusion layers," *Journal of Power Sources*, vol. 187, no. 2, pp. 487–492, 2009.

[292] J. Bear, "Dynamics of fluids in porous media," *American Elsevier, New York*, 1972.

[293] B. Markicevic, A. Bazylak, and N. Djilali, "Determination of transport parameters for multiphase flow in porous gas diffusion electrodes using a capillary network model," *Journal of Power Sources*, vol. 171, pp. 706–717, sep 2007.

[294] K.-J. Lee, J. H. Kang, J. H. Nam, and C.-J. Kim, "Steady liquid water saturation distribution in hydrophobic gas-diffusion layers with engineered pore paths: An invasion-percolation pore-network analysis," *Journal of Power Sources*, vol. 195, pp. 3508–3512, jun 2010.

[295] B. Markicevic and N. Djilali, "Analysis of liquid water transport in fuel cell gas diffusion media using two-mobile phase pore network simulations," *Journal of Power Sources*, vol. 196, pp. 2725–2734, Mar. 2011.

[296] P. P. Mukherjee, Q. Kang, and C.-Y. Wang, "Pore-scale modeling of two-phase transport in polymer electrolyte fuel cellsâĂŤprogress and perspective," *Energy & Environmental Science*, vol. 4, no. 2, p. 346, 2011.

[297] S. P. Kuttanikkad, M. Prat, and J. Pauchet, "Pore-network simulations of two-phase flow in a thin porous layer of mixed wettability: Application to water transport in gas diffusion layers of proton exchange membrane fuel cells," *Journal of Power Sources*, vol. 196, pp. 1145–1155, feb 2011.

[298] E. Gauthier, Q. Duan, T. Hellstern, and J. Benziger, "Water Flow in, Through, and Around the Gas Diffusion Layer," *Fuel Cells*, vol. 12, pp. 835–847, oct 2012.

[299] R. Alink and D. Gerteisen, "Modeling the Liquid Water Transport in the Gas Diffusion Layer for Polymer Electrolyte Membrane Fuel Cells Using a Water Path Network," *Energies*, vol. 6, pp. 4508–4530, sep 2013.

[300] B. S. Kim and P. Harriott, "Critical entry pressure for liquids in hydrophobic membranes," *Journal of Colloid And Interface Science*, vol. 115, no. 1, pp. 1–8, 1987.

[301] F.-A. Fortin, F.-M. De Rainville, M.-A. Gardner, M. Parizeau, and C. Gagné, "DEAP : Evolutionary Algorithms Made Easy," *Journal of Machine Learning Research*, vol. 13, pp. 2171–2175, 2012.

[302] Y. Hold-Geoffroy, O. Gagnon, and M. Parizeau, "Once you SCOOP, no need to fork," *Proceedings of the 2014 Annual Conference on Extreme Science and Engineering Discovery Environment - XSEDE '14*, pp. 1–8, 2014.

[303] A. Z. Weber, "Improved modeling and understanding of diffusion-media wettability on polymer-electrolyte-fuel-cell performance," *Journal of Power Sources*, vol. 195, no. 16, pp. 5292–5304, 2010.

[304] L. Gao and T. J. McCarthy, "Contact angle hysteresis explained.," *Langmuir : the ACS journal of surfaces and colloids*, vol. 22, no. 14, pp. 6234–6237, 2006.

[305] J. T. Gostick and A. Z. Weber, "Resistor-Network Modeling of Ionic Conduction in Polymer Electrolytes," *Electrochimica Acta*, vol. 179, pp. 137–145, 2015.

[306] M. Schalenbach, M. A. Höh, J. T. Gostick, W. Lueke, and D. Stolten, "Gas Permeation through Nafion. Part 2: Resistor Network Model," *Journal of Physical Chemistry C*, vol. 119, no. 45, pp. 25156–25169, 2015.

[307] I. V. Zenyuk, E. Medici, J. Allen, and A. Z. Weber, "Coupling continuum and pore-network models for polymer-electrolyte fuel cells," *International Journal of Hydrogen Energy*, pp. 1–15, 2015.

[308] E. F. Medici, I. V. Zenyuk, D. Y. Parkinson, A. Z. Weber, and J. S. Allen, "Understanding Water Transport in Polymer Electrolyte Fuel Cells Using Coupled Continuum and Pore-Network Models," *Fuel Cells*, no. 0, pp. 1–9, 2016.